POLITECHNIKA WARSZAWSKA

WYDZIAŁ MECHATRONIKI

Rozprawa doktorska

mgr inż. Krzysztof Malowany

System cyfrowej korelacji obrazu do badania
złożonych obiektów inżynierskich

Promotor
prof. dr hab. inż. Małgorzata Kujawińska

Promotor pomocniczy
dr inż. Marcin Malesa

WARSZAWA 2019

Streszczenie

Podstawą pracy jest cykl dwunastu publikacji, w tym jedenastu z listy czasopism JCR i jednej publikacji w recenzowanych materiałach konferencyjnych. W niniejszym przewodniku podsumowałem badania zrealizowane w trakcie przygotowania rozprawy. Celem pracy jest rozszerzenie aplikacyjności metody cyfrowej korelacji obrazu (CKO) do pomiaru złożonych obiektów inżynierskich, poprzez opracowanie nowych metodyk pomiarowych i ścieżek przetwarzania danych oraz rozbudowę układu pomiarowego o nowe konfiguracje pomiarowe i moduły obliczeniowe. Aby osiągnąć założony cel w pracy przedstawiono rozwiązania trzech zagadnień.

W ramach pierwszego zagadnienia rozszerzyłem aplikacyjność tradycyjnych układów 3D CKO poprzez opracowanie szeregu modyfikacji w metodyce przetwarzania wyników CKO umożliwiających zastosowanie tej metody do efektywnej analizy wybranych złożonych procesów zachodzących w obiektach inżynierskich. Przykłady implementacji opracowanych modyfikacji obejmują analizę przemieszczeń i odkształceń w obrazach olejnych na podłożu płóciennym (struktura kompozytowa), rurociągów przemysłowych, rozpór stalowych wykorzystywanych w budownictwie, zwierciadeł optycznych segmentowych teleskopów astronomicznych oraz wysokociśnieniowych zbiorników na wodór i metan.

W ramach drugiego zagadnienia opracowałem wielokamerowy system CKO 3D, umożliwiający pomiary wielu pól pomiarowych rozproszonych w przestrzeni we wspólnym układzie współrzędnych. Opracowany system wykorzystałem do pomiarów instalacji syntezy amoniaku oraz hali magazynowej wykonanej z samonośnej blachy łukowej.

Trzecie zagadnienie obejmowało opracowanie efektywnej metodyki kalibracji i walidacji modeli numerycznych z wykorzystaniem eksperymentalnych danych polowych na przykładzie wielkogabarytowej samonośnej konstrukcji łukowej wykonanej z cienkościennych blach profilowanych.

Udowodniłem, że udoskonalenia metody 3D CKO oraz opracowane w ramach pracy metodyki pomiaru mogą w przyszłości stanowić, wraz z opracowaniami udostępnionymi przez inne grupy badawcze, zestaw narzędzi eksperymentalnych, bardzo dobrze dopasowanych do wymagań hybrydowej, eksperymentalno-numerycznej analizy istniejących i opracowanych w przyszłości skomplikowanych obiektów inżynierskich.

Słowa kluczowe: *mechanika eksperymentalna, cyfrowa korelacja obrazu, opto-numeryczne systemy pomiarowe, testy nieniszczące, metoda elementów skończonych*

Abstract

The basis of the thesis is a series of 12 articles, including 11 in the journals from the JCR list and 1 in peer-reviewed conference materials. The guide summarizes the research carried out during preparation of the thesis. The main objective of the thesis is to enhance the applicability of a digital image correlation method (DIC) for measuring complex engineering structures via developing new measuring methodologies and data processing paths as well as expanding the measuring system by adding new measuring configurations and computational modules. In order to meet the set goal, the thesis provides the solutions to three problems.

Within the first one, I enhanced the applicability of traditional 3D DIC systems by developing a number of modifications in the methodology of processing DIC results that allow for using this method for the effective analysis of the selected complex processes occurring in engineering structures. The examples of the implementation of the developed modifications include the analysis of displacements and deformations in paintings on canvas (composite structure), industrial pipelines, steel struts used in construction industry, optical mirrors of segmented astronomical telescopes and high pressure hydrogen and methane vessels.

As part of the second problem, I developed a multi-camera 3D DIC system allowing for the measurements of a number of measurement fields distributed in space in a common coordinate system. The developed system was used to measure the installation for ammonia synthesis and storage hall made of self-supporting arch-shaped steel sheets.

The third problem covered the development of the effective methodology for calibration and validation of numerical models with the use of experimental full field data by the example of a large self-supporting arch-shaped structure made of thin-walled profiled steel sheets.

I proved that the refinements of the 3D DIC method and the measurement methodologies developed within the thesis may become, along with the developments provided by other research groups, a set of experimental tools, well-adjusted to the requirements of hybrid, experimental-numerical analysis of the existing and future complex engineering structures.

Keywords: *experimental mechanics, digital image correlation, opto-numerical measurement systems, nondestructive testing, finite element method*

Spis treści

1. Wstęp

1.1. Działalność naukowa w trakcie realizacji rozprawy doktorskiej

W lutym 2012 roku rozpocząłem studia doktoranckie pod kierunkiem prof. dr hab. inż. Małgorzaty Kujawińskiej na Wydziale Mechatroniki Politechniki Warszawskiej. Jako doktorant prowadziłem badania naukowe skoncentrowane na rozwoju optycznych metod pomiarowych, w szczególności dostosowaniu ich funkcjonalności do potrzeb docelowych użytkowników. Tematyka prowadzonych przeze mnie badań naukowych i prac rozwojowych obejmuje rozwój numerycznych i eksperymentalnych modyfikacji metody cyfrowej korelacji obrazu (CKO) do pomiaru złożonych obiektów inżynierskich. Zainteresowanie tą tematyką rozpoczęło się wraz z moim udziałem w realizacji projektu MONIT („Monitorowanie Stanu Technicznego Konstrukcji i Ocena jej Żywotności", POIG.0 101.0 2-00-013/0 8-00). W ramach prac prowadzonych od 2009 do 2013 roku w zespole prowadzonym przez prof. dr hab. inż. Małgorzatę Kujawińską, brałem udział w opracowywaniu innowacyjnych rozwiązań technologicznych w zakresie metod i systemów do monitorowania stanu konstrukcji oraz ostrzegania o możliwych sytuacjach awaryjnych dla obiektów o wymaganym niskim poziomie ryzyka awarii. W ramach projektu brałem udział w opracowaniu metodyki pomiarów *in-situ* obiektów przemysłowych metodą cyfrowej korelacji obrazu (CKO) . W wyniku realizacji prac zaimplementowałem metodę CKO w budownictwie do pomiaru zapraw cementowych podczas próby ściskania murków ceglanych i belek betonowych podczas próby ściskania (we współpracy z Instytutem Techniki Budowlanej) oraz w energetyce do pomiaru rurociągów technicznych (we współpracy z PGE S.A. oraz TAURON S.A.).W trakcie realizacji rozprawy byłem głównym wykonawcą w dwóch grantach Dziekana Wydziału Politechniki Warszawskiej w 2012 i 2013 roku. Przeprowadzone prace umożliwiły zastosowanie metody CKO w praktyce konserwatorów dzieł sztuki do oceny jakości napraw obrazów olejnych będących złożonymi strukturami kompozytowymi. Prace nad rozwojem metody CKO kontynuowałem w projekcie OPT4BLACH („Opto-numeryczne metody badań i monitorowania nisko-kosztowych obiektów użyteczności publicznej z cienkościennych blach profilowanych", NCBiR PBS1/A2/9/2012). W ramach prac prowadzonych w OPT4BLACH od 2012 do 2016 roku opracowałem metodykę pomiarów cienkościennych konstrukcji z blachy łukowej (z wykorzystaniem metody CKO), która umożliwiła kalibrację i walidację modeli numerycznych tego typu konstrukcji.

W 2012 roku wraz z współpracownikami z Instytutu Mikromechaniki i Fotoniki założyłem firmę KSM Vision Sp. z o.o. będącą *spin-off'em* Politechniki Warszawskiej. Na początku swojej działalności firma była nastawiona na komercjalizację systemu CKO opracowanego w ramach projektu MONIT, na podstawie licencji wydanej przez Politechnikę Warszawską. W ramach działań komercyjnych wdrożyłem system CKO do pomiaru obiektów przemysłowych. Na szczególną uwagę zasługują wdrożenia:

- pomiar przemieszczeń newralgicznych połączeń na rurociągach pary świeżej (trójniki, czwórniki) na blokach energetycznych w TAURON Wytwarzanie S.A.,
- pomiar przemieszczeń i temperatury newralgicznych połączeń na rurociągach technicznych w Zakładach Azotowych w Puławach oraz Kędzierzynie-Koźlu,
- pomiar przemieszczeń i temperatury pompy zębatej oraz zaworu wysokociśnieniowego w trakcie rozruchu na instalacji w Basell Orlen Polyefilens Sp. z o.o.,
- pomiar przemieszczeń kompensatorów mieszkowych w miejskiej sieci ciepłowniczej dla Veolia Energia Warszawa S.A..

Za zrealizowane w 2013 roku w tej tematyce prace otrzymałem, jako członek pięcioosobowego zespołu pod kierunkiem prof. dr hab. inż. Małgorzaty Kujawińskiej, Nagrodę Naukową Politechniki Warszawskiej za szczególne osiągnięcia uwieńczone transferem prac naukowych i technicznych na potrzeby gospodarki.

W latach 2013 – 2016 brałem udział w trzech konferencjach międzynarodowych: *Validation of Computational Mechanics Models* w Londynie, Wielka Brytania (prezentacja ustna, 2013), *13th IMEKO TC10 Workshop on Technical Diagnostics - Advanced measurement tools in technical diagnostics for systems' reliability and safety* w Warszawie, Polska (prezentacja ustna, 2014), *Sensors and Smart Structures Technologies for Civil, Mechanical, and Aerospace Systems* w Las Vegas, Stany Zjednoczone Ameryki (sesja plakatowa, 2016). W 2017 roku brałem udział w programie akceleracji MIT Enterprise Forum Poland, realizowanym we współpracy z dużymi przedsiębiorstwami dla start-up'ów w branży energetycznej, surowcowej, ochrony zdrowia oraz finansowej.

Na mój dorobek naukowy składa się szereg publikacji (Tab. 1.1) związanych przede wszystkim z tematyką metody CKO oraz wykorzystaniem optycznych metod pomiarowych w przemyśle.

Oprócz prac badawczych i wdrożeniowych związanych z wykorzystaniem metody CKO, w ramach pracy naukowej zajmuję się optycznymi systemami kontroli jakości na liniach

produkcyjnych, ze szczególnym uwzględnieniem metody triangulacji laserowej oraz dedykowanych konstrukcji optycznych. Na zaprojektowane i wdrożone urządzenie do obserwacji kołowej zamknięć butelek w 2018 roku uzyskałem Patent RP. Od 2017 jestem kierownikiem projektu „Innowacyjne systemy optycznej kontroli jakości w procesach pakowania w przemyśle farmaceutycznym i spożywczym", realizowanego w ramach grantu *Szybka Ścieżka* NCBiR, w firmie KSM Vision Sp. z o.o..

Tabela 1.1. Wskaźniki bibliometryczne dorobku naukowego.

	Rozprawa	Dorobek naukowy
Recenzowane publikacje	12	23
Publikacje z listy JCR	11	13
Pierwszy autor	4	5
Pierwszy autor na liście JCR	4	4
Patent	0	1
Sumaryczny Impact Factor	23,555	28,911
Suma punktów MNiSW	340	520
Index Hirscha (Scopus)	6	8
Index Hirscha (Scopus) bez autocytowań	6	6
Liczba cytowań (Scopus)	109	159

1.2. Motywacja i cel pracy

Na etapie projektowania i eksploatacji złożonych struktur inżynierskich wykorzystywane są techniki hybrydowe, w których metody eksperymentalne i numeryczne uzupełniają się wzajemnie [1] w trakcie procesu analizy złożonych konstrukcji. Powszechną praktyką w mechanice eksperymentalnej jest walidacja modelu numerycznego za pomocą czujników punktowych (np. czujników tensometrycznych). Są one przymocowane do badanej struktury w miejscach, w których spodziewane są największe koncentracje naprężeń (na podstawie analizy modelu numerycznego). Jest to podejście proste i tanie, ale problem może wystąpić, jeśli wstępny (uproszczony) model numeryczny nie wskaże wszystkich miejsc, w których występują koncentracje naprężeń. To z kolei może powodować błędy w procesie walidacji modelu

9

numerycznego. Dlatego też zaawansowana ocena modelu numerycznego jest coraz częściej wspierana danymi uzyskanymi za pomocą polowych metod optycznych, które określają przemieszczenia i deformacje w krytycznych obszarach obiektów [2, 3]. W przypadku pomiarów dużych struktur inżynieryjnych najczęściej stosowaną techniką jest metoda cyfrowej korelacji obrazu [4-6].

Dobrym przykładem dużych, złożonych struktur inżynierskich są samonośne struktury łukowe wykonywane z cienkościennych blach profilowanych metodą walcowania na zimno [7], które charakteryzują się karbowanymi ściankami profilu. Takie obiekty początkowo budowano jako tymczasowe budynki wykorzystywane do celów wojskowych. Bezpośrednie dostosowanie tej technologii do celów cywilnych, stwarza nowe wyzwania dla projektantów i konstruktorów, którzy muszą sprostać wymaganiom związanym ze zwiększeniem bezpieczeństwa, wydłużeniem żywotności elementów i jednoczesnym zmniejszeniem kosztów inwestycji i eksploatacji. W przypadku konstrukcji wykonywanych z profili ze ścianek płaskich znane są (z dokumentów normatywnych, m. in. norma PN-EN 1993-1-3:2008) zasady projektowania, w szczególności w zakresie stabilności i przenoszenia obciążenia. Natomiast w przypadku profili ze ściankami karbowanymi nośność konstrukcji łukowej w dużej mierze zależy od lokalnych zjawisk związanych z miejscową niestatecznością w obszarze karbowania ścianek profilu. Lokalnie w obszarze karbowania mogą formować się przeguby plastyczne, które znacząco wpływają na właściwości wytrzymałościowe całego profilu. Do wyznaczania nośności profili z karbowanymi ściankami nie ma w chwili obecnej uniwersalnych metod obliczeń i badań.

Kolejnym przykładem dużych złożonych struktur inżynierskich są rurociągi przemysłowe, a w szczególności ich połączenia [8]. Przykładowo na instalacjach syntezy amoniaku wykorzystywanych w zakładach azotowych, kluczowym elementem są rurociągi reaktora i gazu, które podatne są na częste rozszczelnienia, wybuchy, a nawet pożary. Parametry robocze instalacji to ciśnienie 200 bar, temperatura 300 - 400°C, natomiast przewodzone medium to wysoce wybuchowy wodór. W przypadku starszych instalacji, w wyniku wybuchów i rozległych pożarów wyższych poziomów reaktora i rurociągów, rurociągi ulegają trwałym odkształceniom, a właściwości układu zawieszenia i podpór ulegają zmianie. W celu zapewnienia bezpieczeństwa pracy instalacji należy opracować nowy, zaktualizowany model numeryczny instalacji i najważniejszych złączy, symulujący rzeczywiste warunki pracy, co umożliwi modernizacje połączeń i dobór optymalnych typów uszczelnień.

Złożoną strukturą kompozytową są również obrazy olejne na podłożu płóciennym, w skład których wchodzą następujące warstwy: płócienne podobrazie, klej przeklejenia, grunt oraz zaprawa warstwy malarskiej [9]. Właściwości mechaniczne płótna malarskiego zależą od właściwości poszczególnych składników oraz ich zawartości procentowej w kompozycie. Ze względu na różne techniki powstawania płócien malarskich rozwijane przez stulecia, trudne jest określenie generalnych właściwości mechanicznych płócien. Sposób splotu wątku i osnowy w płótnie (ich procentowa zawartość na jednostkę powierzchni, siła naciągu podczas tkania, rodzaj użytych nici) może powodować różne kurczenie się lub rozciąganie – płótna malarskiego w jednym lub dwóch kierunkach. Dobór rodzaju i sposobu naprawy uszkodzonych dzieł sztuki jest głównym wyzwaniem w praktyce konserwatorów dzieł sztuki. W przypadku reperacji podobrazia kluczowym czynnikiem jest dobór uzupełnień, tak aby ich właściwości mechaniczne pokrywały się z właściwościami płótna malarskiego. Gdy warunek ten zostanie spełniony, w płótnie po reperacji nie powinny występować dodatkowe naprężenia pod wpływem działania czynników zewnętrznych.

Przedstawione powyżej przykładowe problemy reprezentujące różnorodne zapotrzebowanie i aplikacje, mogą zostać rozwiązane w sposób efektywny poprzez wykorzystanie danych eksperymentalnych uzyskanych za pomocą polowych metod optycznych, które umożliwiają pomiar przemieszczenia i deformacji obiektów w krytycznych obszarach. W przypadku pomiarów dużych struktur inżynieryjnych najczęściej stosowaną techniką jest trójwymiarowa metoda cyfrowej korelacji obrazu (CKO 3D). Metoda ta cechuje się dużym zakresem pomiarowym (od kilkunastu mm do kilkudziesięciu cm) oraz dużym zakresem skalowalności pola pomiarowego (od 15 mm x 20 mm do 2 m x 3 m), a dzięki prostej konstrukcji systemu pomiarowego możliwe jest jej przystosowanie do pomiarów pozalaboratoryjnych. Jednakże, aby metodę CKO w pełni wykorzystać do pomiaru złożonych obiektów inżynierskich niezbędne jest opracowanie wielu zasadniczych modyfikacji tej metody.

W związku z powyższym, **celem pracy jest rozszerzenie aplikacyjności metody cyfrowej korelacji obrazu do pomiaru złożonych obiektów inżynierskich, poprzez opracowanie nowych metodyk pomiarowych i ścieżek przetwarzania danych oraz rozbudowę układu pomiarowego o nowe konfiguracje pomiarowe i moduły obliczeniowe.**

Aby osiągnąć założony cel należało zrealizować następujące zadania:

- rozszerzyć aplikacyjność tradycyjnych układów 3D CKO poprzez opracowanie szeregu modyfikacji w metodyce przetwarzania wyników CKO umożliwiających zastosowanie tej metody do efektywnej analizy wybranych złożonych procesów zachodzących w obiektach inżynierskich,
- opracować wielokamerowy system CKO 3D, umożliwiający pomiary rozproszone we wspólnym układzie współrzędnych,
- opracować efektywną metodykę kalibracji i walidacji modeli numerycznych z wykorzystaniem eksperymentalnych danych polowych na przykładzie wybranych złożonych obiektów inżynierskich.

Udoskonalenia metody 3D CKO oraz opracowane w ramach pracy metodyki pomiaru mają w przyszłości stanowić, wraz z opracowaniami udostępnionymi przez inne grupy badawcze, zestaw narzędzi, które mogą być dopasowane do analizy eksperymentalno-numerycznej istniejących i opracowanych w przyszłości skomplikowanych obiektów inżynierskich.

1.3. Wstęp teoretyczny

Pomiary przemieszczeń wykonywane w mechanice eksperymentalnej wymagają wysokiej dokładności rzędu 10^{-5} [m]. Aby uzyskać wymaganą dokładność z wykorzystaniem optycznych metod polowych oraz uprościć stosowane układy pomiarowe w latach osiemdziesiątych XX wieku opracowano metodę cyfrowej korelacji obrazu [10, 11]. Metoda ta w porównaniu do pozostałych metod optycznych (głównie z wykorzystaniem światła koherentnego) wykorzystywanych w mechanice eksperymentalnej umożliwia badanie w dużym zakresie pól pomiarowych (od 20 x 15 [mm^2] do 3 x 2 [m^2]) oraz z dużym zakresem pomiarowym (od mikrometrów do cm), a także posiada małe wymagania sprzętowe. Układ składający się z jednej kamery (CKO 2D) umożliwia pomiar przemieszczeń w płaszczyźnie (u,v), natomiast układ składający się z dwóch kamer (CKO 3D) umożliwia pomiar przemieszczeń w płaszczyźnie i pozapłaszczyznowych (u,v,w) (rys. 1.1). Ze względu na małe skomplikowanie układu pomiarowego łatwe jest jego dostosowanie do pozalaboratoryjnych warunków pomiarowych.
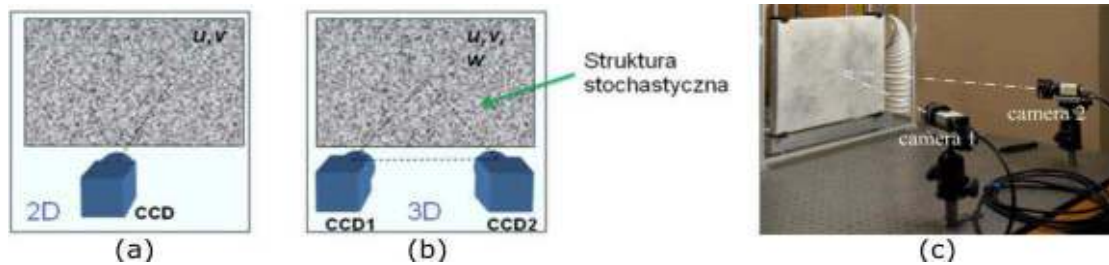
Rysunek 1.1. Schemat układów: a) CKO 2D i b) CKO 3D, c) przykładowe stanowisko pomiarowe CKO 3D [A1].

1.3.1. Cyfrowa korelacja obrazu 2D

Metoda CKO 2D umożliwia pomiar przemieszczeń oraz wyznaczanie odkształceń w płaszczyźnie z wykorzystaniem zdjęć szaroodcieniowych z jednej kamery pomiarowej. Aby umożliwić pomiar metodą CKO należy pokryć badany obszar strukturą stochastyczną. Dzięki zastosowaniu takiej struktury jesteśmy w stanie przyjąć założenie, że po odpowiednim podziale zdjęcia badanego obiektu na małe obszary (subsety) będą one niepowtarzalne w całym polu pomiarowym (przykład struktury stochastycznej został pokazany na rys.1.2a).
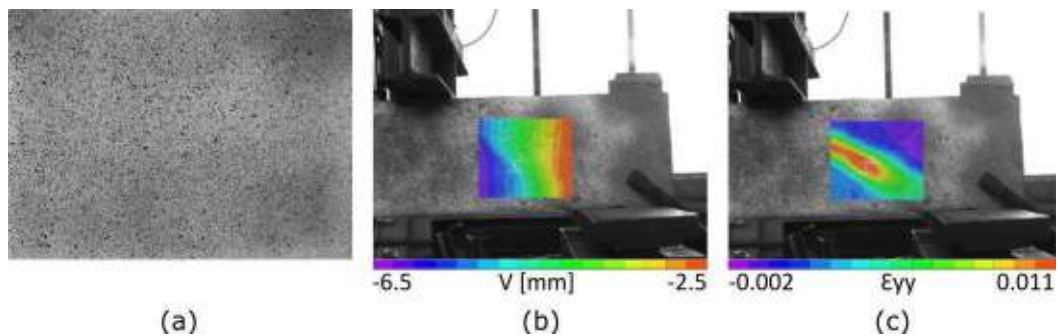
Rysunek 1.2. a) Przykładowa struktura stochastyczna wykonana za pomocą farb w spray'u oraz przykładowe mapy w kierunku poziomym b) przemieszczeń i c) odkształceń zarejestrowane tuż po pęknięciu nadproża w trakcie próby wytrzymałościowej.

Pomiar metodą CKO polega na zebraniu serii obrazów, z której wybrany jest obraz referencyjny. Na obrazie referencyjnym zaznaczony jest obszar zainteresowania (pomiarowy) (AOI, ang.: area of interest), który dzielony jest na subsety (prostokąty o bokach od kilku do kilkunastu pikseli), następnie z dokładnością subpikselową śledzone jest położenie subsetów na obrazach pomiarowych z wykorzystaniem współczynnika cyfrowej korelacji obrazu. Na podstawie wyliczonych przemieszczeń pojedynczych subsetów wyznaczana jest wektorowa mapa przemieszczeń w AOI (rys. 1.2b), mapa ta następnie może zostać przeliczona na mapę odkształceń (rys. 1.2c).

1.3.2. Współczynnik korelacji

Metoda CKO polega na znajdowaniu przemieszczeń subsetów w kolejnych obrazach pomiarowych względem obrazu referencyjnego. Aby było to możliwe należy wprowadzić współczynnik, który pozwoli wykonać tą operacje. W praktyce wykorzystywane są dwa współczynniki opisane poniżej.

W statystyce matematycznej jako współczynnik korelacji przyjmuje się współczynnik korelacji liniowej Pearsona dwóch zmiennych, jako iloraz kowariancji oraz iloczynu odchyleń standardowych tych dwóch zmiennych:

$$r_{ij} = \frac{cov\,(G,F)}{\sigma_G \sigma_F} = \frac{\sum_i \sum_j [F(x_i, y_j) - \bar{F}][G(x_i + d_x, y_j + d_y) - \bar{G}]}{\sqrt{\sum_i \sum_j [F(x_i, y_j) - \bar{F}]^2 \sum_i \sum_j [G(x_i + d_x, y_j + d_y) - \bar{G}]^2}} \qquad (1.1)$$

gdzie: F - wartość w odcieniach szarości w punkcie (x_i, y_j) subsetu z obrazu referencyjnego; G - wartość w odcieniach szarości w punkcie $(x_i + d_x, y_j + d_y)$ subsetu z obrazu pomiarowego; $\bar{F}, \bar{G}$ - są uśrednionymi wartościami odcieni szarości z subsetów odpowiednio referencyjnego oraz pomiarowego; d_x, d_y – przemieszczenia odpowiednio w kierunku x i y.

Algorytm oparty na współczynniku korelacji liniowej Pearsona odporny jest na jednorodną zmianę warunków oświetlenia w trakcie pomiarów, dzięki wykorzystaniu wartości uśrednionych odcieni szarości w subsecie $\bar{F}, \bar{G}$. Metoda ta cechuje się unormowaną wartością współczynnika korelacji: $r_{ij} \in [0,1]$; dla subsetów pokrywających się wynosi 1.

Natomiast Michael A. Sutton w swojej monografii [11] jako współczynnik korelacji podaje sumę kwadratową z różnic odcieni szarości (SSD, ang.: sum of squares deviation).:

$$\chi^2_{SSD} = \sum_i \sum_j [G(x_i + d_x, y_j + d_y) - F(x_i, y_j)]^2 \qquad (1.2)$$

W przypadku znalezienia przez algorytm subsetów identycznych współczynnik χ^2 przyjmuje wartość 0, natomiast dla subsetów zupełnie różnych nie ma unormowanej maksymalnej wartości.

Modyfikacją współczynnika SSD jest jego normalizacja względem wartości średniej (ZSSD, ang.: zero-mean sum of square difference).:

$$\chi^2_{ZSSD} = \sum_i \sum_j \left[\left(G(x_i + d_x, y_j + d_y) - \bar{G} \right) - \left(F(x_i, y_j) - \bar{F} \right) \right]^2 \qquad (1.3)$$

Algorytm oparty na tej metodzie odporny jest na jednorodną zmianę warunków oświetlenia.

Kolejną modyfikacją współczynnika SSD jest normalizacja skali szaroodcieniowej dla subsetu w obrazie pomiarowym (NSSD, ang.: normalized sum of squared difference)

$$\chi^2_{NSSD} = \sum_i \sum_j \left[\frac{\sum_i \sum_j G(x_i + d_x, y_j + d_y) F(x_i, y_j)}{\sum_i \sum_j [G(x_i + d_x, y_j + d_y)]^2} G(x_i + d_x, y_j + d_y) \right.$$
$$\left. - F(x_i, y_j) \right]^2 \qquad (1.4)$$

Algorytm oparty na tej metodzie odporny jest na liniową zmianę warunków oświetlenia.

Połączeniem współczynników ZSSD oraz NSSD jest współczynnik ZNSSD (ang.: zero-mean normalised sum of squared difference).:

$$\chi^2_{ZNSSD} = \sum_i \sum_j \left\{ \frac{\sum_i \sum_j G(x_i + d_x, y_j + d_y) F(x_i, y_j)}{\sum_i \sum_j [G(x_i + d_x, y_j + d_y)]^2} \left[\left(\left(G(x_i + d_x, y_j + d_y) \right. \right. \right. \right.$$
$$\left. \left. \left. \left. - \bar{G} \right) - \left(F(x_i, y_j) - \bar{F} \right) \right] \right\}^2 \qquad (1.5)$$

Algorytm oparty na tej metodzie odporny jest na jednolitą oraz liniową zmianę warunków oświetlenia.

1.3.3. Sub-pikselowa dokładność algorytmu CKO

Podczas pomiaru na badany obiekt działa wymuszenie powodujące przemieszczenie oraz deformacje subsetów (Rys.1.3), w pomiarach na płaszczyźnie można zaobserwować składowe u, v, $\frac{\partial u}{\partial x}, \frac{\partial u}{\partial y}, \frac{\partial v}{\partial x}, \frac{\partial v}{\partial y}$, gdzie: u - przemieszczenia w kierunku osi x, v - przemieszczenia w kierunku osi y. Subset pomiarowy nie będzie identyczny w porównaniu z subsetem referencyjnym, z tego powodu algorytm CKO musi najpierw wyznaczyć zgrubnie położenie subsetu (z dokładnością pikselową), a następnie optymalizować iteracyjnie jego kształt tak, aby wyznaczyć przemieszczenie sub-pikselowe.
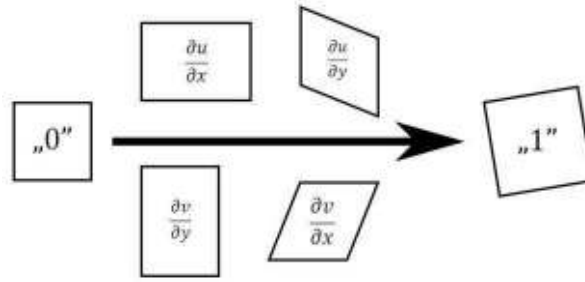
Rysunek 1.3. Schemat deformacji subsetu.

Optymalizacja z wykorzystaniem współczynnika korelacji liniowej Persona oraz algorytmów opartych na funkcji SSD oraz jej pozostałych wariantów, polega na modyfikacji współczynników d_x oraz d_y.:

$$d_x = u_i + \frac{\partial u}{\partial x}\Delta x + \frac{\partial u}{\partial y}\Delta y \tag{1.6}$$

$$d_y = v_j + \frac{\partial v}{\partial x}\Delta x + \frac{\partial v}{\partial y}\Delta y \tag{1.7}$$

Teoretycznie uzyskiwana dokładność pomiaru przemieszczeń wynosi 0,005 piksela [11], jednak w praktyce wykorzystania metody w pomiarach pozalaboratoryjnych wartość ta nie jest większa niż 0,02 piksela.

1.3.4. Wyznaczenie odkształceń

Odkształcenie w metodzie CKO wyznaczane są najczęściej na podstawie wzorów wyprowadzonych na potrzeby optycznych metod polowych [10]:

$$\varepsilon_{xx} \cong \frac{\partial u}{\partial x} + \frac{1}{2}\left[\left(\frac{\partial u}{\partial x}\right)^2 + \left(\frac{\partial v}{\partial x}\right)^2\right] \tag{1.8}$$

$$\varepsilon_{yy} \cong \frac{\partial v}{\partial y} + \frac{1}{2}\left[\left(\frac{\partial u}{\partial y}\right)^2 + \left(\frac{\partial v}{\partial y}\right)^2\right] \tag{1.9}$$

$$\varepsilon_{xy} \cong \frac{1}{2}\left(\frac{\partial u}{\partial y} + \frac{\partial v}{\partial x}\right) + \frac{1}{2}\left[\frac{\partial u}{\partial x}\frac{\partial u}{\partial y} + \frac{\partial v}{\partial x}\frac{\partial v}{\partial y}\right] \tag{1.10}$$

Należy zwrócić uwagę, że metoda CKO umożliwia pomiar przemieszczeń na płaszczyźnie badanego obiektu, dlatego też odkształcenia są wyznaczanie wyłącznie w płaszczyźnie badanego obiektu.

1.3.5. Cyfrowa korelacja obrazu 3D

Do pomiaru przemieszczeń 3D wykorzystywane jest układ stereowizyjny [12], który składa się z dwóch kamer. W metodzie CKO 3D jedna z kamer wybierana jest jako referencyjna (kamera 1), natomiast druga stanowi kamerę dodatkową (kamera 2). W pierwszej fazie pomiarów CKO 3D wyznaczane są przemieszczenia w płaszczyźnie względem kamery 1, następnie z wykorzystaniem kamery 2 wyznaczane są przemieszczenia pozapłaszczyznowe. Odnajdywanie obszarów odpowiadających sobie na kamerze 1 i 2 odbywa się poprzez funkcje korelacji (schematyczny diagram został przedstawiony na rys. 1.4). W publikacji [11] udowodniono, że kąt $30°$ między kamerami zapewnia najlepszą dokładność pomiarów pozapłaszczyznowych (iloczyn dokładności pomiarów w płaszczyźnie (0,005 piksela) oraz tangensa kąta rozstawu kamer) przy minimalizacji wpływu cieni i maksymalizacji obszaru wspólnego pola pomiarowego obu kamer.
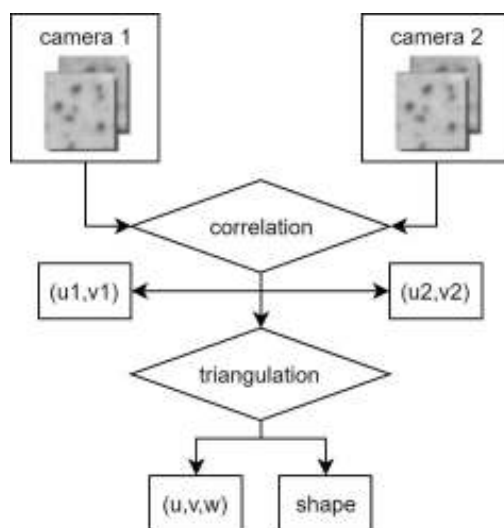
Rysunek 1.4. Schemat wyznaczania przemieszczeń i kształtu metodą CKO 3D [A1].

1.3.6. Podsumowanie

Metoda CKO dzięki prostej konfiguracji sprzętowej jest łatwa w implementacji w pomiarach obiektów inżynierskich, natomiast wysoka dokładność pomiaru i skalowalność pola pomiarowego umożliwia jej wykorzystanie w mechanice eksperymentalnej. Jest to bardzo uniwersalna metoda, jednak aby w pełni wykorzystać jej potencjał, należy opracować szereg modyfikacji w metodyce przetwarzania wyników CKO w celu umożliwienia efektywnej analizy złożonych procesów zachodzących w wybranych obiektach inżynierskich. Ponadto należy zwrócić uwagę, że w przypadku pomiarów złożonych struktur inżynierskich, ograniczenie metody do pojedynczego pola pomiarowego zmniejsza poważnie aplikacyjność metody.

2. Przewodnik po publikacjach

2.1. Cykl spójnych tematycznie publikacji stanowiących przedmiot rozprawy

Nr	Publikacja	Udział %	Impact factor	Punkty MNiSW	Cyt. (Scopus)
A1	M. Malesa, **K. Malowany**, L. Tymińska-Widmer, E. A. Kwiatkowska, M. Kujawińska, B. J. Rouba, P. Targowski, „Application of Digital Image Correlation (DIC) for tracking deformations of paintings on canvas" *Proc. SPIE* 8084, 80840L (2011).	30	-	15	8
A2	A. Piekarczuk, M. Malesa, M. Kujawińska, **K. Malowany**, "Application of hybrid FEM-DIC method for assessment of low cost building structures", *Experimental Mechanics* 52 (9), 1297-1311 (2012).	15	1.548	35	20
A3	M. Malesa, **K. Malowany**, U. Tomczak, B. Siwek, M. Kujawińska, A. Siemińska-Lewandowska, "Application of 3D digital image correlation in maintenance and process control in industry", *Computers in Industry* 64 (9), 1301-1315 (2013).	30	1.457	35	28
A4	**K. Malowany**, L. Tymińska-Widmer, M. Malesa, M. Kujawińska, P. Targowski, B.J. Rouba, "Application of 3D digital image correlation to track displacements and strains of canvas paintings exposed to relative humidity changes", *Applied Optics* 53 (9), 1739-1749 (2014).	55	1.784	30	5

A5	A. Piekarczuk, **K. Malowany**, P. Więch, M. Kujawińska, P. Sulik, "Stability and bearing capacity of arch-shaped corrugated shell elements: experimental and numerical study", *Bulletin of the Polish Academy of Sciences* 64 (1), 113-123 (2015).	25	1.087	25	13
A6	M. Rataj, M. Malesa, M. Kujawińska, Ł. Płatos, P. Wawer, K. Seweryn, **K. Malowany**, "3D DIC Tests of Mirrors for the Single-Mirror Small-Size Telescope of CTA", *Experimental Astronomy* 39 (3), 513-525 (2015).	10	2.867	20	2
A7	**K. Malowany**, K. Magda, J. Rutkiewicz, M. Malesa, J. Kantor, J. Michoński, M. Kujawińska, "Measurements of geometry of a boiler drum by Time-of-Flight laser scanning", *Measurements* 72, 88-95 (2015).	55	1.742	30	4
A8	A. Piekarczuk, **K. Malowany**, "Comparative analysis of numerical models of arch-shaped steel sheet sections", *Archives of Civil and Mechanical Engineering* 16 (4), 645-658 (2016).	30	2.216	30	9
A9	M. Malesa, **K. Malowany**, J. Pawlicki, M. Kujawinska, P. Skrzypczak, A. Piekarczuk, T. Lusa, A. Zagorski, "Non-destructive testing of industrial structures with the use of multi-camera Digital Image Correlation method", *Engineering Failure Analysis* 69, 122-134 (2016).	25	1.676	30	13

19

A10	**K. Malowany**, M. Malesa, T. Kowaluk, M. Kujawińska, "Multi-camera Digital Image Correlation method with distributed fields of view", *Optics and Lasers in Engineering* 98, 198-204 (2017).	75	3.388	30	6
A11	P. Gąsior, J. Kaleta, R. Rybczyński, M. Malesa, M. Kujawińska, **K. Malowany**, "Application of Complementary Optical Methods for Strain Investigation in Composite High Pressure Vessel", *Composite Structures* 203, 718-724 (2018).	10	4.101	35	1
A12	**K. Malowany**, A. Piekarczuk, M. Malesa, M. Kujawińska, P. Więch, "Application of 3D digital image correlation for development and validation of FEM model of self-supporting arch structures", *Applied Sciences* 9 (7), 1305 (2019).	70	1.689	25	0

2.2. Rozszerzenie aplikacyjności tradycyjnych układów 3D CKO

2.2.1. Wstęp

Metoda cyfrowej korelacji obrazu w jej wersjach 2D i 3D jest szeroko stosowana w praktyce inżynierskiej, jednak na co dzień pojawiają się nietypowe wyzwania pomiarowe związane z samym charakterem obiektu, warunkami lub wymaganiami funkcjonalnymi samych pomiarów. Zadaniem naukowców i inżynierów jest znajdowanie efektywnych rozwiązań i wspomaganie realizacji pomiarów i analizy danych pod kątem wymagań zdefiniowanych przez praktyczne zagadnienia.

W ramach mojej pracy w ZIF IMiF PW rozszerzyłem aplikacyjność tradycyjnych układów CKO 3D obsługiwanych przez komercyjne oprogramowanie VIC (firmy Correlated Solution) o następujące zagadnienia ważne w praktyce inżynierskiej:

- zaproponowałem i zaimplementowałem metody przestrzenno-czasowej analizy danych CKO poprzez mapowanie profili przemieszczeń/deformacji w funkcji czasu dla takich zastosowań jak: monitorowanie zmian w obrazach olejnych [A1, A4], podporach stalowych wykopów [A3] oraz podłoży do zwierciadeł teleskopów astronomicznych [A6] pod wpływem zmian środowiskowych i/lub obciążeń zewnętrznych;

- zaproponowałem i zaimplementowałem metody wyznaczania lokalnych map przemieszczeń/odkształceń z pominięciem wpływu zmian globalnych w obiekcie na przykładzie badań obrazów olejnych [A4];

- opracowałem metodykę analizy danych z CKO 3D w cylindrycznym układzie współrzędnych na przykładzie pomiarów wysokociśnieniowego zbiornika kompozytowego na wodór/metan [A11].

Opracowane metody analizy (w szczególności analiza danych w cylindrycznym układzie współrzędnych) wykorzystałem do pomiarów i analizy kształtu walczaka na bloku energetycznym [A7].

W każdym praktycznym zagadnieniu oprócz zaproponowania i implementacji wymienionych wyżej modyfikacji procesu analizy danych niezbędne było opracowanie specyficznego dla danego zagadnienia układu i scenariusza pomiarowego, natomiast powyższe modyfikacje metodyki analizy danych wykorzystywane były również jako standardowe narzędzie w pracach przedstawionych w dalszych rozdziałach przewodnika.

2.2.2. Przestrzenno-czasowa analiza danych CKO

W wyniku analizy metodą CKO 3D uzyskiwane są dwuwymiarowe mapy przemieszczeń i odkształceń w całym polu widzenia układu. Podczas monitorowania zmian jednym z podstawowych narzędzi analizy danych są przekroje linowe, w wyniku których uzyskiwane są profile przemieszczeń/odkształceń na odcinkach zaznaczonych na analizowanej mapie. Jednak w przypadku porównywania danych dla kilku stanów obiektu narzędzie to jest niewygodne. W związku z powyższym do analizy danych uzyskanych metodą CKO zaadaptowałem, analizę danych opartych na przestrzenno-czasowych mapach (skanach) wykorzystywanych m. in. w optycznej tomografii koherencyjnej (ang. Optical Coherence Tomography) [A1]. Uzyskane profile przemieszczeń/odkształceń uzyskane na danym odcinku zostały połączone w funkcji czasu, dzięki czemu możliwe było utworzenie map zmian przemieszczeń (rys. 2.1) i odkształceń w przekroju i w czasie (x,y,t).
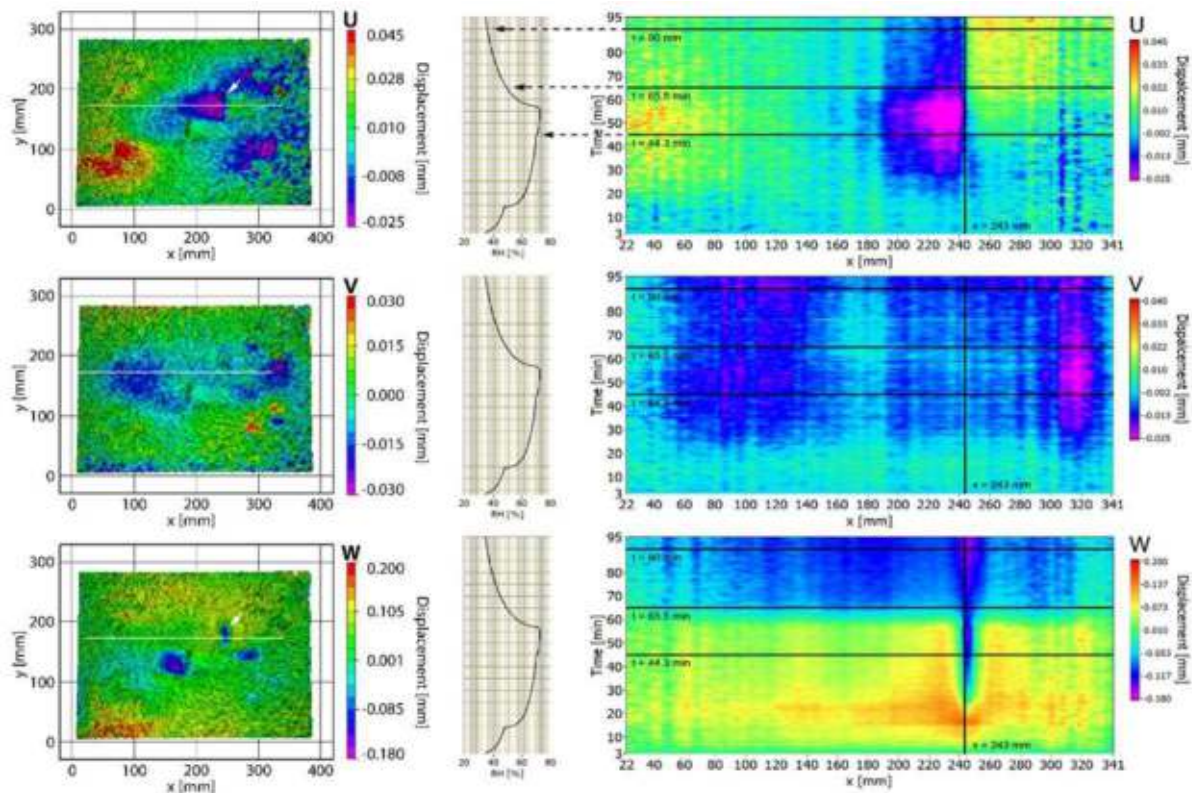
Rysunek 2.1. Po prawej przykładowy zestaw pól przemieszczeń (U(x), V(y), W(z)) w momencie maksymalnej deformacji próbki; po lewej profile przemieszczeń w funkcji czasu (dla przekroju zaznaczonego białą linią na mapach przemieszczeń), dla całego cyklu obciążeń wilgotnościowych (pokazanych na wykresie bocznym)[A1].

Zaproponowana przeze mnie wizualizacja danych umożliwiła efektywną analizę procesów zachodzących w badanej strukturze pod wpływem wymuszenia zewnętrznego. W przypadku pomiaru obrazów płóciennych wyeksportowane dane umożliwiają konserwatorom sztuki ocenę ilościową wpływu badanych typów napraw na pracę całego płótna (współpraca z Uniwersytetem Mikołaja Kopernika w Toruniu). Przykładowo na wizualizacji przekrojów w czasie (rys. 2.1) można dokładnie ocenić wpływ zmiany wilgotności na przemieszczenia (i odkształcenia materiału) w obszarach poszczególnych napraw. Na podstawie przeprowadzonych przeze mnie testów wyselekcjonowano naprawy konserwatorskie, które najmniej wpływały na odpowiedź danego płótna na wymuszenie wilgotnościowe [A4]. Obecnie zmodyfikowana metoda CKO została wpisane na listę technologii, które będą wykorzystywane w European Research Infrastructure for Heritage Science (E-RIHS ERIC).

Mapowanie profili przemieszczeń/deformacji w funkcji czasu posłużyło również do analizy danych uzyskanych z pomiaru rozpór stalowych wykorzystywanych w budownictwie [A3] oraz zwierciadeł optycznych segmentowych teleskopów astronomicznych [A6]. W

przypadku rozpór stalowych wykorzystywanych w budownictwie do rozpierania ścian szczelinowych (rys. 2.2 a, b), przeprowadziłem pomiary przemieszczeń metodą CKO 3D skorelowane z pomiarem temperatury wykonanym techniką termowizji. Przeprowadzone pomiary oraz analiza danych pozwoliły dokładnie określić wpływ zmian temperatury na przemieszczenia rozpór stalowych i na przemieszczenia ścian szczelinowych. Przykładowy profil odkształceń rozpory w funkcji czasu dla dobowego cyklu zmiany temperatury pokazany został na rys. 2.2 c. Wykonane pomiary mogą posłużyć do wspomagania metod projektowania ścian szczelinowych (współpraca z Wydziałem Inżynierii Lądowej PW). Uwzględnienie deformacji termicznych podczas symulacji numerycznych pozwoli w przyszłości na oszczędności materiałowe przy budowie wzmacnianych ścian. W przypadku zwierciadeł, badania dotyczyły nowego typu zwierciadeł do segmentowych teleskopów astronomicznych wykonywanych z kompozytów (rys. 2.2 d), opracowanych jako alternatywa dla klasycznych szklanych zwierciadeł (współpraca z Centrum Badań Kosmicznych PAN). Technologia ta ma na celu zminimalizowanie kosztu produkcji setek zwierciadeł dla sieci teleskopów, przy jednoczesnym zachowaniu wysokich parametrów jakości obrazowania. W celu zbadania wpływu temperatury na odkształcenia badanych zwierciadeł przeprowadziłem testy, podczas których prototypowe zwierciadło zostało umieszczone w komorze klimatycznej. Opracowałem metodę nakładania tekstury na zwierciadła (rys. 2.2 d), niezbędną do wykorzystania CKO w tym nietypowym zastosowaniu. Odkształcenia zwierciadeł spowodowane zmianą temperatury obserwowane były z wykorzystaniem metody CKO 3D (rys. 2.2 e). Przykładową mapę oraz profil przemieszczeń pozapłaszczyznowych dla zwierciadła podczas próby termicznej pokazano na rys. 2.2 f-g. W wyniku przeprowadzonych testów wprowadzono zmiany w projekcie zwierciadeł, które poprawiły technologię ich produkcji.
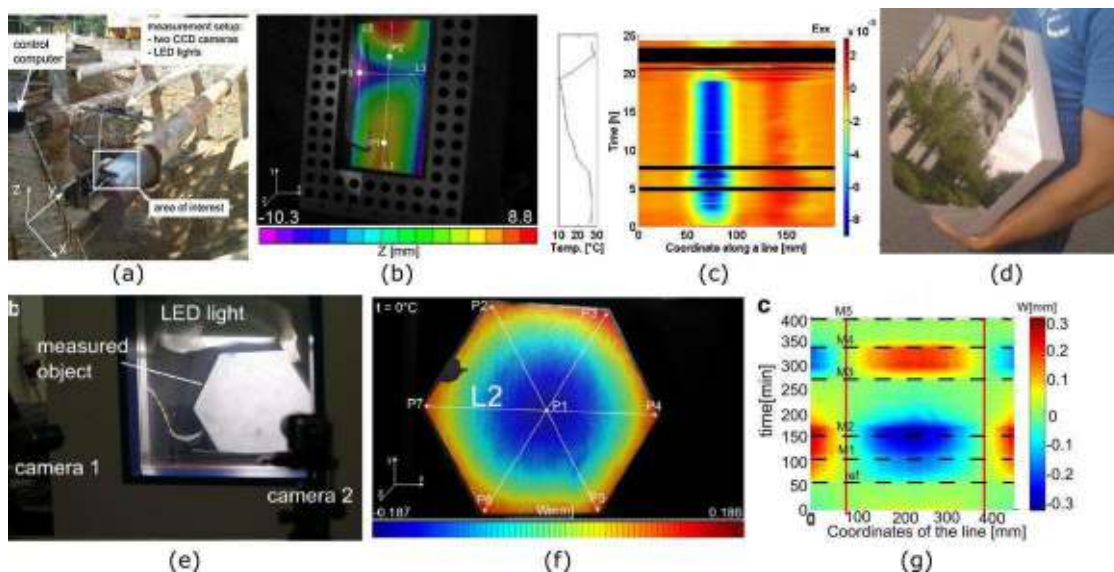
Rysunek 2.2. a) Pomiar rozpory stalowej z wykorzystaniem systemu CKO 3D, b) mapa kształtu podpory stalowej z zaznaczonymi profilami do analizy odkształceń, c) przykładowy profil odkształceń wzdłuż profilu L2, dla dobowego cyklu zmiany temperatury [A3]; d) zwierciadło optyczne wykonane z kompozytów, e) zwierciadło optyczne pokryte strukturą plamkową w komorze klimatycznej, w trakcie pomiaru systemem CKO 3D, f) przykładowa mapa przemieszczeń pozapłaszczyznowych w trakcie zmiany temperatury z zaznaczonym przekrojem L2, g) przykładowy profil przemieszczeń wzdłuż linii L2, dla próby termicznej [A6].

2.2.3. Wyznaczanie map przemieszczeń lokalnych

W badaniach wielu struktur mechanicznych ważne jest jednoczesne badanie przemieszczeń i deformacji obiektów w trzech kierunkach, podczas poddawania tych obiektów różnego rodzaju obciążeniom (mechanicznym, termicznym, środowiskowym). Dobrym przykładem takiego typu obiektów są zabytkowe obrazy olejne (które można traktować jako złożoną strukturę kompozytową). Są one najczęściej zamocowane luźno na ramie, w związku z czym podczas zmiany współczynnika wilgotności otoczenia na skutek pęcznienia obraz deformuje się w kierunku normalnym do płaszczyzny ramy. Standardowo polowe pomiary optyczne umożliwiają pomiar przemieszczeń w trzech kierunkach, natomiast analizę odkształceń w dwóch kierunkach, na płaszczyźnie badanego obiektu. W celu analizy odkształceń poza-płaszczyznowych wykorzystywane są skomplikowane techniki pomiaru, takie jak rentgenowska tomografia komputerowa, rezonans magnetyczny lub optyczna tomografia koherentna. Jednak w przypadku pomiarów oddziaływania zmian środowiskowych na obrazy płócienne metody te są niepraktyczne/niewystarczające. W przypadku dwóch pierwszych metod, ze względów finansowych, nierealne jest zbudowanie komory do symulacji warunków środowiskowych, w której mogłyby pracować systemy rentgenowskie/rezonansu

magnetycznego. Natomiast metoda optycznej tomografii koherencyjnej ma zbyt małe pole pomiarowe, aby monitorować globalne deformacje obrazu olejnego na płótnie [13]. W związku z powyższym powstało zagadnienie interpretacji danych uzyskiwanych z polowych metod optycznych, tak aby uzyskać informacje o lokalnych pozapłaszczyznowych deformacjach obiektu wynikających ze zmian materiałowych . W ramach współpracy z konserwatorami dzieł sztuki z Uniwersytetu Mikołaja Kopernika w Toruniu, przeprowadziłem badania metodą CKO 3D oddziaływania różnych rodzajów napraw konserwatorskich na pracę płótna podczas próby wilgotnościowej. Celem badań było wybranie najbardziej neutralnego sposobu naprawy (nie wprowadzającego dodatkowych naprężeń) spośród tych, które zostały zastosowane na płótnie modelowym (płótnie o analogicznych cechach względem obiektu poddawanego konserwacji). W wyniku analizy danych stwierdzono, że przemieszczenia pozapłaszczyznowe W były o rząd większości większe niż przemieszczenia w płaszczyźnie U, V, na podstawie których wyznaczane są odkształcenia ε_{xx} i ε_{yy}. W celu uzyskania informacji o deformacjach pozapłaszczyznowych opracowałem prosty i efektywny algorytm do wyznaczania przemieszczeń lokalnych [A4].

Lokalne przemieszczenia pozapłaszczyznowe W związane z oddziaływaniem napraw na płótno są znacznie mniejsze niż globalne przemieszczenia całego płótna. Wykorzystując filtracje dolnoprzepustową mapy przemieszczeń, elementy mapy o dużej częstotliwości (przemieszczenia lokalne) zostaną usunięte. Do operacji filtrowania wykorzystany został filtr uśredniający, rozmiar filtra uzależniony jest od rozmiarów napraw. W opisanym przypadku rozmiary napraw były podobne, więc rozmiar filtra był stały w całym polu widzenia. W przypadku dużych różnic w rozmiarach napraw wielkość filtra powinna być dostosowana lokalnie zgodnie z wcześniejszą wiedzą o obiekcie. Mapa uzyskana po filtracji została odjęta od mapy przed filtracją, w ten sposób uzyskana została mapa przemieszczeń lokalnych (rys. 2.3 b), schemat algorytmu postępowania przedstawiony został na rys. 2.3 a.
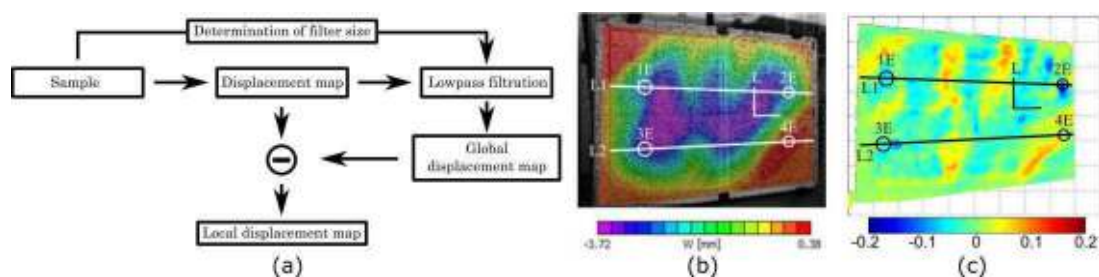
Rysunek 2.3. a) Schemat procedury wyznaczania map lokalnych; przykładowa mapa przemieszczeń pozapłaszczyznowych (b) na podstawie, której wyznaczono mapę przemieszczeń lokalnych (c) dla obrazu płóciennego podczas próby wilgotnościowej (na mapie zaznaczono naprawy defektów) [A4].

Uzyskane dane pozwoliły ocenić wpływ napraw na deformacje pozapłaszczyznowe badanego płótna, w połączeniu z informacją o przemieszczeniach globalnych oraz odkształceniach (w płaszczyźnie płótna) uzyskana została pełna informacja o oddziaływaniu napraw na pracę płótna podczas zmiany wilgotności.

2.2.4. Analiza danych w walcowym układzie współrzędnych

Zazwyczaj do modelowania 3D obiektów inżynierskich oraz pomiarów przemieszczeń wykorzystywany jest kartezjański układ współrzędnych. Jednak w przypadku części obiektów podejście to jest nieoptymalne z punktu widzenia analizy wyników, do grupy tej zaliczają się obiekty cylindryczne, jest to dużo grupa obiektów do której należą m.in. wały maszyn, rurociągi, zbiorniki (na paliwo, silosy), kominy. Dla tej grupy obiektów istotnymi parametrami geometrii są tolerancje okrągłości, walcowatości, współosiowości, natomiast w przypadku analizy wytrzymałościowej istotne są odkształcenia obwodowe. Aby ułatwić analizę danych eksperymentalnych dla tej klasy obiektów istotne jest, aby wyniki były dostępne w cylindrycznym układzie współrzędnych.

W ramach prowadzonych prac wykonałem pomiary geometrii walczaka na bloku energetycznym (cylindryczny obiekt wielkogabarytowy, o średnicy 1,6 m i długości 16 m) z wykorzystaniem techniki pomiaru ToF (ang.: Time of Flight) [A7]. Pomiar został zrealizowany w trakcie remontu, celem sprawdzenia czy obróbka termiczna (wyżarzanie odprężające) nie spowodowała znacznych deformacji walczaka, które mogą wpłynąć niekorzystnie na bezpieczeństwo eksploatacji obiektu. Wyznaczone zostały miejsca, w których średnica walczaka odbiega w sposób znaczący od wartości nominalnej, dzięki czemu w tych miejscach zwrócono szczególną uwagę na pasowanie separacji, ich błędne dopasowanie może doprowadzić do wycieków pary w trakcie pracy bloku. Na potrzeby analizy wyników pomiaru opracowałem metodykę analizy danych w cylindrycznym układzie współrzędnych (rozłożona na płaszczyznę mapa kształtu mierzonej konstrukcji pokazana na rys. 2.4), w wyniku której uzyskiwane są parametry łatwe do interpretacji przez dział diagnostyki technicznej. Dzięki wykorzystaniu dedykowanej analizy danych możliwe było w łatwy sposób wyznaczenie następujących parametrów:

- lokalnej odchyłki walcowości na całej długości walczaka (pomiar średnicy),

- strzałki ugięcia w płaszczyźnie pionowej i poziomej na całej długości,

- średnicy walczaka w płaszczyźnie poziomej i pionowej,

- odchyłki współosiowości pomiędzy sektorami płaszcza walczaka.
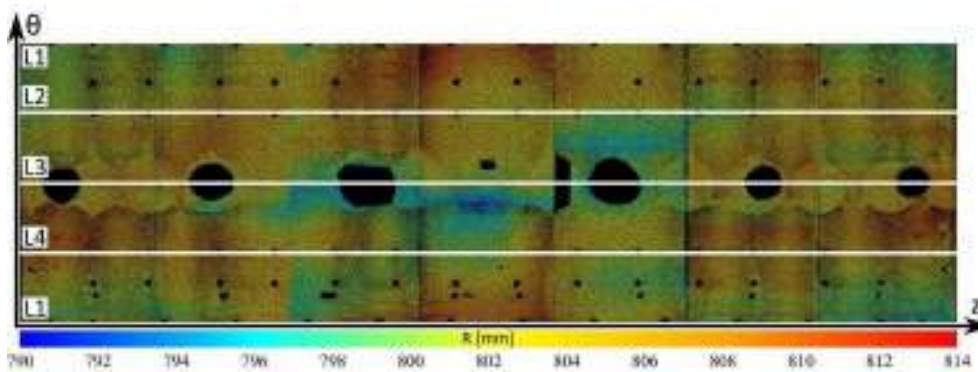
Rysunek 2.4. Rozłożenie na płaszczyznę mapy promienia cylindrycznej powierzchni walczaka, mapa kształtu została wyznaczona w cylindrycznym układzie współrzędnych (na mapie zaznaczono linie, które były analizowane w ramach przeprowadzonych prac) [A7].

Metodyka analizy wyników w cylindrycznym układzie współrzędnych wykorzystana została przy badaniach odkształceń wysokociśnieniowego zbiornika na wodór i metan [A11] (Współpraca z Politechnika Wrocławską). Metoda CKO 3D oraz czujniki światłowodowe oparte na siatkach Bragga (FBG, ang.: Fiber Bragg Grating) wykorzystane zostały do pomiaru przemieszczeń/odkształceń zbiornika w trakcie próby ciśnieniowej (rys. 2.5). Czujniki FBG (prace zespołu z Politechniki Wrocławskiej) były rozpięte na powierzchni cylindrycznego zbiornika, przez co mierzyły odkształcenia obwodowe (na wycinkach łuków). W związku z powyższym, aby umożliwić porównanie danych eksperymentalnych uzyskanych obydwiema metodami, dane otrzymane przeze mnie metodą CKO 3D przeliczyłem do cylindrycznego układu współrzędnych. Wartości odkształceń globalnych uzyskane z wykorzystaniem metody CKO 3D posłużyły do kalibracji czujników FBG. Jednocześnie dane z obydwu czujników zostały wykorzystane do opracowania modelu numerycznego badanego zbiornika. Wykazano, że dane uzyskane metodą CKO 3D mogą posłużyć do identyfikacji defektów na zbiorniku oraz wspierać optymalizacje rozłożenia czujników FBG, które przeznaczone są do wkomponowania w kompozytową strukturę zbiornika. Opracowana metodyka wspomaga rozwiązanie trudnego problemu budowy wydajnego systemu monitorowania (w czasie eksploatacji) stanu konstrukcji (SHM, ang.: *structural health monitoring*) dla zbiorników wysokociśnieniowych dla paliw gazowych.
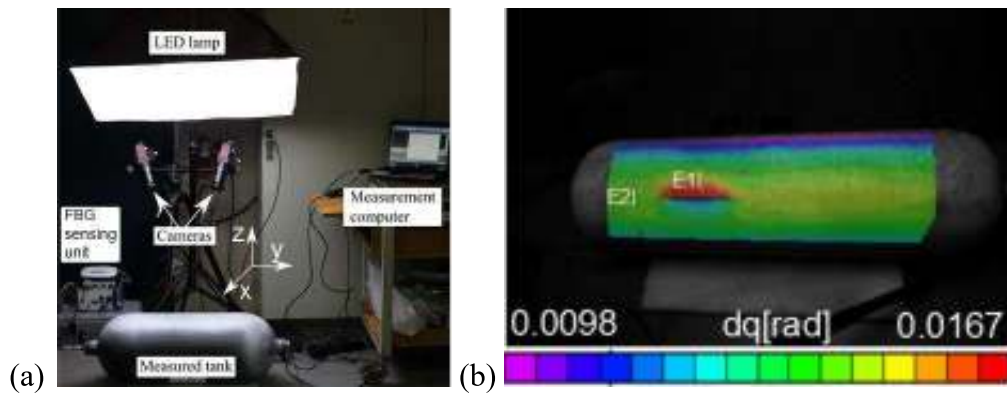
Rysunek 2.5. a) Stanowisko do pomiaru przemieszczeń/odkształceń zbiornika na wodór/metan; b) przykładowa mapa przemieszczeń kątowych zbiornika w trakcie próby ciśnieniowej, z zaznaczonymi wirtualnymi tensometrami używanymi do wyznaczania odkształceń [A11].

2.3. Wielokamerowy system CKO 3D, umożliwiający pomiary rozproszone we wspólnym układzie współrzędnych

W ramach pomiaru wielkogabarytowych obiektów inżynierskich niejednokrotnie wymagane jest, aby pola pomiarowe znajdowały się w kilku oddalonych od siebie obszarach, ponieważ przy złożonym stanie obciążeń, koncentracje naprężeń nie występują wyłącznie w jednym miejscu. W przypadku optycznych pomiarów polowych realizacja tego typu pomiarów jest problematyczna, ponieważ z jednej strony pola pomiarowe (przy oczekiwanej dokładności) są stosunkowo niewielkie (np. 1mx1m), a z drugiej brak jest metodyki łączenia danych z obszarów pomiarowych oddalonych od siebie o kilka metrów. Natomiast wykorzystanie danych o przemieszczeniach z nieskorelowanych układów współrzędnych może wprowadzać błędy w interpretacji wyników, m.in. w kalibracji modeli numerycznych konstrukcji.

System CKO 3D umożliwia polowy pomiar optyczny, dokładność pomiaru uzależniona jest od wymiaru pola pomiarowego. Im większe pole pomiarowe tym mniejsza dokładność pomiaru przemieszczeń/odkształceń. W celu zachowania wymaganych dokładności pomiarowych do pomiaru konstrukcji wielkogabarytowych oraz obiektów o skomplikowanej geometrii (które wymagają obserwacji z więcej niż jednej perspektywy) opracowane zostały wielokamerowe systemy CKO 3D, umożliwiające pomiar we wspólnym układzie współrzędnych. Z publikacji [14 - 16] znane są systemy z nachodzącymi polami pomiarowymi, jednak jest to częściowe rozwiązanie problemu, w przypadku konstrukcji rozłożonych (np. rurociągi) lub wielkogabarytowych (np. duże konstrukcje budowlane) pola pomiarowe powinny być odseparowane od siebie o kilka/kilkanaście metrów. Aby umożliwić pomiar tej

klasy obiektów opracowałem wielokamerowy system CKO 3D z rozproszonymi polami pomiarowymi, który wykorzystałem do pomiaru obiektów przemysłowych, hali magazynowej oraz rurociągów na instalacji w zakładach azotowych. Wykonane prace opisałem w artykułach [A9, A10].
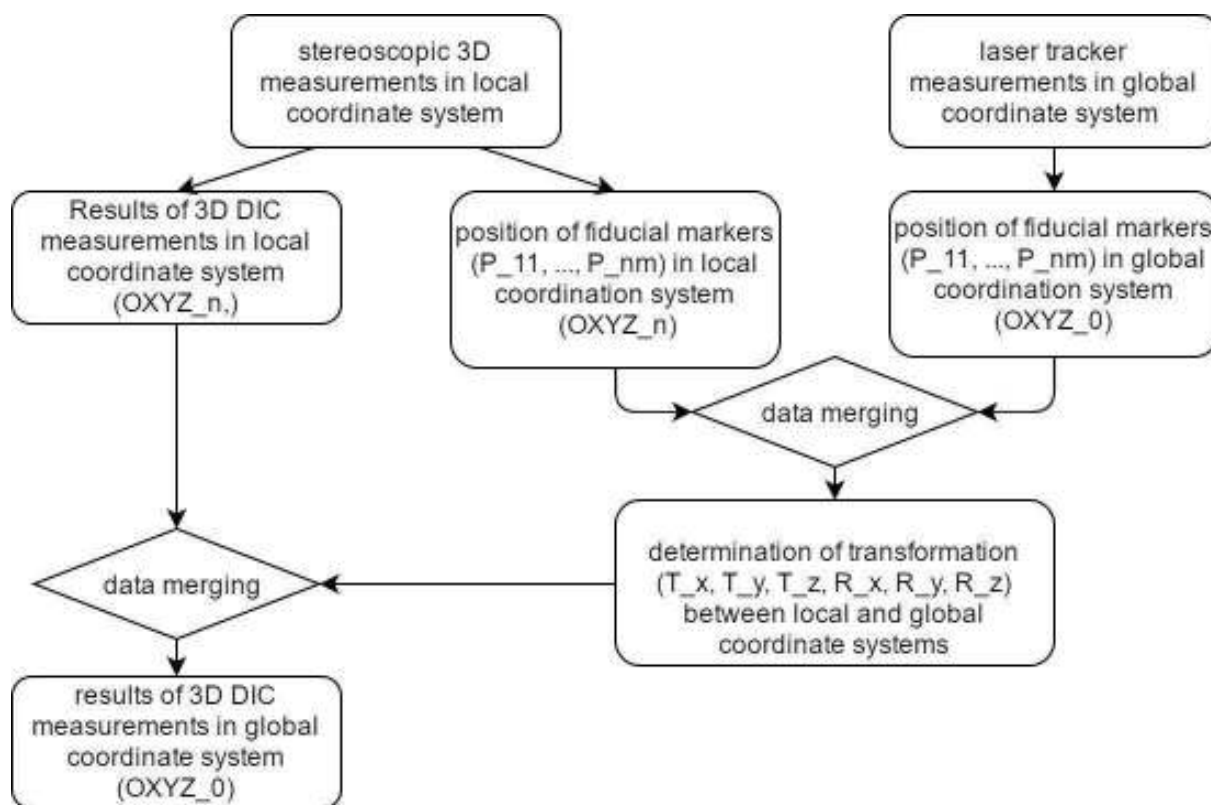
2.3.1. Koncepcja wielokamerowego systemu CKO 3D z rozproszonymi polami pomiarowymi

Głównym wyzwaniem podczas pomiaru obiektu w wielu rozproszonych (nienakładających się) polach pomiarowych jest transformacja lokalnych układów współrzędnych pojedynczych systemów CKO 3D ($OX_1Y_1Z_1$, ..., $OX_nY_nZ_n$, gdzie n oznacza numer systemu CKO 3D) do jednego globalnego układu współrzędnych ($OX_0Y_0Z_0$). Opracowana procedura oparta jest na transformacji geometrycznej między lokalnymi układami współrzędnych systemów CKO 3D i globalnym układem współrzędnych zewnętrznego systemu pomiarowego. Do wyznaczenia globalnego układu współrzędnych zaproponowałem tracker laserowy [17], który wyznacza z wysoką dokładnością położenie markera (precyzyjnie wykonanej kuli stalowej z wbudowanym retroreflektorem). Należy nadmienić, że zasięg pomiarowy trackerów laserowych przekracza 100 metrów, a więc spełniają one wymaganie wspomagania łączenia znacznie oddalonych obszarów zainteresowania.

Schemat ogólnego podejścia do wyznaczenia transformacji lokalnych układów współrzędnych systemów CKO 3D do globalnego układu współrzędnych z wykorzystaniem trackera laserowego pokazany został na rys. 2.6, na przykładzie dwóch systemów CKO 3D. Transformacja geometryczna obliczana jest na podstawie wyznaczenia wielu pozycji markera (P_{11}, ..., P_{nm}, gdzie n – numer systemu CKO 3D, m - pozycja punktu w n-tym polu pomiarowym), który umieszczany jest w kolejnych polach pomiarowych systemów CKO 3D (co najmniej 4 pozycje markera powinny zostać zmierzone w pojedynczym polu pomiarowym). Pozycja markera w lokalnych układach współrzędnych obliczana jest za pomocą procedur przetwarzania obrazów (wyznaczenie pozycji 2D środka markera dla pojedynczej kamery) i triangulacji (w celu obliczenia współrzędnych 3D markera w lokalnym układzie współrzędnych). Równocześnie wyznaczana jest pozycja markera w globalnym układzie współrzędnych, z wykorzystaniem trackera laserowego. Parametry transformacji (obrót: R_x, R_y, R_z i translacja: T_x, T_y, T_z) między lokalnymi i globalnymi układami współrzędnych (dokładniej między wektorami pozycji 3D markerów) uzyskuje się przy użyciu metody SVD (ang.: Singular Value Decomposition) [18]. Schemat blokowy opisanej procedury przedstawiony został na rys. 2.7.
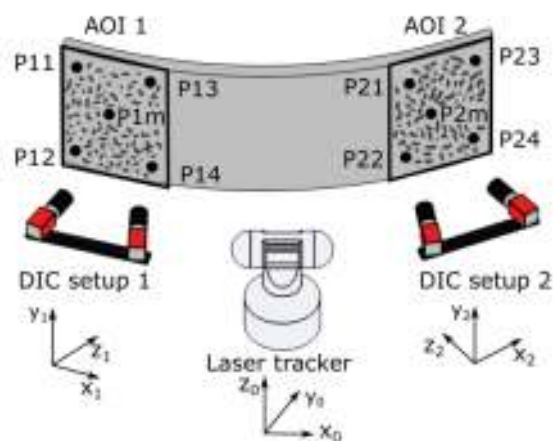
Rysunek 2.6. Schematyczny rysunek konfiguracji wielokamerowego (n = 2) systemu CKO 3D z rozproszonymi polami pomiarowymi, z zaznaczonym trackerem laserowym [A10].

Rysunek 2.7. Schemat procedury transformacji lokalnego układu współrzędnych do globalnego układu współrzędnych dla wielokamerowego systemu CKO 3D (n – numer układu pomiarowego) [A10].

2.3.2. Analiza błędów i walidacja dokładności pomiaru przemieszczeń opracowanego systemu

Na błąd pomiaru przemieszczeń wielokamerowym systemem CKO 3D mają wpływ dwa czynniki:

- dokładność pomiaru przemieszczenia poszczególnych układów CKO 3D,
- wpływ transformacji danych między lokalnymi i globalnymi układami współrzędnych.

Dokładność pomiaru przemieszczeń wielokamerowym systemem CKO 3D, zależy od najmniejszej dokładności jednego z systemów CKO 3D wchodzącego w skład systemu wielokamerowego. Dobrą miarą dokładności pomiarów przemieszczeń 3D jest błąd reprojekcji, wyznaczany w trakcie kalibracji systemu CKO 3D. Wpływ transformacji danych między lokalnymi i globalnymi układami współrzędnych przyjmuje postać błędu kosinusa. Aby wyliczyć błąd kosinusowy, wyznaczony jest kąt pomiędzy dwiema płaszczyznami dopasowanymi do dwóch grup punktów. Pierwsza grupa obejmuje pozycje markerów zmierzonych przez system CKO 3D w jego polu pomiarowym, druga grupa obejmuje pozycje tych samych markerów zmierzone przez tracker laserowy.

W celu walidacji dokładności pomiaru opracowanego systemu, wykonałem pomiary laboratoryjne z wykorzystaniem pojedynczego systemu CKO 3D, dokładność systemu wielokamerowego determinowana jest przez najniższą dokładność pojedynczego systemu CKO 3D. Ze względu na małe pole pomiarowe podczas pomiarów laboratoryjnych do transformacji układów współrzędnych oraz walidacji systemu wykorzystałem maszynę współrzędnościową Carl Zeiss ACCURA 7 (dokładność pomiaru położenia: 2 µm). Układ pomiarowy został przestawiony na rys. 2.8. Zgodnie z opracowaną procedurą, wyznaczyłem błąd pomiaru przemieszczeń systemu, błąd reprojekcji wynosił 90 µm, natomiast błąd kosinusowy- 0,08 µm/m (kąt między dopasowanymi płaszczyznami wyniósł 0,03 stopnia), czyli całkowity błąd wynosił: 90 µm +/- 0,08 µm/m. Następnie przeprowadziłem pomiary położenia punktu referencyjnego na wzorcu w 21 pozycjach oraz wyznaczyłem jego przemieszczenia między tymi pozycjami. Błąd pomiaru przemieszczeń obliczyłem na podstawie różnicy między wynikami pomiaru referencyjnego wykonanego maszyną współrzędnościową, a wynikami pomiaru systemem CKO 3D. Maksymalne wartości błędów wyniosły odpowiednio 46, 61, 25 µm dla pojedynczych osi XYZ oraz 84 µm błąd przestrzenny. Niepewność pomiaru przemieszczeń na poziomie ufności 95% wynosi 47 µm (podwójna

31

wartość odchylenia standardowego), dzięki czemu uzyskałem walidacje dokładności pomiaru, której wartość obliczona wynosiła 90 µm +/- 0,08 µm/m.
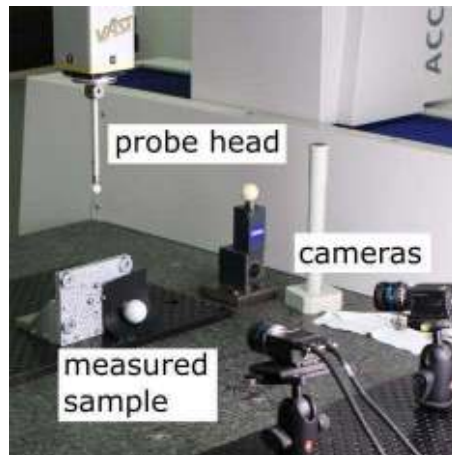

Rysunek 2.8. Stanowisko pomiarowe opracowane na potrzeby walidacji dokładności pomiarowej wielokamerowego systemu CKO 3D, z rozproszonymi polami pomiarowymi [A10].

2.3.3. Implementacja systemu w warunkach przemysłowych

Wielokamerowy system z rozproszonymi polami pomiarowymi został po raz pierwszy wykorzystany do pomiaru przemieszczeń rurociągów na instalacjach syntezy amoniaku, wykorzystywanych w Zakładach Azotowych Kędzierzyn-Koźle, w trakcie odstawiania i rozruchu instalacji przed i po remoncie [A9]. Zmierzyłem przemieszczenia trzech fragmentów instalacji: (i) kostka na reaktorze (połączenie rurociągów zasilającego i dwóch odprowadzającego), (ii) pionowy fragment rurociągu zasilającego, (iii) poziome fragmenty jednego z dwóch rurociągów odprowadzających (rys. 2.9). Była to pierwsza implementacja opracowanego systemu, mająca na celu eksperymentalne potwierdzenie krytycznych funkcjonalności systemu, tj. algorytm obliczania transformacji między układami współrzędnych (eng.: '*proof of concept*'). W związku z powyższym do transformacji lokalnych układów współrzędnych systemów CKO 3D do globalnego układu współrzędnych wykorzystany został pomiar geodezyjny znaczników w obszarach pól pomiarowych. Pomiar geodezyjny jest znacznie mniej dokładny niż pomiar trackerem laserowym, jednak dużo prostszy w implementacji, w szczególności w kontekście prac na obszarze zagrożonym pożarem lub wybuchem (strefa Ex obowiązywała na całej instalacji). Uzyskano średniokwadratowy błąd dopasowania położenia znaczników pomiędzy rozproszonymi polami pomiarowymi poniżej 10 mm, co w tym praktycznym przypadku było akceptowalne.

Uzyskane dane eksperymentalne zostały wykorzystane do identyfikacji rzeczywistych odkształceń konstrukcji oraz weryfikacji i aktualizacji modelu numerycznego instalacji.

Przeprowadzone obliczenia umożliwiły określenie odpowiedzi konstrukcji na wymuszenia związane z rozruchem i pracą instalacji. Pomogło to w analizie przyczyn wycieków na instalacji, wynikających głównie z niewłaściwej konstrukcji uszczelki na badanej kostce. Nowy układ uszczelek rozwiązał problem z pojawiającymi się rozszczelnieniem instalacji w trakcie jej pracy.
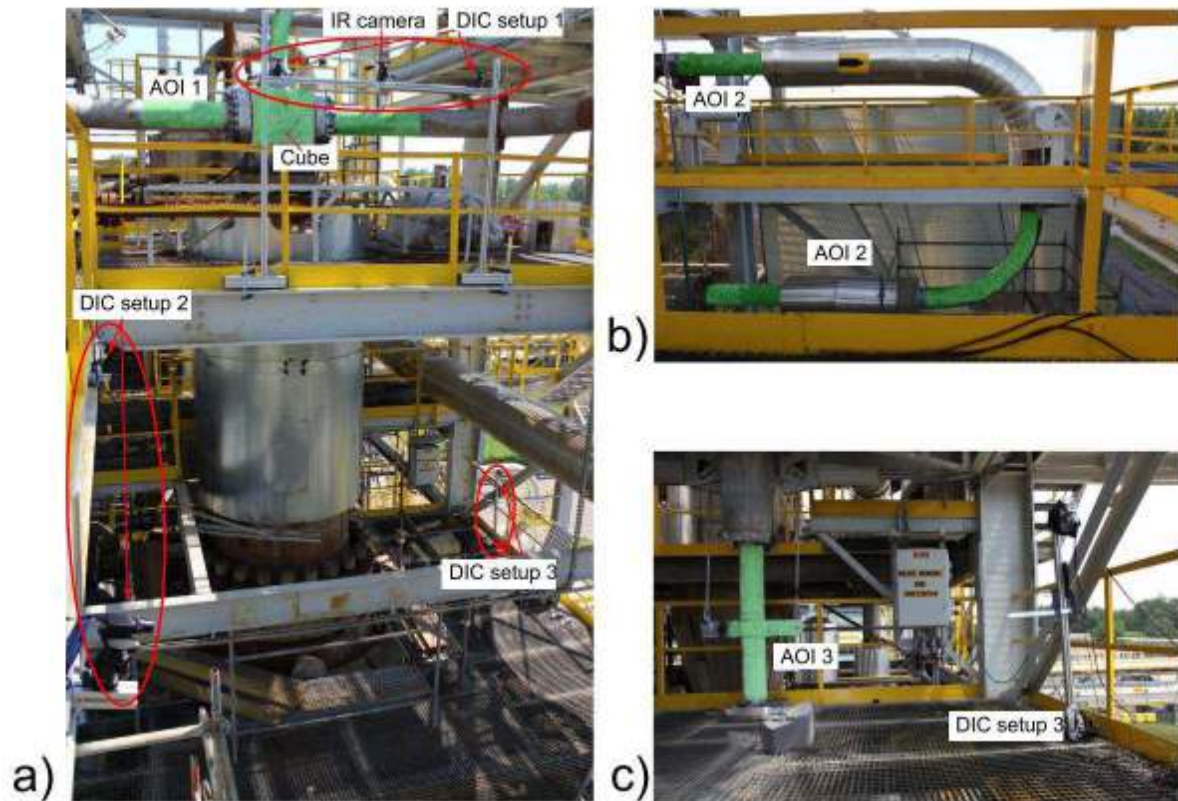

Rysunek 2.9. Zdjęcia monitorowanej instalacji azotowej: a) widok instalacji ze wskazanymi lokalizacjami trzech systemów CKO 3D i pierwszego pola pomiarowego, b) lokalizacji drugiego pola pomiarowego, c) lokalizacja trzeciego systemu CKO 3D i odpowiadającego mu pola pomiarowego [A9].

Wielokamerowy system z rozproszonymi polami pomiarowymi został po raz drugi wykorzystany do pomiaru przemieszczeń hali magazynowej wykonanej z samonośnej blachy łukowej, o przekroju łuku: 8 m wysokości i 18 m rozpiętości [A10]. W tym przypadku do wyznaczenia globalnego układu współrzędnych wykorzystany został tracker laserowy, zgodnie z metodyką opisaną w podrozdziale 2.3.1. Podczas pomiarów system mierzył przemieszczenia hali w trzech polach pomiarowych, które obejmowały lokalizację punktów odpowiadających maksymalnym przemieszczeniom konstrukcji wyznaczonym za pomocą wstępnego modelu numerycznego. Wymiar każdego z pól pomiarowych to 2,5 m x 1,5 m, a odległość między sąsiadującymi polami pomiarowymi to 4 m (rys. 2.10 a-b). W odległości ok. 9 m od

wielokamerowego systemu CKO 3D znajdował się tracker laserowy Leica AT 901 B, dokładność pomiaru systemu w wykorzystanym trybie dalmierza wynosi ± 0,015 mm + 0,006 mm/m.

Zgodnie z przedstawioną metodyką wyznaczyłem dokładność pomiaru pojedynczych układów CKO 3D, która wynosiła odpowiednia 0,21 mm +/- 1,27 μm/m, 0,17 mm +/- 0,05 μm/m i 0,24 mm +/- 0,16 μm/m, dla pierwszego, drugiego i trzeciego systemu CKO 3D. Jako dopuszczalny błąd wielokamerowego systemu CKO 3D przyjmuje maksymalny błąd systemów składowych, który wynosił 0,24 mm +/- 0,16 μm/m. W wyniku pomiarów uzyskałem mapy przemieszczeń badanej konstrukcji, przykładowe mapy pokazano na rys. 2.10 c-e. Dane posłużyły do kalibracji i walidacji modelu numerycznego badanej konstrukcji, która zostanie dokładniej opisana w podrozdziale 2.4.
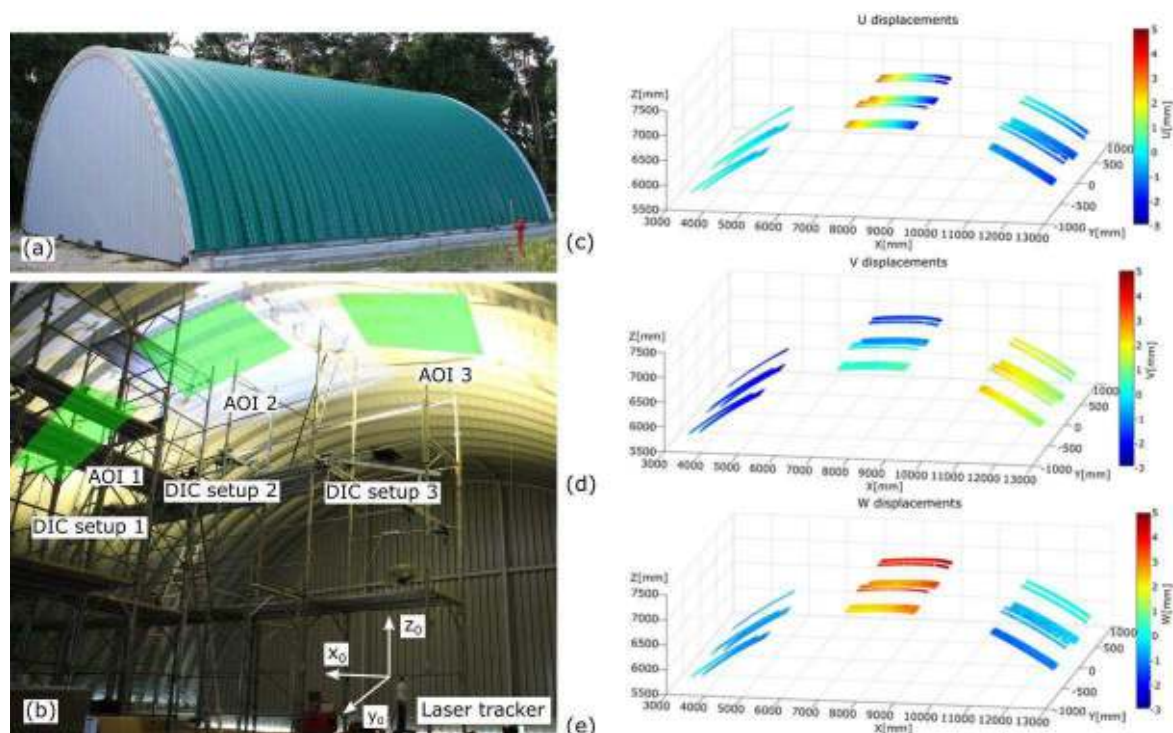

Rysunek 2.10. Zdjęcia: a) badanej hali oraz b) układu pomiarowego. Przykładowe wyniki pomiarów w globalnym układzie współrzędnych, mapy przemieszczeń: a) U, b) V c) W [A10].

2.4. Metodyka kalibracji i walidacji modeli numerycznych blachy łukowej z wykorzystaniem eksperymentalnych danych polowych

Do projektowania złożonych struktur inżynierskich wykorzystywane są techniki hybrydowe, w których metody eksperymentalne i numeryczne uzupełniają się wzajemnie [1]. W mechanice eksperymentalnej najczęściej wykorzystywane są czujniki punktowe (np.

czujników tensometrycznych) do pomiaru przemieszczeń i odkształceń. Dane z tych pomiarów służą do kalibracji modeli numerycznych. Jest to podejście proste i tanie, ale problem może wystąpić, jeśli wstępny (uproszczony) model numeryczny nie wskaże wszystkich miejsc, w których występują koncentracje naprężeń. To z kolei może powodować błędy w procesie walidacji modelu numerycznego. W związku z powyższym, coraz częściej optyczne metody polowe wykorzystywane są do kalibracji i walidacji modeli numerycznych złożonych struktur inżynierskich. Jedna z implementacji CKO realizowanych przeze mnie wspólnie z Instytutem Techniki Budowlanej w Warszawie, dotyczyła pomiarów blachy łukowej, wykorzystywanej w konstrukcjach niskokosztowych [A2]. Praca ta stała się punktem wyjścia do opracowania eksperymentalno-numerycznej metodyki kalibracji modeli numerycznych. Model numeryczny (MES) konstrukcji z blachy łukowej został opracowany przez dr hab. inż. Artura Piekarczuka, natomiast jego ewaluacja stanowiła przedmiot jego rozprawy habilitacyjnej [19], która została zakończona w 2018 roku. Ewaluacja modelu numerycznego była wspierana przez dane eksperymentalne, które uzyskałem z wykorzystaniem metody CKO.

Model numeryczny MES wielkogabarytowej samonośnej konstrukcji łukowej wykonanej z cienkościennych blach profilowanych, które charakteryzują się karbowanymi ściankami profilu jest bardzo trudny do opracowania, ze względu na skomplikowaną geometrię i charakterystykę materiałową. W związku z powyższym zaproponowaliśmy trzy etapową eksperymentalno-numeryczną metodę kalibracji i walidacji modelu numerycznego takiej konstrukcji. W ramach wykonanych prac opracowałem metodykę pomiaru i wykorzystania eksperymentalnych danych polowych uzyskanych metodą CKO 3D na każdym etapie kalibracji i walidacji modelu numerycznego konstrukcji. Na pierwszym etapie prac badałem w warunkach laboratoryjnych wycinki łuków o długości 1 m i szerokości 0,7 m: badania były prowadzone w celu określenia modelu geometrycznego kształtu powierzchni do analizy MES [A5, A8, A12]. W następnym etapie w testach laboratoryjnych wykorzystaliśmy strukturę złożoną z czterech pojedynczych segmentów w celu zbadania stabilności globalnej i określenia reakcji mechanicznej podpór [A2, A9, A12]. Ostatnim krokiem były testy pełnowymiarowego obiektu (hala 8 m wysokości o podstawie 18m x 18m). W efekcie uzyskaliśmy skalibrowany model MES konstrukcji, który umożliwia symulację wpływu obciążeń środowiskowych na pracę tego typu konstrukcji [A10, A12]. Opracowana wspólnie z dr hab. A. Piekarczukiem procedura została podsumowana i przedstawiona na rys. 2.11, natomiast przedstawione etapy zostały dokładniej opisane poniżej.
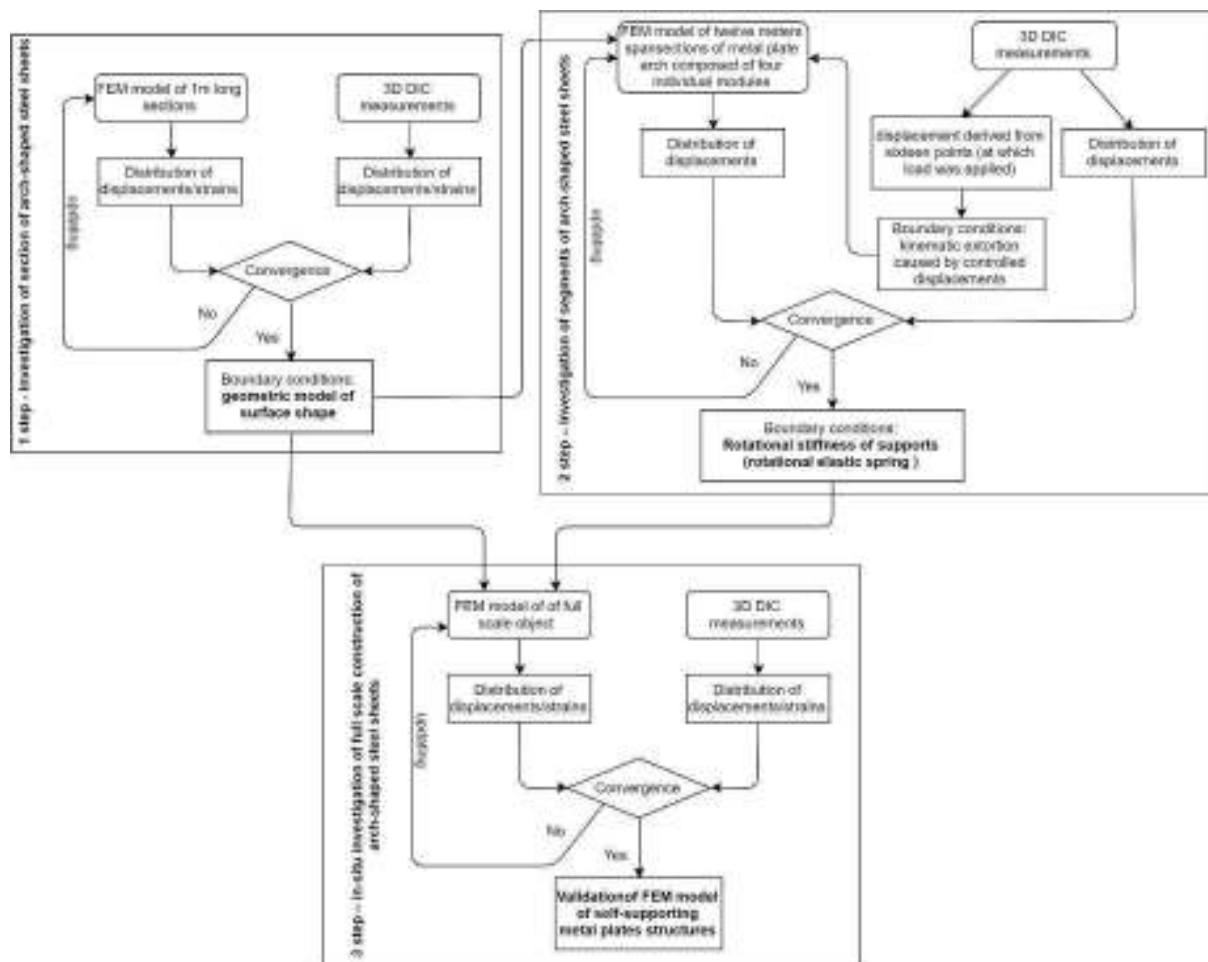
Rysunek 2.11. 1Schemat blokowy 3-etapowej kalibracji i walidacji modelu numerycznego konstrukcji z blachy łukowej z wykorzystaniem eksperymentalnych danych polowych uzyskanych metodą CKO 3D [A12].

2.4.1. Badanie wycinków blachy łukowej

W pierwszym etapie prac symulowano lokalną utratę stateczności na odcinkach o długości 1 m [A5, A8], na specjalnie zaprojektowanym stanowisku testowym, które umożliwiało mimośrodowe obciążanie badanych odcinków w kierunku osi przechodzącej przez środek ciężkości przekrojów (rys. 2.12 a–c). Uzyskane wyniki pomiarów przemieszczeń pozwoliły na określenie dopuszczalnych uproszczeń geometrii modelu. Porównaliśmy trzy modele numeryczne o zróżnicowanej geometrii z danymi eksperymentalnymi. W celu wykonania analizy ilościowej, porównałem uzyskane przemieszczenia w wybranych punktach, następnie dla modelu, który wykazywał najlepszą zbieżność dokonałem jakościowego porównania uzyskanych map przemieszczeń (rys. 2.12 d–g). Mapy przemieszczeń uzyskane za pomocą analizy numerycznej wykazują dobrą korelację z danymi eksperymentalnymi, uwzględniając ich charakter i wartości. Pewne rozbieżności, które można zaobserwować, mogą być

spowodowane nieuniknionymi odchyleniami geometrii próbki i niedoskonałym spełnieniem warunków podparcia.
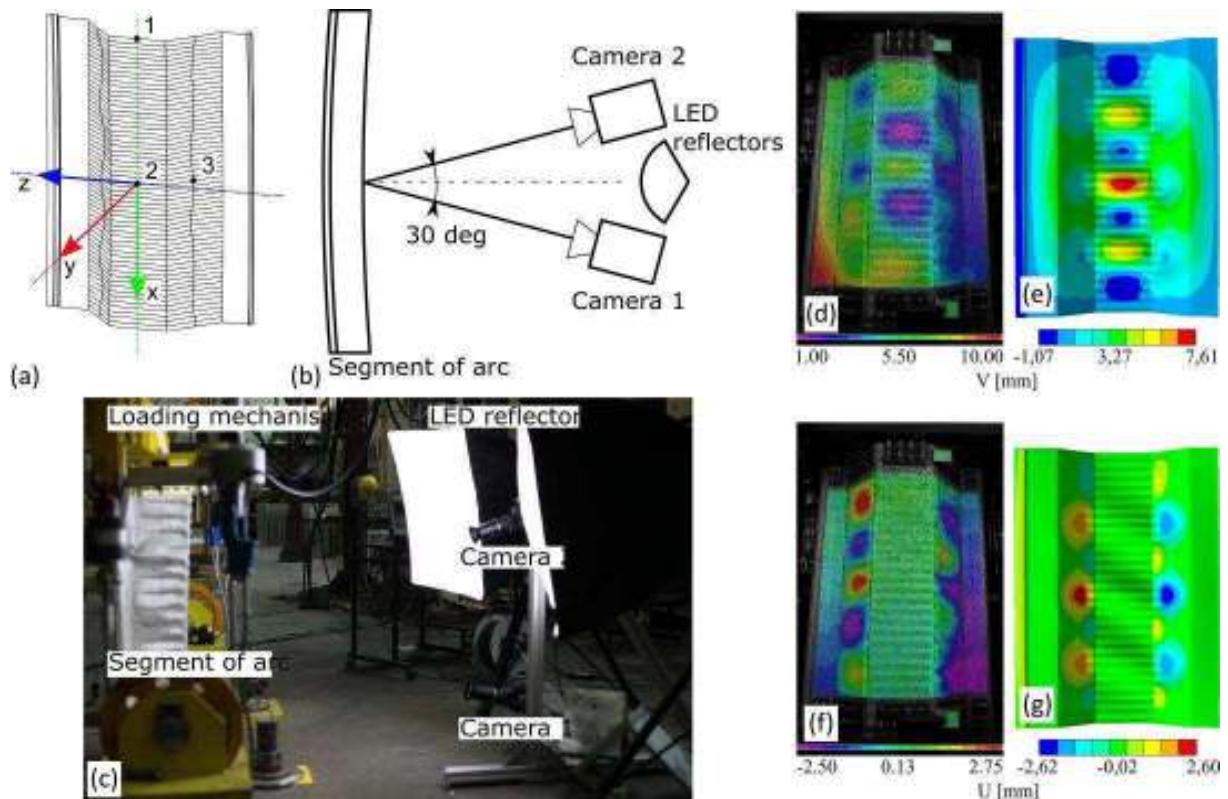
Rysunek 2.12. Układ eksperymentalny: a) schemat wycinka blachy z zaznaczoną lokalizacją układu współrzędnych, przyjętego do dalszej analizy; b) schemat i c) zdjęcie układu pomiarowego CKO 3D. Przykładowe porównanie map przemieszczeń uzyskanych: d) i f) eksperymentalnie oraz e) i g) numerycznie [A5].

2.4.2. Badanie segmentów blachy łukowej

W drugim etapie badań przeprowadzono testy laboratoryjne struktury złożonej z czterech pojedynczych łuków o rozpiętości 12 m. Na specjalnie przygotowanym stanowisku za pomocą zestawu siłowników możliwa była symulacja obciążeniem śniegiem i wiatrem. W celu wykonania pomiaru struktury, wykorzystałem wielokamerowy system CKO 3D z nachodzącymi polami pomiarowymi. Cztery pojedyncze systemy pomiarowe obserwowały badany obiekt, pola obserwacji sąsiadujących systemów zachodziły na siebie, we wspólnych obszarach umieszczono planszę kalibracyjną. Jako znaczniki do transformacji układu współrzędnych wykorzystałem narożniki planszy kalibracyjnej, którą była szachownica. W rezultacie uzyskałem pole pomiarowe o wymiarach 7 m x 4 m (Rys. 2. 13). Średniokwadratowy błąd dopasowania znaczników pomiędzy sąsiadującymi polami pomiarowymi wynosił poniżej 0,5 mm. W wyniku pomiaru uzyskałem ciągłe mapy przemieszczeń w globalnym układzie

pomiarowym związanym z podstawą konstrukcji. W pomiarach skupiłem się na dwóch zewnętrznych powierzchniach łuków, odpowiadających miejscom przyłożenia wymuszeń kinematycznych.
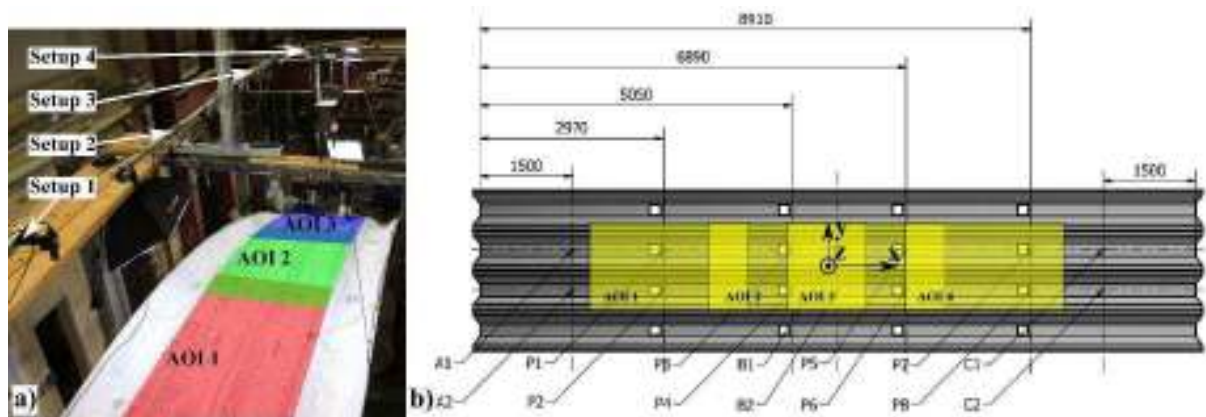
Rysunek 2.13. a) Zdjęcie wielokamerowego systemu CKO 3D oraz badanej konstrukcji; b) schemat badanej konstrukcji z zaznaczonymi polami pomiarowymi oraz punktami charakterystycznymi wykorzystanymi do analizy [A12].

Uzyskane z analizy metodą CKO 3D dane o przemieszczeniach wybranych punktów (rys. 2.13 b, punkty A1, A2, B1, B2, C1, C2) wykorzystano jako wymuszenie kinematyczne w modelu numerycznym konstrukcji, natomiast uzyskane mapy przemieszczeń porównano z symulacjami numerycznymi. Na rys. 2. 14 przedstawiono przykładowe porównanie dla połowy maksymalnego obciążenia. W symulacji MES badaną konstrukcję podparto na dwóch końcach, z wykorzystaniem obrotowego podparcia sprężystego, które pozwala na obrót zamocowanego elementu wyłącznie wzdłuż osi równoległej do osi symetrii badanej konstrukcji. Poprzez porównanie wyników eksperymentalnych i symulacji wyznaczono wartość współczynnika sztywności obrotowej zasymulowanego zamocowania.
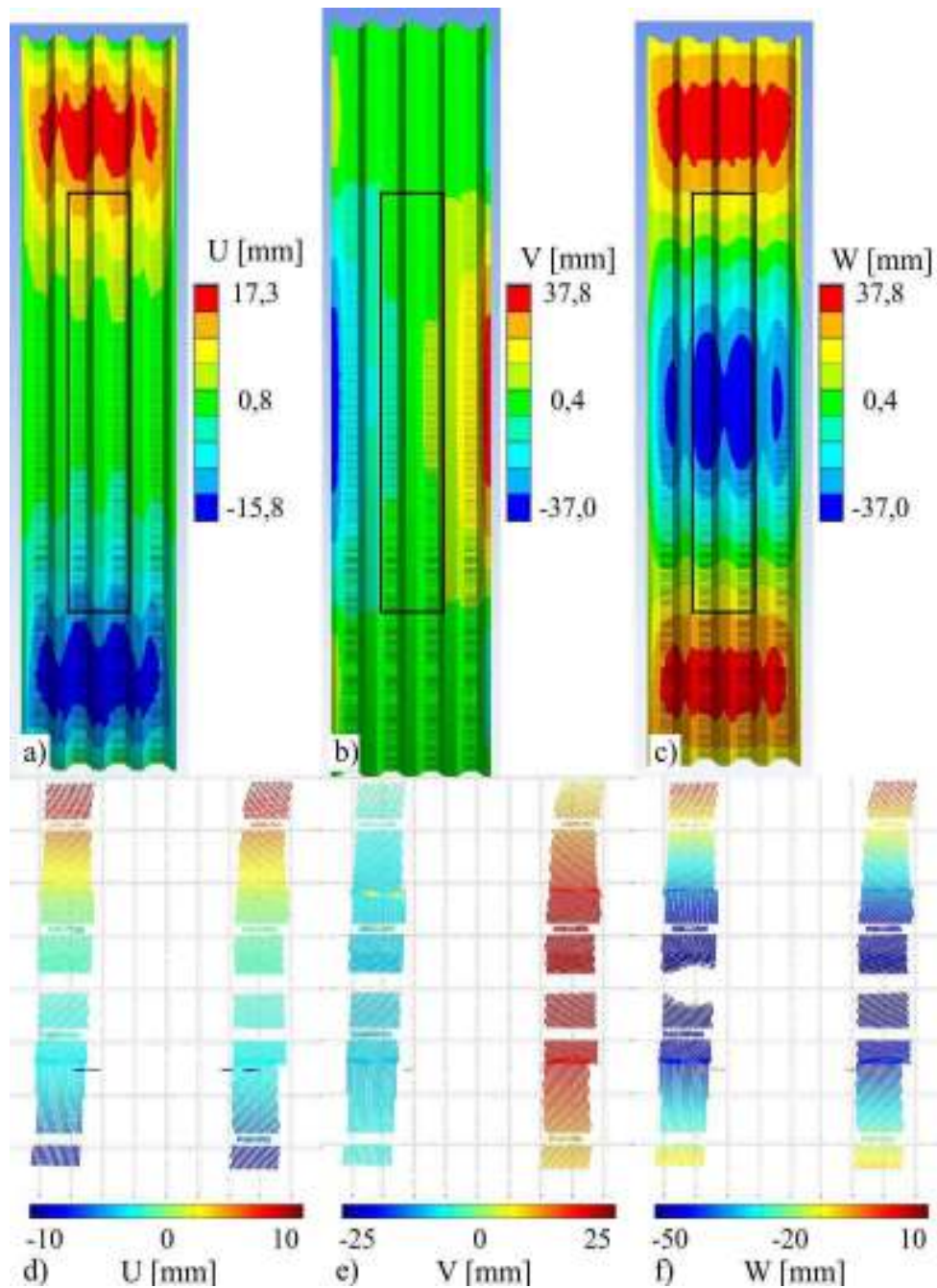
Rysunek 2.14. Porównanie rozkładu przemieszczeń: widok z góry przemieszczeń uzyskanych z modelu MES (a-c), całej próbki i wyników eksperymentalnych (d-f) obejmujących dolną powierzchnię dwóch środkowych łuków o długości 7 metrów (obszar zaznaczony czarnymi ramkami na danych z symulacji numerycznej) [A12].

2.4.3. Badanie pełnowymiarowego obiektu z blachy łukowej

W ostatnim etapie przeprowadziłem badana *in-situ* pełnowymiarowego obiektu (hala 8 m wysokości o podstawie 18 m x 18 m), który był poddawany obciążeniom termicznym i działaniom wiatru (podczas przeprowadzanych badań nie wystąpiły opady śniegu). Do pomiaru wykorzystałem system wielokamerowy CKO 3D z rozproszonymi polami pomiarowymi,

opisany w podrozdziale 2.3.3 (rys. 2.10) [A10]. System ten został umieszczony na rusztowaniu budowlanym o wysokości 6 m i szerokości 10 m, natomiast pomiary były prowadzone przez kilka miesięcy (od marca do października). Na potrzeby długoterminowego pomiaru opracowałem metodę kompensacji wpływu przemieszczeń rusztowania w związku ze zmianami temperatury na wyniki pomiarów. Z wykorzystaniem trackera laserowego zmierzyłem w funkcji temperatury (panującej wewnątrz hali) przemieszczenia elementów na których zamocowane były bezpośrednio systemy pomiarowe. Uzyskaną korektę uwzględniłem przy analizie wyników pomiaru.

Pomiary przemieszczeń realizowane były w trzech polach pomiarowych, które obejmowały lokalizację punktów odpowiadających maksymalnym przemieszczeniom konstrukcji wyznaczonym za pomocą wstępnego modelu numerycznego. Do walidacji modelu numerycznego wybrano po trzy punkty referencyjne dla każdego z obszarów, w sumie dziewięć punktów. Badania były prowadzone przez kilka miesięcy, natomiast do walidacji modelu numerycznego wybrano okres 12 godzin i 25 min., podczas którego gradient temperatur zarówno zewnętrznej jak i wewnętrznej był największy. Uzyskane wyniki pozwoliły na walidacje modelu numerycznego, który może zostać wykorzystany do obliczeń nośności i stateczności dowolnej konstrukcji łukowej wykonanej z cienkościennych blach profilowanych.

2.4.4. Implementacja opracowanej metodyki w praktyce inżynierskiej

Przedstawiona metodyka może posłużyć do określenia właściwości użytkowych w tym nośności i stateczności różnych odmian samonośnych struktur łukowych systemu K-span, które są wymagane w procesie wdrażania wyrobu do stosowania w budownictwie zgodnie z zasadami przedstawionymi w Rozporządzeniu Parlamentu Europejskiego i Rady (UE) NR 305/2011. Instytut Techniki Budowlanej jest zainteresowany w przyszłości podjęciem prac regulujących zasady oceny właściwości użytkowych wyrobu w tym także na poziomie regulacji dokumentów normatywnych w zakresie zgłoszeniem aneksu do norm dotyczących projektowania elementów cienkościennych PN-EN 1993-1-3.

2.5. Wkład autora w publikacje

We wszystkich pracach opisanych w publikacjach byłem odpowiedzialny za konstrukcję i budowę układu pomiarowego oraz opracowanie danych eksperymentalnych. Szczegółowe zadania zrealizowane jako wkład do poszczególnych publikacji przedstawiłem poniżej. W publikacjach A4, A7, A10 i A12 jestem wiodącym autorem odpowiedzialnym za strukturę artykułu i jego finalne opracowanie. We wszystkich przedstawionych w przewodniku publikacjach brałem udział w przygotowaniu treści manuskryptu – tekstu oraz ilustracji.

Publikacja	Zrealizowane zadania w trakcie przygotowania publikacji	Udział (%)
A1	Opracowanie metodyki pomiarów metodą CKO 3D oraz analizy wyników metodą przestrzenno-czasową. Analiza wyników tą metodą.	30
A2	Opracowanie metodyki pomiarów metodą CKO 3D konstrukcji z blachy łukowej oraz analiza wyników.	15
A3	Opracowanie metodyki polowych pomiarów multimodalnych przemieszczeń i temperatury oraz analizy danych dla pojedynczych serii pomiarów. Opracowanie danych eksperymentalnych m.in. przygotowanie map profili przemieszczeń w funkcji czasu.	30
A4	Opracowanie metodyki pomiarów podobrazi płóciennych podczas próby wilgotnościowej, opracowanie procedury wyznaczania map przemieszczeń lokalnych oraz map profili przemieszczeń w funkcji czasu.	55
A5	Opracowanie metodyki pomiarów umożliwiającej porównanie danych eksperymentalnych (uzyskanych metodą CKO 3D) i numerycznych (symulacja MES).	25
A6	Wykonanie pomiarów oraz opracowanie danych eksperymentalnych, m. in. przygotowanie map profili przemieszczeń w funkcji czasu.	10

A7	Opracowanie metodyki pomiarów i analizy kształtu (w cylindrycznym układzie współrzędnych) obiektu typu walczak, które wykorzystywane są na blokach energetycznych w elektrowni.	55
A8	Opracowanie metodyki pomiarów umożliwiającej porównanie danych eksperymentalnych (uzyskanych metodą CKO 3D) i numerycznych (symulacja MES).	30
A9	Opracowanie metody i implementacja wielokamerowego systemu CKO 3D z rozproszonymi polami pomiarowymi do pomiaru rurociągów. Implementacja wielokamerowego systemu CKO 3D z nachodzącymi polami pomiarowymi do pomiaru blachy łukowej.	25
A10	Opracowanie wielokamerowego systemu CKO 3D z rozproszonymi polami pomiarowymi, walidacja dokładności pomiaru przemieszczeń opracowanej metody w warunkach laboratoryjnych oraz implementacja systemu do pomiaru hali z blachy łukowej.	75
A11	Opracowanie metody analizy danych o przemieszczeniach i odkształceniach zbiornika ciśnieniowego na wodór/metan w cylindrycznym układzie współrzędnych.	10
A12	Opracowanie trzy etapowej metodyki pomiaru i wykorzystania eksperymentalnych danych polowych uzyskanych metodą CKO 3D na każdym etapie kalibracji i walidacji modelu numerycznego konstrukcji.	70

2.6. Podsumowanie

Rozprawa składa się z przewodnika oraz jedenastu publikacji z listy czasopism JCR i jednej publikacji w recenzowanych materiałach konferencyjnych. Prowadzone przeze mnie prace w trakcie realizacji doktoratu ukierunkowane były na rozszerzenie aplikacyjności metody cyfrowej korelacji obrazu do pomiaru złożonych obiektów inżynierskich, poprzez opracowanie nowych metodyk pomiarowych i ścieżek przetwarzania danych oraz rozbudowę układu pomiarowego o nowe konfiguracje pomiarowe i moduły obliczeniowe. Osiągnięte udoskonalenia metody 3D CKO oraz opracowane w ramach pracy metodyki pomiaru mają w przyszłości stanowić, wraz z opracowaniami udostępnionymi przez inne grupy badawcze, zestaw narzędzi, które mogą być dopasowane do analizy eksperymentalno-numerycznej istniejących i opracowanych w przyszłości skomplikowanych obiektów inżynierskich. Aplikacyjność opracowanych przeze mnie metodyk pomiarowych potwierdza współpraca z licznymi ośrodkami naukowymi i przemysłowymi w Polsce, do których można zaliczyć: Uniwersytet Mikołaja Kopernika w Toruniu, Instytut Techniki Budowlanej w Warszawie, Wydziałem Inżynierii Lądowej PW, Centrum Badań Kosmicznych PAN, Politechnikę Wrocławską, TAURON Wytwarzanie S.A., Grupa Azoty Zakłady Azotowe Kędzierzyn S.A., z którymi bezpośrednio współpracowałem w czasie realizacji pracy doktorskiej.

Najważniejsze rezultaty moich badań to:

– Opracowanie i implementacja metody przestrzenno-czasowej analizy danych CKO poprzez mapowanie profili przemieszczeń/deformacji w funkcji czasu dla takich zastosowań jak: monitorowanie zmian w obrazach olejnych [A1, A4], podporach stalowych wykopów [A3] oraz podłoży do zwierciadeł teleskopów astronomicznych [A6] pod wpływem zmian środowiskowych i/lub obciążeń zewnętrznych.

– Opracowanie metody wyznaczania lokalnych map przemieszczeń/odkształceń z pominięciem wpływu zmian globalnych w obiekcie na przykładzie badań obrazów olejnych [A4].

– Opracowanie metody analizy danych z CKO 3D w cylindrycznym układzie współrzędnych i jej implementacja do pomiarów wysokociśnieniowego zbiornika kompozytowego na wodór/metan [A11]. Opracowana metodyka analizy danych w cylindrycznym układzie współrzędnych wykorzystana została do analizy kształtu walczaka na bloku energetycznym [A7].

– Opracowanie i zbudowanie wielokamerowego systemu CKO 3D z rozproszonymi polami pomiarowymi. Opracowanie metody transformacji lokalnych układów współrzędnych pojedynczych systemów CKO 3D do jednego globalnego układu współrzędnych oraz przeprowadzenie analizy błędów i walidacja dokładności przemieszczeń opracowanego systemu [A10]. System został wykorzystany do pomiaru obiektów przemysłowych, hali magazynowej [A10] oraz rurociągów na instalacji w zakładach azotowych [A9].

– Opracowanie trzy etapowej eksperymentalno-numerycznej metody kalibracji i walidacji modelu numerycznego konstrukcji z blachy łukowej. Dla każdego etapu kalibracji i walidacji modelu numerycznego konstrukcji opracowana została metoda pomiaru i wykorzystania eksperymentalnych danych polowych, uzyskanych metodą CKO 3D. Na pierwszym etapie prac w warunkach laboratoryjnych wykonano testy obciążenia wycinków łuków o długości 1 m i szerokości 0,7 m, badania były prowadzone w celu określenia modelu geometrycznego kształtu powierzchni do analizy MES [A5, A8, A12]. W następnym etapie w testach laboratoryjnych struktury złożonej z czterech pojedynczych segmentów zbadano stabilność globalną konstrukcji i określono reakcje mechaniczne podpór [A2, A9, A12]. W ostatnim kroku przeprowadzono testy pełnowymiarowego obiektu (hala 8 m wysokości o podstawie 18m x 18m). W efekcie uzyskany został skalibrowany model MES konstrukcji, który umożliwia symulację wpływu obciążeń środowiskowych na pracę tego typu konstrukcji [A10, A12].

2.7. Przyszłe prace

W trakcie pracy nad rozprawą zidentyfikowałem dalsze potencjalne kierunki rozwoju i wdrażania opracowanych metod i narzędzi:

– **Systematyczne prace w zakresie implementacji opracowanych metod:** w ramach licencji wydanej przez Politechnikę Warszawską na rzecz firmy KSM Vison (której jestem współzałożycielem) panuję wdrożyć opracowane metodyki pomiarowe jako dobre praktyki w pracy konserwatorów dzieł sztuki oraz pracowników utrzymania ruchu w zakładach przemysłowych.

– **Opracowanie aplikacji mobilnej:** na pierwszym etapie CKO 2D a następnie CKO 3D dla potrzeb nadzoru budowlanego i zakładów ubezpieczeń (zwłaszcza w zakresie szkód budowlanych).

– **Opracowanie aneksu do normy PN-EN 1993-1-3 dotyczącej projektowania elementów cienkościennych** we współpracy z Instytutem Techniki Budowlanej, uwzględniającego

44

wykorzystanie opracowanej metodyki do określenia właściwości użytkowych, w tym nośności i stateczności różnych odmian samonośnych struktur łukowych systemu K-span.

– **Badanie konstrukcji z blachy łukowej w kontrolowanych warunkach pożaru:** kalibracja modelu numerycznego konstrukcji pełnowymiarowego obiektu odbywała się w granicy sprężystej odkształcalności stali, w przyszłości planowana jest kalibracja modelu numerycznego pełnowymiarowej konstrukcji w którym wprowadzone zostaną odkształcenia plastyczne, na skutek symulacji pożaru.

Bibliografia

[A1]   M. Malesa, **K. Malowany**, L. Tymińska-Widmer, E. A. Kwiatkowska, M. Kujawińska, B. J. Rouba, P. Targowski, „Application of Digital Image Correlation (DIC) for tracking deformations of paintings on canvas" *Proc. SPIE* 8084, 80840L (2011).

[A2]   A. Piekarczuk, M. Malesa, M. Kujawińska, **K. Malowany**, "Application of hybrid FEM-DIC method for assessment of low cost building structures", *Experimental Mechanics* 52 (9), 1297-1311 (2012).

[A3]   M. Malesa, **K. Malowany**, U. Tomczak, B. Siwek, M. Kujawińska, A. Siemińska-Lewandowska, "Application of 3D digital image correlation in maintenance and process control in industry", *Computers in Industry* 64 (9), 1301-1315 (2013).

[A4]   **K. Malowany**, L. Tymińska-Widmer, M. Malesa, M. Kujawińska, P. Targowski, B.J. Rouba, "Application of 3D digital image correlation to track displacements and strains of canvas paintings exposed to relative humidity changes", *Applied Optics* 53 (9), 1739-1749 (2014).

[A5]   A. Piekarczuk, **K. Malowany**, P. Więch, M. Kujawińska, P. Sulik, "Stability and bearing capacity of arch-shaped corrugated shell elements: experimental and numerical study", *Bulletin of the Polish Academy of Sciences* 64 (1), 113-123 (2015).

[A6]   M. Rataj, M. Malesa, M. Kujawińska, Ł. Płatos, P. Wawer, K. Seweryn, **K. Malowany**, "3D DIC Tests of Mirrors for the Single-Mirror Small-Size Telescope of CTA", *Experimental Astronomy* 39 (3), 513-525 (2015).

[A7]   **K. Malowany**, K. Magda, J. Rutkiewicz, M. Malesa, J. Kantor, J. Michoński, M. Kujawińska, "Measurements of geometry of a boiler drum by Time-of-Flight laser scanning", *Measurements* 72, 88-95 (2015).

[A8]   A. Piekarczuk, **K. Malowany**, "Comparative analysis of numerical models of arch-shaped steel sheet sections", *Archives of Civil and Mechanical Engineering* 16 (4), 645-658 (2016).

[A9]   M. Malesa, **K. Malowany**, J. Pawlicki, M. Kujawinska, P. Skrzypczak, A. Piekarczuk, T. Lusa, A. Zagorski, "Non-destructive testing of industrial structures with the use of multi-camera Digital Image Correlation method", *Engineering Failure Analysis* 69, 122-134 (2016).

[A10] **K. Malowany**, M. Malesa, T. Kowaluk, M. Kujawińska, "Multi-camera Digital Image Correlation method with distributed fields of view", *Optics and Lasers in Engineering* 98, 198-204 (2017).

[A11] P. Gąsior, J. Kaleta, R. Rybczyński, M. Malesa, M. Kujawińska, **K. Malowany**, "Application of Complementary Optical Methods for Strain Investigation in Composite High Pressure Vessel", *Composite Structures* 203, 718-724 (2018).

[A12] **K. Malowany**, A. Piekarczuk, M. Malesa, M. Kujawińska, P. Więch, "Application of 3D digital image correlation for development and validation of FEM model of self-supporting arch structures", *Applied Sciences* 9 (7), 1305 (2019).

[1] K.H. Laerman, *Hybrid techniques in experimental solid mechanics, in: Optical Methods in Experimental Solid Mechanics*, Springer, Wien, 1-72, 2002.

[2] G.N. Lampeas, V.P. Pasialis, "A hybrid framework for nonlinear dynamic simulations incl. full-field opt. meas. & image decomposition algorithms", *J. Strain Analysis for Eng. Design* 48 (1), 5-15 (2013).

[3] Ch. Sebastian, E. Hack, E. Patterson, "An approach to the validation of computational solid mechanics models for strain analysis", *J. Strain Analysis for Eng. Design* 48(1), 36-47, (2013).

[4] X. Shao, X. Dai, Z. Chen, Y. Dai, S. Dong, X. He, "Calibration of stereo-digital image correlation for deformation measurement of large engineering components", *Measurement Science and Technology* 27, 125010 (2016).

[5] S. Dong, S. Yu, Z. Huang, S. Song, X. Shao, X. Kang, X. He, "Target-based calibration method for multifields of view measurement using multiple stereo digital image correlation systems", *Optical Engineering* 56 (12), 124102 (2017).

[6] B. Pan, "Digital image correlation for surface deformation measurement: Historical developments, recent advances and future goals" *Measurement Science and Technology* 29 (8), 082001 (2018).

[7] K.L. Roye, *Metal Building Construction Using the MIC-240 ABM K-Span Machine*, Naval Postgraduate School: Monterey, CA, USA, 1996.

[8] P.N. Sabapathy, M.A. Wahab, M.J. Painter, "Numerical models of in-service welding of gas pipelines" *Journal of Materials Processing Technology* 118(1-3), 14-21 (2001).

[9] J. D. Carr, C. R. T. Young, A. Phenix, and R. D. Hibberd, "Development of a physical model of a typical 19th century English canvas painting", *Studies in Conservation* 48(3), 145-154 (2003).

[10] T.C. Chu, W.F. Ranson, M.A. Sutton, W.H. Peters, "Applications of digital-image-correlation techniques to experimental mechanics", *Experimental Mechanics* 25(3), 232-244 (1985).

[11] M.A. Sutton, J.J. Orteu, H. Schreier, *Image correlation for shape, motion and deformation measurements. Basic concepts, Theory and Applications*, Springer, New York 2009.

[12] G. Bradski, A. Kaehler, *Learning OpenCV*, O'Reilly Media, CA, USA, 2008.

[13] P. Targowski, B. Rouba, M. Gora, L. Tyminska-Widmer, J. Marczak, A. Kowalczyk, "Optical coherence tomography in art diagnostics and restoration", *Applied Physics A* 92, 1-9 (2008).

[14] J.-J. Orteu, F. Bugarin, J. Harvent, L. Robert, V. Velay, "Multiplecamera instrumentation of a single point incremental forming process pilot for shape and 3d displacement measurements: Methodology and results", *Experimental Mechanics* 51 (4), 625-639 (2011).

[15] Y. Wang, P. Lava, S. Coppieters, P. V. Houtte, D. Debruyne, "Application of a multi-camera stereo dic set-up to assess strain fields in an erichsen test: Methodology and validation", *Strain* 49, 190-198 (2013).

[16] X. Chen, L. Yang, N. Xua, X. Xie, B. Sia, R. Xu, "Cluster approach based multi-camera digital image correlation: Methodology and its application in large area high temperature measurement", *Optics and Lasers Technology* 57, 318-326 (2014).

[17] B. Muralikrishnan, S. Phillips, D. Sawyer, "Laser trackers for large-scale dimensional metrology: A review", *Precision Engineering* 44, 13-28 (2016).

[18] P. J. Besl, N. D. McKay, "A method for registration of 3-d shapes", *IEEE Transactions on Pattern Analysis and Machine Intelligence* 14 (2), 239-256 (1992).

[19] A. Piekarczuk, *Doświadczalne i obliczeniowe metody oceny łukowych przekryć z blach podwójnie giętych*, Instytut Techniki Budowlanej, Warszawa, 2018.

3. Publikacje stanowiące przedmiot rozprawy

PROCEEDINGS OF SPIE

Application of digital image correlation (DIC) for tracking deformations of paintings on canvas

Marcin Malesa, Krzysztof Malowany, Ludmila Tymińska-Widmer, Ewa A. Kwiatkowska, Malgorzata Kujawńska, et al.

Application of Digital Image Correlation (DIC) for tracking deformations of paintings on canvas

Marcin Malesa[*a], Krzysztof Malowany[a], Ludmiła Tymińska-Widmer[b], Ewa A. Kwiatkowska[c],
Małgorzata Kujawińska[a], Bogumiła J. Rouba[b], Piotr Targowski[c]
[a]Institute of Micromechanics and Photonics, Warsaw University of Technology, ul. Sw. Boboli 8,
02-525 Warszawa, Poland
[b]Institute for the Study, Restoration and Conservation of Cultural Heritage, Nicolaus Copernicus
University, ul. Gagarina 7, 87-100 Toruń, Poland
[c]Institute of Physics, Nicolaus Copernicus University, ul. Grudziądzka 5, PL-87 100 Toruń, Poland

ABSTRACT

A non-invasive and non-contact optical method for tracking overall and local deformations of canvas painting is presented. The technique was tested on a model painting on canvas with inhomogeneities introduced by infilling gaps, mending tears, and applying patches on the reverse of the canvas. The deformation of the sample was induced by changes of relative humidity. The feasibility of 3D Digital Image Correlation technique for evaluation of conservation methods is discussed.

Keywords: strain distribution testing, structural conservation-restoration of canvas, optical methods, artwork, easel painting

1. INTRODUCTION

Canvas paintings are complex, multilayer structures composed of hygroscopic materials of different properties and thus they are sensitive to cyclic changes of relative humidity in their surroundings.[1-6] The components of a painting: canvas support, glue size, ground, oil paint and varnish react differently and cause inner stress to the structure. Therefore, during storage in unstable environment significant distortions of the picture plane but also cracking or cleavage can appear. In case of any discontinuities in the whole structure or in separate strata, these effects become more complicated and pronounced. These local discontinuities may be inherent to the painting technique or caused by a damage. Crackles, interlayer delamination, cuts, tears, gaps fall into the latter category, as well as improper repairs and patches which may introduce harmful stress concentrations into the structure.

Therefore when developing new conservation materials for local treatments such as consolidation, tear mending or gap filling, it is important to evaluate their compatibility to the original structures. Features like hygrostability and mechanical properties in changing climatic conditions are particularly important in such an assessment since the repairs should restore the continuity of the layers as completely as possible and should react the same way as the original structure in any condition.

The problem is significant when restored paintings are exhibited in museums, especially those placed in historical buildings. In such cases the strict requirements for climate control are in practice difficult to be fulfilled. Moreover, the recent attempt to reconsider and loosen the requirements for climate control in museums[7, 8] demands extended research into the actual sensitivity of different types of artworks and artefacts to environmental changes. For this purpose suitable measuring and monitoring systems need to be developed and applied.

Experiments reported in this paper concentrated on assessment of feasibility of the three dimensional Digital Image Correlation method[9] (3D DIC) for materials studies focused on developing new methods for structural conservation of canvas paintings. Specifically, the application of the technique for measurements of local deformations of canvas painting models will be introduced. The perspectives for future works enabling the method to be applied for examination of real artworks in museum environment will be presented in conclusions.

* m.malesa@mchtr.pw.edu.pl; phone 48 222348635; fax +48 222348601

2. METHODOLOGY

Paintings on canvas are objects relatively flexible and considerably sensitive to deformations. To reveal discontinuities or inhomogeneities in the structure of a painting or to assess the compatibility of primary and added materials a method capable of tracking of local displacements against a background of significant overall surface deformation is required. Hence, such a method should combine a large field of view with a sub-millimetre resolution and accuracy in three dimensions. In case of painting canvases mounted on traditional wooden stretchers, out-of-plane deformation happens to be considerably high and can influence readings of the strain observed in plane.[10] Therefore, it is essential to use a method capable of recording in-plane and out-of-plane displacements simultaneously within a reasonably wide range of displacements.

Most of the methods used for structural damage measurements in the conservation of the art works such as use of strain gauges or optical fibre sensors, holographic and electronic speckle pattern 2D interferometry (ESPI), photoelastic stress analysis, photogrammetry, thermography, ultrasonic and X-ray imaging do not satisfy these main requirements.[11] Only in the recent account by Debashis and Young[12] the simultaneous 3D interferometry in reported. Similarly, Optical Coherence Tomography (OCT) may be used for precise 3D tracking of the canvas deformation but it is point-wise only in a present version.[10, 13]

On the contrary, the 3D DIC seems to meet these requirements well and provides some extra features like scalable field-of-view (FOV), flexibility with data acquisition frequency, relatively cheap hardware configuration.[9] The Digital Image Correlation is now widely used in the field of experimental mechanics, material engineering and monitoring of engineering structures.[14, 15] Recently it has been successfully applied in the field of conservation of art for strain monitoring in historic tapestries.[16, 17] The authors demonstrated the feasibility of the DIC method for non-contact full-field quantitative analysis of three-dimensional displacement and in-plain strains in large textiles. Moreover, the method has been used for a long-term monitoring of textile deformations caused by fluctuations of climatic conditions in museum environment.

3. EXPERIMENTAL

3.1 Digital Image Correlation

The two-dimensional DIC (2D DIC) measurement procedure is very simple and it requires to capture a series of images of a tested object before and after a load (or during loading). The surface of the object however, must have a natural random texture or it has to be covered by a random (speckle) pattern before the measurements start. One of images of the series is chosen as a reference image for all consequent analyses. All images are divided into small rectangular regions (subsets) consisting of N × N pixels. Dimensions of the subsets are dependent on the quality of the random pattern on the measured object. They can vary from 7 × 7 pixels (conventionally) to 70 × 70 pixels and even more. The DIC algorithm is then tracking the position of each subset from the reference image in all other images of the series. Corresponding subsets are matched by finding the maximum of the normalized cross-correlation function coefficient. For each subset in-plane displacement vectors (U and V) are then calculated. Sub-pixel accuracy is achieved by sophisticated interpolation methods. The output data is provided as a set of displacement maps, which can be consequently used for strain calculation.

In 3D DIC used in the presented experiment, for each state of an object two images are registered simultaneously by two cameras viewing the object from slightly different directions (Fig. 1a). The DIC method combined with stereovision methods[18] provides the maps of out-of-plane and in-plane displacements of and within an object which have occurred between acquisitions of images.[9] The 3D DIC measurement procedure is presented in figure 1b.

For the 3D DIC setup (Fig. 2a) two AVT Stingray 2MPx (1624x1232 pixels) cameras equipped with 8mm Schneider Kreuznach lenses have been used. The setup was stiffly mounted on the same optical table as specimen, thus its mechanical stability relative to the specimen could be assumed. The FOV was 0.4 m x 0.3 m and the estimated accuracy was 0.02 mm. In order to ensure sufficient lighting conditions, the 650W halogen lamp was additionally used. The measurements were hindered because of the reflexes on the front glass of the climate chamber. Reflexes were eliminated by optimizing the direction of illumination and black masking tape. Two cameras were capturing images simultaneously every 20 seconds. Total time of a single test was approximately 2.5 h. Analysis were carried out with the commercial software VIC-3D.
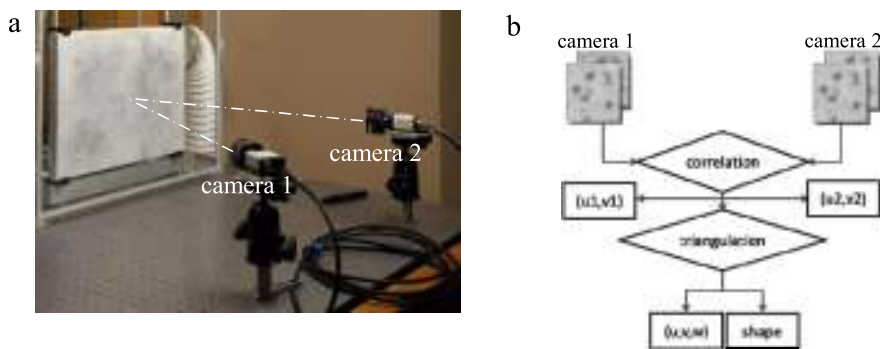
Figure 1. Three-dimensional Digital Image Correlation; a: set-up; b: data processing flow chart

3.2 Model sample

A model painting on canvas 40 cm wide and 30 cm high was used as the object under examination. In order to diminish the number of factors that could influence and complicate interpretation of the results of experiment, the sample was made of uniform, commercially primed fine plain weave canvas stretched over a keyed wooden stretcher with weft in the vertical direction. To create discontinuities in its structure four sets of regular circular gaps of various sizes ranging from 4 to 12 mm of diameter were made symmetrically through the stencil in all the four corners of the model according to the prepared template (Fig. 2a). Additionally two L-shaped cuts were made in the central part of the model. Each of the sets of gaps was filled in with traditional and experimental inserts, different in respect of structure, mechanical properties and sensitivity to climatic changes and thus the match to the surrounding original structure of the canvas painting (Fig. 2b). To allow image correlation a random speckle pattern was sprayed onto the face of the sample with a black ink (Fig. 3c).

Figure 2. Model painting on canvas repaired with various methods; a: template showing positions of discontinuities introduced to the canvas and used further as a reference for analysis of the data extracted from DIC records; b: reverse with inserts and patches; c: face of the painting with a random pattern

As an example of detailed analysis presented in Results section a cut butt-joined with dispersive adhesive (Osakryl + Winacet DP 50 in ratio 1:1 by weight) was chosen. An emulsive gesso (based on chalk, carboxymethylcellulose, polyvinyl alcohol, with plasticizers: Venetian turpentine and dammar in oil of turpentine) was used for infilling the ground. The repair was partially reinforced from the reverse with a rectangular piece of a flax tissue adhered with 3% carboxymethylcellulose (lap join).

54

3.3 Climate control chamber

The sample was subjected to environmental stress caused by rapid changes of relative humidity in a custom designed airtight climate chamber. The chamber was connected with large diameter air ducts to a simple external set-up to control relative humidity level in the range from 30% to 75% RH. The parameters of temperature and RH inside the chamber were monitored and recorded with a HygroClip® S sensor from Rotronic (Switzerland).

4. RESULTS

During the experiment DIC data were collected every 20 seconds together with the relative humidity (RH) and temperature values. After processing, the displacement maps were correlated with humidity data and combined into video animations for convenient inspection. In Fig. 3 examples of such maps are given for 55 min of experiment, when the relative humidity reached its maximum value of 73 %. It is worthwhile to note that the in-plane displacement (U, V) are one order of magnitude lower than the displacement observed out of plane.
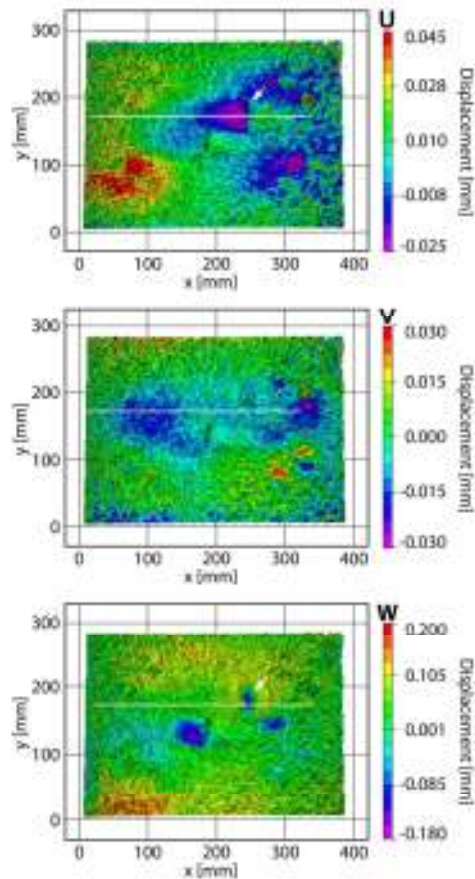

Figure 3. Relative displacement maps: U – in x direction, V – in y direction, W – in z direction at 73% RH. Displacements are colour-coded, separately for each map. White lines indicate position of a cross-section over the discontinuity (arrow) analysed in details in Figs 4 and 5

Such images are very useful for qualitative inspection and observation of overall deformations. The behaviour observed in the figure 3 is typical for canvas paintings mounted over a quite stiff traditional wooden stretcher. The changes in the dimensions of canvas induced by variations of relative humidity result in immediate changes in stress and are observed as bulging and waving of the surface out of plane. As one can see from the figure, in-plane deformations (U, V) are different in warp (x - horizontal) and weft (y - vertical) directions. At the maximum of humidity, canvas displacements along warp treads are directed towards the centre of the picture. The behaviour in weft direction is more complicated: at the perimeters of the canvas movements are generally outward whereas in the centre two zones of strain in opposite directions are present. The out-of-plane (W) overall deformations are much more pronounced. Additionally, the local effects caused by discontinuities introduced to the structure of canvas are visible on U, V, W displacement maps in the form of regular displacements different in colour from the surrounding background (upper right and lower right corner of the sample). However, for their quantitative analysis another approach to data presentation suits better. In Fig. 4 displacements at points along a chosen line (marked as a white segment in Fig. 3.) located across the centre of a vertical cut butt-joined with synthetic adhesive are presented as a function of time. Such imaging of the data shows development of a very characteristic deformation in the area of the repair.
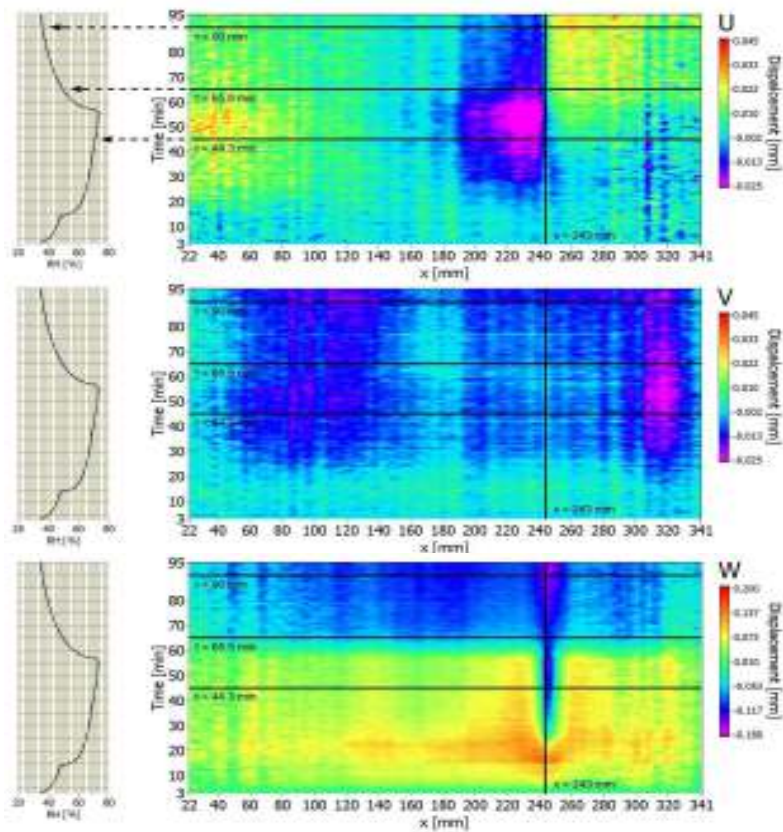

Figure 4. Relative displacements at points along a white line in Fig. 3 (y = 171 mm) shown as a function of time. Corresponding changes in relative humidity are given for reference. Horizontal and vertical black lines indicate locations of cross-sections presented at Fig. 5 and 6 respectively.

Images in Figure 4 comprise more global information whereas figures 5 and 6 may be used for more precise, quantitative evaluation. In Fig. 5 displacements along the white line in Fig. 3 are shown for the chosen moments of time, while in Fig. 6 displacements in one point (x = 243 mm, y = 171 mm) together with the concurrent relative humidity are shown as a function of time for a whole duration of the experiment.
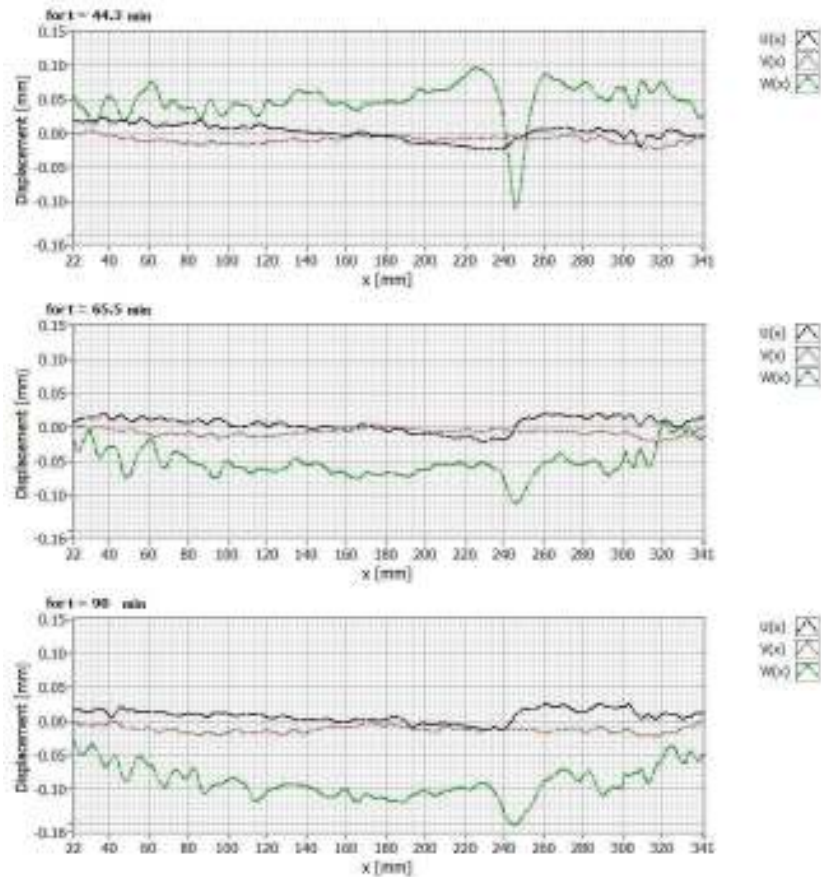

Figure 5. Relative displacements at y = 171 mm shown for chosen moments in time after the beginning of the experiment (t = 44.3 min at RH = 70%, t = 65.5 min at RH = 50%, t= 90.5 min at RH = 36%).

From the Figure 4 one can read that distinct out-of-plane displacements (W) occur immediately with a variation of climatic conditions while in-plane deformations (U, V) are registered later (after c. 20 min.). It is worth to point out the effect of hysteresis: painting doesn't return to its original state when humidity comes back to its initial value. On the background of overall deformation of the canvas painting, the local behaviour of the surface in vicinity if the discontinuity can be analysed. The increase of humidity causes the elevation of the edges of a cut (located at x = 243 mm) and then the process of disconnection of the join starts at t ≈ 20 min (at RH = 63%). On the map of out-of-plane displacements (W) a crack appears distinctly. At the same time, as it is clearly visible on the map of U displacements (x direction), slow opening of the crack begins. The canvas on the left side of the crack crimps towards the centre of the

painting whilst the on the right seems to be still. When the humidity reaches its maximum of 73 % RH, the displacement of the edges of the crack develops in both directions. Then, during drying, deformation of the right side toward the edge of the painting dominates and rises constantly until the end of experiment. Concurrently the edges of the crack deform out of plane and bend backwards. The amplitudes of overall displacements during all the experiment can be read from the colour scale in Fig. 4 and directly from Figs 5 and 6.

Specifically, from the Fig. 6 it is evident that any rapid change of relative humidity (t = 3, 14, 57 min.) causes an immediate out-of-plane reaction of the painting. It is also possible to define precisely the moment of failure of the glue-join (t = 17 min) as the point of reverse of the direction of out-of-plane deformation.
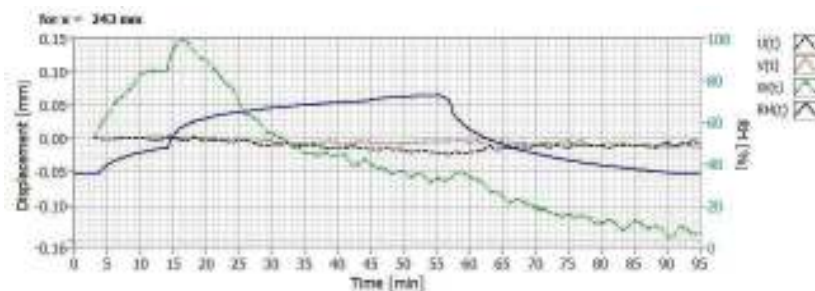

Figure 6. Displacements at a chosen point (x= 243 mm, y = 171 mm) as a function of time together with the relative humidity in the climate chamber.

5. CONCLUSIONS

Feasibility studies on 3D DIC method proved its suitability for canvas paintings measurements. The method is capable of detecting deformations: their location, range and shape and also their development in time. The results are unambiguous and their interpretation is straightforward. The registration of deformation is automatic, and made with at a high rate over a long period of time. Therefore this method may used for monitoring of processes with time resolution of single seconds. With the described technique it is possible to track quantitatively overall deformations of the whole canvas as well as local strains caused, in our case, by discontinuities introduced deliberately to the structure of canvas.

However, further research and readjustments of the set-up need to be undertaken in order to decrease uncertainties of the received data. Specifically, cameras with bigger resolution need to be used and consequently more precise calibration needs to be performed. It is expected that such improvement would extend a selection of detectable discontinuities in painting structure (e.g. cleavages, delaminations, crackles) and also would permit examination of larger variety of canvas supports with different hygrostability. In the presented experiment a random pattern was applied on the face of the sample. Such approach is possible in the case of materials studies since it is invasive although reversible. The usage of the DIC for examination of real artworks demands further studies that will specify certain features of the surface of the painting that may be sufficient as a random pattern for correlation. Consequently the parameters of the experimental set-up and data analysis must be adjusted. It is expected that some painting techniques or irregular texture of canvas visible from under the paint layer can appear to provide a pattern sufficient enough to carry out experiments on real artworks.

ACKNOWLEDGEMENTS

58

REFERENCES

[1]   Mecklenburg, M. F., "The Structure of Canvas Supported Paintings", Preprints of the International Conference on Painting Conservation - Canvases: Behaviour, Deterioration and Treatment, 119-155 (2005).

[2]   Mecklenburg, M. F., "Micro Climates and Moisture Induced Damage to Paintings", Conference on Micro Climates in Museums, 19-25 (2007).

[3]   Mecklenburg, M. F., [Meccanismi di cedimento nei dipinti su tela: approcci per lo sviluppo di protocolli di consolidamento (Failure Mechanisms in Canvas Supported Paintings: Approaches for Developing Consolidation Protocol)], Il prato, Padova (2007).

[4]   Rouba, B., "Die Leinwandstrukturanalyse und ihre Anwendung für Gemäldekonservierung", Restauratorenblätter 13, 79 – 90 (1992).

[5]   Rouba, B. J., [Podobrazia płócienne w procesie konserwacji (Canvas Painting Supports in the Process of Conservation)], Wydawnictwo UMK, Toruń (2000).

[6]   Rouba, B. J., "Płótna jako podobrazia malarskie (Canvases as Painting Supports)", Ochrona Zabytków 3-4, 222-244 (1985).

[7]   Erhardt, D., Tumosa, C. S. and Mecklenburg, M. F., "Applying science to the question of museum climate", Museum microclimates: contributions to the Copenhagen conference, 11-18 (2007).

[8]   Michalski, S., "Relative Humidity: A Discussion of Correct/Incorrect Values", Preprints of ICOM 10th Triennial Meeting, Vol. II, 624-629 (1993).

[9]   Sutton, M., Orteu, J.-J. and Schreier, H., [Image correlation for shape, motion and deformation measurements], Springer, (2009).

[10]   Targowski, P., Góra, M., Bajraszewski, T., Szkulmowski, M., Rouba, B., Łękawa-Wysłouch, T. and Tymińska, L., "Optical Coherence Tomography for Tracking Canvas Deformation", Laser Chemistry DOI: 10.1155/2006/93658, (2006).

[11]   Dulieu-Barton, J. M., Dokos, L., Eastop, D., Lennard, F., Chambers, A. R. and Sahin, M., "Deformation and strain measurement techniques for the inspection of damage in works of art", Reviews in Conservation 6, 63-73 (2005).

[12]   Debashis, M. and Young, C. R. T., "3D ESPI measurement of the strain fields introduced by strip-lining paintings", Proceedings of ICOM-CC Triennial Conference, 661 (2008).

[13]   Tymińska-Widmer, L., Targowski, P., M., G., M., I., Łękawa-Wysłouch, T. and Rouba, B., "Optical Coherence Tomography – a Novel Tool for the Examination of Oil Paintings", Proceedings of Conservation Science 2007, 175-182 (2008).

[14]   Malesa, M., Szczepanek, D., Kujawińska, M., Świercz, A. and Kołakowski, P., "Monitoring of Civil Engineering Structures Using DIC Technique", Book of Abstracts ICEM14, 31014 (2010).

[15]   Orteu, J.-J., "3-D computer vision in experimental mechanics", Optics and Lasers in Engineering 47, 282-291 (2009).

[16]   Dulieu-Barton, J. M., Khennouf, D., Chambers, A. R., Lennard, F. and Eastop, D., "Long term condition monitoring of tapestries using image correlation", Proceedings of the SEM Annual Conference, (2010).

[17]   Khennouf, D., Dulieu-Barton, J. M., Chambers, A. R., Lennard, F. J. and D.D., E., "Assessing the Feasibility of Monitoring Strain in Historical Tapestries Using Digital Image Correlation", Strain 46, 19-32 (2010).

[18]   Hartley, R. and A., Z., [Multiple View Geometry in computer vision], Cambridge University Press, Cambridge & New York (2003).

Application of Hybrid FEM-DIC Method for Assessment of Low Cost Building Structures

A. Piekarczuk · M. Malesa · M. Kujawinska ·
K. Malowany

Abstract In this work pre-operating tests of low-cost building structures have been presented. A hybrid experimental-numerical methodology has been used to determine the influence of an external, environmental load on the overall endurance of a hangar made of self-supporting metal-plates. Numerical simulations carried out on a FEM model have been consequently verified by measurements of the structure performed with the 3D Digital Image Correlation method and as a result, a detailed, calibrated FEM model of the structure has been developed.

Introduction

The collapse of a building may be caused by overcrowding, negligence during the design stage or by an excessive load (e.g. caused by weather conditions). Two of these causes occurred together when an exhibition hall in Katowice (Poland) collapsed in 2004 killing 65 people [1]. The roof of the structure was overloaded by the presence of a thick layer of snow. That is just one example among many low cost building structures (temporary exhibit halls, storage buildings etc.), whose collapse can lead to tragic events. For designers of such structures, the priority is to minimize building costs (incl.: design, materials, preliminary tests) and therefore they often exhibit relaxed norms in regard to safety. At the same time, the maintenance costs are being cut, so assessment of the health of the structure is minimized or not performed at all.

An another cause of a building failure can be the lack of sufficient engineering knowledge, particularly when a new, specific design is applied in an inadequate environment. A typical example of such structures is a hall's arch (Fig. 1(a)) [2]. The arch is made of a graded metal plate, whose thickness varies from 0.7 mm to 1.5 mm. The typical dimensions of a single module are 60 cm×(12÷24 cm). Individual segments are connected by kneading unbounded edges or by screws. A curved surface which is being formed from the segments has a length equal to the multiplied length of a singular module. The metal plate shaping technology causes the characteristic goffer pattern to appear on the surface of an object.

Graded metal plate structures (span up to 18 m) were initially being built temporarily for military applications [3] and were expected to be utilized in homogeneous climatic conditions over a period of a few months. However, the simple and fast technology of manufacturing and assembling called the attention of civilian investors, who adopted the technology to build bigger objects (span up to 30 m) with the purpose of civil engineering applications and with a much longer utilization period.

The straightforward adaptation of the technology combined with parameters and purpose modification causes constructional issues particularly in regard to stability and load capacity. Moreover, the irregular metal plate surface is difficult to be numerically modeled [4] and hence, the local

A. Piekarczuk
Building Research Institute,
1 Filtrowa St.,
00-611, Warsaw, Poland

M. Malesa (✉) · M. Kujawinska · K. Malowany
Warsaw University of Technology,
Institute of Micromechanics and Photonics,
8 Sw. Boboli St.,
02-525, Warsaw, Poland
e-mail: m.malesa@mchtr.pw.edu.pl

61

Fig. 1 Examples of a structure (**a**) in good condition, (**b**) after failure

loss of stability can occur in unexpected regions. Furthermore there is a lack of formal regulations (standards, instructions, guidelines), pertaining to methods of calculations of such structures. Simplified designs lead to crucial parameters being left out in the stability analysis which in consequence can lead to a catastrophic collapse. An example of a failure of the hall's arch is presented in Fig. 1(b).

The failure occurred in winter after snowfall. The weight of a thick layer of snow was the direct cause of a loss of stability. During the design stage, local loss of stability and lateral buckling were not taken into account.

SHMs are expensive in maintenance and not very efficient. Also the most commonly used monitoring systems (based on strain gauges, optical fiber sensors, ultrasound imaging) [5–13], utilize pointwise methods. The application of these sensors [14] forces engineers to prepare superfine numerical models and predict crucial points to be monitored, which in many cases is difficult or impossible. Sometimes monitoring is performed by a hierarchical system of full-field methods [15, 16], which includes interferometric and noncoherent image-based methods (moire fringe method, fringe projection, digital image correlation) [17, 18]. However, even if the more efficient, full-field techniques are applied, SHM systems are still too expensive to be applied to monitoring of existing low-cost building structures in the course of their utilization. However, it is urgent to answer the question: in what conditions is it safe to exploit such structures?

It is possible to do it off-line through carrying out extensive laboratory tests on a 1:1 scale model in combination with FEM numerical analysis in order to provide a numerical model which is as close to the real structure, as possible [19]. This determines the hybrid experimental-numerical methodology, in which the laboratory measurements are performed to obtain a precise response to the simulated natural load. The closer the overall dimensions of the model are to the dimensions of the true object, the more the results will be immune to scaling error and in consequence the more reliable they will be. Additionally, simulated laboratory conditions enable full control over the load and data acquisition modules. However, despite the obvious advantages,

many obstacles appear during the measurements of 1:1 scaled models. The main problems are related to the introduction of a load mechanism and the selection of a measurement method. The choice of a method is crucial in many cases and should be made with respect to the most informative parameter that can be measured. A good selection for low cost building structures are displacements, which can be determined by vision-based measurement systems, which are relatively simple and inexpensive. Digital displacement maps can be easily converted to strains, which are the primary object of interest in the assessment of an object.

**Hybrid Experimental-numerical Methodology**

A schematic representation of the hybrid experimental-numerical methodology [19] is shown in Fig. 2.

The geometry of the object, the material and the load characteristics are taken as input. This data makes it possible to develop a simplified FEM model. The model is then used to determine the range of loads and regions, where the possibility of a failure is highest. The simplified FEM analysis is crucial for the consequent steps. The indicated range of permitted loads is used for the design of the loading system, while the most probable regions of failure determine the localization of the field of view of measurement equipment. Once the areas of interest are defined, the measuring methods, which determine the real displacement of the structure in the selected areas of interest (AOI) need to be chosen. The goal is to obtain mutually complementing data from pointwise and full-field sensors, which can be easily compared with FEM analysis.

The data obtained in the course of the experiment is used to develop a detailed FEM model, which is the output of the hybrid measurement method. The result of the comparison between the experimental and numerical data is put back into the method as a feedback information signal. If the FEM model analysis does not match the experimental results, more tests need to be performed in order to complement the numerical model, which is modified after each experiment loop.

Fig. 2 A block diagram of the hybrid experimental-numerical procedure
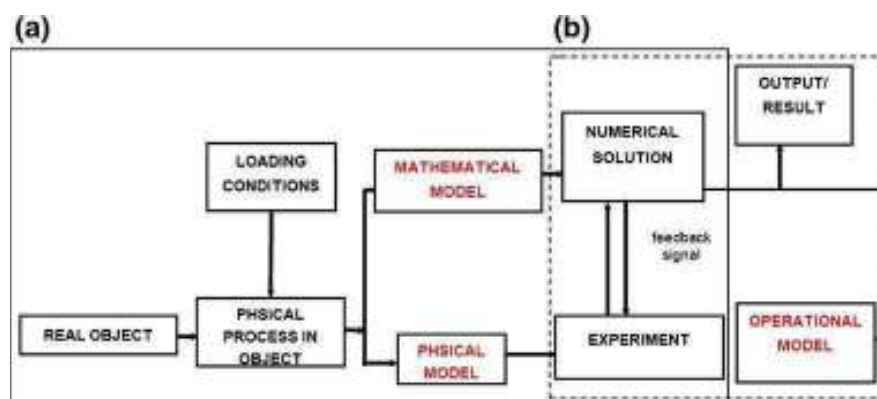
Description of the Object

The real-world object, its physical model and two FEM models will be described in this section.

The Real-world Object and its Physical Representation

The object (Fig. 3(a)) is a part of a warehouse complex and its construction is that of a self-supporting roof, founded directly on a continuous spread. The span of the hall is 12 m and the length is 45 m. The roof does not have an insulating layer and the hall is not heated. The top-side walls are made of cold-formed profiles (pillars, spandrel beams), covered by a trapezoidal metal-plate.

The specimen used in the experiment was a part of a metal plate arch composed of four individual modules (Fig. 3(b)). Each module was made of a 1,25 mm thick, S355 steel cold-milled metal plate, which was composed of 3 m length segments. The segments were connected with M6 bolts. The dimensions of the cross-section of the metal-plate are presented in Fig. 3(c). The arch was fixed to the steel beam through a gusset, which was mounted with a dowel bar to the concrete foundation.

Simplified FEM Model

Before the laboratory tests were performed, a preliminary analysis of the simplified, computational bar FEM model (reduced to a singular arch module) had been carried out. The arch was divided into 36 line segments, which is sufficient for deformation estimation and determination of the maximal inner forces (bending moments and compression forces). A mesh grid was generated using the Coons method. The arch was pin jointed. The elasticity of support has been determined through experiments on an universal testing machine. The aim of the preliminary analysis was to determine a substitute load of a thick layer of snow and to establish regions to be observed by sensors. The analysis was carried out using the simplified model, as the gofferings on the metal plates could not be described mathematically and were impossible to model. The gofferings introduced geometrical orthotropy, (despite the material being

Fig. 3 The object and its physical model: (**a**) a photo of a part of the warehouse complex, (**b**) the experimentally investigated object and (**c**) the dimensions of an individual module
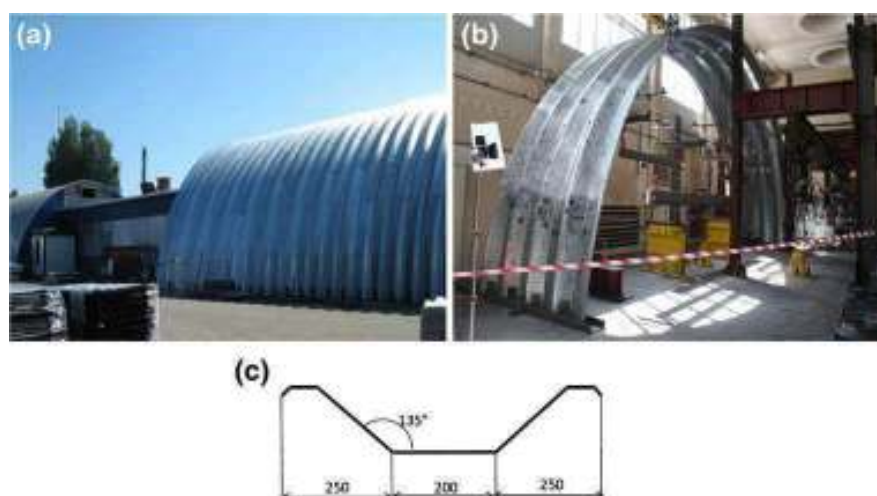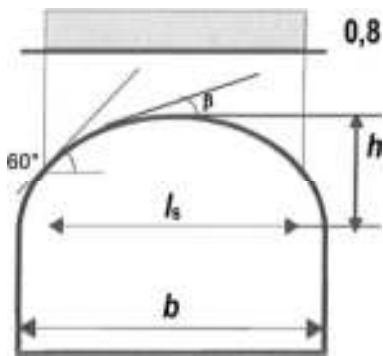
Fig. 4 The general load distribution scheme

isotropic) whose influence had to be accounted for through the course of the experiment. The introduced load was distributed uniformly, as shown in Fig. 4.

A linear load (Fig. 4) was introduced by four aggregated forces. It was assumed (based on additional research), that if the inner forces and deformations caused by the introduced, equivalent load are correlated with the inner forces and deformations caused by the linear load, then the load conditions are modeled properly. Second-order analysis was utilized in order to take the flexural buckling phenomenon into account. In this case, the load and inner forces' values do not contribute to the dimensioning of the structure but are used solely for the comparison of their consequences. An example distribution of bending moments and deformations introduced by the equivalent load has been presented in Fig. 5(a) and (b) respectively.

The normal and shearing forces were also taken into account in the analysis. The effects introduced by the linear and equivalent loads are comparable, so the selected model is assumed to be correct. The deformation of the arch indicates regions with maximum displacements, which occur in the mid-height and the mid-span, at both sides of the arch (the same region as the maximum bending moment). These regions were chosen as target positions for the inductive displacement sensors, strain gauges and the field of

view of the digital image correlation sensor. The strain gauges (SG) were placed in locations of maximal interaction of bending and compression forces and inductive displacement sensors (DS) were placed in the same region in locations of maximal deformations. The region of interest selected for DIC included the locations of the strain gauges and displacement sensors.

The simplified FEM model was utilized to check the correctness of the equivalent load and to indicate the regions to be observed by sensors. The simplified bar model does not take the detailed support conditions and the local loss of stability into account. These problems are the subject of laboratory tests and further calculations based on the detailed, shell FEM model.

Detailed FEM Model

The detailed FEM model was developed as a spatial cover with dimensions consistent with the dimensions of the test object. The cover was modeled as a curved, orthotropic surface. The orthotrophy directions were perpendicular to the goffering and their values were determined on the basis of preliminary tests of the metal plate fragments. The results of those tests have been presented in Fig. 6.

The material was isotropic, but the orthotropy was introduced to the measured object by the goffering of its surface. The specimen used for preliminary tests was a fragment of the metal plate. The width of the specimen was 100 mm, its length was 300 mm and its thickness was 1 mm. The specimen was subjected to tension crosswise to the goffering. It was assumed that the goffering influences stiffness in the transverse direction only, while the stiffness in the lengthwise direction of the goffering remains unchanged compared to the flat metal plate. Test results have been compared with results of similar tests carried out with a flat metal plate specimen with identical dimensions. The orthotropy coefficient was estimated as 0.85 and it has been used to modify the stiffness matrices.The cover was elastically supported at the location of the gusset plate. The elasticity of

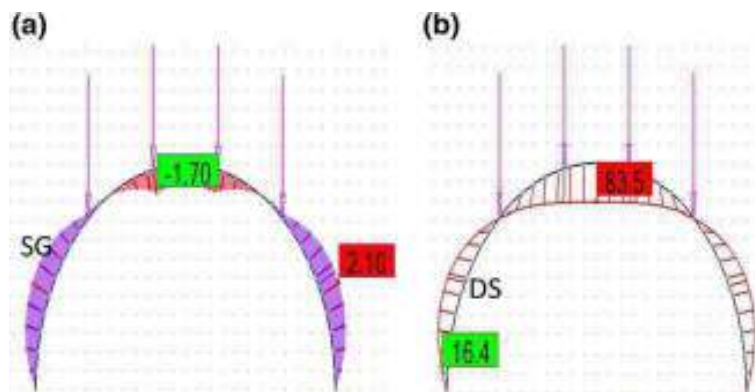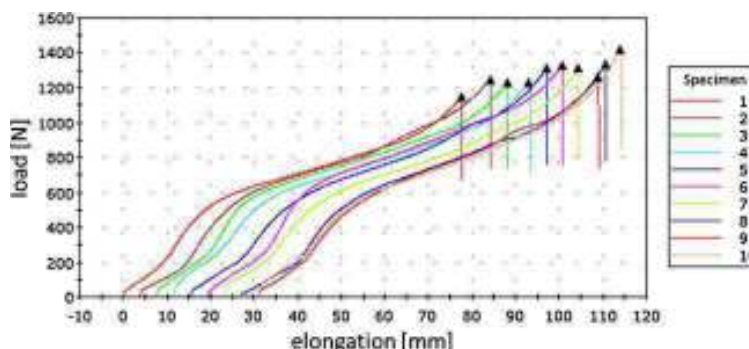**Fig. 5** (**a**) The bending moments and, (**b**) deformations introduced by the equivalent load

the support was determined on the basis of the test results. The equivalent load was introduced to the surface of the cover through a diaphragm (a rigid body model), whose dimensions corresponded to the clamping metal plate.

The calculations were performed in two variants: in the first one, the aim was to determine the critical load and buckling form, while the second one was a nonlinear, static analysis, which aimed to determine the displacements and stress maps in the most significant regions of the structure.

In Fig. 7 the detailed calibration procedure of the model is presented.

The experimental and numerical results were referenced to the selected model's regions as a function of load. Linear analysis does not take into account the local instabilities, nor the cross-section orthotropism and provides comparable results only in the initial linear range up to point A. The discrepancies produced by the linear model in reference to the experiment are too big and thus it is not suitable for calibration outside the linear region. The results of the non-linear FEM calculations are non-linear, which is due to second-order effects, geometrical cross-section orthotropy and geometrical imperfections. An increase of the load causes local stability variations, which are dependent on the range and character of the geometrical orthotropy. The

discrepancies between the experimental results and numerical simulations are manifesting at point B. The specific cause of this phenomenon is uncertain, thus it is imprudent to assume the FEM model as suitable for further evaluation. At this stage it was asserted that the discrepancy between experimental and numerical results cannot exceed the maximal measurement uncertainty of the investigated object, which was approximately 10 % within the analyzed loading range. The assertion is valid up to point B. In consequent points, the discrepancies exceed the acceptance level and an iterative procedure is utilized in order to correct the model. The first correction is carried out at point C, shifting the curve within the B-C range by the "1–2" value, making the result coincide with the point B. The correction is made by modifying the flexural and membrane stiffness matrices of the numerical model. The aim is to diminish the gap between displacements obtained from the experiment and from numerical simulations. This operation was preceded by an analysis of supercritical states, with regard to the local instability. Ultimately, the manipulation of the stiffness matrices minimized the divergence between the experimental results and the non-linear FEM model (resulting in the emergence of the corrected model). The non-linear character of the model is preserved over the course of the correction.

Fig. 7 Detailed FEM model calibration procedure
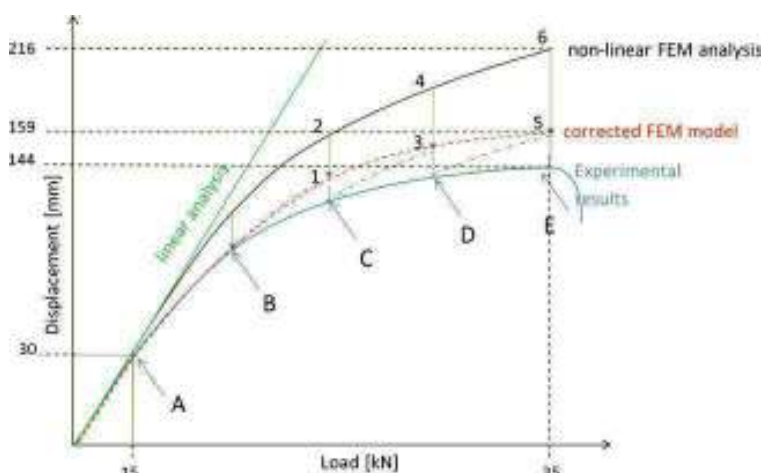
Similar shifts of the FEM model's output were carried out for consequent, higher load states (at point C, the curve shifts the value "3–4", and at point D by the value "5–6"). For each correction, the stiffness matrices are updated and can differ from each other. It is justified, as increasing load values introduce variations of local stability. The assumed acceptance level of discrepancies between the experiment and numerical simulations (10 %) is constant and guarantees sufficient correlation between the experimental and numerical results. However, the acceptance level could be made more strict if accuracy requirements are elevated. In such a case, more iterations would have to be carried out. At the last stage of calibration a new, corrected curve is obtained (the dash curve). It crosses all corrected points A-B-1-3-5 and it can be used to represent experimental results with an error less than 10 %. The obtained curve (the calibrated FEM model) takes the second order effects, geometrical imperfection and geometrical orthotropy into account. This model can be used for calculations of hall's arches with diverse spans and in different loading conditions.

The flexural stiffness and membrane stiffness matrices determined at point E for the simplified and the calibrated model are presented in Fig. 8.

Experimental Methods and Instrumentation

The analysis of the simplified FEM model had determined the approximate localization of the sensors. The most vulnerable region of the object was expected to be localized in the middle of its height, but due to the complexity of the object, it was difficult to predict the exact position.

It was also expected for the structure to respond with in-plane and out-of-plane displacement components when subjected to load. Moreover, the real shape of the object had to be determined. These are the reasons why the standard pointwise measurement techniques like strain gauges [20] were not suited to this task, even if several sensors were applied. In order to monitor the displacements of the object in a large area of interest, a full-field optical measurement technique has to be utilized. Taking into account all requirements and the range of expected displacements, the 3D Digital Image Correlation method (3D DIC) has been selected as the primary method [21–23].

3D DIC is a non-coherent, image-based method. It measures all components of displacements (u, v, w) and the shape of an object. The sensitivity depends on the actual field of view and the resolution of the imagers. The spatial resolution is related to the resolution of the imagers, while temporal resolution depends on the speed of the cameras (number of frames per second). As the 3D DIC method is a full-field optical technique, it is possible to recognize and measure unexpected failures in structures, if only they occurred within the field-of-view (FOV). However, the DIC method is not fully accepted as a standard measurement method for large engineering structures, and therefore this is the reason the displacement measurement at a chosen point were being validated by standard displacement sensors and strain gauges.

Fig. 8 Stiffness matrices of the simplified and calibrated models determined at point E (Fig. 7)
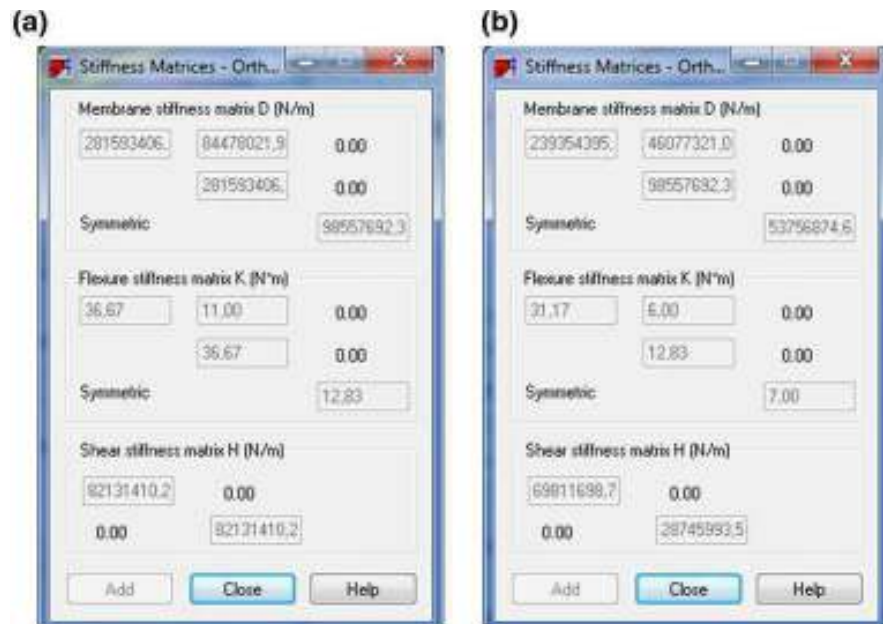
Description of 3D DIC

DIC is a technique based on the analysis of a pair of digital images (reference and deformed) over a certain area of interest (AOI) taken before and after displacement occurs [22]. The information is extracted from changes of intensity in the images. In the most widely known variation of the DIC, the reference image is divided into small subsets (sub-images). The software searches for the most similar subset in all other images, using the maximum cross-correlation function criterion:

$$C_{normfg} = \frac{\sum_{i=1,j=1}^{n,m} f(i,j)g(i,j)}{\sqrt{\sum_{i=1,j=1}^{n,m} f(i,j)^2}\sqrt{\sum_{i=1,j=1}^{n,m} g(i,j)^2}} \qquad (1)$$

where: $f(i,j)$ is the intensity function of the reference image and $g(i,j)$ is the intensity function of the deformed image; n, m are pixel dimensions of the investigated subsets.

The center point of the most similar subset found in a deformed image defines the displacement vector. In order to facilitate matching, each subset needs to be sufficiently distinct in the aspect of intensity variations. Therefore a random speckle pattern is applied (e.g. spray paint, sticker paper, water decals) to the object within the AOI. In some cases, when the texture of the measured surface exhibits sufficient intensity variations, there is no need to apply additional random patterns to the object.

3D DIC is a technique, which combines the Digital Image Correlation (for in-plane displacement analysis) with stereovision (for 3D shape measurement) [24]. By using two cameras for observation of the same area of interest, it is possible to obtain the 3D shape of an object. However, both cameras need to be carefully calibrated [22, 25] in order to calculate the intrinsic (center of projection coordinates, scale factors and distortion coefficients if required) and extrinsic parameters (describing the geometry of the stereo setup). The stereo matching problem is solved by correlation analysis.

In the experiment, the field of view of the 3D DIC sensor was located at the outer side of the arch. The 2 m×2 m area of interest was located 2 m above the floor (Fig. 9), in the region where the simplified FEM model analysis predicted the largest displacements. The images in the 3D setup were captured by two 2MPx AVT Stingray cameras equipped with Schneider Kreuznach 8 mm focal length objective lens. The cameras were connected to a laptop via a FireWire

Fig. 9 The experimental setup: (a) the view of the 3D DIC measuring, (b) location of the 3D DIC AOI and loading mechanism, (c) executed loading program
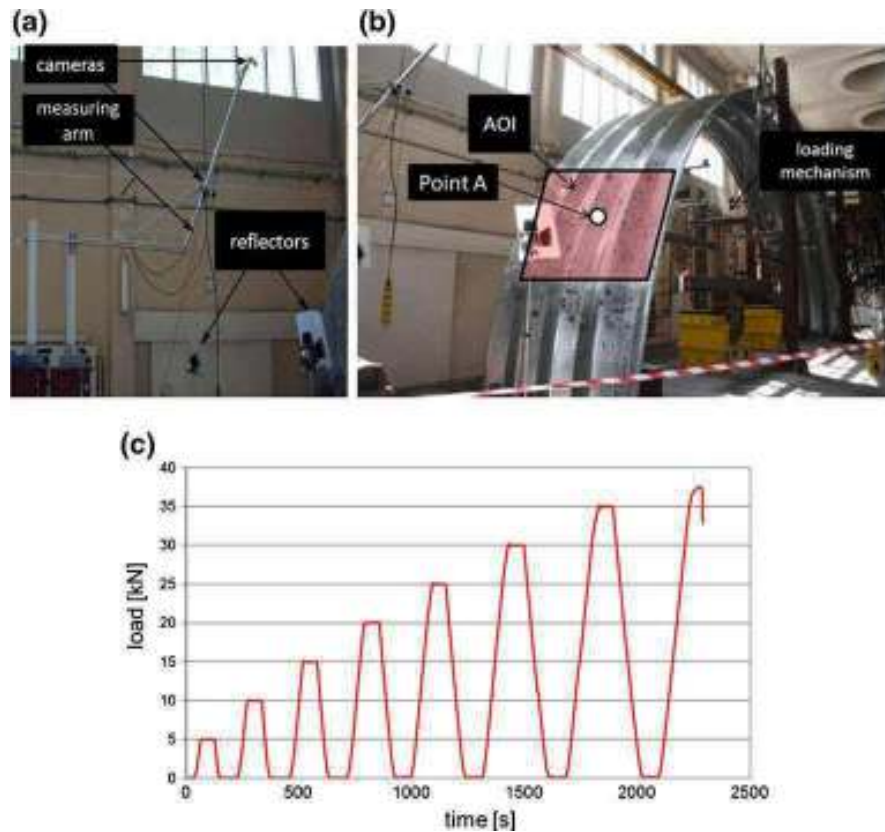
ExpressCard in daisy chain mode. In order to improve lighting conditions, two 650 W halogen reflectors were used. Because of the large FOV, the cameras were set 1,5 m apart from each other with a stereo-angle of 30 °. The angle is always a trade-off between an image displacements sensitivity and an out-of-plane sensitivity. The value of 30 ° introduces modest perspective differences between corresponding image subsets and ensures sufficient out-of-plane sensitivity. According to [22] it is not advisable to maximize the out-of-plane sensitivity at the expense of in-plane sensitivity as the same amount of noise in in-plane analysis causes much larger error than if it occurred in out-of-plane analysis. The setup was installed on a scaffold made of Bosch Rexroth's aluminium constructional profiles (Fig. 9(a)). The measuring arm has been connected by an articulated joint with a horizontal beam and braced by another, short beam, which was screwed down to the horizontal beam and to the measuring arm itself. The horizontal beam was stiffly mounted to two vertical profiles, which were clamped to a 13-ton constructional steel beam by four G-clampings. The double C-shape steel beam was insulated from the ground by a rubber separating layer. The overall weight of the foundation and the rubber made the scaffold immune to vibrations. It also must be mentioned, that the load of the arch was introduced hydraulically—no motors were used during the test. Thus the influence of the flexibility of the scaffold and the vibration can be neglected.

Images were captured at a frequency of 1 Hz, using a commercial software package called Vic Snap [26]. For the 3D DIC analysis, VIC 3D software (by Correlated Solutions) was used.

The in-plane displacement accuracy obtained by DIC analysis is 0.01 pixels [22], which, considering the field of view (3 m) and the camera's resolution (1624 pixels) gives a theoretical accuracy of 18 μm

However, we can expect additional errors due to the divergent local properties of the texture applied at the investigated object and the scaling error during conversion from pixels into micrometers. The experimental accuracy of the in-plane displacement measurement was ultimately estimated at 50 μm (75 μm for out-of-plane displacement).

The measured surface had to be carefully prepared in order to facilitate correlation analysis. The preparation of the surface included cleaning, covering with a ground coat, spraying with white paint and introducing black speckle pattern (with randomly sprayed black paint). Special care was taken to maintain a uniform distribution of the random texture over the AOI. Finally, the measurement area was covered with matte varnish in order to secure the speckle pattern and reduce reflections from the surface. The AOI is an area inside the field of view (FOV) of the sensor which indicates the region where the correlation analysis is to be performed

Pointwise Sensors

Pointwise sensors were used in order to provide additional data for validation of the correlation measurements results. They were placed inside the most vulnerable regions and within the AOI of the 3D DIC sensor. Two types of sensors were used: an inductive displacement sensor and a set of strain gauges for strain measurements.

The inductive displacement sensor was fixed at the middle of the AOI of the DIC sensor, but on the opposite side of the arch (Fig. 10). The sensor measured absolute displacement (resultant from U, V and W displacements), therefore the data obtained was easy to compare with the corresponding DIC data.

The pointwise sensors were located in the regions where the largest displacements were expected based on the simplified FEM model analysis. The arrangement of the sensors located within the AOI of the 3D DIC sensor has been presented in Fig. 10. The inductive displacement sensor (1) was set at an angle of 30 degrees relative to the ground. The strain gauges (2) were placed at the valleys of the goffering on the outer side of the arch. The strain gauges of the other set (3) were sticked on the peaks and valleys of the goffering on the inner side of the arch. The AOI of the 3D DIC sensor has been marked in red in Fig. 10. All pointwise sensors and a force sensor were coupled in an integrated Hotinger measurement system. The data acquisition frequency was 5 Hz and it was synchronized with the 3D DIC sensors.

Introduction of Load

Each segment of the measured arch was loaded at four points (which simulate the load introduced by the presence of snow) arranged uniformly along the arch. The measured
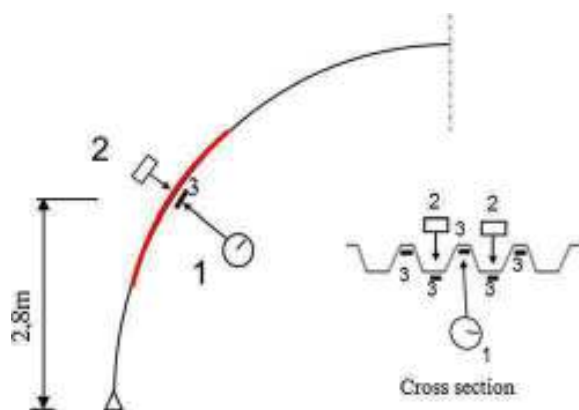

Fig. 10 The arrangement of the pointwise sensors: 1—displacement sensor, 2—strain gauges on the outer side of the arch, 3—strain gauges on the inner side of the arch; the 3D DIC FOV has been marked in red

object was composed of four arch segments, hence the whole object was loaded in sixteen points.

The load was provided by a set of strings and longitudinal and transverse beams (Fig. 9(b)). The beams were clamping all sets of strings up to the joint with the main beam. A dynamometer and pulley blocks with a hydraulic actuator were fixed to the main beam. The force recorded during the test was therefore the sum of 16 component forces applied to the object. The loading program has been presented on Fig. 9(c).

The loading mechanism ensured a consistent force value, regardless of the deformations of the arch. The total mass of the strings, beams and joints amounted to 518 kg. The control of the loading and data acquisition was automated. The load was introduced gradually in 7 cycles from 0 to 35 kN with an increasing value of load in each cycle equal to 5 kN (Fig. 9(c)). The maximum value of load in a cycle was maintained for approximately 60s. The last cycle (above 35 kN) was maintained until the failure of the measured object.

Experiment

The experiment was carried out within the range of loads specified in Fig. 9(c) and progressed in cycles. The aim of the test was to indicate critical load values and identify shortcomings in the FEM model.

3000 measurements at a frequency of 1 Hz have been performed by the 3D DIC sensor. All control computers (force, 3D DIC, pointwise sensors) were time-synchronized with each other. The synchronization of all systems facilitated data comparison procedures and ensured more reliable results.

3D DIC Results

The results of the 3D DIC measurement include: the shape map and a set of U(x,y) and V(x,y) in-plane displacement maps along with the W(x,y) out-of-plane displacement map. The shape map of the measured surface is presented in Fig. 11 and the displacements maps are presented in Fig. 12. In the U(x,y) map (Fig 12(a)), the yellow spot indicates the "A" point (Fig 9(b)), where the displacement sensor was located. The comparison of the displacement data obtained by DIC and inductive sensors was needed in order to validate the results obtained from 3D DIC and to eliminate the possibility of a gross error.

The 3D DIC method provided a large amount of information. Figure 12 presents example displacement maps calculated for a high load value. In the middle section of the FOV, large displacement gradients can be observed. In order to track the failure process and visualize the asymmetry of displacements maps, we extracted three components of displacement vectors at points along two chosen lines (in arcwise direction) (marked as white lines L1 and L2 at the U displacements map in Fig. 12).

Fig. 11 Initial 3D shape map for the AOI at the arch surface
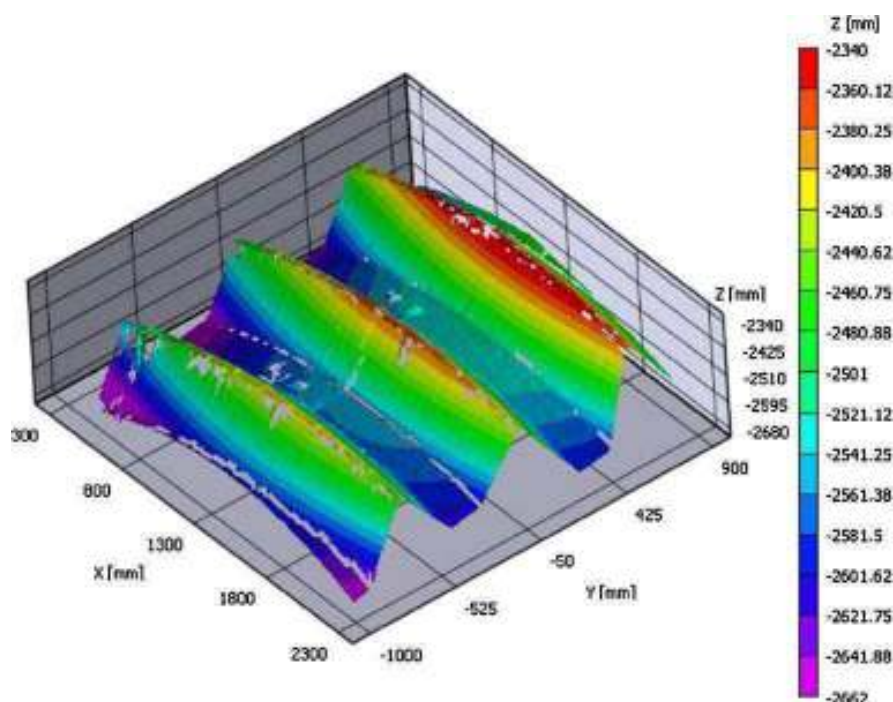
The extracted U, V and W displacements have been presented in Fig. 13 in the function of time. Such presentation of the data shows the development of a characteristic deformation in the area of failure (line L1). The failure process begins at 25kN load (which can be observed in V displacements along L1). At the maximum load, the largest U and V displacement values occur within the A crossection (Fig. 13). W displacements were more pronounced within the B crossection, which is consistent with the numerical predictions. An interesting conclusion can be drawn from the comparison between deformations along line L1 and line L2. The red area in Fig. 12 indicates riveted joints between neighboring metal plates sections. The L2 line was extracted from a region reinforced by these joints. In the region from which line L1 was extracted, the connections between neighboring sections were located to the top and to the bottom of the FOV. As one can observe in Fig. 13, the failure process did not occur in the region with joints (line L2) because the structure was more stable there.

Verification of the 3D DIC Results

In order to enable a more reliable comparison with results obtained from the displacement sensor, absolute displacement values were calculated. The sensor was located at the opposite side of the metal plate in relation to the 3D DIC AOI. The location of the sensor was marked to facilitate the identification of the precise spot. Plots of absolute displacements at Point A as obtained from both sensors are presented in Fig. 14. The analysis proved the measured displacement values of the two sensors to be very close. The maximum discrepancy of measurements is less than 2 %. The small discrepancies could be caused by the fact that the sensors were monitoring the opposite sides of the metal plate. In Fig. 14, displacements

extracted from the same point in the numerical model have been also presented.

An another comparison was made in order to validate strain measurements. Displacement maps, which are the primary output quantities from the correlation calculations, can be consequently differentiated to obtain strain maps. Here in order to obtain a more reliable comparison, the following procedure was implemented. A virtual extensometer was placed next to the strain gauge in a fragment of the AOI of the DIC sensor. Displacement values were extracted from displacement maps at two points, which can be treated as contact points between the virtual extensometer and the measured surface. The distance between these points and their locations matched the strain gauge parameters in respect to the base length, and the direction of measurement (the virtual extensometer was placed parallel to the strain gauge). The extracted displacement values were consequently used to obtain the strain value at a chosen moment in time ('t'):

$$\varepsilon(t) = \frac{disp_A(t) - disp_B(t)}{L} \tag{3}$$

where $disp_A(t)$ and $disp_B(t)$ are displacements extracted at time 't' at points A and B respectively and L is the distance between point A and point B. Strain calculations were carried out on pixel values, so the presented results are free from a scaling error.

The "virtual extensometer" and strain gauge were very close to each other, but still somewhat separated, since the correlation analysis could not be performed inside the area where the strain gauge covered the speckle pattern.

In Fig. 15, a comparison plot between strains calculated through the procedure described above and the strains measured by a strain gauge is presented.

The comparison indicated sufficient correlation between the results obtained from the virtual extensometer and the strain gauge in the elastic range. Discrepancies grow fast
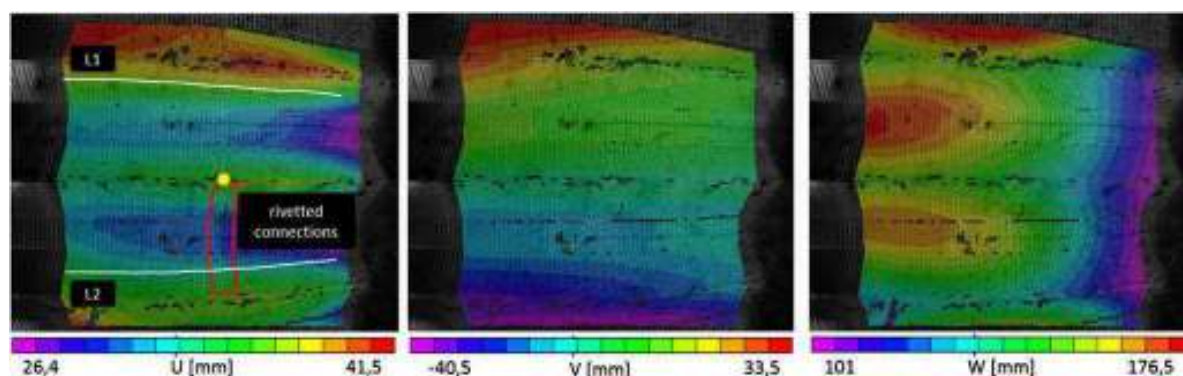

Fig. 12 Example displacement maps: U(x,y), V(x,y) and W(x,y); lines L1 and L2 overlaid on the U(x,y) map were used to generate the visualization of the displacements in time as shown in Fig. 13; the red curve indicates riveted joints between neighboring metal plates segments
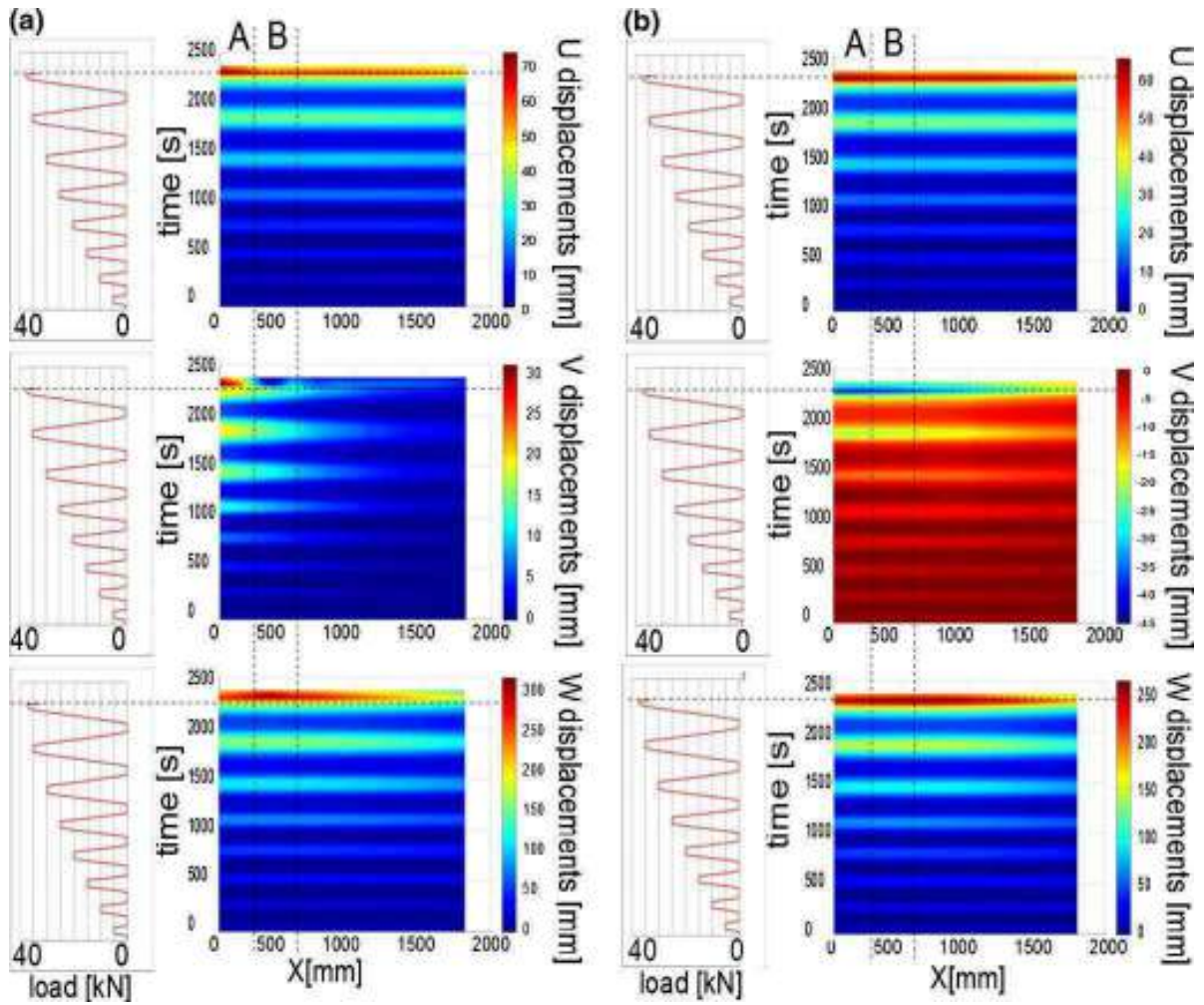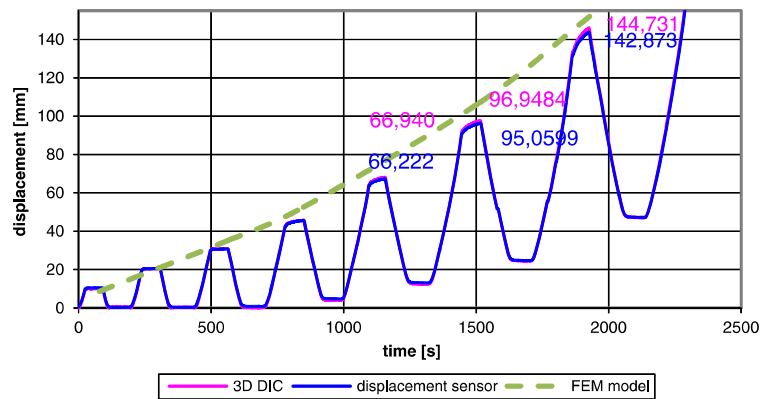
Fig. 13 Representation of U, V, W displacements along two chosen lines (**a**) L1 and (**b**) L2 from Fig. 12 in the function of time; at the left hand side of the color maps, the load program is provided

Fig. 14 Absolute displacement measured by DIC, the displacement sensor and generated from the numerical model
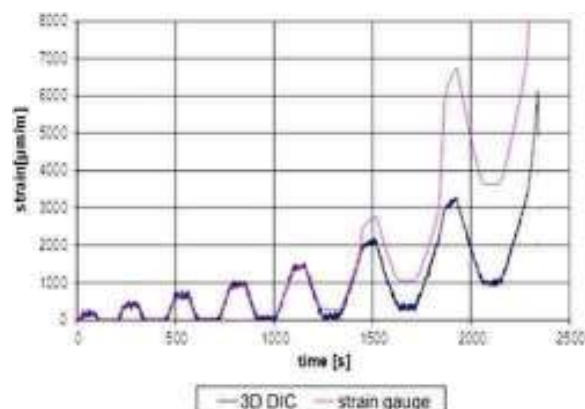
Fig. 15 Comparison of the strain measurement performed by the virtual extensometer and strain gauge

when the structure reaches the plastic range. It was a limit of the utilized strain gauge, which exceeded its range and came unstuck from the surface. The application of the strain gauge was additionally hindered because of the goffering of the metal plates. The discrepancies caused by local loss of stability are small and can be neglected.

Comparison Between Numerical and Experimental Data

The most important issue in regard to the comparison of the test data with numerical data was matching the coordinate systems. All DIC results were initially related to a coordinate system which is assigned by the geometrical DIC configuration. The 'xy' plane was perpendicular to the axis of the sensor (which was located in the middle of the distance between the optical axes of both cameras). In order to reliably compare the results obtained from the experiment with the results numerically generated from the FEM model, it was necessary to transform the data from the DIC coordinate system into the FEM model's coordinate system (or inversely).

In the FEM method, each finite element has its own, local coordinate system, in which in-plane displacements or strain, and out-of-plane displacements are calculated (Fig. 16). In 3D DIC the coordinate system is associated with the AOI and hence quantitative comparison of displacement components obtained from numerical simulations and from the experimental results can only be performed inside a small region at the centre of the AOI (where the directions of the coordinate systems are the same). In order to compare displacement components outside the centre of the AOI, local coordinate systems' transformations need to be performed.

In order to calibrate the detailed FEM model (according to the procedure presented in the "Detailed FEM model section"), absolute displacements' values from the

experiment (which are a square sum of all displacement components) have been used, as they could be quantitatively compared with numerical results. The obtained experimental data was introduced into the detailed FEM model. Displacements determined through the experiment were compared with numerical simulations. In order to calibrate the model (to match experimental data and numerical simulations), the flexural stiffness matrix was altered. The calibration procedure has been presented schematically in Fig. 7. Discrepancies between the numerical model and the real object are lower than 10 %. This validates the utilization of the detailed and calibrated FEM model for the investigation of objects made of similar metal plates but at a different scale. More data points from the experiment could be used to further diminish the gap between the model and the real object.

The consequent analysis of the calibrated, detailed FEM model aimed to determine the critical load in respect to the global buckling and the local loss of stability. The result of these calculations is the critical load for the first (and the most probable) mode of buckling. The view of the FEM model subjected to critical load has been compared with the real image of the object under experimental load (Fig. 17).

At Point 1, buckling can be observed, while at Point 2 the metal plate broke as a result of loss of stability. During the experiment, the loss of stability occurred for the 37.4kN summarized load, which matches the numerically calculated value (36,6kN) very well. Such good correspondence between the FEM model and the real object test results allows to conclude that the model calibration was performed correctly.
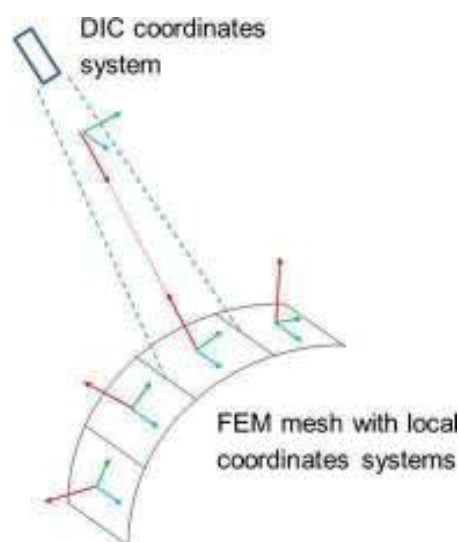

Fig. 16 3D DIC sensor coordinate system orientation and FEM local coordinate systems

Fig. 17 Views of the model and the object during the experiment; the mesh grid of the model has been rescaled for better visualization, original mesh was finer (it contained 4176 finite elements)

The critical load, calculated by means of numerical analysis, was used for creating displacement maps within the AOI of the 3D DIC sensor. The example results (for 5kN, 15kN and 30kN) have been presented in Fig. 18 (the maps obtained from the DIC sensor have been rotated by 90 degrees in order to facilitate visual comparison). The coordinate systems are compatible in the centre of the FOV only and in this region displacement's components can be quantitatively compared. Because of the specific qualities of the measured object, U and V displacements were not compared with experimental results.

Visual comparison of the maps presented in Fig. 18 indicates good correspondence between numerical and experimental data. However, a certain asymmetry in experimental results due to an additional linear component of displacement (tilt of the structure) can be observed.

Discussion

The comparison of the results obtained from the experiment and FEM simulations at the indicated object points showed that they correspond very well. Additionally, the experiment allowed to observe the failure process at the bottom right corner of the structure (Fig. 17).

The discrepancies in displacement measurements could be caused by the fact that the DIC and the displacement sensors were located on the opposite sides of the metal plate. Discrepancies and errors in strain measurements were probably caused by the shape irregularity of the surface measured by the strain gauges. The locations of the comparison points were shifted by a small value from the actual locations of pointwise sensors, as 3D DIC analysis could not be carried out at the precise regions where the strain gauges were attached.

The comparison between experimental data and the detailed FEM model showed very good consistency after just the first iteration of the experimental-numerical hybrid measurement methodology (thanks to the efficient prediction of the failure regions in the simplified model). Therefore, it was not necessary to perform additional tests. In more complicated cases, when the simplified FEM model would not give clear information about the region of failure, it is still economically more efficient to perform more laboratory tests on 1:1 scaled models than to install a SHM system.

To conclude the whole measurement effort, critical loads and vulnerability regions of the object were determined. The detailed FEM model (which includes corrections from the experimental data) can also be used for more precise simulations of accidental load conditions.

The analysis of 1:1 scale models of low-cost civil engineering structures can be a very efficient way to improve the safety of such structures. The 3D DIC method is an easy full-field experimental technique, which provides high accuracy data important to the development of a proper FEM model of the structure.

The 3D DIC method provided large amounts of data, which can be analysed and visualized in many different ways in order to facilitate the evaluation of experimental results. The 4D visualization (Fig. 13) presented in the article can be applied and utilized to track deformations along chosen lines as functions of time, which is a great convenience, e. g. in crack propagation investigation.

Conclusions

The hybrid method for laboratory measurements of low-cost, large scale building structures has been presented in this paper. A 1:1 scale model of the hall's arch made of goffered metal plate has been created and subjected to load, which simulated the natural influence of the presence of snow on the roof. FEM model simulations were complemented by the experimental data and good correspondence has been achieved. Additionally, the failure process has been observed, localized and consequently used for the improvement of the initially created simplified FEM model. The detailed model has been calibrated by manipulating the flexural and membrane stiffness matrices in order to close the gap between the FEM simulations and the experimental data. A discussion in respect to error sources, future works and usability of the method, has been included.

As a result of hybrid testing (with application of traditional and modern, full-field optical methods) and in reference to the simplified FEM model, the calibrated, detailed
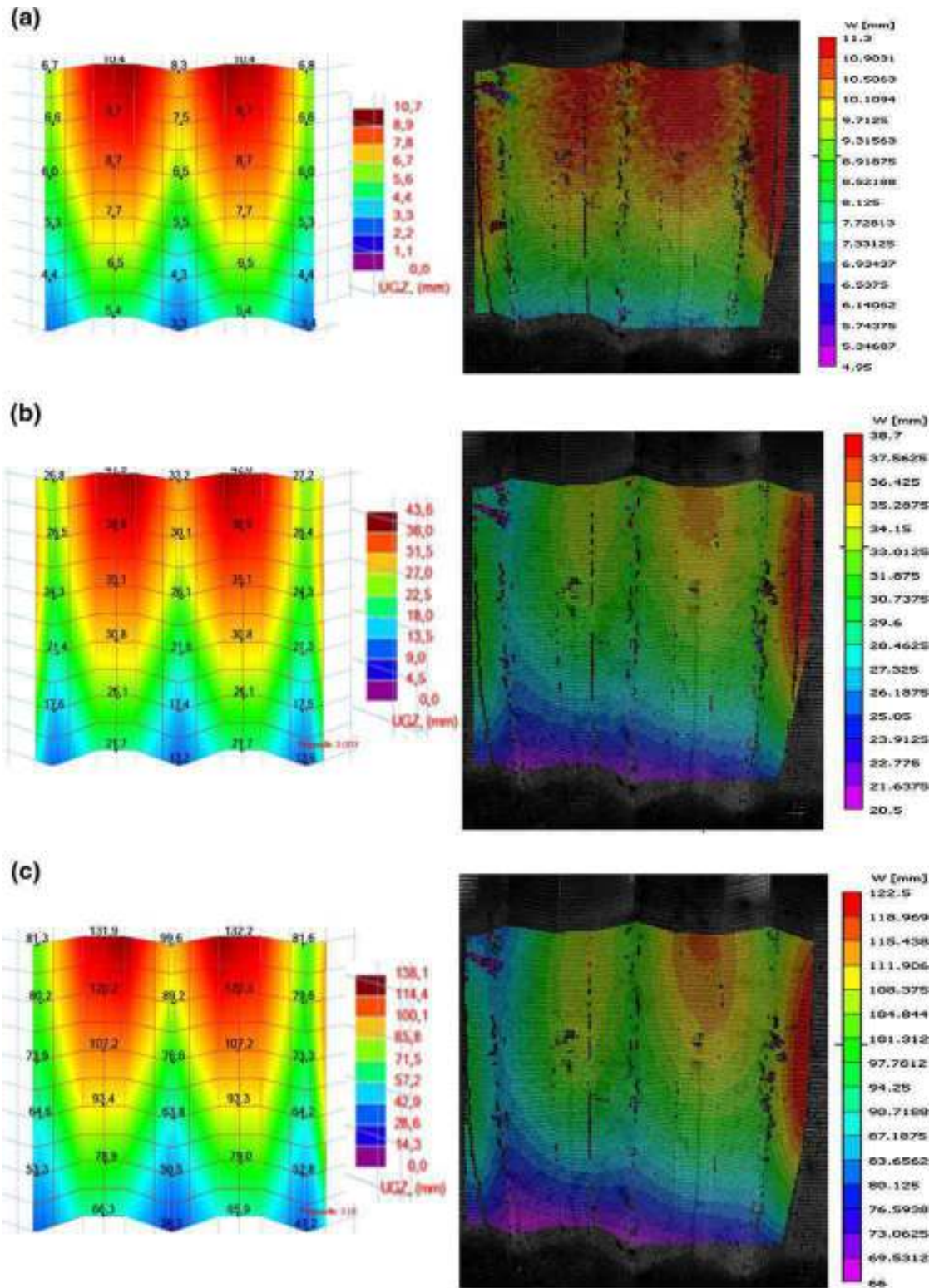
Fig. 18 W displacements maps obtained by FEM modeling and 3D DIC sensor respectively for the loads: (**a**) 5kN, (**b**) 15kN and (**c**) 30kN

numerical model of the large object has been designed. The model has been used consequently to transfer mechanical properties onto the real object with regard to support and foundation conditions. The hybrid methodology provided the FEM model, which can be used to carry out simulations of similar objects at a large scale.

The hybrid measurement technique, applied to low-cost, large scale engineering structures with a typical construction and shape gives new opportunities to engineers and assist in effective and rational design. The overall costs of such a pre-operating test are much smaller than the alternative SHM systems.

Future work will concern measurements of 1:1 scale models of halls manufactured in single shell and double shell (two metal plates arches with an insulating layer between them) variants with different cross-sections of profiles and different types of joints between sections. The aim of the tests will be to establish consistent design methods of arch coverings for low-cost civil engineering structures, which include the influence of utilization conditions, loading conditions and different methods of shaping of the arches.

References

1. Biegus A, Rygaluk K (2009) Collapse of Katowice fair building. Engineering Failure Analysis 16(5):1643–1654
2. Buidling Research Institute's archive (in Polish)
3. www.tgbuildings.com (in Polish)
4. Biegus A (2003) Analiza statyczno—wytrzymałościowa łukowych blach fałdowych. Konstrukcje Stalowe, (in Polish)
5. Housner GW, Bergman LA, Caughey TK, Chassiakos AG, Claus RO, Masri SF (1997) Structural control: past, present, and future. Journal of Engineering Mechanics 123(9):897–971
6. Chana THT, Yua L, Tamb HY, Nia YQ, Liub SY, Chung WH, Cheng LK (2006) Fiber Bragg grating sensors for structural health monitoring of Tsing Ma bridge: background and experimental observation. Engineering Structures 28(5):648–659
7. Rodriguesa C, Félix C, Lagec A, Figueiras J (2010) Development of a long-term monitoring system based on FBG sensors applied to concrete Bridges. Engineering Structures 32(8):1993–2002
8. Berninia R, Minardo A, Zeni L (2007) Accurate high-resolution fiber-optic distributed strain measurements for structural health monitoring. Sensors and Actuators A: Physical 134(2):389–395
9. Ko JM, Ni JQ (2005) Technology development in structural health monitoring of large-scale bridges. Engineering Structures 27 (12):1715–1725
10. Huang YH, Liu L, Sham FC, Chan YS, Ng SP (2010) Optical strain gauge vs. traditional strain gauges for concrete elasticity modulus determination. Optik - International Journal for Light and Electron Optics 121(18):1635–1641
11. Shoukry SN, Riad MY, William GW (2009) Longterm sensor-based monitoring of an LRFD designed steel girder bridge. Engineering Structures 31(12):2954–2965
12. Tennyson RC, Mufti AA, Rizkalla S, Tadros G, Benmokrane B (2001) Structural health monitoring of innovative bridges in Canada with fiber optic sensors. Smart Material Structures 10:560–573
13. Li H-N, Lia D-S, Song G-B (2004) Recent applications of fiber optic sensors to health monitoring in civil engineering. Engineering Structures 26(11):1647–1657
14. Krezel J, Kujawinska M, Dymny G, Salbut L (2008) Design and testing of low-cost full-field integrated optical extensometer. Proc, SPIE 7003:70030X-70030X-7
15. Kujawinska M, Sitnik R, Dymny G, Karaszewski M, Michonski K, Krzeslowski J, Mularczyk K, Bolewicki P (2009) Remote online monitoring and measuring system for civil engineering structures. Proc SPIE 7389:738904-1-10
16. Kujawińska M, Sitnik R, Dymny G, Malesa M, Malowany K, Szczepanek D (2010) Hierarchical, multitasks optical system for health monitoring of civil engineering structures. Proc SPIE 7387:738721
17. Patorski K (1993) Handbook of the Moire Fringe technique. Elsevier
18. Malesa M, Kujawinska M, Szczepanek D, Swiercz A, Kolakowski P (2010) Monitoring of civil engineering structures using DIC technique. EPJ 6:31014
19. Laermann K-H (2000) Hybrid techniques in experimental mechanics. In: Learmann K-H (ed) Optical methods in experimental solid mechanics. Springer, NewYork
20. Pan B (2010) Recent Progress in Digital Image Correlation, Experimental Mechanics, Online Firsr, doi:10.1007/s11340-010-9418-3
21. Kobayashi AS (1993) Handbook on experimental mechanics. SEM
22. Sutton M, Orteu J-J, Schreier H (2009) Image correlation for shape, motion and deformation measurements. Springer
23. Pan B, Qian K, Xie H, Asundi A (2009) Two-dimensional digital image correlation for in-plane displacement and strain measurement: a review. Measurement Science and technology 20 (6):062001
24. Orteu J-J (2009) 3-D computer vision in experimental mechanics. Opt Lasers Eng 47:282–291
25. Bradski G, Kaebler A (2008) Learning OpenCV: Computer Vision with the Open CV Library. O'Reilly
26. www.correlatedsolutions.com

Application of 3D digital image correlation in maintenance and process control in industry

Marcin Malesa [a,*], Krzysztof Malowany [a], Urszula Tomczak [b], Bartłomiej Siwek [c], Małgorzata Kujawińska [a], Anna Siemińska-Lewandowska [b]

[a] Institute of Micromechanics and Photonics, Warsaw University of Technology, 8 A. Boboli St., 02-525 Warsaw, Poland
[b] The Institute of Roads and Bridges, Warsaw University of Technology, 16 Armii Ludowej St., 00-637 Warsaw, Poland
[c] KSM Vision Ltd., 9/117 Sokolowska St., 01-143 Warsaw, Poland

ABSTRACT

3D digital image correlation method is widely used for displacements measurements in laboratory conditions and for experimental applications in industries. In this paper we present enhancements of the standard method, which enable application of 3D DIC for in situ monitoring and process control in industries and out-door environment. Enhancements concern software modifications (new visualization methods and a method for automatic merging of data distributed in time) and hardware improvements (protecting equipment against hard environmental conditions).

The modified 3D DIC system is applied in two interesting cases: measurements of steel struts at construction site and measurements of a pipeline in an intermediate pumping station. In both applications we additionally used an infrared camera in order to correlate deformations of measured objects with temperature changes.

© 2013 Elsevier B.V. All rights reserved.

1. Introduction

In the domain of experimental mechanics and vision-based optical metrology, digital image correlation (DIC) is a validated and well-established method for determining displacements in a wide range of test objects [1–3]. The experimental setup for DIC measurements is very simple. It requires images acquisition hardware, and a computer system for synchronization, data storage and processing. 3D DIC technique provides non-contact, full-field measurements of displacements and strains of an object subjected to mechanical, thermal or environmental loads. All mentioned features make 3D DIC system a good candidate for implementation in industry [4,5]. Development of the standard DIC method within such application areas as measurements of discontinuous fields [6,7], measurements of large deformations [8], or optimization for measurements in extreme environments [9] enable more advanced in situ implementations. Good examples of in situ applications of DIC have been presented in deflection measurements of bridges [10], monitoring of displacement of continuously active landslides in South French Alps [11] and measurement of a velocity field in deformation zones in cold rolling [12]. A number of applications of DIC method in industry

have significantly increased in recent years. However, to the best knowledge of authors, there is still a lack of published implementations of the method into practice for maintenance and process control or long-term monitoring in industrial and civil engineering applications. In order to achieve this goal the standard method needs to be tuned to any particular application and needs to be accepted by engineers responsible for a certain case.

Industrial applications need regular testing for the lifetime, movement, strength, and performance of machines and structures during production process. Measurement equipment applied for these kind of tasks need to be adopted to work in hard environmental conditions. Furthermore a long-term monitoring of objects or processes is often required. In such situations, the use of laboratory test methods is particularly challenging or even impossible. On the other hand, a typical measurement accuracy of DIC can be in many cases relaxed in industry. Taking into account these facts we have developed a method for automatic merging of DIC data distributed in time. Such method is highly required when monitoring should be performed over a long period of time, but measurement equipment due to various reasons cannot stay at the site. Another required enhancement of the standard DIC measurement is adding a new modality, namely temperature or distribution of temperature changes. In the presented applications we used a simultaneous capture of temperature distribution and displacements maps at an object surface. Similar approach was introduced by Orteu in 2008 when he performed simultaneous measurements

---

* Corresponding author. Tel.: +48 608571909.
 E-mail address: m.malesa@mchtr.pw.edu.pl (M. Malesa).

of 3D shape, strain and temperature fields with utilization of CCD camera operating in NIR [13]. Maynadier in 2012 [14] presented another method for combined measurements of temperature and strain maps, in which all data was acquired with a single infrared camera. Somewhat different approach was presented by Chrysochoos [15] and Kujawinska [16], who utilized separate devices for acquisition of infrared and white-light images. This approach has been also implemented in the presented applications

The paper is organized as follows: in Section 2 we report on hardware and software enhancements, which have been introduced in order to fulfill the needs of industrial customers and in order to adapt 3D DIC system to out-of-laboratory conditions; in Section 3 we present application that concerns measurements of building struts' deformations; second application, presented in Section 4 illustrates the case of monitoring of a pipeline subjected to a thermal load. The examples are purposely chosen from different fields in order to present versatility of DIC method in industrial applications. Description of the first application is more detailed as it includes implementation of the method for automatic merging of data distributed in time. The examples presented in the paper show evidently the differences between 3D DIC practice in industries and in its standard, scientific or laboratory applications.

2. Digital image correlation for industrial applications

In the standard DIC [2] the reference image (the first image of the series in the most cases) is divided into small subsets (sub-images). The software searches for the most similar subset in all other images, using the maximum cross-correlation function criterion (Fig. 1). The center point of the most similar subset found in a deformed image defines the displacement vector. In order to facilitate matching, each subset needs to be sufficiently distinct in the aspect of intensity variations. Therefore a random speckle pattern is applied (e.g. spray paint, sticker paper, water decals) to the object within the area of interest (AOI – area of acquired images in which displacement maps are calculated). In order to apply DIC in industrial applications we introduced enhancements in both: software and hardware.

The main goal of hardware enhancement was to minimize the influence of environmental conditions (high temperature gradients and dustiness) on DIC measurements and also to secure the equipment. Hardware enhancements and a visualization method are rather incremental developments of DIC and were necessary in

order to ensure applicability of DIC for particular measurement tasks.

Innovative software enhancements enable long-term measurements. Long-term measurements refers to a case, when 3D DIC setup has to be relocated between consecutive measurements. Two-dimensional version of the method has been described by authors in Ref. [17].

2.1. Hardware enhancements

A standard, laboratory 3D DIC system includes two cameras mounted on a tripod, a reflector and a control computer. For in situ, industrial applications in maintenance tasks or process-control there is a need of much more flexibility in a configuration of a measurement setup [9]. A good solution is aluminum constructional profiles, which are often used in industrial applications of measuring systems. Profiles can be used to build scaffolds or rigs and can be easily rearranged. In our case we used profiles to build a stiff measurement rig. The configuration of rigs depends on application and an object's location; rigs can be mounted directly to tripods or to stationary elements close to the measured object. The flexibility with DIC setup configuration is also important as often an access to the selected area of interest is hindered. The maximum elongation of 1 m profile due to thermal expansion in typical environmental conditions is about 0.3 mm. For the most industrial applications (including examples presented in the paper) this is an acceptable level. However, in cases when better accuracy is necessary we can use profiles/bars made of invar material (the material with an extremely low thermal expansion coefficient).

Artifacts used for the standard stereo-calibration of 3D DIC [2] setup are made of dibond material. Dibond is a strong, flat and lightweight material which is weather and dust-resistant. It is an aluminum composite panel material (ACP) and it is formed by laminating a central core of thermoplastic material with an outer skin of aluminum sheet (18). The most important properties of dibond material are presented in Table 1.These values prove the high applicability of dibond material for in situ calibration of the measurement system.The calibration quality during in situ measurements can be significantly decreased because off in-homogenous lighting conditions (e.g. sunlight and shades). In order to avoid an influence of these factors we utilized boards for protection against sunlight during the calibration.Additionally in
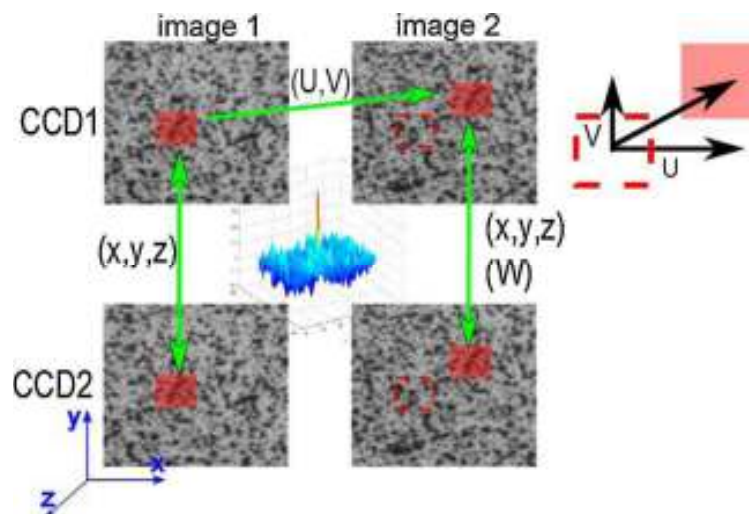

Fig. 1. The principle of 3D digital image correlation method: subimages matching during analysis.

Table 1
Properties of dibond material.

Property	Unit	Value
Thermal expansion	Mn/m at 100 °C variance	2.4
Service temperatures	°C	−50 °C to +90 °C
Water absorption by volume	%	0.01
Rigidity EJ	kNcm^2/m	865 for 3 mm thickness
Tensile strength of the cover sheets	N/mm^2	R_m: 145–185

the reported applications in order to get measurement results on-site and nearly in real-time we used a computer which is resistant to external conditions. The most sensitive components of a computer should be protected from shock and impact as well as from dust and water. There are only a few commercially available computers which fulfill these requirements, among which we had chosen Panasonic Fully Rugeddized Tough Book [19].Also the proposed 3D DIC system for in situ measurements is enhanced by adding an infrared camera which monitors distribution of temperature of an object. Multimodal data provided by DIC-IR configuration is often important information in further data analysis and interpretation of results.

2.2. Software enhancements

3D DIC software enables to calculate displacement maps nearly in a real time. This is a very useful feature, which is used to check if a sensitivity of the method is matched against particular requirements. However, in most of the cases, maintenance and process control in industry are performed over a long period of time during which observed objects are subject to a sequence of mechanical or thermal loads and the measurement system is periodically brought to an object. For such cases we implemented and tested an early version of the procedure for automatic merging of 3D DIC data. The method is an enhancement of the recently published 2D DIC data merging version [17]. In the method a flat calibration artifact (CA) is used as a reference for merging of data acquired by a set of two cameras which may be placed in different positions (Fig. 2a) at the measurement site. The CA (made of dibond material) typically contains a set of black circles printed on a white background and it remains permanently on site and is fixed at the same position between consecutives measurements. We assume that a relative movement between DIC setup and a set of fixed markers is a rigid body movement (the calibration artifact does not deform between consecutive measurements). Each pair of images from each data set (acquired from a slightly different position of cameras) is transformed to the coordinate system of the

reference pair. A transformation matrix T_{3D} is estimated by analysis of 3D positions of markers ($CA_{ref}3D$, $CA_{img}3D$, which are determined by triangulation of corresponding 2D positions from stereo images). The flow-chart of the software procedures is shown in Fig. 2b. Images obtained through the automatic data merging procedure can be subsequently subjected to standard 3D DIC analysis, however, numerical procedures that are performed during merging procedure cause a certain increase of errors of 3D DIC measurements.

Another enhancement of 3D DIC system is associated with visualization of results. DIC measurements provide a large amount of data, which need to be post-processed in order to extract the most valuable information. A sequence of displacement or strain maps can be used to draw conclusions about a global behavior of a measured object and to detect abnormalities, local concentrations of strains, defects etc. Further analysis usually includes plotting of displacements in selected object points against a time. In order to track a failure process and to visualize a possible asymmetry of displacements maps we propose another way of DIC results presentation, which is based on extraction of displacements and strains along chosen lines. Such visualization provides more quantitative data and can be helpful in tracking of a failure process in time. Obtained maps were highly appreciated by specialists from industry. Example figures are presented in next paragraphs.

Measurements and analysis presented in the next paragraphs were carried out with utilization of VIC 3D software [20] as well as with a custom-made software developed in our Institute. Custom-made software provides full functionality for 3D DIC measurements including the automatic merging of data distributed in time. However, some features associated with visualization of strain maps or utilization of more precise interpolation algorithms [21] are still under development. Standard 3D DIC analysis results presented in the paper comes from the commercial software VIC 3D and results of the long-term monitoring come from the custom-made software. Results obtained from the commercial software were also used for a validation of the custom-made software. Stereo-calibration in VIC 3D is carried made with utilization of circular markers and stereo-calibration in custom-made software is carried out with chessboard. Because of this we had to use both types of calibration boards in the presented measurements.

As it was mentioned above 3D DIC method is used simultaneously with an infrared camera in order to combine temperature and displacement/strain maps. This methodology significantly facilitated an interpretation of the obtained data and recognition of sources of abnormal behaviors or structure failures. Displacements/strains and temperature maps were simply overlaid on each other with utilization of image processing tools. More sophisticated methods, which have been mentioned in the introduction [13,14] are of a great interest and can be implemented in future works.
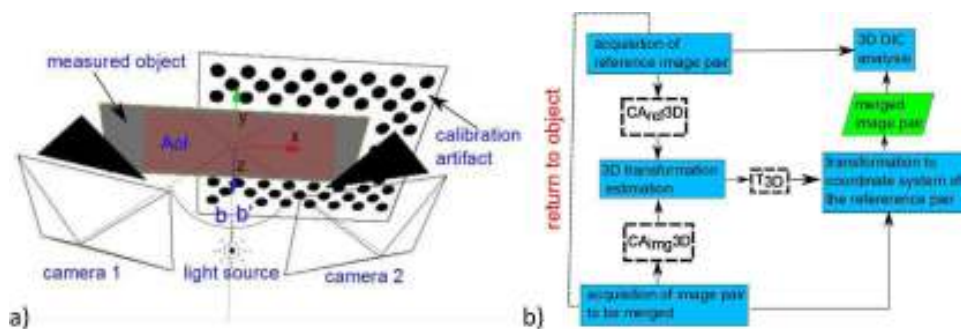

Fig. 2. The method of automatic merging of 3D DIC data: (a) measurement setup and (b) flow-chart of the software prcocedure.

2.3. Data processing and presentation of results

An output from 3D DIC are *U*, *V* and *W* displacement maps and shapes of measured objects. They denote displacements in *x*, *y* and *z* directions respectively. Typically coordinate systems are established after plane fitting of obtained point clouds from a reference image pair. *U* and *V* displacements are in-plane displacements and *W* is an out-of-plane displacement. Strain maps were calculated with utilization of finite-strain equations [22] (Eq. (1)) in VIC-3D software:

$$\varepsilon_{xx} = \frac{\partial u}{\partial x} + \frac{1}{2}\left[\left(\frac{\partial u^2}{\partial x}\right) + \left(\frac{\partial v^2}{\partial x}\right) + \left(\frac{\partial w^2}{\partial x}\right)\right]$$
$$\varepsilon_{yy} = \frac{\partial v}{\partial y} + \frac{1}{2}\left[\left(\frac{\partial u^2}{\partial y}\right) + \left(\frac{\partial v^2}{\partial y}\right) + \left(\frac{\partial w^2}{\partial y}\right)\right] \qquad (1)$$
$$\varepsilon_{xy} = \frac{1}{2}\left(\frac{\partial u}{\partial x} + \frac{\partial v}{\partial y}\right) + \frac{1}{2}\left[\left(\frac{\partial u}{\partial x}\frac{\partial u}{\partial y}\right) + \left(\frac{\partial v}{\partial x}\frac{\partial v}{\partial y}\right) + \left(\frac{\partial w}{\partial x}\frac{\partial w}{\partial y}\right)\right]$$

In most of the cases out-of-plane displacement *W* does not influence in-plane deformation and thus *W* components can be omitted from equation 1 [2].

The Cartesian coordinate system *x*, *y*, *z* is overlaid on each displacement or strain map presented in the paper in order to schematically show directions of each axis. As the measured objects are not flat, the coordinate systems are matched to the planes fitted to point-clouds representing an object. Such simplification is useful and acceptable in the most of industrial applications, as it facilitates visual evaluation of displacement/ strain maps. Presented displacement and strain maps are characterized by *P–V* values (what stands for Peak-to-Valley – a difference between the maximum and the minimum value within a particular map).

3. Measurements of steel struts

The first example of 3D DIC application refers to monitoring of diaphragm walls, which are used as a support for deep excavations. Stability of diaphragm walls is ensured by steel struts, ground anchors or underground slabs [23]. Static analysis of in-plane displacements of diaphragm walls is typically carried out and includes factors such as:

- Active earth pressure.
- Water pressure.
- External loads (roads, buildings etc.).
- Loads from internal construction.

In the case of utilization of steel struts it is also important to evaluate an influence of temperature changes on in-plane displacements of excavation's support, as thermal strains of steel elements are an important factor for security of construction works. So far in typical analysis of a mutual impact between an excavation support and a steel strut, a thermal elongation of the strut was not taken into account.

A cross-section of a typical strutted diaphragm wall is presented in Fig. 3. In this case the stability of the diaphragm wall (thickness 0.60 m) has been provided by one level of steel struts at −0.75 m below the ground level (b. g. l.).

The designed construction stages of steel struts are as follows:

- Soil leveling, forming of a working platform.
- Execution of guide walls.
- Execution of diaphragm walls and a reinforced concrete capping beam.
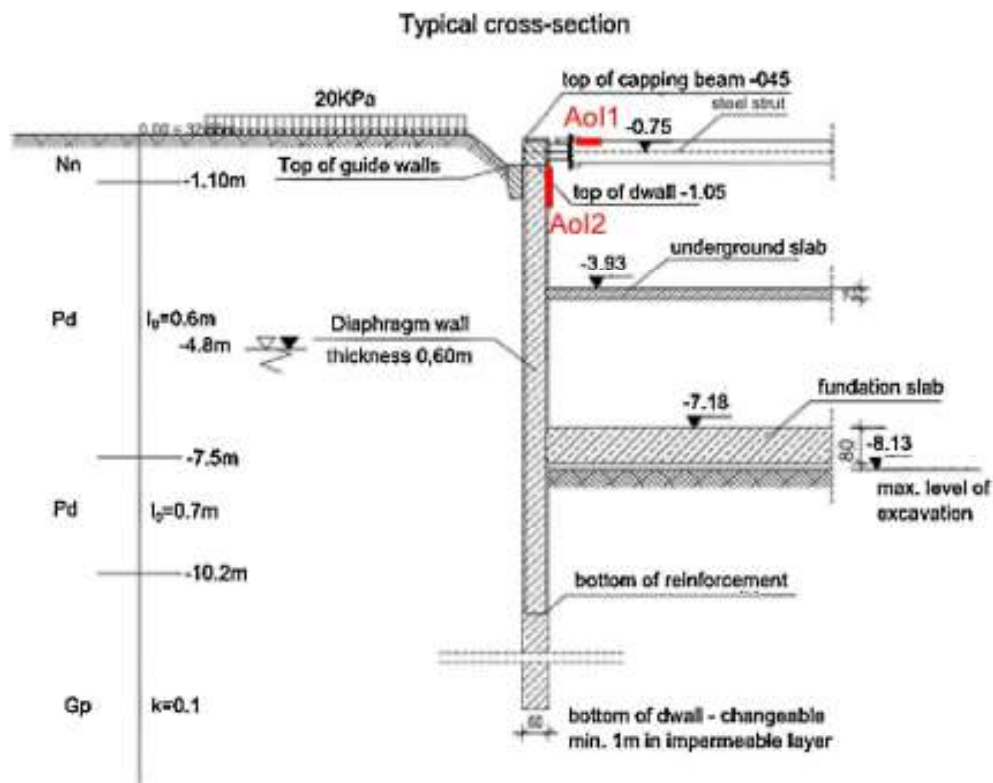- Excavation −1.5 m b.g.l.

Fig. 3. Typical cross-section of strutted diaphragm wall with marked localizations of the areas of interest (AOIs).

- Installation of struts −0.75 m b.g.l.
- Final excavation, max. −8.13 m b.g.l.
- Execution of a foundation slab.
- Execution of a "−1" slab at −3.93 m b.g.l.
- Dismantling of struts after the foundation slab and the "−1" slab reached 100% of its designed strength.
- Execution of a remaining structure.

Struts are mounted during excavations in order to maintain a stability of an excavation support, in our case in a form of diaphragm walls. Big temperature variations, which occur in a day/night cycle, and also a progress of construction works, may result in deformations of struts [24]. The deformed struts may no longer fulfill their function and moreover they cause an unpredictable increase of displacements and strains in diaphragm walls. Monitoring of horizontal and vertical displacements of diaphragm walls is crucial for safety of neighboring buildings and another underground infrastructure.

The most commonly used, commercially available and the cheapest method for measurements of diaphragm walls displacements at building sites with deep excavations is a geodetic method [25]. However, geodic surveys provide small accuracy, which is additionally dependent on weather conditions. Accuracy varies in the interval of 2 mm during good weather and 6–7 mm during bad weather. Also the measurements require applying bench-marks to a structure. In the case, when bench-marks are obscured by an inner-structure of a building, measurements of displacements are no longer possible.

More accurate but also much more expensive are manual inclinometers [26]. The accuracy of the method is in interval of 1–2 mm regardless of weather conditions. Inner-structure does not interfere with measurements, although an access to a measuring tube is required. In the most advanced (as well as the most expensive) monitoring systems, automatic inclinometers provide measurements without requiring access to the inlet pipe (measuring tubes are embedded in the diaphragm wall). Inclinometers are most commonly used during the works performed at centers of big cities.

The aim of the test was to determine an influence of temperature variations on displacements/strains of temporal steel struts and also to introduce more accurate method for monitoring of displacements of diaphragm walls. Compared to the methods

described above, 3D DIC provides much bigger accuracy, what is especially important at building sites, where displacements of diaphragm walls might have a significant influence on safety of works. Furthermore, bigger accuracy is necessary in order to quantitatively study thermal deformations of steel struts.

The presented measurements were carried out on the construction site at Lopuszanska St. 38b in Warsaw. For the first time in Poland we utilized an accurate full-field measurement method for determination of displacements of diaphragm walls.

3.1. Location of 3D DIC setups

The measurements were carried out with 3D DIC technique simultaneously in two areas of interest (AoI) located at the strut and at the reinforced concrete wall (Fig. 3). The first area of interest (AoI1) covered an end part of the longest strut (length of the observed part = 0.5 m). 3D DIC system consisted of two 2Mpx AVT Stingray cameras equipped with 28 mm focal length lenses (F number was set to 11). AoI1 was selected so that within it was a big deformation of the strut, which could be observed even with a naked eye. We do not know when and how the deformation was formed as struts are used multiple times at different building sites. The deformation could occur during transportation or during installation. The first measurement spot is presented in Fig. 4a. The shape of the strut within the AoI is shown in Fig. 4b.

The second area of interest (AoI2) covered a part of reinforced concrete wall and the support element of the steel strut. In this case 3D DIC setup consisted of two 5Mpx PointGrey cameras equipped with 28 mm focal length lenses (F number was set to 11.The measurement setup and AoI2 are shown in Fig. 5. The measurements in AoI2 were carried out in order to determine relative displacements between the steel strut support element and the concrete wall.

The measurement rigs were constructed from aluminum profiles. Cameras of DIC systems and LED reflectors were mounted to tripod heads, which were fixed directly to horizontal beams of the rig (measuring arms). The measuring arms were bolted to transverse beams. In the case of AoI 1, in order to achieve a sufficient stiffness of the rig, the transverse beam and the measuring arm were connected by the third profile. Measurement rigs were easy to carry and install in measurement positions. This feature was extremely necessary for safety reasons; the measure-
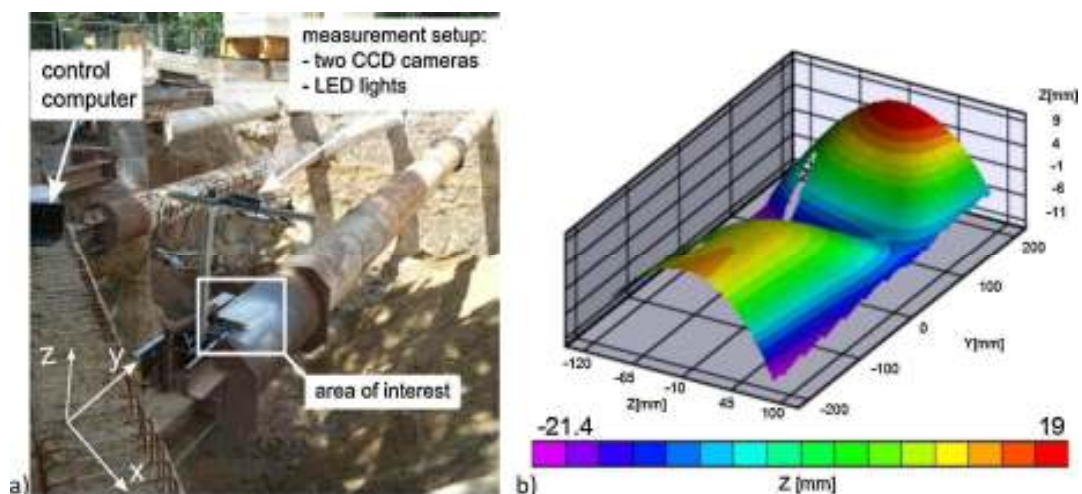

Fig. 4. Illustration of the first area of interest (AoI1): (a) the photo of the measurement setup and AoI1 and (b) the shape of the strut within AoI1; the deformation of the strut is clearly visible.

81

Fig. 5. View of the measurement setup and location of AoI2.

ment spots were located in the narrow area (about 1 m) between the excavation and a fence. Construction of the measuring arm was the same for both AoIs. It was mounted with utilization of G-clamps to the strut's support element (AoI1) and to concrete reinforcement (AoI2). Selection of the mounting location was not perfect, as the profiles were not completely isolated from strut's displacements. This experimental feature could result in errors in determination of linear components of displacements, however, information about strains (calculated as presented in Eq. (1)) was preserved. Because of hard environmental conditions such as wind or vibrations caused by heavy equipment, it was not possible to find another spot to install the measuring equipment.

Both AoIs were illuminated with LED reflectors enclosed in industrial casings. Exposure times in both 3D DIC systems were varied from 5 ms in daytime to 100 ms at night. Tuning of the exposure time was necessary due to sunlight illumination. Because of possible vibrations of DIC setups (due to wind or construction works), the longer exposure time could have an effect on the measurement. In general, longer exposure time could work as an averaging filter on displacements, but on the other hand it could also decrease correlation values. These fluctuations may explain increased amplitude of noise when compared to measurements performed in indoor conditions.

Additionally in both AoIs we mounted calibration artifacts (the planar dibond (Table 1) [18] boards with black circular markers printed on a white background), which were used for long-term measurements. It was assumed that the artifacts remained fixed during the entire test series and during the time between test series.

3.2. Methodology

The goal of measurements was to study two factors, which could influence the building struts:

- Big temperature gradients.
- Progress of construction works.

The first factor was studied through full-day (24 h) monitoring of displacements in both described AoIs. Measurements were carried out on 23 and 24 September 2012, when, full-depth of the trench had been reached in the corner directly below the tested strut (see Fig. 3). Simultaneously with 3D DIC measurements, the temperature of the strut was measured with an infrared camera V60 manufactured by Vigo Systems Ltd. [27]. The combination of the results from both measurement methods enabled analysis of temperature influence on deformations of the strut.
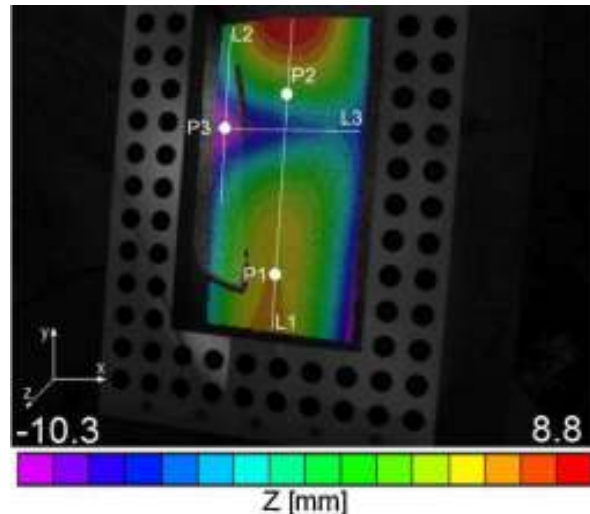

Fig. 6. The shape map of the measured strut with overlaid points of analysis.

The studies of the second factor were much more complicated and required long-term monitoring. The monitoring had to include the time between installing of struts and achieving a full-depth of the trench (approximately 2 weeks). 3D DIC apparatus could not be left unattended for such a long time due to construction works, the risk of theft or damage. The solution for this problem was application of the method of automatic merging of data distributed in time as described in Section 2.2.

3.3. The results of full-day measurements of the strut (AoI1)

The images were acquired every 2 min and in total 748 sets of (U, V, W) displacement maps have been calculated. An initial shape map of the measured strut within AoI1 with the overlaid points (P1, P2, P3) and lines (L1, L2, L3) of further analysis is presented in Fig. 6. The calibration artifact around the map is the artifact used for automatic merging of data (see Section 2.2).

At first we present (Figs. 7 and 8) two sets of in-plane (U, V) and out-of-plane (W) displacement maps (calculated after plane fitting to the obtained point cloud) which refer to two states of the structure:

- Maximum temperature changes when compared with the initial state.
- End of the test.

At the end of the test the temperature reached nearly the same value as at the beginning. However the displacements at the end of the test were not equal to zero. The residual displacements could be caused by rigid movement of the strut, what is acceptable in a small range – the strut is fixed at one side and keyed joint on the other side. Vertical and longitudinal regions with significantly different displacement values observed in all maps are regions affected by bigger correlation errors due to local shades (casted by a fragment of the measurement rig).

ε_{yy} strains (Fig. 9) were calculated from displacement maps according to Eq. (1) (Section 2.3). In this particular case y-axis corresponds to the axis of the strut, what indicates that v displacements corresponds to in-axis displacements (elongation of the strut). ε_{xx} strains have been omitted from analysis as they do not affect deformations of the diaphragm wall.

In Fig. 9 we marked a region with a significantly bigger strain concentration, which occurred in the area close to the initial
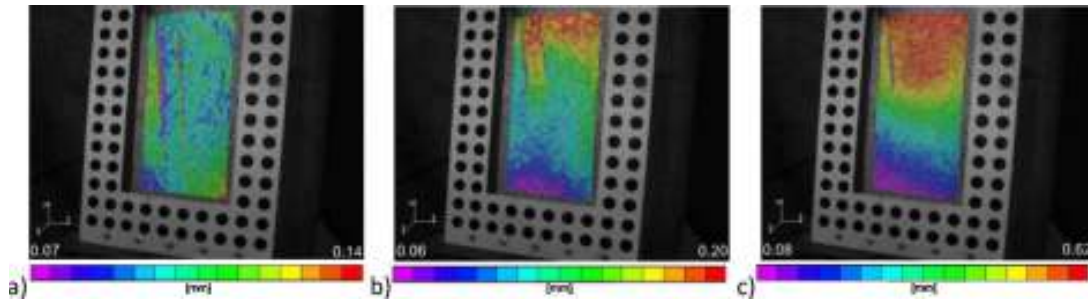
Fig. 7. Displacements maps obtained for maximum temperature changes: (a) *U* displacements *P–V* = 0.07 mm, (b) *V* displacements *P–V* = 0.14 mm and (c) *W* displacements *P–V* = 0.54 mm.
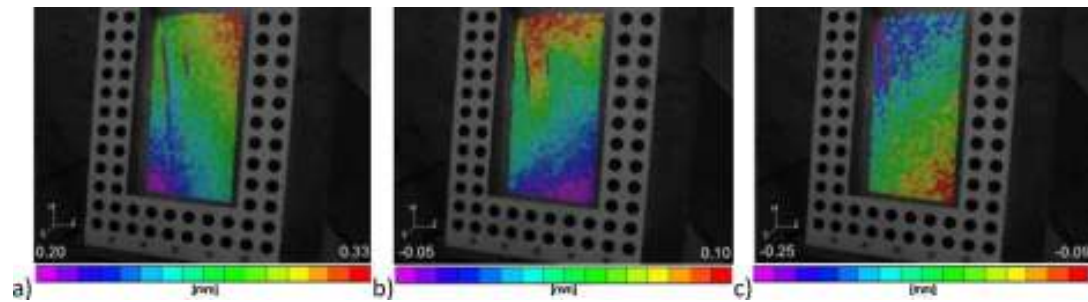

Fig. 8. Displacements maps at the end of the test: (a) *U* displacements *P–V* = 0.13 mm, (b) *V* displacements *P–V* = 0.14 mm and (c) *W* displacements *P–V* = 0.16 mm.
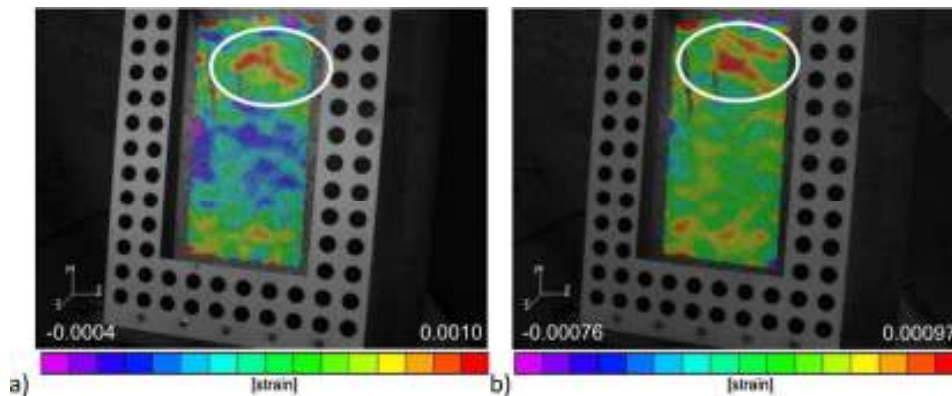

Fig. 9. ε_{yy} strain maps calculated from displacement maps at: (a) maximum displacements (maximum temperature changes) and (b) end of the test.

deformation of the strut (Fig. 4b and Fig. 6). It can be observed at the moment of maximum displacements (maximum temperature changes) as well as at the end of the test. The inhomogeneous strains distribution that one can observe in Fig. 9a, indicates that initial deformation of the strut could influence its behavior at higher temperatures.

In order to better understand the influence of temperature changes on displacements and strains variations of the strut, the local analysis of these values in a function of time was performed in three points indicated in Fig. 6. Points P1 and P2 were located closer to the strut's axis, while point P3 was located at the region in which the biggest deformation occurred. Displacements in each point were actually an average of displacements calculated in a small circle, which radius was equal to 10 pixels. Averaging of displacements reduced the influence of a possible local correlation noise and gave more accurate results.

The displacements in P1, P2, P3 and the temperature *T* plotted against the time (measured from the beginning of the test) are presented in Fig. 10.

The simplified mechanical analysis of an in-axis elongation of the strut show that 0.2 mm *V* displacements produce additional 19 MPa stresses in the strut. This is a significant value and it corresponds to 10% of the overall designed strength.

Additionally as mentioned in Section 2 the area of interest was monitored with IR camera. The selected thermograms which illustrate a distribution of temperature for the representative moments T1, T2, T3 and T4 are shown in Fig. 11.Emissivity of the object, was not calibrated but determined by catalogs (emissivity of the steel).

As one can observe in Fig. 11, the temperature was distributed homogeneously on the surface of the strut. We averaged the temperature determined in a few points of the strut and plotted it
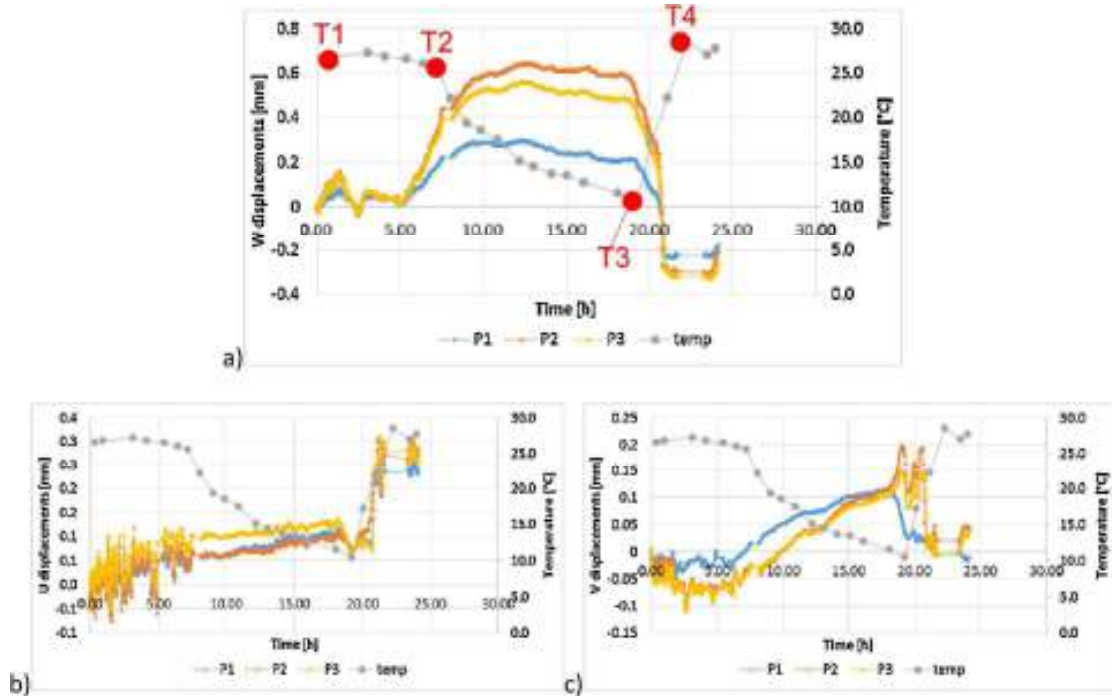
Fig. 10. Displacements: (a) *W*, (b) *U*, and (c) *V* and temperature plotted against time.
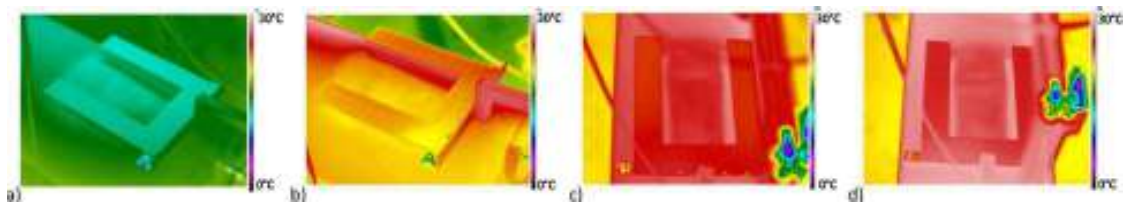

Fig. 11. Thermograms of the steel strut acquired in: (a) T1, (b) T2, (c) T3 and (d) T4.

against a time in Fig. 10. The displacements in all selected points and in all directions (*U*, *V*, *W*) are correlated with temperature variations. This trend is especially emphasized for *W* displacements. One can also observe that a cycle of temperature variations caused a sequential lengthening and shortening of the steel strut and in consequence displacements of the diaphragm wall (which is the cover of excavation).

With increasing temperature, the strut elongates and the diaphragm wall is pushed toward the ground, while decreasing temperature causes movement of the wall in the opposite direction – toward the excavation. Therefore additional stresses and shear forces occur in the diaphragm wall. The analysis of displacements and strains of the diaphragm wall is presented in Section 3.5.

As it was mentioned in Section 2 we have proposed another visualization method to present 3D DIC results. We extracted displacements and strains from points along a selected cross-section (e.g. cross-sections L1, L2, L3 indicated in Fig. 6) and presented them as a function of time (Fig. 12). Black regions mask invalid data: horizontal masks occur in the case when whole images had to be omitted from analysis due to insufficient or too strong illumination (exposure time was not adjusted in time); vertical masks occur in the case when some region within AoI was decorrelated due to shades or reflections. Lines L1, L2 and L3 were chosen in order to examine exact strains around the initial

deformation of the strut: line L1 corresponds to the axis of the strut, line L2 is parallel to line L1 but crosses the initial deformation region and line L3 is perpendicular to line L2 and also crosses the initial deformation.

The biggest variations of strains occur along line L2, which crosses the initial deformation of the strut. The distribution of strains along the chosen lines proves that the initial deformation could influence the strut response to temperature changes. Distribution of strains along lines L1 and L3 change homogenously with temperature changes.

3.4. The results of long-term measurements of the strut (AoI1)

The long-term monitoring of the strut has been carried out with utilization of the automatic merging of 3D DIC method described in Section 2.2. The monitoring started on August 10th and ended on August 24th. The subsequent measurements were taken on August 16th, August 21st and August 23rd. We also tried to acquire data on August 14th however, weather conditions (heavy rain and slippery surface near the measurement spot) made it impossible to take measurements. The calibration artifact (black circles printed on a dibond board) was fixed during the monitoring in the same position, while 3D DIC setup was installed and calibrated (with the standard stereo-calibration) for each subsequent measurement. As
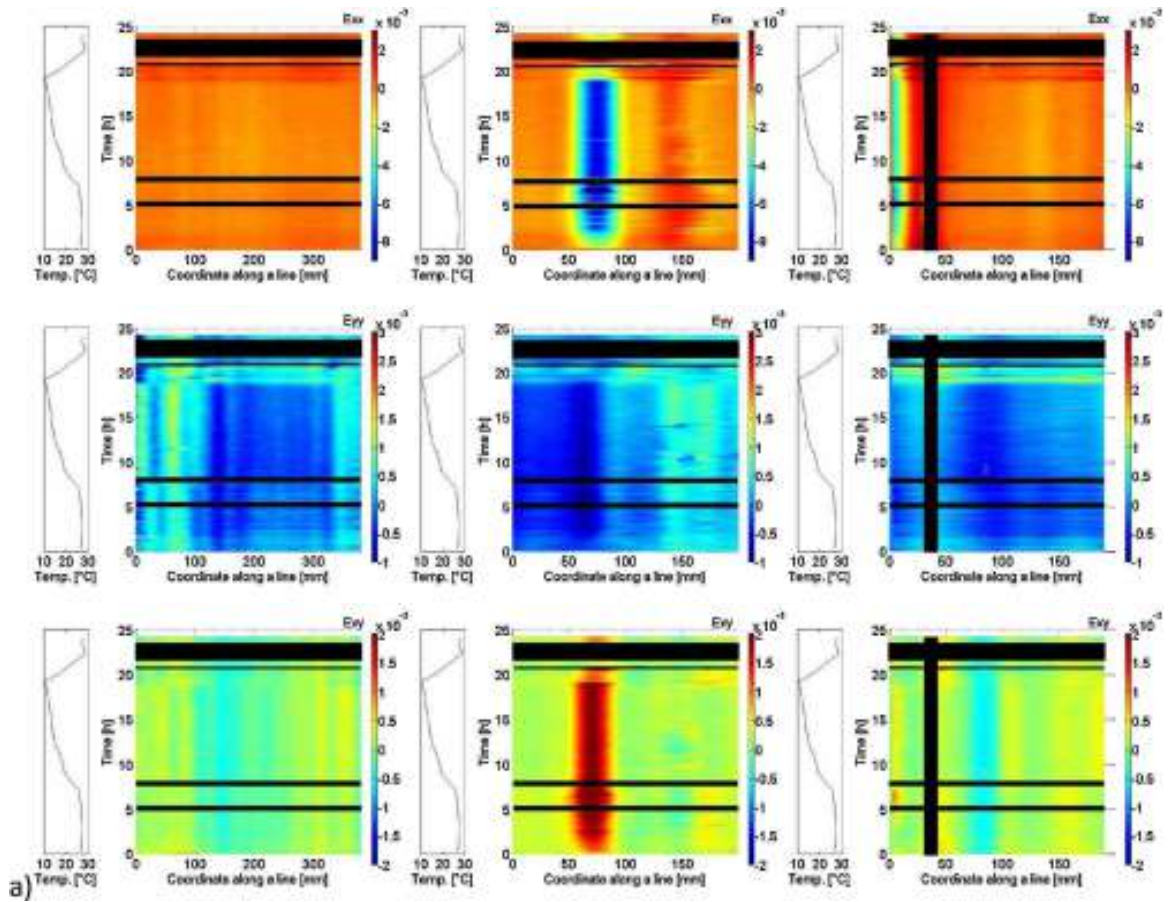
Fig. 12. Strains along a line from Fig. 6 in function of time: (a) line L1, (b) line L2, (c) line L3 (black lines indicates invalid data, which was masked out).

it was mentioned in Section 2.2, 3D DIC analysis with the capability of data merging have been carried out with utilization of the custom-made DIC software. The displacement maps obtained on 21st August (the reference pair of images were acquired on August 10th) are presented in Fig. 13.

Displacement maps presented in Fig. 13 are similar to those presented in Fig. 7. The dominant displacements (similarly to 24 h measurements) are W displacements. Values of displacements in all directions are in the same interval that full-day measurements. The U, V and W displacements extracted from points P1, P2 and P3 are presented in Fig. 14. The points of analysis are approximately in the same positions as in full-day measurements.

The green region marked in Fig. 14 indicates time interval, in which full-day measurements were carried out. One can observe

that similarly to full-day measurements, the biggest W displacements occur in points P2 and P3. In point P1 (closer to the strut support) out-of-plane movement is smaller. Analyzing Figs. 13 and 14 we can take an assumption, that the progress of excavation works had a very limited influence on displacements of steel struts. Values obtained from long-term monitoring are in the same interval as full-day measurements. This also means that thermal deformations of steel struts that occur during construction works causes significant deformations and the research of their influence on diaphragm walls should be carried in the future.

On the other hand, obtained results prove a feasibility of the method of automatic merging of 3D DIC data in long-term measurements/monitoring of displacements in industry.
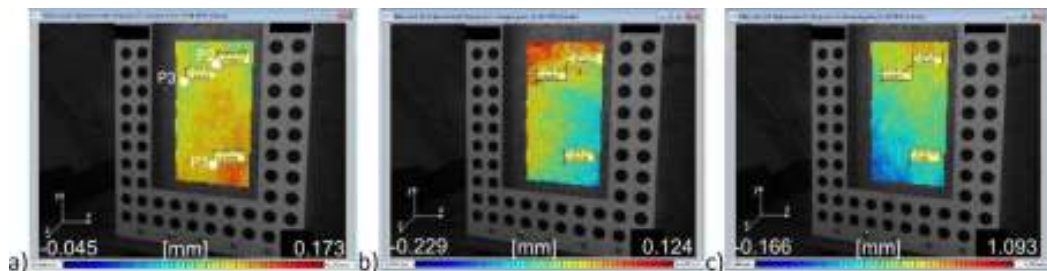

Fig. 13. Displacement maps calculated from images acquired at 21st August and merged to the reference coordinate system from 10th August: (a) U displacements, (b) V displacements and (c) W displacements.
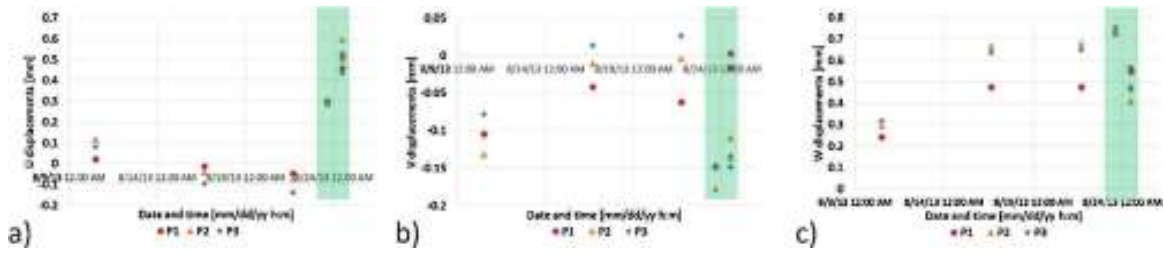
Fig. 14. Results of long-term monitoring of the strut: displacements in points P1, P2 and P3: (a) U, (b) V and (c) W.
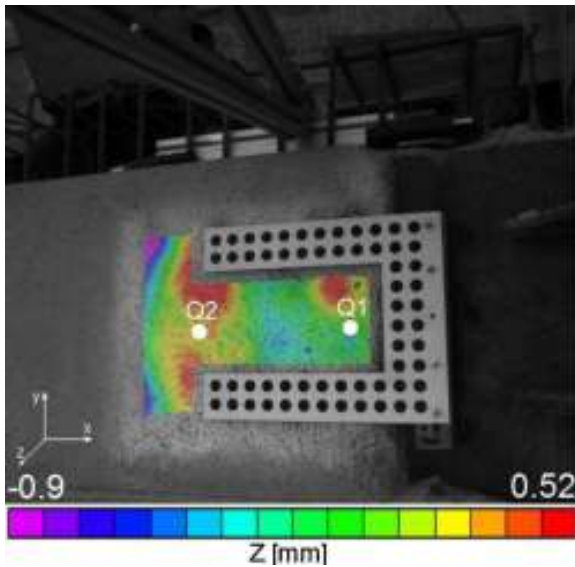

Fig. 15. The initial shape map of the slurry wall in AoI2 with indication of localization of points of local analysis: Q1 and Q2.

3.5. The results of full-day measurements of the diaphragm wall (AoI2)

The methodology of measurements and data analysis was similar to the measurements in AoI1 (see Section 3.3). The aim of measurements in AoI2 was to determine the direction of movements of the diaphragm wall and to correlate these directions with deformations of the steel strut. The shape map within AoI2 with overlaid points (Q1 and Q2) of further analysis is presented in Fig. 15. Displacements maps obtained in two different time moments are presented in Figs. 16 and 17.

The dominant displacements were out-of-plane displacements W in direction toward the excavation. It also can be observed that the biggest W displacements occur near the strut's support, which is consistent with expectations (this is the place most vulnerable to influence of deformations of the strut). In order to better demonstrate this trend we extracted displacement values from selected object points and plotted them against a time together with the temperature variations (Fig. 18).

Similarly to steel struts (AoI1), the dependency between displacement variations and temperature changes can be clearly observed in the results from measurements of the diaphragm wall (AoI2). In the case of low temperatures, the diaphragm wall moves toward the excavation (positive W displacements) and in case of high temperatures, the wall comes back toward the ground (decreasing W displacements). Furthermore one can observe in homogeneity in displacement maps: significantly bigger values of W displacements occurred in point Q1 (which is closer to the steel strut) than in point Q2 (distant from the steel strut). This observation is confirmed by characteristic of thermal deformations of the steel strut presented in Section 3.3. The strut deforms because of temperature variations and in consequence influence on the diaphragm wall. The biggest displacements occur near the struts' support and they are much smaller in regions between neighboring support points. In the case when a distance between neighboring struts is large enough, there are regions of a diaphragm wall, which are not affected by temperature variations of steel struts. This means that an influence of thermal deformations of struts is inhomogeneous in different segments of a diaphragm wall and thus can produce additional shear forces and stresses in the wall. Evaluation of actual values of shear forces and strains caused by temperature variations will be possible after additional measurements, which are planned to be carried out in the future. In these measurements the measuring equipment will be separated from a strut and from a diaphragm wall. This was not possible in the presented case because of technical issues explained in Section 3.1. However, the observed trend of the movement of the diaphragm wall is correct and proves suitability of the proposed method of measurements.
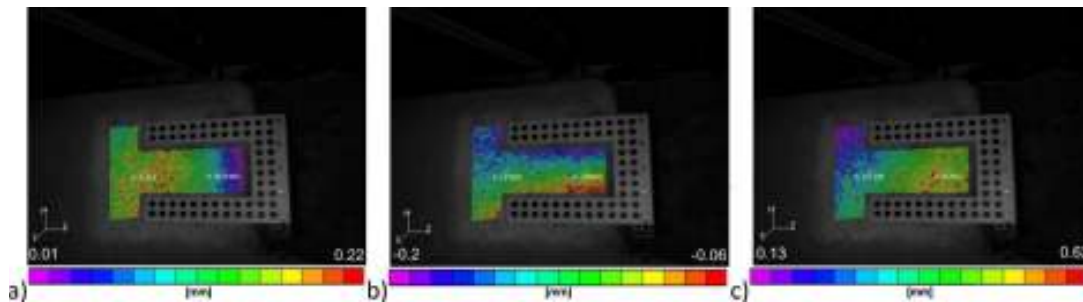

Fig. 16. Displacements maps in AoI2 obtained for maximum temperature changes: (a) 'U' $P–V = 0.22$ mm, (b) 'V' $P–V = 0.14$ mm and (c) 'W' $P–V = 0.5$ mm.
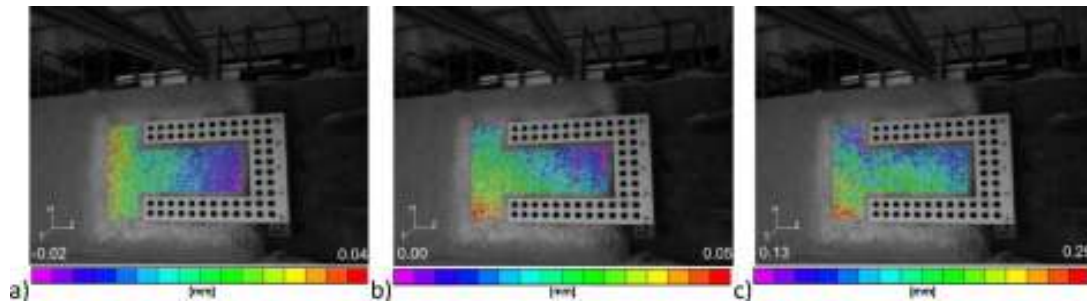
Fig. 17. Displacement maps in AoI2 obtained at the end of the test: (a) 'U' *P–V* = 0.01 mm, (b) 'V' *P–V* = 0.05 mm, c) 'W' *P–V* = 0.16 mm.
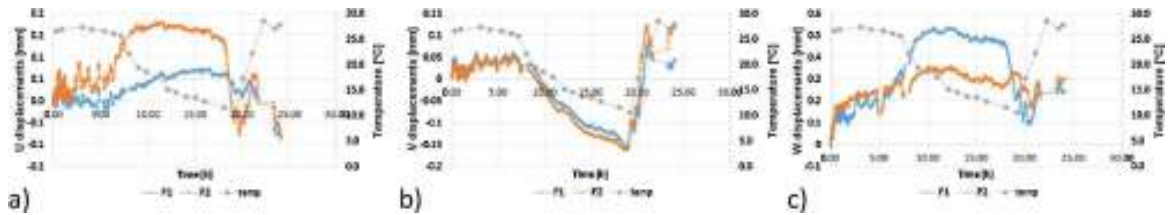

Fig. 18. Displacements in points Q1 and Q2 marked in Fig. 15: (a) *U*, (b) *V* and (c) *W*.

4. Measurements of intermediate pumping station

Displacements and deformations of pipelines are a serious problem in such industries as power engineering, heat engineering or petrochemistry [28]. Big differences of temperatures of liquid inside pipelines combined with big amplitudes of vibrations can lead to failures and can be dangerous for employees and for installations.

Measurements of pipes are essential in industry and especially in a district heating. An amount of heat distributed is dependent on the outside temperature. Therefore the temperature of water and of the pipeline will change accordingly to the amount of heat supplied. The demand for heat may change from day to day. This implies changes of the shape (especially the length) of the pipes due to thermal expansion. A single section of pipes may be even hundreds of meters or even kilometers long what means that the pipe elongation may be as great as a meter. This expansion may cause a non-uniform distribution of stress in the pipeline especially in the joining areas and in consequence may lead to damage. Underground works are extremely costly and may cut off households from heat supply for many days. Therefore it is necessary to monitor the displacements and stresses which may occur in the pipeline. In this way it is possible to determine faulty section and replace them before breakdown. The same methodology can also be used for monitoring of compensators. In normal, healthy condition of the pipeline, compensators should exhibit axial displacements only. Out-of-axis displacements should be minimal. In district heating, out-of-axis displacements of compensators can cause huge forces and in consequence result in failures of underground chambers for heat pipelines. Currently used methods of monitoring are uneconomic and not sufficient. Vibration sensors are often used [19] however they do not provide information about a pipeline condition but allow to estimate a scale of a threat only. Furthermore they cannot be used for monitoring of displacements of many elements of an installation at the same time.

In the presented example we proposed to apply 3D DIC system to carry out measurements of displacements and strains of pipeline elements under a controlled thermal input. The example comes from measurements in the intermediate pumping station in the Institute of Heat Engineering in Warsaw.

4.1. Location of 3D DIC system and methodology of measurements

The experimental setup was much smaller when compared to a real installation and contained elements made of different materials. Smaller scale and relatively low temperature gradients provided us with possibility to check a sensitivity of the proposed method. The aim of measurements was to check suitability of 3D DIC to measurements of displacements and strains of a pipeline and to prepare the implementation to diagnostic tests of real heating networks.3D DIC setup contained two PointGrey Grasshopper 5Mpx cameras equipped with 28 mm focal length lenses and LED reflector.

The measured object was a part of a pipeline working in a closed circuit (Fig. 19a). The circuit contained two compensators and two pumps, which forced the water flow. The temperature changes were produced solely by friction between water and the pipeline (Fig. 19b). In order to speed up the heating process, the observed pipeline have been separated from the main tank with a valve. At the beginning temperature rose quite quickly (blue zone Fig. 19b) from 20 °C (room temperature) up to 55 °C. The temperature of the pipeline began to stabilize after 40 min at 50 °C. After that the pump speed has been reduced and the pipeline began to cool slowly (red zone – approximately 10 min). At that moment the pump has been turn off and the temperature dropped rapidly (gray zone). After another 3 min the pump has been turned on again with reduced speed (green zone). In the yellow zone the valve was open and pump was pouring cold water, what resulted in a sudden decrease of the temperature. The thermograms in crucial time moments (T1, T2, T3, T4) are presented in Fig. 19c–f. Here we can observe big differences of temperature between elements of the pipeline and their connections. The measured temperature was the temperature of the observed pipeline and not the temperature of water.

4.2. Measurement results

At first 3D DIC measurements provided 3D shape of the measured object. The 3D and 2D representations of the shape map is shown in Fig. 20a and b, respectively. Points of further analysis are overlaid on the shape map in Fig. 20b.
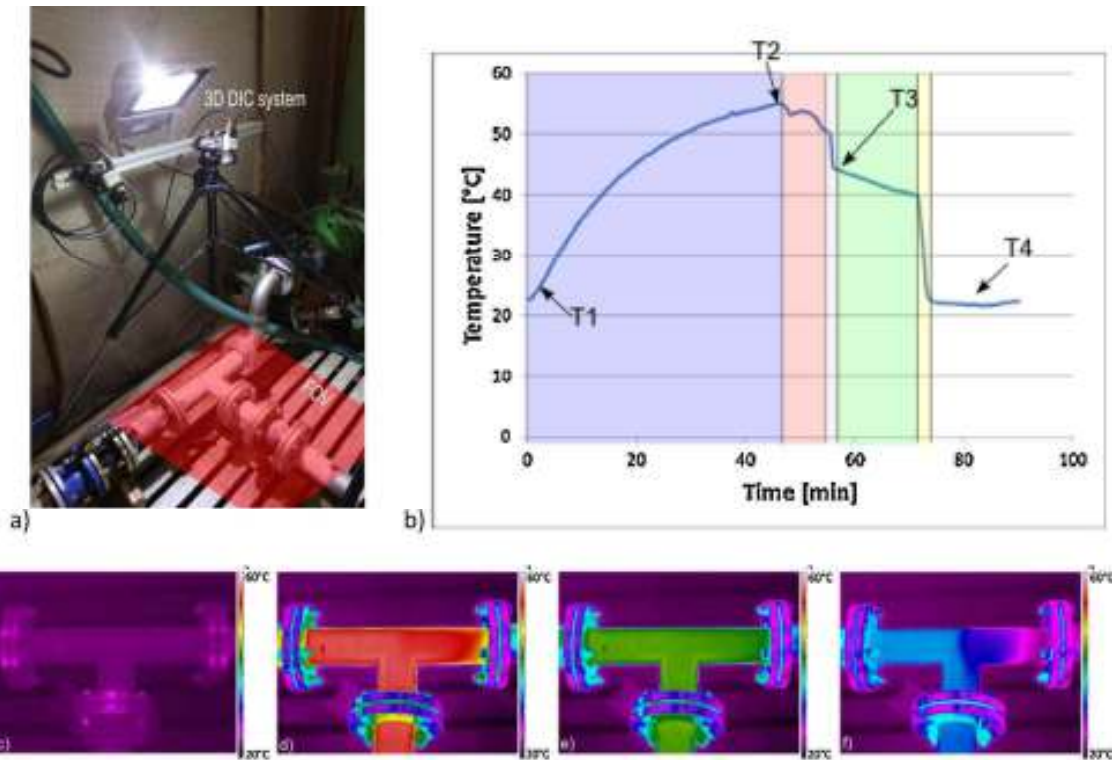
Fig. 19. Experimental conditions for measurements of a pipeline under thermal load: (a) 3D DIC setup and the measured pipeline, (b) measured temperature of the pipeline against time and (c–f) thermograms at the crucial time moments T1, T2, T3 and T4.
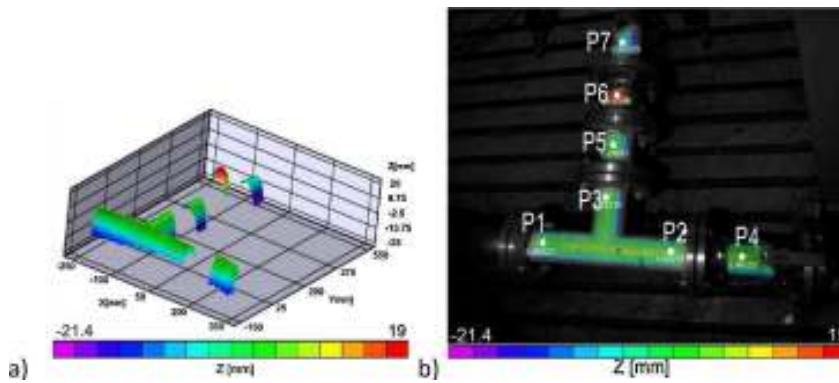

Fig. 20. Shape of the measured object: (a) 3D plot and (b) 2D map with overlaid points of further analysis.

The field of view (FOV) contained a T-pipe (points P1, P2 and P3), compensator 1 (P4), short pipe (P5), compensator 2 (P6) and a part of remainder of the pipeline (P7). The 3D DIC system monitored deformations of 5 elements of the pipeline simultaneously in three dimensions. In each point P (Fig. 20b) displacements U, V, W and strains ε_{xx}, and ε_{yy} have been extracted. In order to reduce the correlation noise, displacements and strains values were averaged in a small region around each point (similarly to struts' measurements).

The analysis of 3D DIC data provided us with a lot of information concerning 3D displacements, strains and deformations of pipeline's elements within FOV. The results

for each element can be considered independently or with respect to the other elements (and temperature changes). Provided with these data as well as the material and the geometry of whole installation we can draw conclusions about condition of the pipeline and indicate elements that can affect the malfunctioning of the pipeline. The set of displacement and strain maps obtained at maximum temperature are presented in Figs. 21 and 22 respectively. Strains were calculated with the methodology described in Section 2.3 (Eq. (1)).

As shown in Figs. 21 and 22, the biggest displacements and strains occur in the compensators which are made of rubber
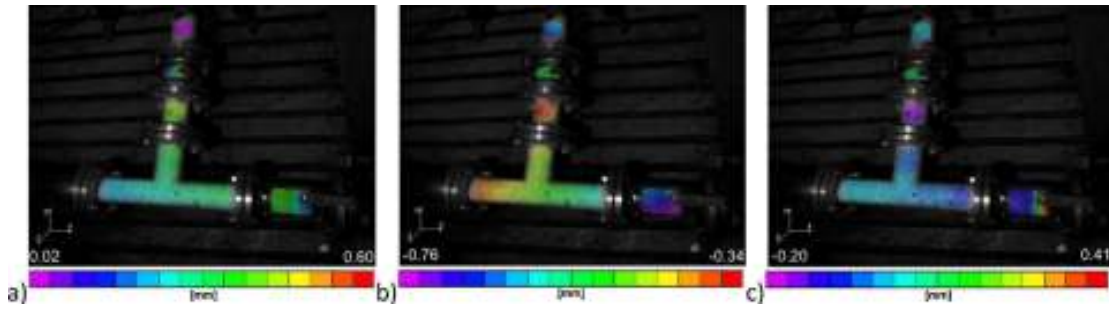
Fig. 21. The displacement maps at maximum temperature: (a) U with $P–V$ = 0.62, (b) V with $P–V$ = 0.42, and (c) W with $P–V$ = 0.61.
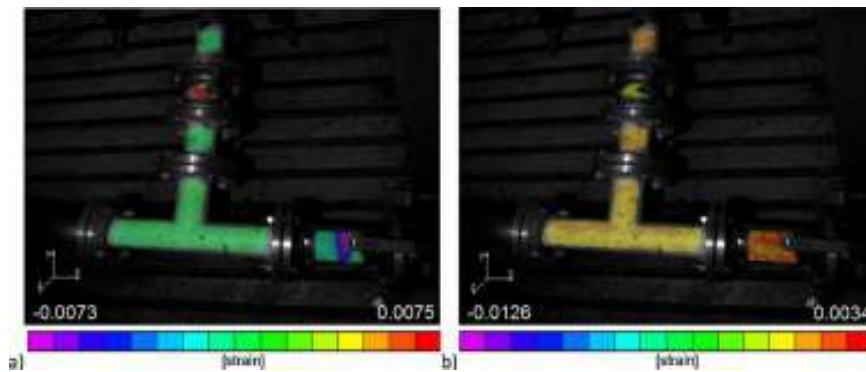

Fig. 22. The strain maps at maximum temperature: (a) ε_{xx} and (b) ε_{yy}.
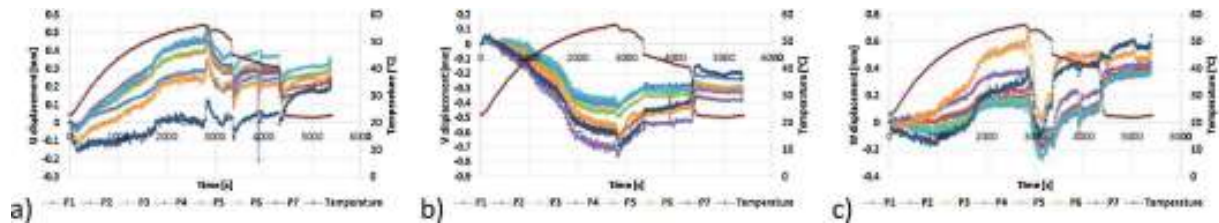

Fig. 23. Displacements in the selected points of interest: (a) U, (b) V, and (c) W.

(indicated by P4 and P6). Distribution of strains in other elements is much more homogenous, which is in line with expectations.

In order to analyze the behavior of the structure in selected points of interests in details, the displacements, strains and temperature in points P1, P2, P3, P4, P5, P6 and P7 are plotted against the time (Fig. 23).

Variations of displacements and strains obtained from each point P are very well correlated with the temperature trend. Increase of temperature by 30 °C induced approximately 0.6 mm displacements in all directions. Cooling of water reduced displacements, but pipeline did not return to its initial position (residual displacements occurred in all directions: U, V and W). In Fig. 24 one can observe that the biggest strain values occurred in
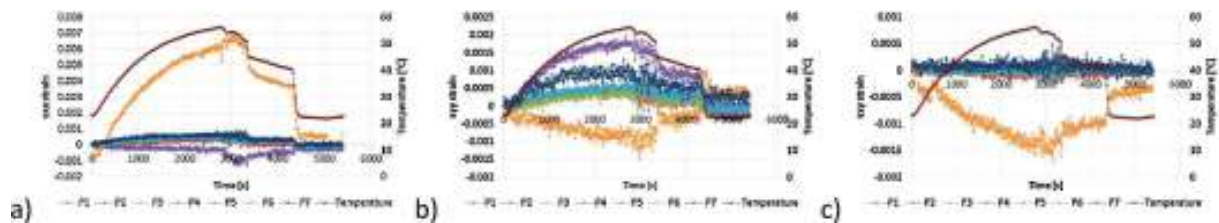

Fig. 24. Strains in selected points of interest: (a) ε_{xx}, (b) ε_{yy}, and (c) shear strain ε_{xy}.

both compensators (points P4 and P6). Unlike displacements, strain values in all points P have returned to their initial state (close to zero strain). This implies that displacements of the T-pipe have been compensated by compensators 1 and 2. This also means that utilization of compensators in the monitored piping system effectively protected the individual components from the risk of damage due to heating-up the system.

5. Conclusions and future works

In the paper we presented two applications of 3D DIC method in different fields of industry. We described measurements of steel struts displacements and strains caused by changing temperature and measurements of displacements of a fragment of a pipeline caused by flowing water. In both examples accuracy and suitability of 3D DIC method has been proven. However in order to facilitate measurements we applied some modifications in both software and hardware. Hardware ones concerned equipment protection against environmental conditions, while software modifications concerned developing of visualization methods and application of the novel method for automatic merging of data distributed in time. Maps and graphs presented in the paper (especially displacements over a line as a function of time) have been approved by specialists from industries and are considered as a very useful method for quick (even real-time) assessment of the measured objects.

The automatic merging of data method has been used in order to analyze long-term behavior of steel-struts. These analyses provided us with information about an influence of progress of construction works on deformations of steel struts and a diaphragm wall. Correlation between results obtained in full-day measurements and results obtained in the long-term monitoring proves the feasibility of the method.

The measurements of displacements with high accuracy (better than geodetic methods) and high frequency (in a real time), in combination with simultaneous temperature measurements enable to accurately determine the effect of temperature changes on steel struts displacements and on diaphragm walls displacements. Presented measurements showed strong correlation between temperature changes and displacements. The results show that elongation of the strut due to temperature changes can cause additional stress in the strut, which is in order of 10% of overall designed strength Performing measurements with a measuring system separated from struts and from the diaphragm wall (what is planned to be done in future works) will give a possibility to quantify the phenomenon and derive mathematical formulas. As a result, it will affect the development of design methods of diaphragm walls. Taking thermal deformations into account during numerical simulations will also ensure material savings when building reinforced walls.

Taking into account the presented results and the big demand for both short and long term, full-field monitoring of industrial and civil engineering structures the authors strongly believe that the applications of the modified digital image correlation method will significantly expand in the near future.

Acknowledgements

References

[1] J.J. Orteu, 3-d computer vision in experimental mechanics, Optics and Lasers in Engineering 47 (2009) 282–291.

[2] M. Sutton, J.J. Orteu, H. Schreier, Image Correlation for Shape, Motion and Deformation Measurements, Springer, New York, 2009.

[3] B. Pan, Recent progress in digital image correlation, Experimental Mechanics 51 (7) (2011) 1223–1235.

[4] M. Poncelet, G. Barbier, B. Raka, S. Courtin, R. Desmorat, J. Le-Roux, L. Vincent, Biaxialhigh cycle fatigue of a type 304l stainless steel: cyclic strains and crack initiation detection by digital image correlation, European Journal of Mechanics A/Solids 29 (2010) 810–825.

[5] G. Payen, H. Klocker, A. Lens, D. Wilkinson, J. Embury, Design of an in situ mechanical test for spot-welded joints, Engineering Fracture Mechanics 96 (2012) 528–538.

[6] T.N. Nguyen, J.M. Huntley, R.L. Burguete, C.R. Coggrave, Shape and displacement measurement of discontinuous surfaces by combining fringe projection and digital image correlation, Optical Engineering 50 (10) (2011) 101505–101511.

[7] E. Fagerholt, T. Borvik, O. Hopperstad, Measuring discontinuous displacement fields in cracked specimens using digital image correlation with mesh adaptation and crack-path optimization, Optics and Lasers in Engineering 51 (2013) 299–310.

[8] Z. Tang, J. Liang, Z. Xiao, Large deformation measurement scheme for 3d digital image correlation method, Optics and Lasers in Engineering 50 (2) (2012) 122–130.

[9] B. Pan, D. Wu, L. Yu, Optimization of a three-dimensional digital image correlation system for deformation measurements in extreme environments, Applied Optics 51 (19) (2012).

[10] S. Yoneyama, A. Kitagawa, S. Iwata, K. Tani, H. Kihuta, Bridge deflection measurement using digital image correlation, Experimental Techniques 31 (1) (2007) 34–40.

[11] J. Travelletti, C. Delacourt, P. Allemand, J.-P. Malet, R. Schmittbuhl, R. Toussaint, M. Bastard, Correlation of multi-temporal ground-based optical images for landslide monitoring: application, potential and limitations, ISPRS Journal of Photogrammetry and Remote Sensing 70 (2012) 39–55.

[12] E. Li, A. Tieu, W. Yuen, Application of digital image correlation technique to dynamic measurement of the velocity field in the deformation zone in cold rolling, ISPRS Journal of Photogrammetry and Remote Sensing 39 (4) (2003) 479–488.

[13] J.J. Orteu, Y. Rotrou, T. Sentenac, L. Robert, An innovative method for 3-d shape, strain and temperature full-field measurement using a single type of camera: principle and preliminary results, Experimental Mechanics 48 (2) (2008) 163–179.

[14] A. Maynadier, M. Poncelet, K. Lavernhe-Taillard, S. Roux, One-shot measurement of thermal and kinematic fields: infrared image correlation (IRIC), Experimental Mechanics 52 (3) (2012) 241–255.

[15] A. Chrysochoos, V. Huon, F. Jourdan, J.-M. Muracciole, R. Pevroux, B. Wattrisse, Use of full-field digital image correlation and infrared thermography measurements for the thermomechanical analysis of material behaviour, Strain 46 (1) (2010) 117–130.

[16] M. Kujawińska, R. Sitnik, G. Dymny, M. Malesa, K. Malowany, D. Szczepanek, Hierarchical, multitasks optical system for health monitoring of civil engineering structures, Proc. SPIE 7387 (2010) 738721.

[17] M. Malesa, M. Kujawińska, Modified two-dimensional digital image correlation method with capability of merging of data distributed in time, Applied Optics 51 (36) (2012) 8641–8655.

[18] Clarity. http://www.reactivepolymers.com.

[19] Panasonic. http://www.panasonic.com.

[20] C. Solutions. http://www.correlatedsolutions.com.

[21] R. Keys, Cubic convolution interpolation for digital image processing, IEEE Transactions on Acoustics, Speech and Signal Processing 29 (6) (1981) 1153–1160.

[22] T. Chu, W. Ranson, M. Sutton, W. Peters, Applications of digital image-correlation techniques to experimental mechanics, Experimental Mechanics 25 (3) (1985) 232–244.

[23] A. Siemi'nska-Lewandowska, Deep excavations. Design and execution, Wydawnictwo Komunikacji Łączności 96 (2010) 528–538, in Polish.

[24] A. Sieminska-Lewandowska, M. Mitew-Czajewska, U. Tomczak, The study of displacements of diaphragm walls built in Warsaw quaternary soils, in: Proc. of the 7th International Symposium on Geotechnical Aspects of Underground Construction in Soft Ground, CRC Press Taylor FrancisGroup, 2011.

[25] C. Thorley, R. Forth, Settlement due to diaphragm wall construction in reclaimed land in Hong Kong, Journal of Geotechnical and Geoenvironmental Engineering 128 (6) (2002) 473–478.

[26] C. Hope, M. Chuaqui, Precision surveying monitoring of shoring and structures, in: FMGM 2007: Seventh International Symposium on Field Measurements in Geomechanics, vol. 175, 2007, pp. 105–119, ASCE.

[27] V.S. SA. http://www.vigo.com.pl.

[28] M. Kujawinska, M. Malesa, K. Malowany, P.M. Błaszczyk, Application of image based methods for monitoring and measurements of structures in power stations, Key Engineering Materials 518 (2012) 24–36.

Marcin Malesa PhD student of applied optics at Warsaw University of Technology. His scientific interest includes full-field optical metrology, application of non-coherent optical methods of measurements in industry, image processing and computer vision. During PhD studies he developed significant upgrades of digital image correlation method and validated their applicability in heat and power engineering, building engineering or conservation of art.

Krzysztof Malowany PhD student of applied optics at Warsaw University of Technology. Areas of interest: full-field optical metrology in civil engineering and power engineering industry, hybrid opto-numerical methods in mechanics, image and data processing, design of novel photonics systems. Current research focuses on development of a method for calibration of FEM models with utilization of full-field optical methods (in particular with digital image correlation).

Urszula Tomczak assistant at Warsaw University of Technology at Geotechnics and Underground Structures Division at Institute of Roads and Bridges. Licensed designer of underground structures, deep excavations, deep foundation (more than 150 executed designs). She is specialized in monitoring of diaphragm wall's displacements.

Bartlomiej Siwek PhD student of applied optics at Warsaw University of Technology. Areas of interest: combined methods of thermovision and full-field optical techniques in use in civil engineering and industry, image and data processing, design of novel hybrid photonics systems. Current research focuses on development of hybrid technique based on thermography and digital image correlation method.

Malgorzata Kujawinska SPIE Fellow, full professor of applied optics at Warsaw University of Technology, head of Photonics Engineering Division at Institute of Micromechanics and Photonics. Expert in full-field optical metrology, hybrid opto-numerical methods in mechanics, image processing, automatic data analysis and design of novel photonics systems. She has been involved in the optical metrology topics since 1980 including: development of interferometric, holographic, grating, digital image correlation and structured light based methods. Author of one monograph, several book chapters and more than 200 papers in international scientific journals.

Anna Siemińska-Lewandowska, full professor of civil engineering at Warsaw University of Technology, head of Geotechnics and Underground Structures Division at Institute of Roads and Bridges. Expert in mechanized tunneling, underground structures, deep excavations. She has been involved in the consultancy and design of ground anchors and diaphragm walls for a number of projects in Poland. She is also a consultant for the 1st and 2nd metro line construction in Warsaw. Author of one monograph, several book chapters and more than 100 papers. She is also President of Polish Group of International Tunneling and Underground Space Association, Member of TC28 "Tunneling in Soft Ground" ISSMGE.

Application of 3D digital image correlation to track displacements and strains of canvas paintings exposed to relative humidity changes

Krzysztof Malowany,[1,*] Ludmiła Tymińska-Widmer,[2] Marcin Malesa,[1]
Małgorzata Kujawińska,[1] Piotr Targowski,[3] and Bogumiła J. Rouba[2]

[1]Institute of Micromechanics and Photonics, Warsaw University of Technology, ul. Sw. Boboli 8,
02-525 Warszawa, Poland

[2]Institute for the Study, Restoration and Conservation of Cultural Heritage, Nicolaus Copernicus University,
ul. Gagarina 7, 87-100 Toruń, Poland

[3]Institute of Physics, Department of Physics, Astronomy and Informatics, Nicolaus Copernicus University,
Grudziądzka 5, 87-100 Toruń, Poland

*Corresponding author: k.malowany@mchtr.pw.edu.pl

This paper introduces a methodology for tracking displacements in canvas paintings exposed to relative humidity changes. Displacements are measured by means of the 3D digital image correlation method that is followed by a postprocessing of displacement data, which allows the separation of local displacements from global displacement maps. The applicability of this methodology is tested on measurements of a model painting on canvas with introduced defects causing local inhomogeneity. The method allows the evaluation of conservation methods used for repairing canvas supports. © 2014 Optical Society of America

OCIS codes: (100.2000) Digital image processing; (200.3050) Information processing; (120.0120) Instrumentation, measurement, and metrology.
http://dx.doi.org/10.1364/AO.53.001739

1. Introduction

This paper presents a study on the application of 3D digital image correlation (DIC) for examination of the dimensional response of model canvas paintings to changes in environmental conditions, in particular relative humidity (RH). This work was initiated within a larger project on new methods and materials for infilling voids in canvas supports. It came out of the need to complete comparative laboratory tests of properties of materials with examination that would directly show the behavior of traditional and new types of repairs introduced into a structure of a painting and their interaction with the original (the results will be presented elsewhere). It was assumed that it is essential to find a method that would allow the testing of the materials in conditions closest to the natural environment—in paintings on wooden stretchers subjected to changes of climatic conditions that can occur in their environment, optimally also in original paintings.

Canvas paintings are very complex multilayer composites, composed usually of a textile support stretched on a rigid or keyed wooden frame, a glue size, a ground, design layers, and a varnish (Fig. 1). These various and hygroscopic materials independently respond to variations of the RH in their environment [1–5]. The mechanical properties and dimensional stability of a canvas painting depend
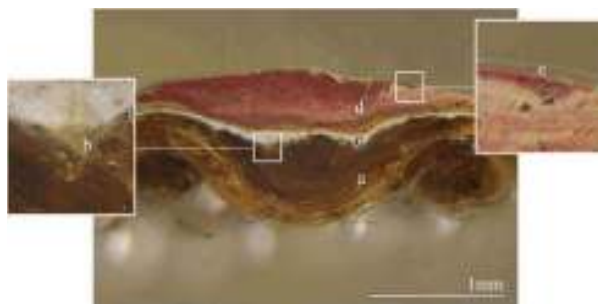
Fig. 1. Multilayer structure of a canvas painting (exemplary cross-section from 20th century painting). The structure includes: a canvas (a), a glue size layer (b), a ground layer (c), oil paint layers of different thicknesses (here with high impastos) (d), and a varnish (e) [photo W. Grzesik].

thus on the composition of the structure and properties of its constituents. It is difficult to specify a general model that could be applied to all canvas paintings, even in frames of a certain period of art history. For instance, advanced research on properties of 19th century paintings based on laboratory tests [6–9] and on the analysis of the relationship between the details of structure and state of preservation of original paintings [10] still shows a great variety of cases within this group. There is an infinite variety of combinations of materials introduced into painting technology that has been used over centuries. Not only the selection of materials but even the way they were applied—cold or hot [1,4,11], thin or thick—can profoundly affect the properties and behavior of a particular painting. Also the different age and degradation processes that paintings undergo in various storage conditions influence their mechanical properties and dimensional response to changes in RH. Usually the structure of the weave and particular threads of canvas [4,12–14], as well as the type and characteristic of the size layer, influence sensibility to climatic changes of the surrounding and extent of global deformation of all the structure, although mostly the composition of ground and paint layers (the type of pigments, fillers, binders, and their ratio) also determines the final behavior of the structure [5,15]. Since canvas paintings are often mounted on a considerably stiff stretcher, expansion of glue size and/or canvas support causes loss of tension of the painting, slacking, sagging, and out-of-plane bulging and waving of all the structure. On the contrary, contraction of these layers causes an increase in tension and inner stress in the structure, leading in extreme situations to such types of damage as plastic deformation of certain layers, formation of tears in canvas, cracks, delamination, and flaking in ground and paint layers. The strain/stress distribution is not uniform on all of the surface of the canvas painting tensioned on the stretcher [16,17]. Moreover, the structure of the composite is not symmetrical over its cross-section. The asymmetry of the composite is responsible for local out-of-plane deformations that occur when continuity/homogeneity of particular layers or all the structure is disturbed

or lost. The plane of a painting can also be affected by inappropriate treatments in areas of damage. For instance, some repairs: glue joints, patches, or infillings made of materials of parameters different from the ones constituting the original or changing local water vapor permeability and moisture absorption of a painting are able to disrupt the homogeneity of the structure significantly and ultimately disturb the integrity of the paintings (Fig. 2).

Inhomogenity, anisotropy, and variations in the structure and state of preservation make examination of canvas paintings as well as the choice and evaluation of methods for their conservation very difficult. Such studies demand a universal yet individual and flexible approach and 3D full-field measurements. For this reason, standard point-wise measurement devices, such as strain gauges and optical fiber sensors [19–21] are not sufficient.

Canvas paintings mounted on traditional wooden stretchers in certain conditions can be relatively flexible. The range of displacements resulting from changes of RH can even be of a range of a few millimeters; additionally their out-of-plane displacements are much higher than in-plane displacements [22] and increase with the size of an object. Thus, the main challenge in tracing canvas paintings' distortions is to capture simultaneously very small local
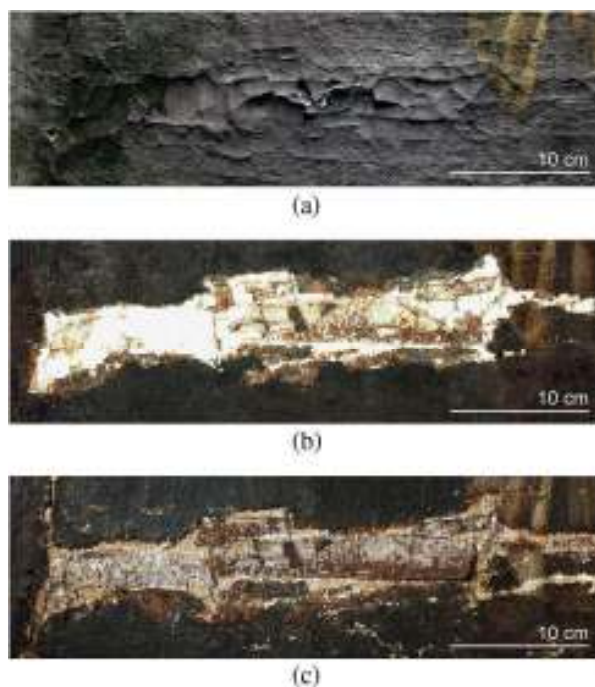
Fig. 2. Fragment of 17th century painting with deformation of the surface: (a) unfitting pattern of deep craquelures, cupping, loss, and delamination of ground and paint layer. Conservation treatment revealed in this spot improper and incompatible repair done in the second-half of 19th century and (b) Thick layer of a rigid gesso (visible after removal of overpainting) and (c) unfitted canvas inserts (visible after removal of secondary gesso) [photo. A. Hadała, M. Zacharska [18]].

94

deformations as well as considerably large global ones over the entire surface and in a wide range.

The full-field 3D measurements of an arbitrary displacement vector of a surface of works of art, which are caused by mechanical or small temperature load, are usually performed with holographic interferometry (HI) and electronic speckle pattern interferometry (ESPI). The comprehensive reviews of these methods when applied to works of art were published by Dulieu-Barton et al. [23] and Tornari [24]. In the case of canvas paintings, interferometric techniques are effective for localizing and identifying local defects and discontinuities of the structure, such as cracks or delamination [17,25–27] rather than for full-field measuring of large-scale, real-time deformations. Therefore, due to a high sensitivity, ESPI was very successfully used in laboratory tests to generate maps of in-plane strain/stress distribution in small tensioned canvas painting samples for assessment of conservation methods for local tear mending [27], lining [28], and system of mounting on a stretcher [17]. The method was improved and 3D ESPI was applied permitting simultaneous in- and out-of-plane measurement [29].

However both techniques, HI and ESPI as interferometric ones, require a highly stable optical setup and a stable environment between the object and the measuring instrument, and thus it is difficult to use them in practice for tests of the environmental response of canvases. In such tests, even small thermal or RH gradients that occur during a change of conditions lead to fluctuations of the refractive index of the air and thus a decrease of signal-to-noise ratio. Placing the object in a transparent environmental chamber does not solve this problem entirely due to unwanted reflections from the glass that severely reduce the field of view that can be measured. Specifically, in the full-field measurements performed with ESPI on canvasses on a stretcher, the size of the object is limited and it works best for in-plane displacements. Additionally, global out-of-plane displacements often exceed the measurement range [29], when calculated versus the first reference image. However, this can be extended with a more complicated processing scheme and sufficient sampling frequency over the time of displacement [30].

The above-mentioned problems inspired the search for alternative image-based methods that would satisfy the requirement of the simultaneous measurement of all displacement components in a relatively broad range (up to a few millimeters) and with usually sufficient accuracy (a few micrometers). Since high-resolution CCD and CMOS detectors became available, DIC appeared to be the method to satisfy these requirements. It has been used successfully for examination of strains in tapestries [31–33]. The DIC method [34] enables noncontact, full-field measurements of displacements, simultaneously in two (2D DIC) [35–37] or three dimensions (3D DIC) [38–40], with an accuracy scalable with the field of measurement. The additional advantages of 3D

DIC, when compared to the interferometric techniques, is an inexpensive and portable hardware setup consisting of two cameras mounted on a rigid frame, an incoherent light source, and a computer. The significant limitation of the DIC method is the necessity to provide a surface of an object with a stochastic texture. The 3D DIC method was applied for investigation of distortions of canvas paintings for the first time in 2011 [41–43]. Tests described in [42,43] showed promising results of using a natural texture of paint layer as a stochastic pattern permitting DIC measurements. In parallel, an experiment focused on measuring displacements of model canvas paintings induced by changes of RH was performed in a climatic chamber. The homogeneity of these specimens covered with an artificial stochastic texture was disturbed by infillings of regular gaps, mended tears, and of patches on the reverse. The aim of the test was to prove the feasibility of 3D DIC for detection of minor defects in the structure of canvas paintings and evaluation of the correctness of different repair methods. In the case described in [41] the modern, polyester-cotton (65%:35%) plain weave canvas commercially primed with acrylic ground was used to limit uncertainties connected with manual preparation of the sample and the out-of-plane distortions limited enough so the direct monitoring of displacements and strains in the area of repairs was possible. However, in the case of tests of specimens on a modern linen canvas, the standard analysis of displacements performed with the DIC method shows that the global out-of-plane movement of the support is so significant that it obscures possible deformations caused by repairs in the canvas structure. Such a situation can also take place in the case of old paintings on linen canvases and wooden stretchers when they lack tautness due to a progressive decrease in tension caused by stress relaxation, repeated environmental stress, and creep [44,45]. To bring out the information on how the repairs influence the out-of-plane displacements, a postprocessing method has to be developed.

In this paper, the specimen and the experimental setup are described in Sections 3 and 4. The results and their interpretation are presented in Section 5. Finally the applicability of the proposed experimental data analysis methodology for planning and supporting of conservation works is discussed in Section 6.

2. Description of 3D DIC

3D DIC is a technique that combines 2D DIC (for in-plane displacement analysis) with stereovision (for 3D shape measurement) [34,46]. 2D DIC measurement consists of the acquisition of a sequence of grayscale images of an object, over a certain area of interest (AOI). One of the images serves as a reference for the others (deformed). The information is extracted from changes of intensity in the images. The reference image is divided into small subsets (subimages). The software searches for the most similar

subset in all other subsequent images, using the maximum zero-mean normalized sum of squared difference function criterion. The algorithm [34] is insensitive to an offset and a scale in lighting. The location of the center point of the most similar subset found in a deformed image defines the displacement vector. In order to facilitate matching, each subset needs to be sufficiently distinct in the aspect of intensity variations. Therefore, a random speckle pattern is applied (e.g., spray paint, sticker paper, water decals) onto the object within the AOI. By using two cameras for observation of the same AOI, it is possible to obtain the 3D shape of the surface of an object and measure out-of plane displacements.

In general, the accuracy of DIC strongly depends on the phase accuracy of the interpolation filter, used to reconstruct gray values at noninteger locations of the images. In order to minimize the phase error of the interpolation filter, cubic B-spline and optimized eight-tap interpolation filters have been chosen for subset matching (using VIC 3D software). According to [34], this approach minimizes errors introduced by the interpolation filters to less than 0.001 pixels. However, it must be pointed out that in real applications, the accuracy of measurements depends also on other sources of errors, such as image noise and stability of experimental condition. The analysis presented in [34] shows that utilization of optimized interpolation algorithms allows one to achieve 0.01 pixel accuracy of image displacements, for images contaminated by Gaussian noise. The papers [47,48] confirm that a variation in DIC measurement results can be limited by isolating DIC setup from vibrations and isolating cameras from temperature variations. In the case of presented measurements, the experimental conditions were carefully controlled to limit the variability of results: the DIC setup was fixed to the optical table (mechanical unstability less than 2 μm) and LED lights were used in order to avoid temperature changes larger than 1°. It is worthwhile to note that the out-of-plane measurement error is larger than the in-plane one and strongly depends on a stereo angle [34,47,48].

As mentioned above, displacements are the quantities obtained directly from DIC. Displacements in the x direction are given as u in [pixels] and after scaling are expressed as U in [mm]; similarly displacements in the y and z direction are given as v [pixels], V [mm], and w [pixels], W [mm], respectively, while testing mechanical properties of artworks along with displacements and strains at the surface of an object should also be considered [12]. Strains (ε_{xx}, ε_{yy}—strains along x and y coordinates) can be calculated from displacements, as described in [34,36]:

$$\varepsilon_{xx} = \frac{\partial u}{\partial x} + \frac{1}{2}\left[\left(\frac{\partial u}{\partial x}\right)^2 + \left(\frac{\partial v}{\partial x}\right)^2\right]$$
$$\varepsilon_{yy} = \frac{\partial v}{\partial y} + \frac{1}{2}\left[\left(\frac{\partial u}{\partial y}\right)^2 + \left(\frac{\partial v}{\partial y}\right)^2\right]. \quad (1)$$

For strain analysis, Vic-3D 2009 software [49] was used. From available tensor types [Lagrange, Hencky (Logarithmic), Euler-Almansi, Logarithmic Euler-Almansi [50]], the Lagrangian finite strain tensor was chosen, since the velocity and displacement fields of the object have been determined and numerically differentiated in space, at each point of view [34].

3. Model Canvas Painting

As described in the Section 1, the main goal of the described work was to evaluate the possibility of extracting detailed data on small local displacements from strongly dominating global deformation of the canvas. Thus, the specimen chosen to demonstrate the developed postprocessing method (Fig. 3) was made of a new, unbleached, fine plain-weave linen canvas, which was showing considerably little dimensional stability when dampened, despite prior washing and shrinking in boiling water.

To imitate the common construction of a canvas painting, the textile support was stretched over a rectangular keyed pinewood stretcher with a hand tension. To minimize the creep effect, the weft of the canvas was in a vertical direction. The size of the model −40 cm wide and 30 cm high—was limited by the dimensions of climatic chamber used for the experiment. A cold 10% water solution of hide glue was used as a size and then an emulsive gesso [comprising chalk, methylcellulose (MC), polyvinyl alcohol (PVA) with plasticizers: Venetian turpentine and dammar in oil of turpentine] was applied as a ground layer. This formula has been used and tested for the past 35 years [51] at the Department of
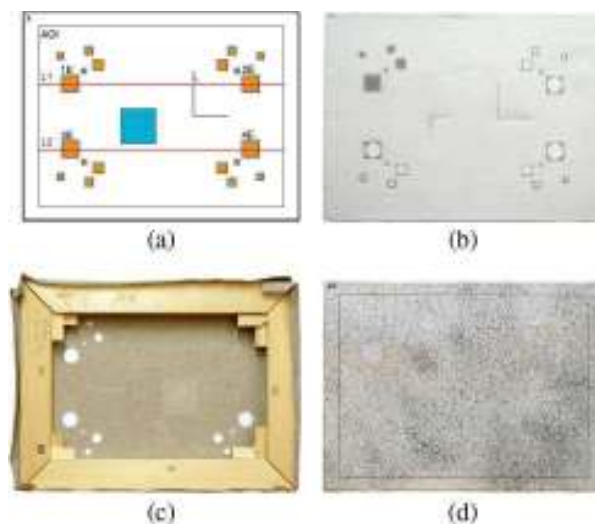

Fig. 3. Specimen used in experiment. (a) Template of the model painting (orange—fillings in canvas, grey—fillings in ground layer, blue—a patch adhered to the reverse of canvas, red—position of cross-sections analyzed in Fig. 7). (b) Face of the specimen during preparation with repaired defects in canvas support. (c) Backside of the specimen with repairs of the canvas visible. (d) Face of specimen with unified ground layer and a random speckle pattern sprayed on the surface.

96

Conservation of Painting and Polychrome Sculpture of Nicholaus Copernicus University as a material for infilling emulsive and oil grounds in canvas paintings. It was chosen as a primer since in conservation practice it could cover tested infillings and surrounding original canvas. To create controlled and easily detectable discontinuities in the structure, four sets of regular circular gaps of various sizes ranging from 4 to 12 mm of diameter were cut out symmetrically through the stencil in all the four corners of the specimen out of a zone protected by the wooden stretcher, according to the prepared template [Fig. 3(a)]. Additionally, two L-shaped cuts were made in the central part of the painting. The cuts were fixed and the sets of gaps were filled in with various traditional and experimental materials [Figs. 3(a) and 3(b)] different in respect of structure and assumed various mechanical properties and dimensional stability. Introducing four different kinds of infilling materials was supposed to permit direct comparison of their possibly different interactions with the structure of specimen. The full description of the materials and methods of conservation treatments is given in Table 1. The surface of the painting was unified with fillings made with the same gesso as used for priming. It was decided to limit the layers of specimen to the canvas and a uniform ground layer to permit visual observation of possible deformation in area of repairs and still to minimize uncertainties in the interpretation of results. To allow image correlation, a random speckle pattern was sprayed onto the face of the specimen with a black ink [Fig. 3(d)] and then secured with two layers of varnish: Neutral Firnis (Schmincke) applied in even layer all over the surface.

4. 3D DIC Setup and Climate Control System

Measurements were performed with the 3D DIC system that comprises two CANON EOS 5D Mark II (5616 × 3774 pixels) cameras equipped with 28 mm CANON lenses, set on an angle of 30° and pointing to the same area (AOI) at the specimen (Fig. 4). Before performing the experiment, the system was calibrated with utilization of the commercial software VIC 3D. Standard deviation of residuals for 22 views of the calibration target and from both cameras was 0.058. Distortions of the 28 mm lenses were included in the calibration process. A combined distortion model in the form of the second-order polynomial (with two distortion coefficients) was used [34]. The setup and the investigated specimen were mounted on an optical table to provide mechanical stability. In order to ensure sufficient lighting, two 100 W LED lamps (8500 lm) equipped with a light diffuser ("soft box") were used. The utilization of LED lamps ensured that the investigated object was not being overheated, which is important from the point of view of preventive conservation practice. The capture of images by both cameras was synchronized and pairs of frames were collected every 20 seconds during 1 h and 38 minutes of the experiment. The field of view (FOV) was 0.6 m × 0.4 m. The analysis of collected data was carried out with the commercial software VIC-3D [49].

The sample was subjected to an environmental stress caused by rapid changes of RH from 21% to 70% (within 57 minutes) and back to 20% (within 41 minutes) in a custom-designed climate control system. It consists of an airtight transparent environmental chamber connected by tubes with a simple manually operated conditioning unit. The unit is equipped with a small fan providing air circulation in the system and a space for placing humidifying and dehumidifying materials. The rise of humidity was achieved by inserting a container of water and a set of air-permeable and water-conducting nonwoven fabrics in the unit. For dehumidification, a set of bags filled with silica gel absorbing moisture was used. The rate of change of humidity was controlled by changing the level of the effective area of input materials and the speed (0.23–0.89 m/s) of an air stream.

The humidity profile was designed according to a measurement (performed by the authors) of climate conditions in historic buildings where transient jumps of RH up to about 10% within 10 minutes were recorded occasionally. The range of humidity was extended over naturally occurring to c. 50% to provide a wide range of conditions in which a large global displacement was expected and in which incompatibility of materials could appear. The temperature was stabilized to a value of 24°C by an air-conditioning

Table 1. Materials and Methods Used for Repairs in the Canvas of a Specimen

Defect Number	Filling in Canvas
1A-1E	Linen-canvas inserts sized with 3% MC butt joined with dispersive adhesive (Osakryl + Winacet DP 50 in ratio 1:1), ironed with a hot spatula (70°C)
2A-2E	Cotton-flax fibrous pulp disintegrated in water and mixed with 3% MC; applied wet into the gaps, sized twice with 20% Akrylkleber 498 HV (Lascaux) and dried on a suction table
3A-3E	Fibrous pulp: dry cellulose fibers Arbocel BC 200 mixed with 3% MC (in ratio 1:5 by volume); applied wet into gaps, dried on a suction table and impregnated twice with cold 20% Beva 371 in white spirit, ironed with a hot spatula (70°C)
4A-4E	Fibrous pulp: dry cellulose fibers Arbocel BC 200 mixed with 3% MC (in ratio 1:5 by volume); applied wet into the gaps, sized twice with 20% Akrylkleber 498 HV (Lascaux) and dried on a suction table
L	Cut butt joined with Polyamide Textile Welding Powder 5060 (Lascaux)
6	Cut butt joined with Polyamide Textile Welding Powder 5060 (Lascaux), reinforced from the backside of the canvas with a square patch of polyester nonwoven Cerex (10 g/m^2) adhered with BEVA 371 of foil

97

system in the laboratory. The temperature and RH inside the chamber were monitored and recorded with a HygroClip S sensor from Rotronic (Switzerland). To enable optical measurements, glass with an antireflective coating [Clear Color Plus (2 mm), Nielsen] was used for the camera facing the chamber wall. The painting (weft of canvas in the vertical direction) was mounted vertically and the coordinate system was assigned to describe the displacements [Figs. 4(a) and 4(b)].

5. Results

From the reference pair of images (captured at the start of the test, at RH: 22.2%) and the sequential pair of images (captured for subsequent RH values), the sets of displacement and strain maps were calculated and linked with humidity data. The sequence of maps was combined into video animations (Media 1). These visualizations are very useful for qualitative inspection and observation of overall deformation.

The shape of reference surface (z axis expanded and false-color-coded) is shown in Fig 5(a). It is worth noting that it shows that already before the experiment the canvas painting was not highly tensioned over the stretcher. Also, a small disturbance of planarity of the surface was recorded, as a result of manual introduction of repairs in canvas and ground layer. For detailed analysis, the displacement and strain maps obtained for the maximum value of RH, i.e., 70,0% (Figs. 5 and 6), will be discussed. The displacement maps (false-color-coded and presented separately for U, V, W displacement components— a key to symbols of displacements and strains is given in Section 2) are shown in a diagonal perspective as seen from Camera 2, superimposed on the b/w photography from this camera (the rare data)— Figs. 5(b)–5(d). In-plane displacements (U, V) registered at 70% RH are caused mostly by expansion of the painting due to a rise in RH, although it cannot be interpreted directly as elongation in weft and warp direction for the sample on the relatively rigid wooden stretcher since they are a component of general three-dimensional deformation [Figs. 5(b)–5(d)]. The inversion of canvas reaction that can take place at higher values of RH in linen canvases sized with animal glue size (usually above 70% RH but sometimes at its lower values [8,14]) was not observed.
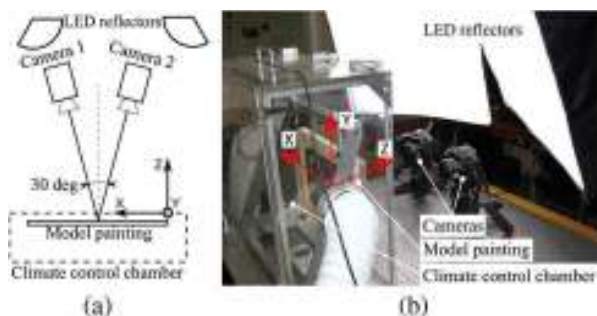

Fig. 4. 3D DIC setup with the model painting and orientation of the coordinate system (a) scheme and (b) view.
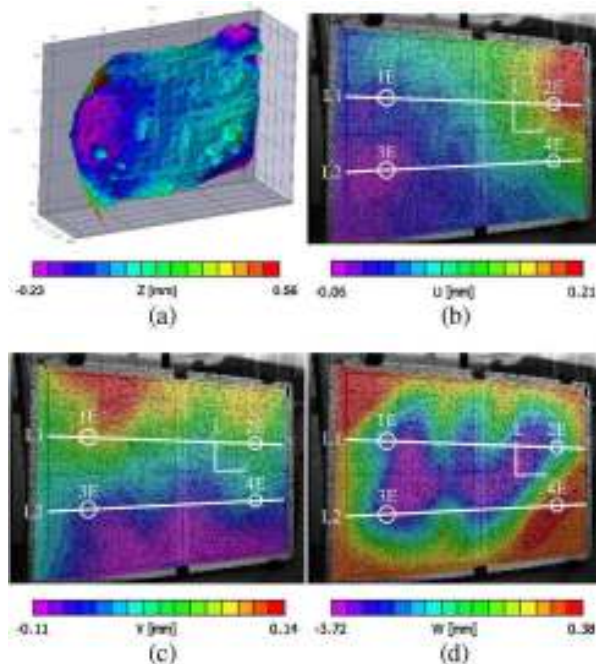

Fig. 5. (a) Shape of reference surface. Displacement maps at maximum (70,0%) RH, (b) U (in x direction), (c) V (in y direction), and (d) W (in z direction); white lines L1 and L2 indicate position of a cross-section analyzed in Fig. 7, also the location of repairs in canvas: 1E, L, 2E, 3E, 4E is marked in white. The sequence of displacements maps and information of RH changes were combined into video animation Media 1.

Expansion of the hygroscopic constituents of the structure resulted in a loss of tension and finally waving and bulging of the canvas support in an out-of-plane direction toward the back of the specimen [Fig. 5(d)]. Low-value negative in-plane displacements (U, V) at the edges of AOI, which were close to the edges of the specimen could also have been caused by expansion (relaxation and/or swelling) of the wooden stretcher but this was not measured independently. Stretching of the specimen at hand tension and uneven keying-out of the stretcher could be the reason for the slightly diagonal orientation of global deformation and some irregularity in
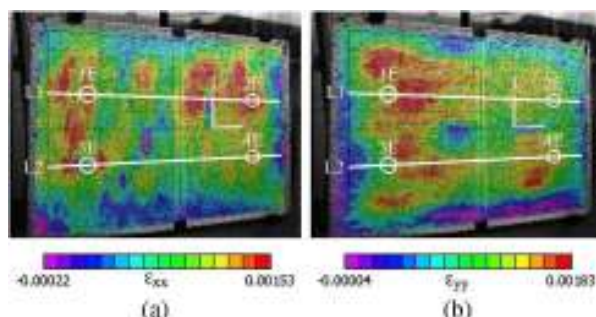

Fig. 6. Strain maps: (a) ε_{xx} and (b) ε_{yy} at maximum (70,0%) RH. White lines L1 and L2 indicate position of a cross-section analyzed in Fig. 7, also the location of repairs in canvas: 1E, L, 2E, 3E, 4E is marked in white.

98

displacements along the individual boarders of the stretcher.

As shown in Fig. 5, the out-of-plane displacement is dominant, and it is an order of magnitude bigger than both in-plane components. It must be noted that on any displacement map there is no clear information how repairs influence the behavior of support. Since the textile was not very tightly tensioned over a keyed wooden stretcher, the global deformation dominates and obscures the local deformation connected with the inserts, mends, and a patch. On the other hand, the strain maps calculated out of u and v in-plane displacement maps (Fig. 6) provide information on the localization of some of the repairs that have an influence on the dimensional response of the canvas painting. Repairs of cuts (L) and inserts in left bottom corner (type 3E) restrain the movement of canvas since strains in these areas (color-coded in violet) are smaller than the surrounding general deformation.

In order to more closely investigate the local behavior of canvas in the areas of repairs, the spatio-temporal maps (Q, t) were generated (Fig. 7). In this case, the analysis at selected profiles [L1 and L2 in Figs. 5(b)–5(d)] of displacements/strains ($Q = U$, V, W, ε_{xx}, ε_{yy}) as a function in time is performed. The profiles L1 and L2 chosen for this analysis cross all the biggest repairs (1E, 2E, 3E, 4E) and one of the cuts (L), where the biggest deformations were expected. As can be seen from Figs. 7(a)–7(c), the noticeable displacements are related to the global movement of canvas starting and increasing rapidly in the upper levels of RH (39% → 70% → 38%). The in-plane strains (ε_{xx}, ε_{yy}) can be calculated using a standard approach [Figs. 7(d) and 7(e)] [34]. Such diagrams visualize development of variations in in-plane strain distribution and are more suitable for indicating inhomogenity in the structure.

It must be noted that the in-plane displacements (U, V) were of an order of magnitude smaller than the observed out-of-plane displacement (W). The range of displacement was between −0.07 and 0.23 mm for direction x (U), −0.12 and 0.14 mm for direction y (V) and between −4.04 and 0.42 mm for direction z (W). For conservation-restoration purposes and full evaluation of materials used for repairs in the canvas, it is crucial to get information about the influence of inserts on the out-of-plane deformation of the surface of the painting. However the strain ε_{zz} cannot be calculated, as there is no physical meaning of differentiation of W in z direction, since the object surface is a shell projected on x–y plane, without neighborhood in z direction [36].

Therefore, it can be assumed that local W displacements are spatially much smaller than the global out-of-plane deformation, so they have different (higher) spatial frequency characteristics. Such an assumption is fully justified in the case when the repairs are much smaller than the entire AIO. In such a case, it is possible to filter local disturbances using a low pass filter applied in an image or frequency
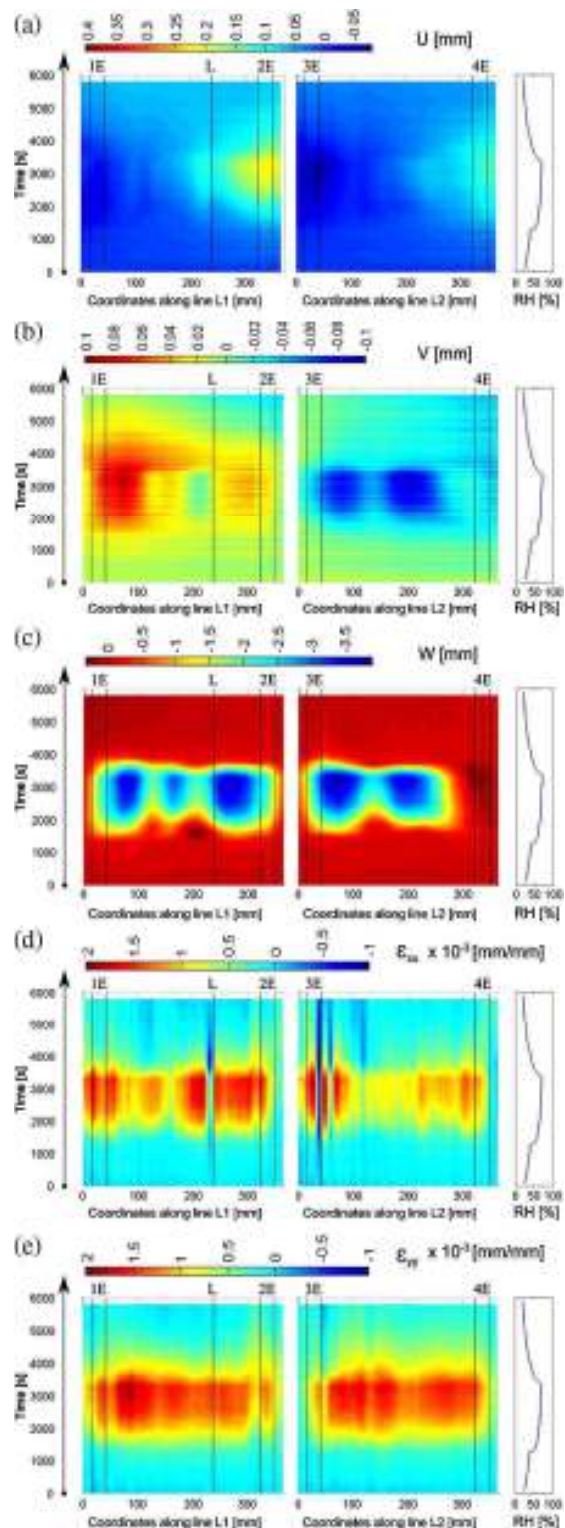

Fig. 7. Displacements and strains at points along lines L1 and L2 shown as a function of time, (a) displacements U (in x direction), (b) displacements V (in y direction), (c) displacements W (in z direction), (d) strains ε_{xx} (in x direction), and (e) strains ε_{yy} (in y direction). Corresponding changes in RH are given for reference, the location of repairs in canvas: 1E, L, 2E, 3E, 4E is marked as black lines.
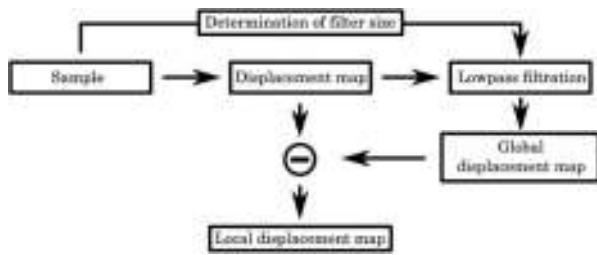
Fig. 8. Scheme of the method for obtaining a local displacement map.

plane [52,53]. This operation will deliver an approximate global displacement map, which can later be subtracted from the original displacement map W, yielding the local displacement map (W') as shown in Fig. 8.

An average filter that produces the largest edge blurring [52,53] is used as the low pass filter in the procedure shown in Fig 8. The size of the filter depends on the sizes of repairs. In this experiment, the repair sizes were similar, so the filter size was constant over the full field of view. In the case of big differences in sizes of repairs, the size of the filter should be locally adapted according to prior knowledge about an object. The best results were obtained with the filtration mask of 23 × 23 [points of a displacement map]. It must be noted that the points of a displacement map are not equivalent to pixels in the analyzed images, but they are centers of the subsets (separated here by 9 pixels in the x and y directions). The procedure was performed for all W displacement maps using the Matlab commercial software package. The final local displacement map calculated from the map given in Fig. 5(d) is shown in Fig. 9.

This visualization reveals deformations associated with repairs and also with large-scale bulges of the canvas formed as a response of the canvas to changes in climate conditions. The influence of inserts in canvas on out-of-plane deformation of the surface of specimen can also be evaluated on the basis of the local displacement along lines L1 and L2 shown as a function of time in Fig. 10.
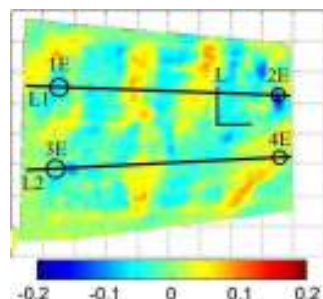

Fig. 9. Local displacement map W' (in z direction) at maximum (70,0%) RH, with black lines L1 and L2 indicate position of a cross-section analyzed in Fig. 10, also the location of repairs in canvas: 1E, L, 2E, 3E, 4E is marked in black.
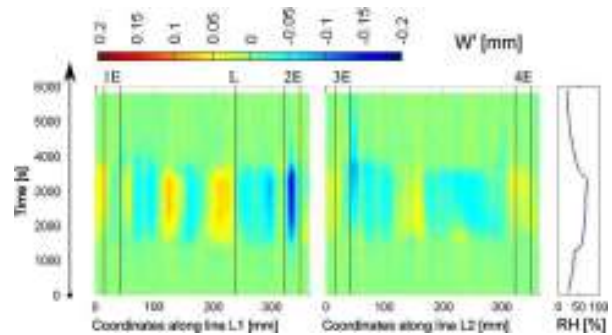

Fig. 10. Local displacements W' (in z direction) along lines L1 and L2 show as a function of time. Corresponding changes in RH are provided for reference, the location of repairs in canvas: 1E, L, 2E, 3E, 4E is marked as black lines.

6. Interpretation of the Results

The analysis of deformations (which coincide with the location of the repair in the canvas) may be used to validate the data processing described in this contribution. Inspection of graphs in Fig. 7 compared to respective ones in Figs. 9 and 10 leads to the conclusion that some defects, not detectable by usual analysis of displacements (U, V, W), are seen in strain (ε_{xx}) analysis, and furthermore the defect (2E) not detectable by strain analysis is clearly visible when the local displacement (W') is considered. The details are given in Table 2. A plus sign has been placed in the table to mark evident correlation between respective graphs and distortions introduced to the canvas structure.

To demonstrate how the presented approach may be used for the analysis, important for the conservation-restoration practice, the exemplary interpretation of the results obtained with the 3D DIC method is given below. The results presented here belong to a broader research on the feasibility of various techniques of tear mending and gap filling. From the results summarized in Table 2, it can be concluded that the inserts 1E (traditional canvas insert—Table 1) and 4E (fibrous pulp insert made of Arbocel 200 and 3%MC, impregnated with 20% Akrylkleber 498 HV) reacted to environmental changes similarly to the original structure of this particular canvas painting—in Figs. 7(a)–7(e) and 10 there is no significant reaction visible. The infilling

Table 2. Qualification of the Influence of Particular Repairs in Canvas Support on Deformation of the Surface of the Painting According to Displacements (U, V, W), Strains (ε_{xx}, ε_{yy}), and Local Out-of-Plane Displacements (W') (+, Distinct Deformation; –, Neutral Deformation)

	1E	L	2E	3E	4E
U	–	+	+	–	–
V	–	+	–	–	–
W	–	–	–	–	–
ε_{xx}	–	+	–	+	–
ε_{yy}	–	–	–	–	–
W'	–	+	+	+	–

100

pulp of repair 2E, varying from 4E just by the type of fibers, in high levels of RH reacted differently than the painting. Temporal deformation of 2E is visible just on the map W' (Fig. 10) where it is more concave at high RH than any other place along the cross-section L1 or L2 (hence just $\approx 0,15$ mm different from surrounding). This could mean that it swells more from the backside that is not covered by gesso. It is still comparably flexible since differences in strains ε_{xx} and ε_{yy} [Figs. 7(d) and 7(e)] are not distinct. On the contrary, the joint of cut L and the insert 3E are detectable particularly at maps of strains ε_{xx} [Fig. 7(d)]. Almost constant and permanent low level of strain at the edge of 3E infilling (dark blue line on the map) can indicate a development of the crack on the right side of insert 3E during the experiment. The sharp border in this place on the map of local displacements W' (Fig. 10), and the difference between the area of the insert and the painting in the end of test at the map ε_{yy} [Fig. 7(e)] seem to confirm this hypothesis. The appearance of the crack can be caused by an incompatibility of the insert or damage of the joint that happened during execution of repair. The joint of cut L made of nonhygroscopic Polyamid Welding Powder is reacting less than the surrounding area of canvas painting [strain maps ε_{xx} at Figs. 6(a) and 7(d)] and its vicinity has a tendency to temporal out-of-plane deformation at high RH levels (Fig. 10).

It is worth mentioning that the proposed analysis of strains and local displacements enabled visualization of deformations that are not visible by the naked eye but indicate the possible danger of development of serious damage or deformation of the surface of the painting in the future. For the purpose of evaluation of different materials for infilling voids in canvas, a further more detailed quantitative analysis of behavior of all kinds and sizes of the repairs localized precisely could be carried out, thanks to the template of specimen (described in Section 3).

7. Conclusions and Future Works

In this paper, the test of applicability of the 3D DIC method for evaluation of restoration treatments for canvas paintings was presented. It delivers quantitative data on displacements and strains appearing in paintings in response to certain changes of the surrounding climate. The presented methodology can support a choice of materials and methods in art conservation.

The proposed modification of data processing in 3D DIC allows the detection of local out-of-plane displacements resulting from conservation treatments even in the presence of significant global displacements of an object. The filtering procedure is simple, time effective, and provides results with accuracy sufficient in most of the cases to recognize the quality of repairs. However in order to serve as an arbitrary tool for evaluation of repairs in composite materials, further work on the filtering algorithm should be conducted in order to provide full adaptivity to the

sizes and shapes of the local repairs. The presented methodology, due to proper implementation of local out-of-plane displacement information, supports effectively the analysis based on ε_{xx} and ε_{yy} strain maps. Also, the proposed spatiotemporal visualization of load displacement/strain changes seems to be an excellent tool for future monitoring of canvas paintings and other composite materials behavior, due to environmental changes.

It is worthwhile to note that in the presented laboratory study, the approach common for the experimental mechanics to apply the stochastic texture by putting additional materials on a surface of the investigated object was used. In the case of actual artworks, this kind of treatment, even with the use of inert and theoretically reversible materials, would be in contradiction to the principle of minimum necessary interference with the original structure. Therefore, in future experiments on original canvas paintings, only the natural texture can be considered as a source of correlation data, provided that the features on a painting have sufficient local contrast so that a subset size can be identified, which can be accurately matched across the image. Some painting surfaces, such as the impressionistic technique with a vibrant texture of optically mixing relatively small, thin, yet visible brush strokes of different colors can prove to fulfill this requirement. Also distinct brush strokes, craquelure pattern, uneven texture of canvas, together with discoloration, dirt deposits, etc., can improve the stochastic pattern of the natural painting surface. The preliminary results [42,43] obtained with selected pictures from the Nicolaus Copernicus University Museum, hold the promise of at least limited applicability of the DIC method to real canvas paintings. The proposed methodology, when linked with analysis of materials and structure of particular objects, could be used to broaden the general knowledge on properties, processes, and phenomena relevant to canvas paintings.

References

1. B. J. Rouba, *Podobrazia płócienne w procesie konserwacji [Textile Painting Supports in the Process of Conservation]* (Wydawnictwo UMK, 2000).
2. M. F. Mecklenburg, "Micro climates and moisture induced damage to paintings," in *Contributions to the Copenhagen Conference Museum Microclimates*, T. Padfield and K. Borchersen, eds. (National Museum of Denmark, 2007), pp. 19–25.
3. A. von Reden, "Uncertainties in the interaction between a canvas painting support and moisture," in *Climate for Collections. Standards and Uncertainties, Postprints of the Munich Climate Conference*, J. Ashley-Smith, A. Burmester, and M. Eibl, eds. (Doerner Institute, 2013), pp. 248–256.
4. B. J. Rouba, "Płótna jako podobrazia malarskie [Canvases as Painting Supports]," Ochrona Zabytków **1985**, 222–244 (1985).

5. M. F. Mecklenburg, *Meccanismi di cedimento nei dipinti su tela: approcci per lo sviluppo di protocolli di consolidamento. Failure Mechanisms in Canvas Supported Paintings: Approaches for Developing Consolidation Protocol* (Il prato, 2007).

6. G. Hedley, "Relative humidity and stress strain response of canvas paintings: uniaxial measurements of naturally aged samples," Stud. Conserv. **33**, 133–148 (1988).

7. J. D. Carr, C. R. T. Young, A. Phenix, and R. D. Hibberd, "Development of a physical model of a typical 19th century English canvas painting," Stud. Conserv. **48**, 145–154 (2003).

8. C. Young and P. Ackroyd, "The mechanical behaviour and environmental response of paintings to three types of lining treatment," National Gallery Technical Bulletin **22**, 85–104 (2001).

9. L. Carlyle and C. R. T. Young, "The mechanical response of flour paste grounds," in *Preparation for Painting*, J. Townsend, T. Doherty, G. Heydenreich, and J. Ridge, eds. (Archetype Books, 2008), pp. 123–131.

10. B. Rouba, *Budowa techniczna obrazów XIX-wiecznych malowanych na handlowych podobraziach płóciennych i problematyka ich konserwacji [Technical Structure of 19th c. Paintings on Commercially Prepared Canvas Supports and Issues Concerning Their Conservation]* (UMK-rozprawy, 1988).

11. P. Ackroyd and C. R. T. Young, "Preparation of artist's canvases: factors that affect adhesion between ground and canvas," in *Preprints of the 12th Triennial Meeting*, J. Bridgland and J. Brown, eds. (ICOM Committee for Conservation, James and James, 1999), pp. 265–270.

12. B. J. Rouba, "Die Leinwandstrukturanalyse und ihre Anwendung für die Gemäldekonservierung [The analysis of canvas structures and its application in paintings conservation]," Restauratorenblätter **13**, 79–89 (1992).

13. C. R. T. Young and R. Hibberd, "Biaxial tensile testing of paintings on canvas," Stud. Conserv. **44**, 129–141 (1999).

14. C. R. T. Young, "History of fabric supports," in *Conservation of Easel Paintings*, J. Hill Stoner and R. Rushfield, eds. (Routledge, 2012), pp. 116–133, 137–147.

15. S. Michalski, "Paintings —their response to temperature, RH, shock and vibration," in *Art in Transit: Studies in the Transport of Paintings*, M. Mecklenburg, ed. (National Gallery of Art, 1991), pp. 223–248.

16. J. Colville, W. Kilpatrick, and M. M. Mecklenburg, "A finite element analysis of multi-layered orthotropic membranes with application to oil paintings on fabric," in *Science and Technology in the Service of Conservation. Preprints of the Contributions to the Washington Congress* (International Institute for Conservation, 1982), pp. 146–150.

17. C. R. T. Young and R. Hibberd, "The role of attachments in the degradation and strain distribution of canvas paintings," in *Tradition and innovation: Advances in Conservation, Contributions to the IIC Melbourne Congress*, A. Roy and P. Smith, ed. (IIC, 2000), pp. 212–220.

18. A. Hadała and M. Zacharska, Adoration of the Shepherds. Documentation of Conservation-Restoration Treatment, unpublished report on diploma work supervised by B. J. Rouba, E. Szmit-Naud, K. Szczepińska, T. Łękawa-Wysłouch, and L. Tymińska-Widmer, No 1283 (Department of Conservation and Restoration of Paintings and Polychrome Sculpture Nicolaus Copernicus University, 2009).

19. J. M. Dulieu-Barton, C.-C. Ye, A. R. Chambers, F. L. Lennard, and D. E. Eastop, "Optical fibre sensors for monitoring damage in historic tapestries," in *SEM XI International Congress on Experimental and Applied Mechanics* (Society for Experimental Mechanics, 2008), p. 8.

20. W. Zawadzki, M. Bartosik, K. Dzierżga, Ł. Bratasz, M. Łukomski, and E. Peacock, "Application of fiber Bragg gratings for strain measurement in historic textiles and paintings on canvas," Optica Applicata **42**, 503–517 (2012).

21. C. C. Ye, J. M. Dulieu-Barton, D. J. Webb, C. Zhang, G.-D. Peng, A. R. Chambers, F. J. Lennard, and D. D. Eastop, "Applications of polymer optical fibre grating sensors to condition monitoring of textiles," Proc. SPIE **7503**, 75030M (2009).

22. P. Targowski, M. Góra, T. Bajraszewski, M. Szkulmowski, B. Rouba, T. Łękawa-Wysłouch, and L. Tymińska, "Optical coherence tomography for tracking canvas deformation," Laser Chem. **93658**, 1–8 (2006), http://www.hindawi.com/archive/2006/093658/abs/.

23. J. M. Dulieu-Barton, L. Dokos, D. Eastop, F. Lennard, A. R. Chambers, and M. Sahin, "Deformation and strain measurement techniques for the inspection of damage in works of art," Rev. Conserv. **6**, 63–73 (2005).

24. V. Tornari, "Laser interference-based techniques and applications in structural inspection of works of art," Anal. Bioanal. Chem. **387**, 761–780 (2007).

25. E. Tsiranidou, E. Bernikola, V. Tornari, T. Fankhauser, M. Läuchli, C. Palmbach, and N. Bäschlin, "Preliminary investigation on monitoring transportation effects by full field methods: a digital holographic speckle pattern interferometry study on canvas paintings," Proc. SPIE **8084**, 80840J (2011).

26. E. Tsiranidou, E. Bernikola, V. Tornari, T. Fankhauser, M. Läuchli, N. Bäschlin, and C. Palmbach, "Studying transportation effects on canvas paintings by full field digital holographic techniques," in *Lasers in the Conservation of Artworks IX*, D. Saunders, M. Strlic, C. Korenberg, N. Luxford, and K. Birkhölzer, eds. (Archetype, 2013), pp. 67–74.

27. C. Young, "The mechanical requirements of tear mends," in *Alternatives to Lining, BAPCR & UCIK Conference* (Archetype, 2003), pp. 55–58.

28. C. Young, R. Hibberd, and P. Ackroyd, "An investigation into the adhesive bond and transfer of tension in lined canvas paintings," in *Proceedings of the 13th Triennial Meeting of the ICOM Committee for Conservation* (ICOM-CC, Rio de Janeiro, 2002), pp. 370–378.

29. C. Young, "The application of 3D electronic speckle pattern interferometry (ESPI) for the structural analysis of paintings on canvas," in *Lasers in the Conservation of Artworks IX*, D. Saunders, M. Strlic, C. Korenberg, N. Luxford, and K. Birkhölzer, eds. (Archetype, 2013), pp. 108–115.

30. N. K. Mohan and P. Rastogi, "Recent developments in digital speckle pattern interferometry," Opt. Lasers Eng. **40**, 439–445 (2003).

31. D. Khennouf, J. M. Dulieu-Barton, A. R. Chambers, F. J. Lennard, and D. Eastop, "Assessing the feasibility of monitoring strain in historical tapestries using digital image correlation," Strain **46**, 19–32 (2010).

32. J. M. Dulieu-Barton, D. Khennouf, A. R. Chambers, F. Lennard, and D. Eastop, "Long term condition monitoring of tapestries using image correlation," in *Proceedings of the SEM Annual Conference* (Society for Experimental Mechanics, 2010).

33. F. Lennard, D. Eastop, J. Dulieu-Barton, A. Chambers, D. Khennouf, C. C. Ye, and H. Williams, "Strain monitoring of tapestries: results of a three-year research project," in *Preprints of ICOM-CC 16th Triennial Conference* (Critério, 2011), pp. 1–8.

34. M. Sutton, J.-J. Orteu, and H. Schreier, *Image Correlation for Shape, Motion and Deformation Measurements. Basic Concepts, Theory and Applications* (Springer, 2009).

35. M. A. Sutton, W. J. Wolters, W. H. Peters, W. F. Ranson, and S. R. McNeill, "Determination of displacements using an improved digital correlation method," Image Vis. Comput. **1**, 133–139 (1983).

36. T. C. Chu, W. F. Ranson, M. A. Sutton, and W. H. Peters, "Applications of digital-image-correlation techniques to experimental mechanics," Exp. Mech. **25**, 232–244 (1985).

37. B. Pan, K. Qian, H. Xie, and A. Asundi, "Two-dimensional digital image correlation for in-plane displacement and strain measurement: a review," Meas. Sci. Technol. **20**, 062001 (2009).

38. P. F. Luo, Y. J. Chao, M. A. Sutton, and W. H. Peters III, "Accurate measurement of three dimensional deformations in deformable and rigid bodies using computer vision," Exp. Mech. **33**, 123–132 (1993).

39. P. F. Luo, Y. J. Chao, and M. A. Sutton, "Application of stereo vision to 3-d deformation analysis in fracture mechanics," Opt. Eng. **33**, 981–990 (1994).

102

40. J. D. Helm, S. R. McNeill, and M. A. Sutton, "Improved 3-D image correlation for surface displacement measurement," Opt. Eng. **35**, 1911–1920 (1996).
41. M. Malesa, K. Malowany, L. Tymińska-Widmer, E. A. Kwiatkowska, M. Kujawińska, B. J. Rouba, and P. Targowski, "Application of digital image correlation (DIC) for tracking deformations of paintings on canvas," Proc. SPIE **8084**, 80840L (2011).
42. M. Kujawinska, M. Malesa, K. Malowany, A. Piekarczuk, L. Tymińska-Widmer, and P. Targowski, "Digital image correlation method: a versatile tool for engineering and art structures investigations," Proc. SPIE **8011**, 80119R (2011).
43. L. Tyminska-Widmer, K. Malowany, M. Malesa, B. J. Rouba, M. Kujawińska, and P. Targowski, "Digital image correlation (DIC) as a novel tool for monitoring response of canvas paintings to variations in environmental conditions," in *Book of Abstracts, Indoor Air Quality, 10th International Conference Indoor Air Quality in Heritage and Historic Environments "Standards and Guidelines"* (UCL Centre for Sustainable Heritage, 2012), p. 110. http://www.ucl.ac.uk/iaq2012/documents/IAQ2012_Book_of_Abstracts_on-line.pdf.
44. A. I. Idelson, "About the choice of tension for canvas paintings," CeROArt, 4 | 2009: Les dilemmes de la restauration, Un choix et des valeurs; http://ceroart.revues.org/1269?lang=en#tocto1n2 (2013).
45. G. A. Berger and W. H. Russell, *Conservation of Paintings. Research and Innovations* (Archetype, 2000), p. 255.
46. J.-J. Orteu, "3-D computer vision in experimental mechanics," Opt. Lasers Eng. **47**, 282–291 (2009).
47. Y.-Q. Wang, M. A. Sutton, X.-D. Ke, and H. W. Schreier, "Error propagation in stereo vision: part i: theoretical developments," Exp. Mech. **51**, 405–422 (2011).
48. X.-D. Ke, H. W. Schreier, M. A. Sutton, and Y.-Q. Wang, "Error propagation in stereo vision: part ii: experimental validation," Exp. Mech. **51**, 423–441 (2011).
49. www.correlatedsolutions.com.
50. http://correlatedsolutions.com/support/index.php?_m=knowledgebase&_a=viewarticle&kbarticleid=2.
51. T. Łękawa-Wysłouch, "Badania materiałów stosowanych do uzupełniania ubytków zapraw w malowidłach na płótnie [Research on the materials used for reintegration of the injuries of priming in paintings on canvas]," AUNC Zabytkoznawstwo i Konserwatorstwo **38**, 187–282 (2010).
52. A. R. Weeks, *Fundamentals of Electronic Image Processing* (SPIE, 1996).
53. J. C. Russ, *The Image Processing Handbook*, 5th ed. (CRC Press, 2007).

103

Stability and bearing capacity of arch-shaped corrugated shell elements: experimental and numerical study

A. PIEKARCZUK[1*], K. MALOWANY[2], P. WIĘCH[1], M. KUJAWIŃSKA[2], and P. SULIK[1]

[1] Building Research Institute, 1 Filtrowa St., 00-611 Warsaw, Poland
[2] Institute of Micromechanics and Photonics, Warsaw University of Technology, 8 Św. A. Boboli St., 02-525 Warsaw, Poland

Abstract. The paper presents problems related to the numerical modeling of profiled steel sheets used as self-supporting arch structures for roof covering. The rules of preparing and full analysis of a set of numerical models of these elements with a different level of complexity are given. The models are evaluated by comparing numerical results with the results of extended experimental tests performed by 3D Digital Image Correlation (DIC) method. For each model the comparison of numerical and experimental results has been made for samples of a single-wave trapezoidal profile with corrugated web and lower flanges subjected to compression and bending. The full-field analysis allows to determine the allowed simplification of numerical models which do not affect in significant way the reliability of the results. The proposed methodology is the first step in the development of full assessment methodology for different types of self-supporting arch structures produced by ABM technology.

Key words: ABM technology, arch-shaped corrugated steel structure, FEM model, digital image correlation, data processing.

1. Introduction

Self supporting arch structures made of steel sheets were initially adopted as temporary agricultural and military structures, usually erected in countries with climate that exclude or limit in significant way load caused by wind and snow in winter season. They gained significant popularity in these applications, mainly because of low cost and short time of erection in comparison with traditional steel, timber or reinforced concrete structures. Nowadays this type of structers is increasingly often adopted as public facilities in middle and eastern European countries. The components of these structures are manufactured directly on building site using mobile production unit. First, single-wave trapezoidal profile is cold-shaped from a 0.7–1.5 mm thick coiled steel sheet (Fig. 1, stage 1). After that, the curvature of a desired radius (from 6 to 30 m) is obtained by means of appropriate corrugation of profile (Fig. 1, stage 2). The ABM 240 (Automatic Building Machine) system [1] creates profile with characteristic corrugation on web and lower flanges. The profiles are connected to each other by means of cold pressing of seams situated at the edges of upper flanges.

The considered structures are of simply supported circular arch type, subjected to dead, technological [3] and environmental loads (the latter consists of snow [4] and wind [5] action). These loads induce in the cross-section of a profile internal forces such as compression, bending and shearing. As the considered structure due to the thickness and slenderness of its web and flanges falls into the 4-th category of cross-section acc. to EN 1993-1-1 [6] standard, the structural failure is triggered with local buckling of profiles walls. Additionally, due to the compressive forces, global loss of stability of whole arch also has to be taken into account.
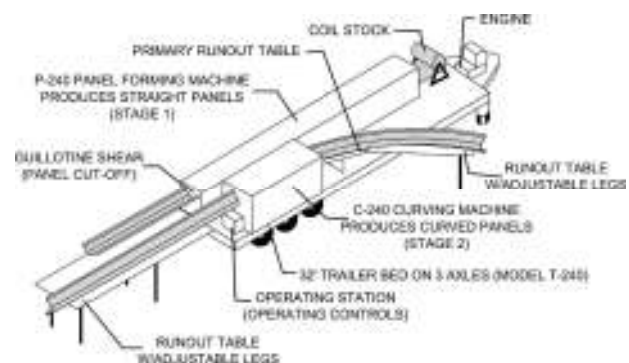

Fig. 1. The scheme of the process of cold shaping of a single profile performed at ABM 240 system (Ref. 2)

The bases for the design of the thin-walled self supporting structures are given in EN 1993-1-3 [7] and PN-B-03207:2002 [8] standards. The general rules for calculations of stability and load carrying capacity are covered by these documents. The author of the work [9] gives valuable advises concerning the application of [7] and [8] standards in engineering practice. He also stresses the importance of taking into account geometrical and physical nonlinearities and suggests that numerical analysis could be the efficient solution to this problem. However due to the corrugation of profile walls these methods prove to be insufficient and leading to overestimation of both its stiffness and ultimate load. The other reliable methods of design of such structures are also non-existent at the moment.

The influence of corrugation depth and radius of curvature of profiles on their mechanical properties has been discussed in [1, 11]. The shape of cross section investigated in [11] varies from the one considered in our paper, but the analysis of the results obtained from numerical calculations and

*e-mail: a.piekarczuk@itb.pl

113

standard [10] gives the valuable insight into the limitations of the latter. It showed satisfying correlation for plain-walled profile; however that was not a case for a curved profile with corrugated wall. This confirms the limitations of standard [10] design method in the case of considered structures.

The mode of local stability loss of corrugated profiles subjected to axial and eccentric compression loads had been investigated in paper [12]. The results of numerical calculations and experimental tests had been compared and they showed discrepancies in critical load value ranging from 8% to 24%. However in this work the axial and compression stiffness of tested profiles had not been taken into account.

The initial works concerning stability and load carrying capacity of self-supporting arch structures made of profiled steel sheets have been also made in Building Research Institute. The test of a full scale model of arch consisting of 4 trapezoid profiles of 12 m span and 6 m radius and its numerical evaluation was a subject of paper [13]. The simplified distribution of internal forces assumed in this paper (simulating a uniform snow load) is shown in Fig. 2. The variability of direction of bending moment and its ratio to compressive load across the arch span is clearly visible. The failure mode of the structure consists of local buckling and loss of load carrying capacity as well as global loss of an arch stability. The exact order of occurrence of these incidents depends on many factors such as the arch curvature, its slenderness, cross-section geometry, mechanical properties of utilized material, load distribution etc. According to EN 1993-1-1 [6] slenderness of cross section walls corresponds to the 4th class section. In such case it is assumed that if load level corresponding to local buckling of cross-section walls is approached the effective width of the walls is reduced. As a result the neutral axis is shifted, bending and axial stiffness reduced and consequently load distribution affected. These factors result in the emergence of local instability. The compressive loads simultaneously cause the global buckling of whole arch structure.
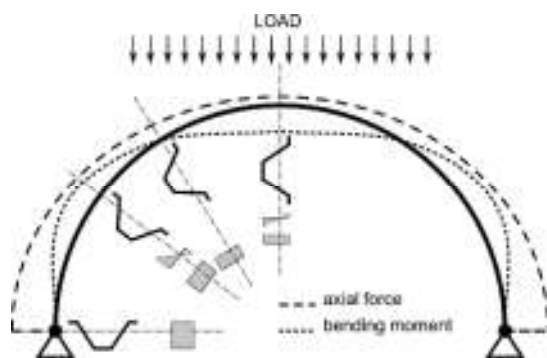

Fig. 2. Simplified distribution of internal loads

During the tests significant nonlinear behavior of the structure had been observed. For experimental tests 3D Digital Image Correlation method had been applied and it has been proved that it is well suited and extremely helpful to perform full field monitoring and measurement of displacement maps during experiments. The comparison of the results obtained from calculation and experiment showed that the mode of global loss of stability is significantly influenced by local buckling. It was also shown that the failure occurs in sudden manner and is not signaled with significant increase in an arch displacement. The applied numerical model has been assumed as being capable of only coarse estimation of an ultimate load and insufficient for displacement calculation.

This was mainly caused by the corrugations and waves occurring in the profiles produced by ABM 240 system, which make code calculation methods largely inadequate. Satisfying analytical models of such structures are currently unavailable, while the existing ones do not describethe mechanism of local loss of stability in sufficient way.In the structural analysis identification of an actual failure mechanism is of uttermost importance. The interpretation of full-scale tests is difficult due to the insufficient control of applied load, problems with prediction of failure location and resulting limitations to quality of measurements. The coexistence of global buckling phenomena further impairs usefulness of such tests results. All these facts provide motivation to perform systematic studies of the problem starting from analysis of a test specimen consisting of a profile section of a limited length which can be considered as sufficient for the purpose of investigation of load carrying capacity and local buckling of profile. Such a specimen can be subjected to load acting with known eccentricity in an attempt to simulate interaction between axial load and bending moment that occurs in an arch structure. The short length of the specimen allows observation of failure mode on a limited area and suppress global buckling influence. Based on the previous positive experience [12] the 3D DIC method has been applied for the purpose of measurement of displacement and strain fields. Obtained data are intended to be used for the purpose of validation of an arch section numerical model. The finally chosen numerical model would be used for prediction of failure mode, ultimate load and stiffness of an arch section and it is going to be applied for analysis of sections with various curvature radius, sheet thickness, load eccentricity. Thus, the numerical models would substitute experimental tests greatly decreasing their number and form a basis for the evaluation of the entire range of products.

In the paper we at first present the methodology of the laboratory tests including the description of samples, loading conditions and 3D Digital Image Correlation method. Next three numerical models of the loaded sample with different level of its simplification are introduced and the results of stress and displacement calculations are compared. Finally the numerical results obtained for different FEM models are compared with point-wise and full-field experimental results in order to gain more knowledge and verify numerical models.

2. Experimental methodology

2.1. Test sample. The tests have been performed with 1.0 m long sample of a profile of 18 m curvature radius (Fig. 3). The relatively short sample was chosen to exclude the influence of global loss of stability. The sample has been made of S355

grade steel sheet of 1.4 mm nominal thickness. Initial location of the neutral axis X and Y has been calculated without taking into account the influence of corrugation of profile walls. Take a note that the actual neutral axis Y is shifted in the direction of upper flange. The actual dimensions of the sample have been included in Table 1. The meanings of symbols used in the table are explained in Fig. 3.
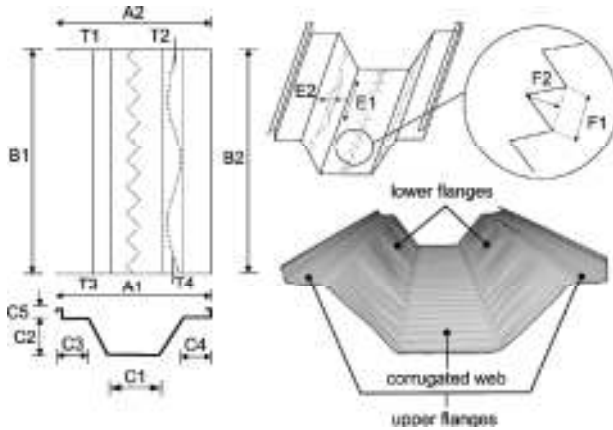

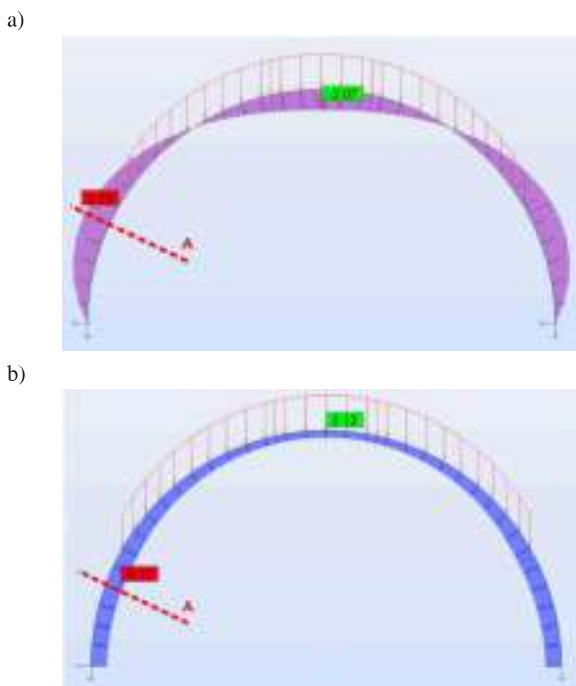Fig. 3. The sample view and explanation of the symbols used in Table 1

a)

b)

Fig. 4. Example diagrams of the internal forces:a) bending moment and b)axial force

The load system selected for the experiments enables simultaneous compression and bending section. A set of loads causes compressive stress in the web section. Such a system guarantees an extreme load stress at the most vulnerable to loss of stability site. Figure 4 shows the diagrams of bending moment and axial force resulting from linear snow load. The dashed line represents the greatest place bending moments and longitudinal forces.

In the section A bending causes compression of the web in municipal occurrence corrugating, additionally there is a compressive force directed along the longitudinal axis. To capture a clear effect of the local loss of stability, it is assumed that the axial force acts on the eccentricity $e = 105$ mm which corresponds to the position of force compression on the web corrugated profile.

The load scheme and location of the sample at the loading rig is shown in Fig. 5.
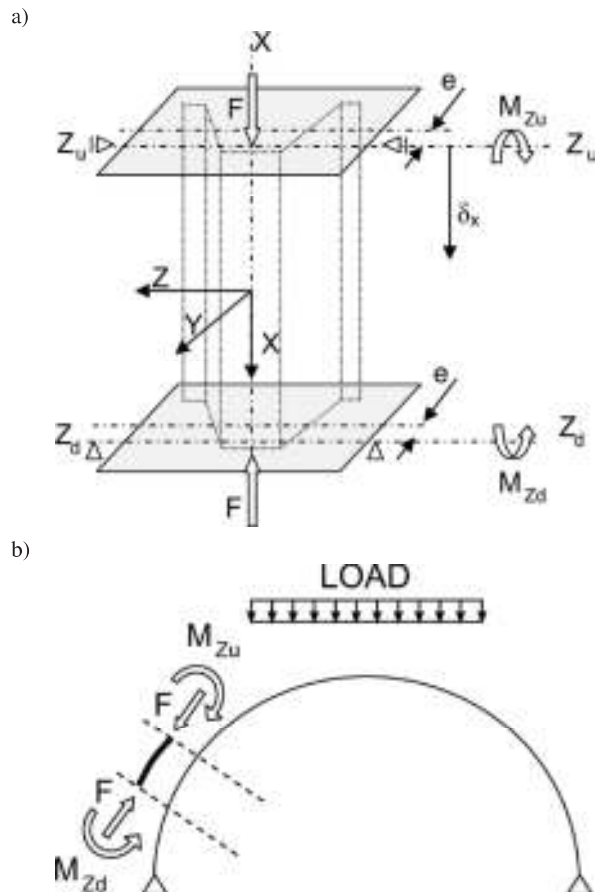
a)

b)

Fig. 5. Diagram of the support and load: a) the terms and conditions of load and support research, b) representation conditions

Table 1
Actual dimensions of the sample (all values are given in mm)

Width and height of web and flanges									Depth and length of the wave		Depth and length of corrugation		Sheet thickness			
A1	A2	B1	B2	C1	C2	C3	C4	C5	E1	E2	F1	F2	T1	T2	T3	T4
696	675	1016	1016	201.7	160.9	80.0	87.5	27.3	204.7	11.4	33.8	2.2	1.38	1.37	1.38	1.37

Actual values of tensile strength and yield stress of sample material have been obtained from the tensile tests made accordingly to standard ISO 6892-1 [14]. 30 samples have been tested, with average values of $R_{p0.2}$ and R_m being 337 MPa (yield point) and 388 MPa (tensile strenght) respectively.

2.2. Test bench. The main purpose of the tests was to establish the profile load carrying capacity as well as the relationship between load and deformation. It was assumed from the beginning that test bench has to fulfill the following requirements:

- limitation of a failure mode to local buckling,
- prevention of deplanation of the sample's support zones,
- elimination of any loads other than axial despite any sample deformation during the test.

A test sample is placed between the rigid plates. The axis of rotation extends along the load device and is off set by the value of eccentricity. The top plate is able to move along the axis of $\delta(X)$ and rotation of both plates with respect to Z_u and Z_d axes is also allowed. Figure 5 shows the load and support scheme at the test bench and its representation in the full-size element.

On the basis of the above assumptions a prototype test rig had been built. The schematic view and the photo of the test set-up are shown in Fig. 6.
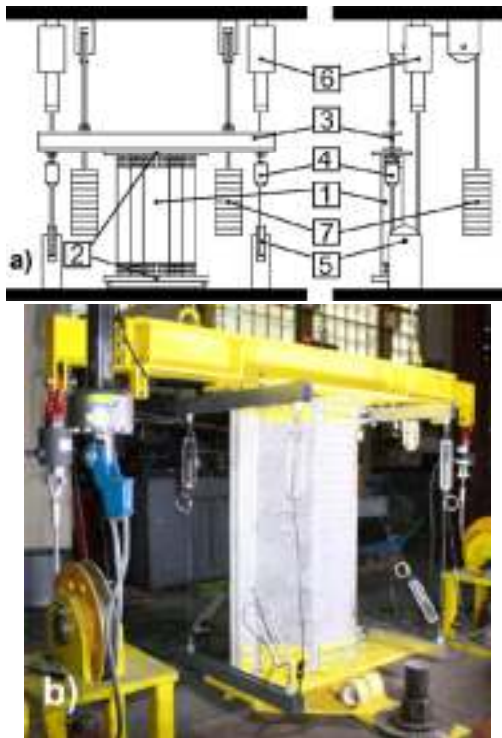

Fig. 6. The experimental set-up: a) the scheme of the rig and b) the photo of the sample at the test bench

The setup deplanation has been prevented by rigid steel plates (pos. 2) fastened to the sample (pos. 1) by means of

number of bolts. Lower plate has been standing on a support allowing its rotation in one direction. I-beam (pos. 3) has been attached to upper plate. Counterweights (pos. 7) attached to this beam via ropes and pulleys kept sample in upright position. Load has been applied by means of pulleys (pos. 5) and ropes attached to the same I-beam (pos. 2) as counterweights were.

Except of an axial load it is possible for limited amount of torsional moment to occur only. However the measurements made during the tests shown that the torsional deformation of a sample and any moment induced by it is negligible up to the moment of the sample's failure. Friction during the test is limited to rotational degree of freedom of lower support only and it was reduced by applying of graphite-molybdenum lubricant. The load has been measured by the strain gauge transducers (pos. 4) and, due to the application of PID controlled hydraulic actuators (pos. 6), it maintained the same value for both tendons during the tests. The value of eccentricity of an applied load can be changed in 15 mm increments.

2.3. DIC set-up and data analysis. Due to the complicated geometry of corrugated, thin walled profiles the preparation of numerical model is significantly error-prone. Thus DIC method has been used during the tests as it gives reliable information about the actual buckling modes that are important for the verification of FE model. DIC is a non-coherent light based method which enables full-field measurements of shape, displacements, and strains [15, 16]. The two-dimensional version of DIC (2D DIC) measurement consists of the acquisition of a series of images of a tested object before and after load (or during loading), over a certain Area of Interest (AOI). The surface of the measured object needs to have random texture which is in our case applied within the AOI by spraying black paint (dotted pattern) at the white paint background. One of the images serves as a reference for the others (deformed). The reference image is divided into small rectangular regions (subsets) consisting of $N \times N$ pixels. Dimensions of subsets are dependent on the quality of the random pattern. The DIC algorithm is then tracking the position of each subset from the reference image in all other subsequent images, using the maximum zero-mean normalized sum of squared difference function criterion (or any other correlation metric). The location of the center point of the most similar subset found in a deformed image defines the in-plane displacement vector (u_x denotes displacements in 'x' axis and u_z denotes displacements in 'z' axis; Fig. 7a). Repeating this process over the AOI provide a displacement map, that is sampled as defined by the separation of adjacent subsets (step size). The 3D DIC is a technique, which combines the 2D DIC with stereovision, by using two cameras for observation of the same AOI, it is possible to obtain the 3D shape of the surface of an object and measure out-of plane displacements (u_y denotes displacements in 'y' axis), however the out-of-plane measurement error is larger than the in-plane one, and strongly depends on a stereo angle [17, 18]. According to [15] minimum displacement error can be less than 0.001 pixels, indicated by data post-processing. However, it must be highlight that in real ap-

plications the accuracy of measurements strongly depends on such factors as image noise and stability of experimental condition. Strains (ε_{xx}, ε_{zz} – strains along x and z coordinates) are calculated from displacements [15, 19] using equations:

$$
\begin{aligned}
\varepsilon_{xx} &= \frac{\partial u}{\partial x} + \frac{1}{2}\left[\left(\frac{\partial u}{\partial x}\right)^2 + \left(\frac{\partial w}{\partial x}\right)^2\right], \\
\varepsilon_{zz} &= \frac{\partial w}{\partial z} + \frac{1}{2}\left[\left(\frac{\partial u}{\partial z}\right)^2 + \left(\frac{\partial w}{\partial z}\right)^2\right].
\end{aligned}
\tag{1}
$$

It is worthwhile to note that the DIC 3D method is working in full-field and in experimental test provides much more data than point wise techniques. The measurements are carried out in thousands or millions of points of the measured object simultaneously and in three directions. The measurements of the sample were performed with the 3D DIC system which comprises of two AVT Pike F-1600 (4872×3248 pixels) monochromatic cameras equipped with 28 mm lenses, set on an angle of 30° and pointing to the same AOI at the specimen (Fig. 7b,c). Before performing the experiment, the system was calibrated with utilization of the commercial software VIC 3D [20]. Standard deviation of the residuals projection errors for 24 views of the calibration target and from both cameras was 0.058 pixel. Distortions of the 28 mm lenses were included in the calibration process. The setup was mounted on aluminum frame to enable easy modification and mobility. In order to ensure sufficient lighting, two 200 W LED lamps (13 000 lumen) equipped with a light diffuser ('soft box') were used. The capture of images by both cameras was synchronized and pairs of frames were collected every 2 seconds during 300 seconds of the experiment. The Field of View (FOV) of the systemwas 1.5×1 m, so it was well fitted to the size of the samples.
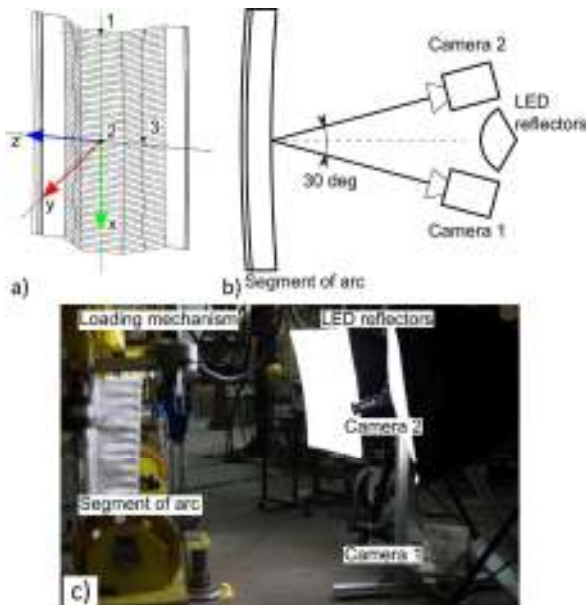

Fig. 7. The experimental system: a) orientation of coordinate system and location of three points adopted for further analysis; b) scheme and c) photo of measurement system based on 3D DIC

The displacements and strain maps were calculated with the Vic3D software [20]. The quality of data and resulting accuracy of measurements at a given point was determined by the confidence interval for match at points within the Area of Interest and it is given by sigma value in pixels (Fig. 8a). The range of sigma for maximum load was 0–0.3 pixel. This values after scaling based on 3D DIC system parameters provided the estimate of the acuracy of displacement measurements for ±0.01 mm. The maximum values of sigma (low level of confidence) were located at the bending edges of the sample (incl. the peaks of the corrugation). The results of measurements are not displayed at these points as can be seen at the shape map shown in Fig. 8b, where data at several locations are incomplete (white spots).
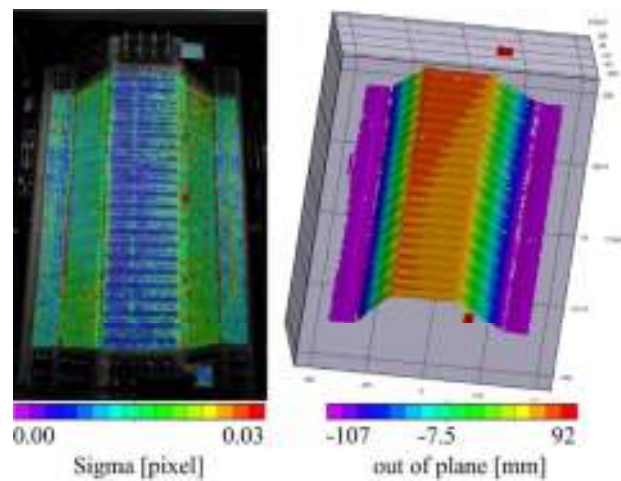

Fig. 8. Example results of measurement: a) the map of sigma – confidence interval for the match at the points within AOI, and b) the shape of measured segment of arch

3. Numerical models and their analysis

Numerical models have been created with Ansys Finite Element Method software. Three different models have been prepared, each with different degree of simplifications of geometrical properties. All models have the same 18 m curvature radius, 1 m length and were based on actual geometry of the tested sample included in Table 1. In order to simulate accurately the experimental conditions, the assumed boundary conditions (Fig. 9) allowed: movement of upper edge in the direction of the force load and rotation of both (upper and lower) edges around z axis only.

Both upper and lower edges have been modeled as rigid by means of multiple point constrains (so called "remote support" in Ansys software). All nodes belonging to the given edge stay in a plane and the initial shape of the edge is preserved during deformation. Both upper and lower plane can move during deformation, in the direction of unconstrained degrees of freedom. Thus, according to Fig. 9, the plane including upper edge can be translated in x axis direction and rotated with respect to z axis ($X_1 \neq 0$ and $R_{z1} \neq 0$). The

plane including lower edge is only permitted to rotate with respect to z axis ($R_{z2} \neq 0$).
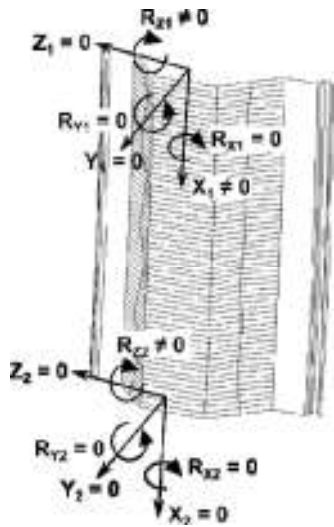

Fig. 9. Boundary conditions of upper and lower edges of the modeled sample, with local coordination systems.

Non-linear stress analysis accounting for material and geometrical nonlinearities has been made. Bilinear material model have been assumed on a basis of $R_{p0,2}$ and R_m values obtained from the tests. Newton-Raphson method of nonlinear analysis has been applied and influence of large displacement taken into account. The S281 general purpose quadratic 4-sided shell element with 8 nodes and 6 degree of freedom in each node has been chosen. The node numbering and the direction of the normal to the surface are shown in Fig. 10.
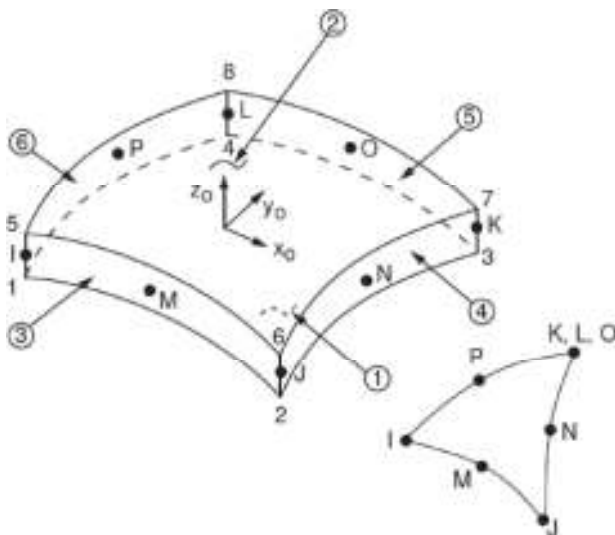
Fig. 10. The Ansys S281 shell element

Three numerical models, with the geometries shown in Fig. 11, were considered. The first model is the simplest one, omitting corrugations and wave-like disturbance in lower flanges shapes. In the second model corrugation of web and

lower flanges have been taken into account and in the third model wave-shaped disturbance have been added to the webs.
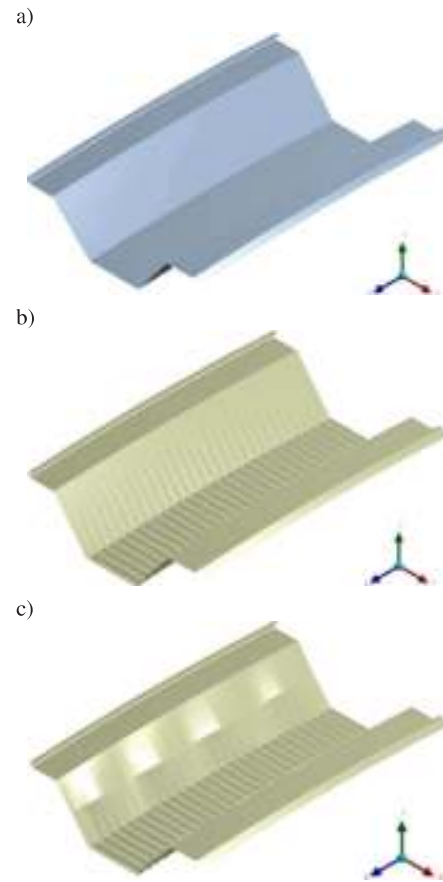

Fig. 11. The geometry of numerical models: a) planar model (1st), b) corrugation model (2nd) and c) corrugation and wavy model (3rd)

To compare the behaviour of all three models, the calculations of inter alia maps of equivalent von Mises stresses and total displacements for the ultimate load (according to Table 2)had been performed and the respective maps of both quantities are presented in Figs. 12 and 13.
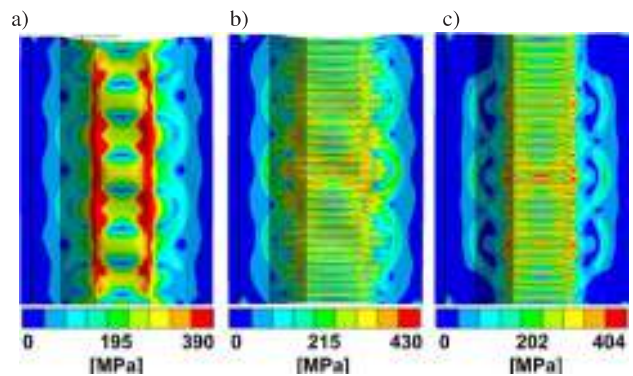

Fig. 12. The maps of equivalent von Mises stress at the ultimate load for: a) 1st model, b) 2nd model and c) 3rd model
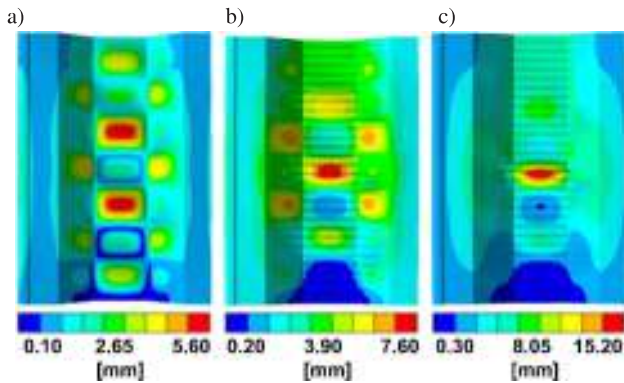
a)   b)   c)

Fig. 13. The maps of total displacement at the ultimate load for:
a) 1st model, b) 2nd model and c) 3rd model

It is clear, that omitting corrugations increase the stiffness of lower flanges and web and shifts the neutral axis towards the middle of the cross-section height. Due to this fact, despite the identical boundary conditions in all three models, the 1st model suffers from different relationship between the axial force and resulting bending moment. In the case of 2nd and 3rd models the von Mises stress distribution is quite similar except for the webs. It should be kept in mind that the profile webs have much less significant impact on its load carrying capacity as well as on the axial and bending stiffness (for the considered direction of bending moment). Therefore it should not be of much importance if the results from the numerical model of profile section are to be implemented in the simplified beam model.

The results of calculations obtained with the 1st model again differ significantly from the two others. In the case of 1st and 2nd model the displacement maps confirms, that the differences are limited to profile webs.

4. Validation of numerical models

Validation of the numerical models is performed in two main stages. At first the comparison of the displacements u_x, u_y, and u_z in selected points of the structure in the function of load is performed between all three models and experimental data. Secondly the full-field comparison of the failure mode maps and between DIC and numerical displacement maps is provided.

4.1. Matching of experimental and numerical results. It is crucial to match properly the coordinate systems, in which the numerical and experimental results are calculated, before validation of numerical models by experimental results. It is also important to remove from experimental data the unwanted additional data connected to imperfection of experimental set-up, e.g. impact of backlash in joints.

Typically in the 3D DIC analysis the coordinate system is based on information of the initial shape of a sample. The origin of this system is located at the mass centroid of all object points, with y axis normal to the best-fit plane of the shape data [20]. In our case to match the coordinate system

we transform DIC coordinate system using the markers integrated with stochastic texture (Fig. 14a,b).
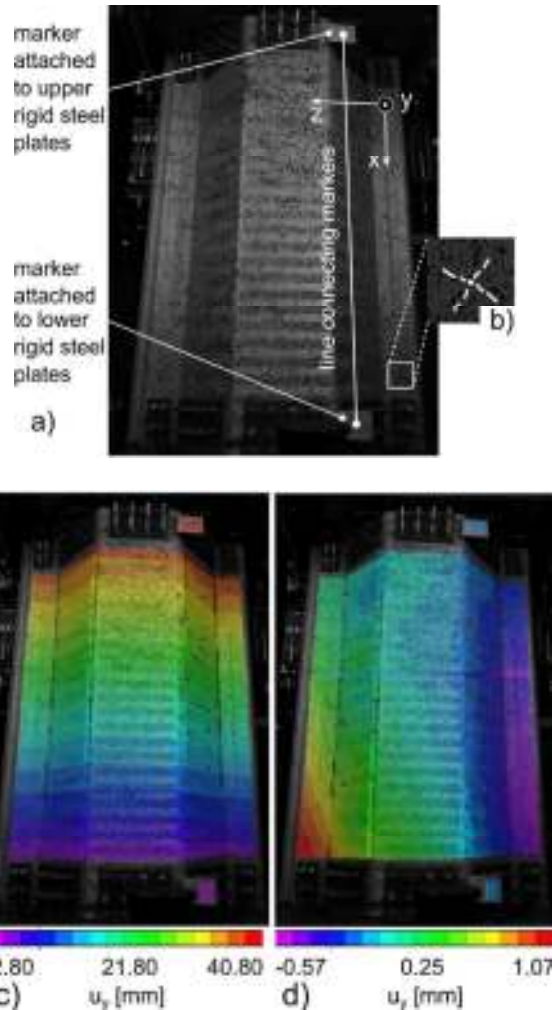

Fig. 14. The principles of data post-processing: a) the image of the sample with markers' positions and line used for data post-processing operations, b) one of markers used for transformation of coordinate system; example of out of plane displacements maps for 0.6 kN force, c) before and d) after post-processing of data

Next the unwanted displacement data have to be removed. The good example of such operation is the process of backslash elimination at the first stage of applying load. The backslash resulted in random displacements (Fig. 14c) and rotations which were not allowed in numerical simulations (as discussed in Sec. 3). In order to enable comparison between numerical and experimental data the dedicated post-processing method was implemented based on transformation of the obtained displacements [21]. Using the markers attached to the rigid steel plates (Fig. 14a), the line was determined (parallel to the direction of force load). The applied transformations of displacements removed the rotations of the determined line. It should be pointed out, that the markers were not directly attached to the lower support and location of force applying, therefore rotation of determined line

111

around an axis z is not equivalent to R_{Z2}. In relation to the boundary condition of a numerical model (see Sec. 3), the following terms and conditions have been preserved: rotations R_{X2} & R_{Y2} were forbidden and rotations R_{Z1} & R_{Z2} were allowed. However, in experimental data in contrast to numerical model, the rotations of R_{X1} & R_{Y1} could appear, caused by uncontrolled skew of the upper rigid steel plates (Fig. 6a). The example of post-processing of out – of-plane displacement maps obtained for 0.6 kN are shown in Fig. 14c,d.

4.2. Point-wise validation of numerical models. The extreme values of u_x, u_y, and u_z displacements are observed in points 1 (located at the top of corrugated web section), 2 (located at the middle of corrugated web) and 3 (located at middle of corrugated flange) (see Fig. 7a). The points 1 and 2 concern the maximum displacement in the x and y directions, respectively. Point 3 refers to the maximum displacement of the entire sample in the z direction. This configuration of the measurement points allows for the assessment of representative movements for the entire sample. The values of these displacements obtained for all three numerical models have been compared with the experimental results. The load-displacement relationships are shown in Figs. 15–17.
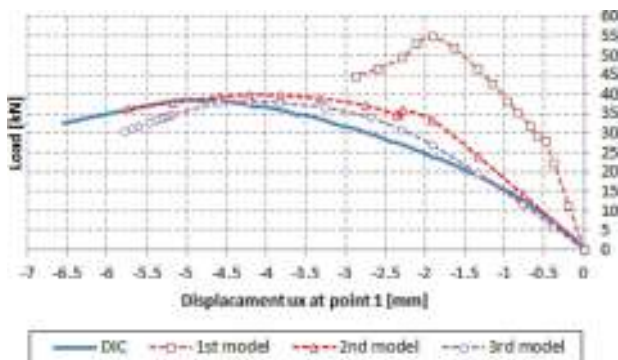

Fig. 15. The comparison of load u_x displacement functions obtained for 1st, 2nd, 3rd numerical models and experimental data (results for point 1)
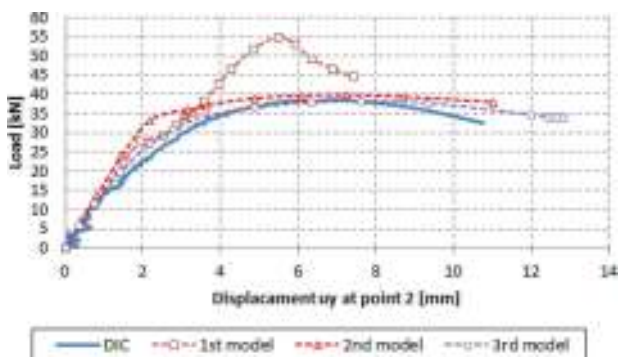

Fig. 16. The comparison of load u_y displacement functions obtained for 1st, 2nd, 3rd numerical models and experimental data (results for point 2)
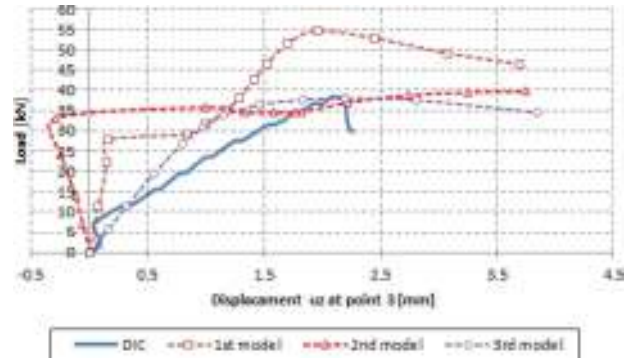

Fig. 17. The comparison of load u_z displacement functions obtained for 1st, 2nd, 3rd numerical models and experimental data (results for point 3)

The simpliest 1st model significantly overestimate both stiffness and ultimate load values. The differences between 2nd and 3rd models are less significant, particularly in case of u_x and u_y displacement. In the case of 2nd model displacements in point 3 the u_z direction still differs significantly from experimental values. This is due to the unaccounted influence of wave like disturbances of webs shape. 2nd model also still slightly overestimates load carrying capacity of the profile. The values of the displacements at ultimate load obtained from DIC and FEM models are gathered in Table 2.

Table 2
Displacements at ultimate load

	Ultimate load	Displacement at ultimate load		
	F_m [kN]	u_x [mm] at p.1	u_y [mm] at p.2	u_z [mm] at p.3
DIC experimental	38.5	−5.08	7.23	2.24
1st FEM model 1	54.7	−1.91	5.48	1.96
2nd FEM model 2	39.8	−4.20	7.23	3.75
3rd FEM model 3	38.1	−4.21	7.61	2.20

For the purpose of comparison of the results Δ_i parameter is introduced, both for the force:

$$\Delta_{Fm} = \frac{F_{DIC} - F_{FEM}}{F_{DIC}} \cdot 100 \ [\%] \qquad (2)$$

and displacement values:

$$\Delta_u = \frac{\left(F/d_{U,V,W}\right)_{DIC} - \left(F/d_{U,V,W}\right)_{FEM}}{\left(F/d_{U,V,W}\right)_{DIC}} \cdot 100 \ [\%]. \quad (3)$$

The Δ_i values for all three models are included in Table 3.

Table 3
Comparison of values of Δ_i parameters

	Ultimate load	Displacement at ultimate load		
	Δ_{Fm}	Δ_{u_x} at p.1	Δ_{u_y} at p.2	Δ_{u_z} at p.3
1st FEM model 1	−42.0%	−277%	−87.6%	−62.5%
2nd FEM model 2	−3.3%	−24.8%	−10.0%	38.4%
3rd FEM model 3	1.1%	−19.2%	6.0%	1%

112

The results obtained without taking into account corrugations and wave-like disturbance in webs shape differ from the experimental results to the level which prevent practical application of 1st model. Unfortunately this level of model simplification is used in a design process quite often, leading both to the overestimation of ultimate loads and incorect load distribution along an arch. 2nd model with corrugated lower flanges and web gives acceptable estimation of ultimate load, u_x and u_y values. The displacement u_z differ significantly (38%) from the experimental value. Including additional disturbance of webs shape in 3rd model decrease the error in calculated u_z value, but the quality of the other results remains in affected in significant way.

The corrugation of web and lower flanges of a profile can be seen as a form of geometrical imperfections, determining the mode of failure. It was observed that without the corrugation the numerical model exhibits poor convergence requiring greater number of load steps in an analysis and greater computing power. This is especially true in the case, when initial deformations taken from buckling analysis are not applied to the model. This drawback can be however at least partially offseted by potentially less number of elements required to sufficient description of a simplified geometry.

Beside displacements, the strains in the vicinity of point 2 have been investigated with 3rd model. In Fig. 18 the relationship between load and strains in directions perpendicular and parallel to longitudinal axis of profile (that is ε_{zz} and ε_{xx} respectively).
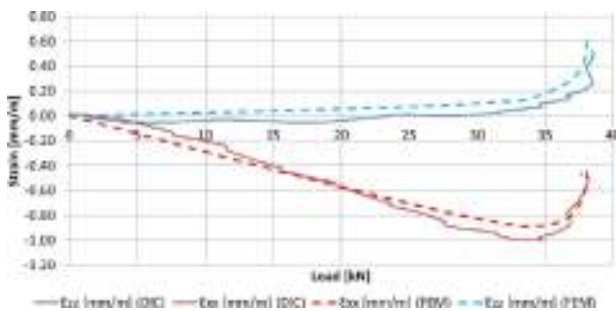

Fig. 18. Comparison of strains in point 2 vicinity (FEM results for 3rd model)

The difference between strain values obtained from DIC and FEM 3rd model varies from 2% to 20%, depending on load level. It should be noted, that due to the corrugated surface values of ε_{xx} strains exhibit large variability from point to point. Therefore it is necessary to carefully select areas both for DIC and FEM model used for the integration of ε_{xx} values intended for comparison. In x direction this area should cover length of a single corrugation to obtain the useful results and cause "smear" of corrugation. This effect is of course much less pronounced in the case of ε_{yy} strain values.

4.3. Full-field validation of numerical models. The good way to check qualitatively the correctness of a model is to compare numerical and experimetal failure mode maps. As shown in Fig. 19 the photo of the experimental failure region

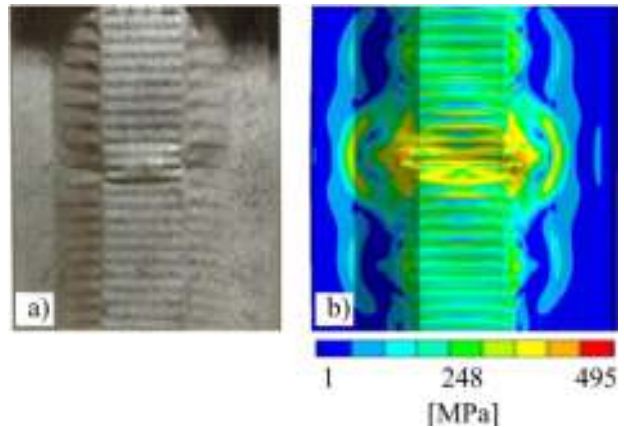is in very good agreement with the failure mode map obtained for the 3rd model.

Fig. 19. The failure mode maps obtained from: a) experiment (photo) and b) 3rd model

In order to perform full-field quantitative comparison, the displacements maps u_x, u_y, and u_z obtained from DIC and numerical analysis, are shown respectively in Figs. 20–22.
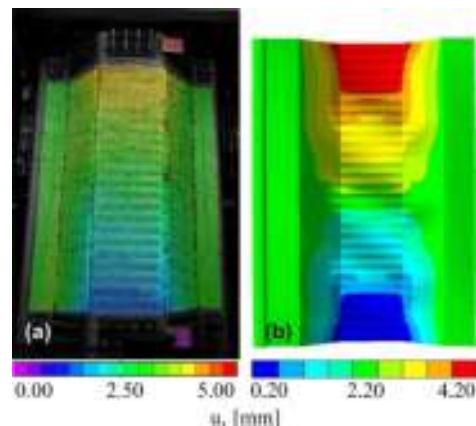

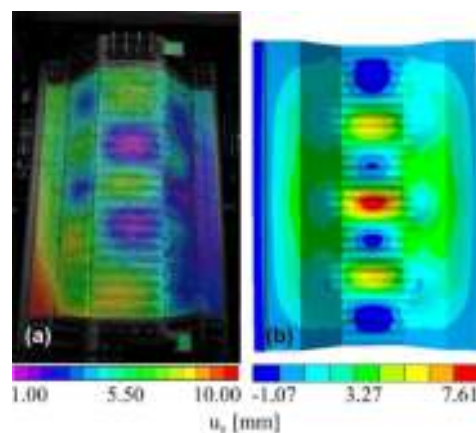Fig. 20. The displacement u_x obtained from: a) experiment and b) 3rd model

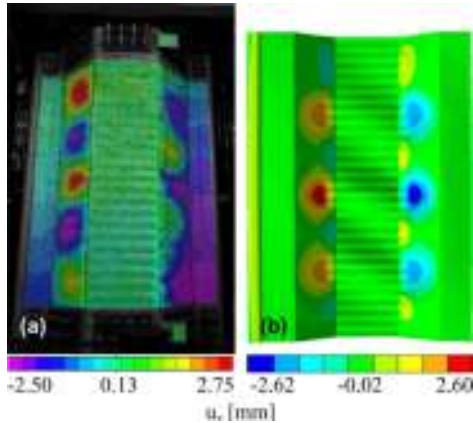Fig. 21. The displacement u_y obtained from: a) experiment and b) 3rd model

Fig. 22. The displacement u_z obtained from: a) experiment and b) 3rd model

The displacement maps u_x, u_y, and u_z obtained from the calculations show good convergence in both: the character and values with the test results. In some cases (Figs. 21, 22) slight disturbances of displacement maps obtained with DIC method can be observed. This is caused by unavoidable deviations in the specimen geometry and support conditions (e.g. connected with precision of assembly). This minor disturbances have insignificant influence on the final results and conclusions.

5. Conclusions and further research

The simplest way of modelling of a profile geometry which omits its corrugations and other disturbances of the shape leads to highly overestimated value of ultimate load as well, as highly underestimated values of displacements. These errors occur despite the fact that for the simplified model geometry, the physical and geometric nonlinear effects have been taken into account for the calculations. Unfortunately this level of profile geometry simplification is most frequently used for practical calculations, as it represents the highest detailing of profile geometry that can be directly incorporated in a numerical model of whole arch structure without increasing demand for computing power beyond reasonable level.

The most complicated third model and the second model which omits wave-like disturbances of web shape only, give results close to the experimental ones. If the effects of displacements in z direction are unimportant for the further analysis, the level of geometry details of second model can be seen as optimal with respect to both to quality of results and work consumption. However, if this is not the case, the implementation of all measurable geometrical properties is necessary, like it was made in the case of the third model. Unfortunately both levels of geometry description details are not applicable directly in a numerical model of whole arc structure and require additional analysis steps.

The unique properties of 3D DIC method implemented for the experimental tests allows precise observation of failure mode and enables measurement of displacement values

in locations, that could be otherwise difficult to access for traditional displacement sensors. DIC method also decrease risk of improper placement of sensors, no matter whether it is caused by improper assumptions or unexpected behavior of a specimen and test equipment. The importance of this is easy to see when reading i.e. paper [12]. The placement of the dial gauges during the tests described in [12] requires particularly careful preliminary numerical analysis. Any deviation from the predicted buckling form can have detrimental impact on the measured values and cause misleading conclusions.

In future, the already validated numerical model is going to be used for the estimation of ultimate axial load, ultimate bending moment envelope as well, as flexural and axial stiffness given in terms of axial load and bending moment values. These are going to be implemented in 2-D FEM model utilizing beam elements. It will make possible to perform static calculations of whole structure with computing power available in modern PC grade hardware. The proposed methodology is the first step in the development of full assessment methodology for different types of self-supporting arch structures produced by ABM technology.

REFERENCES

[1] R. Walentyński, R. Cybulski, and K. Kozieł, "Numericalmodels of ABM K-span steel arch panels", *Architecture Civil Engineering Environment* 4, 105–114 (2011).

[2] US Navy Course, *Steel Builder*, NAVEDTRA 14251, 2 (1996).

[3] EN 1991-1-1 Eurocode 1: "Actions on structures – Part 1–1: General actions – Densities, self-weight, imposed loads for buildings".

[4] EN 1991-1-3 Eurocode 1: "Actions on structures – Part 1–3: General actions – Snow loads".

[5] EN 1991-1-4 Eurocode 1:"Actions on structures – Part 1–4: General actions – Wind action".

[6] EN 1993-1-1 Eurokode 3: "Design of steel structure. General rules and rules for buildings".

[7] EN 1993-1-3 Eurokode 3: "Design of steel structure. General rules – Supplementary rules for cold-formed members and sheeting".

[8] PN-B-03207:2002 "Steel structures. Structures of cold formed thin gauge members and sheeting. Design and execution".

[9] A. Biegus, "The static-strength analysis of arc corrugated sheets", *Steel Structures. Scientific andTechnicalSection* 7, 24–28 (2003).

[10] EN 1993-1-5Eurokode 3, "Design of steel structures. General rules - plated structural elements".

[11] R. Walentyński, M. Cybulska, and R. Cybulski, "Influence of geometrical imperfrctions on the local stability of thin – walled elements",*Steel Structures. Theory and Applications* 3, 105–113 (2014).

[12] Li-Li Wu, Xuan-Neng Gao, Young-Jiu Shi, and Yuan-Qing Wang, "Theoretical and experimental study on interactive local

buckling of arch-shaped corrungated steel roof", *Steel Structures* 6, 45–54 (2006).

[13] A. Piekarczuk, M. Malesa, M. Kujawinska, and K. Malowany, "Application of hybrid FEM-DIC method for assessment of low cost building structures", *Experimental Mechanics* 52 (9), 1297–1311 (2012).

[14] ISO 6892-1, "Metallic materials – Tensile testing – Part 1: Method of test at room temperature".

[15] M. Sutton, J-J. Orteu, and H. Schreier, *Image Correlation for Shape, Motion and Deformation Measurements. Basic Concepts, Theory and Applications*, Springer, New York, 2009.

[16] B. Pan, "Recent progress in digital image correlation", *Experimental Mechanics* 51 (7), 1223–1235 (2011).

[17] Y.-Q. Wang, M. A.Sutton, X.-D. Ke, and H.W. Schreier, "Error propagation in stereo vision: Part I: Theoretical developments", *Experimental Mechanics* 51 (4), 405–422 (2011).

[18] X.-D. Ke, H.W. Schreier, M.A. Sutton, and Y.-Q. Wang, "Error propagation in stereo vision: Part II: Experimental validation", *Experimental Mechanics* 51 (4), 423–441 (2011).

[19] T.C. Chu, W.F. Ranson, M.A. Sutton, and W.H. Peters, "Applications of digital-image-correlation techniques to experimental mechanics", *Experimental Mechanics* 25 (3), 232–244 (1985).

[20] http://www.correlatedsolutions.com (01.10.2014).

[21] M. Malesa and M. Kujawińska, "Deformation measurements by digital image correlation with automatic merging of data distributed in time", *Applied Optics* 52 (19), 4681–4692 (2013).

115

ORIGINAL ARTICLE

3D DIC tests of mirrors for the single-mirror small-size telescope of CTA

M. Rataj[1] · M. Malesa[2] · M. Kujawińska[2] ·
Ł. Płatos[1] · P. Wawer[1] · K. Seweryn[1] ·
K. Malowany[2]

Abstract The Cherenkov Telescope Array (CTA) is the next generation very high energy gamma-ray observatory. Three classes of telescopes, of large, medium and small sizes are designed and developed for the observatory. The single-mirror option for the small-size telescopes (SST-1M), of 4 m diameter, dedicated to the observations of the highest energy gamma-rays above several TeV, consists of 18 hexagonal mirror facets of 78 cm flat-to-flat. The goal of the work described in this paper is the investigation of a surface shape quality of the mirror facets of the SST-1M CTA telescope. The mirrors measured are made of composite materials formed using sheet moulding compound (SMC) technology. This solution is being developed as an alternative to glass mirrors, to minimize the production cost of hundreds of mirrors for the network of telescopes, while retaining the optical quality of the telescope. To evaluate the progress of design, production technology and the mirrors' functionality in operating conditions, the three-dimensional (3D) Digital Image Correlation (DIC) method was selected and implemented for testing selected mirrors. The method and measurement procedure are described. The novel measurement approach based on 3D DIC has been proven to be well suited to the investigation of the mirrors' behavior with temperature, producing the necessary accuracy.

✉ M. Rataj
    rataj@cbk.waw.pl

[1] Space Research Centre of the Polish Academy of Sciences, Bartycka St. 18A, 00-716 Warsaw, Poland

[2] Institute of Micromechanics and Photonics, Warsaw University of Technology, Św. A. Boboli St. 8, 02-525 Warsaw, Poland

🙽 Springer

117

1 Introduction

The Cherenkov Telescope Array (CTA) project is an initiative to build the next generation ground-based very high energy gamma-ray instrument [1]. Gamma rays with photon energies ranging from several tens of GeV to beyond 100 TeV will be detected by ground-based telescopes that observe the Cherenkov light emitted in air showers created by gamma rays. To achieve its goals, the array will consist of at least three types of telescopes. The highest energy photons will be observed by Small Size Telescopes (SSTs). About 70 of these will be located in the southern hemisphere array.

A consortium of Polish, Swiss and German institutions is developing an SST prototype called the Single Mirror Small Size Telescope (SST-1M) [2]. The telescope is based on a Davies-Cotton design [3] proven in existing Imaging Atmospheric Cherenkov Telescopes (IACTs). The novel element of the telescope will be a fully digital and lightweight camera based on Geiger avalanche photodiodes [4]. The telescope has a focal length of 5.6 m and offers 9° field of view. The structure of the telescope is formed by a tower, a dish support structure, a counterweight and a camera mast. 18 mirror facets form the telescope dish of 4 m diameter. The mirror tiles are hexagonal, 0.78 m flat-to-flat in size. The effective light collecting area, corrected for the camera and mast shadowing, is 6.47 m^2. Each mirror will be attached to the dish support structure using a set of actuators allowing for the mirror alignment.

In the design phase different solutions and materials are considered for CTA mirrors [5]. Glass mirrors are the baseline solution for the SST-1M. However, in parallel, composite mirrors are being developed by means of sheet moulding compound (SMC) formation [6] to provide a lightweight, reliable and cost-effective alternative. SMC is a proven technology in the automotive industry and some of its advantages include: only a one-step process is needed to produce the substrate, it is a fast process which takes 3 min only and the material shows no shrinkage. In addition, the top surface of the composite mirror does not require polishing, as a smooth surface is obtained. This solution is being investigated to minimize production cost of hundreds of mirrors for the network of telescopes, whilst simultaneously fulfilling the telescope's optical requirements. Ensuring that the surface shape of the mirror facets is maintained under all operation conditions is an essential requirement for the performance of the telescope.

Therefore investigations of the thermal behavior of composite mirrors manufactured using different designs and manufacturing techniques are crucial for optimizing both the design and the manufacturing processes. The measurement method should provide such quantities as shape, deformation and strain distributions as a function of the temperature. The three dimensional Digital Image Correlation (3D DIC) method [7] was selected as the best fitted full-field, vision-based measurement method.

In Section 2 a description of the SST-1M composite mirror and its basic tests are presented. In the next two sections a short description of the 3D DIC method is provided and the measurement system and methodology are described. In Section 5 the results of example measurements of the mirrors are presented in detail and the usefulness of this testing method is assessed.

2 SST-1M composite mirror

The composite mirrors are being developed as an alternative to glass mirrors. The solution is based on a composite substrate formed using SMC technology. Its major feature is that the mirror substrate is composed of one isotropic, thermally conductive material and there is no glass in the structure. The top surface of the composite does not require polishing, and its smooth surface is obtained through the use of a high gloss mold. Since no glass is used as a front surface of the substrate, the coating includes not only reflective and protective layers but also an intermediate layer (lacquer or gel-coat) applied in order to reduce the surface roughness of the composite substrate, and improve both the mechanical resistance and coating adhesion. The achieved surface roughness (R_a) is below 5 nm, which is considered adequate for this application. The reflectivity of the mirror surface is obtained by the use of the intermediate layer followed by aluminium coating and a SiO_2 protective layer. One of the first prototypes, of 0.4 m flat-to-flat, is shown in Fig. 1.

At the presented stage of development of this technology, the surface quality of mirrors made of composite materials does not reach the quality level of glass and ceramic mirrors. Fortunately the mirrors of the SST-1M do not have very demanding optical the Point Spread Function (PSF) requirements, these being that 85 % of the energy should fall within a circle of 32 mm diameter and 80 % of that energy within a 17 mm diameter circle, over a wavelength range of 300 to 550 nm. However this optical performance must be sustained over the whole temperature operating range from −15 to 25 °C. For testing, the temperature range was increased to 40 ° C, to have a picture of the temperature behavior of the mirror in non-operating temperature range. The optical requirements, presented above, are for the first version of the SST telescope. Next version of the telescope has a proportionally reduced focal length and dimensions of the detector. Results of the presented analysis are easy to transfer to the new version by scaling. But the key point for our activities was to evaluate the progress of development of the applied technology.

The optical and geometrical parameters of the prototype mirrors have been measured by means of a Form Talysurf PGI 830 profilometer (surface roughness), a coordinate measuring machine and a 2-f optical measurement system. In the 2-f measurement system, a point-like light source (a pigtailed diode laser with λ=405 nm or 635 nm) is placed at the distance which is equal to the mirror radius of curvature (equivalent to twice the focal length). A detector is placed at the same distance to register the image

Fig. 1 The composite mirror prototype – rear and front side

119

(spot) formed by laser beam reflected by the mirror under test. In this configuration we are able to measure the PSF shape and dimensions, the radius of curvature and the reflectance of the mirror into the focal spot under laboratory conditions. All these parameters are dependent on the shape of the mirror surface. This simple measurement method based on a 2-f system unfortunately cannot be used for the mirror tests inside a climate chamber. The allowed change in the radius of curvature of the mirror over a 55 °C temperature range is ±2 m, which results in a surface deformation of ±20 μm. This value had encouraged us to use a simple image processing based method for shape and deformation measurements, namely the 3D Digital Image Correlation Method (DIC). The additional motivation to choose 3D DIC as the experimental method is its capability to determine strains in an mirror exposed to load (including thermal load), which must be considered for the SST-1M.

3 Three dimensional (3D) digital image correlation method

DIC is a non-coherent light based method which enables both full-field measurements of shape and displacements and the determination of strains in a wide variety of objects [7, 8]. The two-dimensional version of the DIC (2D DIC) measurement procedure is very simple, and requires the capture of a series of images of a tested object before and after load (or during loading). The surface of the measured object needs to exhibit a random texture (a speckle pattern). In most cases it is necessary to cover the measured object with such a pattern before the measurements start. One of the images in a series is selected as a reference image for all subsequent analyses. The reference image is divided into small rectangular regions (subsets) consisting of N×N pixels. The dimensions of the subsets are dependent on the quality and the size of the random pattern on the measured object. The DIC algorithm then tracks the position of each subset relative to the reference image in all other images of the series. Corresponding subsets are matched by finding the maximum of the zero-normalized cross-correlation function coefficient (or any other correlation metric). The difference in position between a reference subset and its matched equivalent defines the in-plane displacement vector at the subset's origin (U denotes displacements along 'x' axis and V denotes displacements along 'y' axis). Repeating this process over the area of interest yields a displacement map, that is sampled at an interval defined by the subset size and the separation of subsequent subsets selected for analysis (step size). Sub-pixel accuracy is achieved by sophisticated interpolation methods.

   In 3D DIC, a pair of images is acquired simultaneously by two cameras viewing the object from different directions. DIC, combined with stereo-vision and triangulation methods [9], provides maps of the shape together with out-of-plane and in-plane displacements of an object which have occurred between acquisitions of images. The 3D DIC measurement procedure is presented in Fig. 2. The cross-correlation function is calculated twice: for the first time in order to determine (x, y, z) coordinates of each subset in a stereo-image pair and for the second time in order to match all subsets against corresponding subsets in other images of the measurement series (providing in-plane and out-of-plane displacements). In the Figures hereafter, displacements along x and y axes are denoted as U and V, while displacements along z axis are denoted as W.
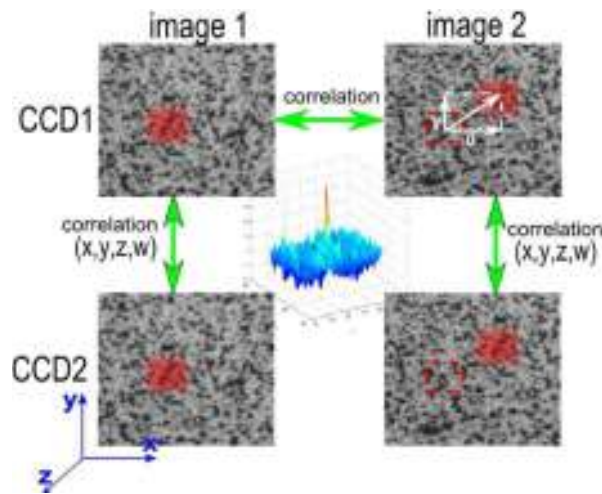
Fig. 2 Scheme of 3D DIC measurement procedure. An example subset from the reference image (the *red rectangle* in the middle) is matched against similar subsets in other images of the series; the contour plot in the middle is an example distribution of the correlation coefficient– the peak indicates the best matched position of the subset

The sensitivity of 2D DIC depends on the dimensions of the fields of view and the resolution of the cameras. In the 3D DIC method, the sensitivity also depends on the triangulation angle between the cameras.

Using the DIC method in experimental tests provides much more data than pointwise techniques. The measurements are carried out using thousands or millions of points on the measured object simultaneously and in all directions. The data obtained can be easily post-processed in order to calculate deformations or strain maps. The feasibility of 3D DIC and its modifications in different domains have been proven in a number of scientific articles published in recent years [10–18].

4 Measurement setup and methodology

The mirror was specially modified before the measurements by spraying with white paint and later introducing a speckle (random) pattern with black paint. The 3D DIC measurement system consisted of two AVT Pike 16 Mpx cameras equipped with 28 mm focal length lenses. The measurement setup is presented in Fig. 5b. According to [7] the accuracy of displacement measurements with these cameras and over a 0.6 m×0.6 m FOV would be as good as 2 μm (corresponding to 0.01 px accuracy). Due to experimental errors [19, 20] and observation through the window, the estimated accuracy was approximately 10 μm.

In each series of measurements, the mirror was placed in a FEUTON K-400 climate chamber, which provided the temperature control. In order to ensure the optimal illumination conditions, the chamber was covered inside with black cardboard (to reduce the influence of light reflections) and the LED light was placed inside the chamber. The 3D DIC cameras monitored the mirror through a window in the door of the chamber. The window consisted of 5 glass layers, which influenced the accuracy of

the measurements. In order to estimate the systematic error caused by the observation window two shape measurements of the mirror at room temperature were performed: the first with the doors of the climate chamber open, and the second with closed doores. The results are presented in Fig. 3.

The measurements through the window introduced a modulation of z coordinate with an amplitude of approximately 0.01 mm, which is small when compared to the recorded W displacements, which are of an order of 0.1 mm.

Figure 4 shows the temperature cycle implemented during the tests in the climate chamber, together with the indication of the time points when the sequential measurements were taken.

In order to ensure a stable temperature and homogeneous temperature distribution, the mirror was kept at each test temperature for about one hour before performing the measurement. The temperature of the mirror was measured with a set of point-like sensors, glued on the rear of the mirror (Fig. 5a). Cooling or heating the mirror by 20 °C took approximately 10 min.

Images of the measured mirror were acquired at 60 s intervals, which resulted in 400 pairs of frames captured by the DIC cameras. The measurement setup is presented in Fig. 5b.

The 3D DIC analysis presented below was made with the CCI software, developed at the Institute of Micromechanics and Photonics, Warsaw University of Technology, in collaboration with KSM Vision (http://ksmvision.pl/en 2014) and with VIC 3D software developed by Correlated Solutions (www.correlatedsolutions.com 2014). All U, V and W displacement maps (or values) presented below correspond to the x, y and z axes respectively. Coordinate systems are overlaid on the displacement maps.

5 Measurement results

This section presents the detailed results of our sample measurements. At the first experimental stage the complete mirror structure (the substrate with intermediate layer) was examined in the climate chamber over the full range of temperatures following the scheme described in Fig. 4. Reference frames were taken at 20 °C. The measurements were then repeated on a mirror having only the substrate and no intermediate layer. The main goal in these two series of measurements was to evaluate the possible influence of
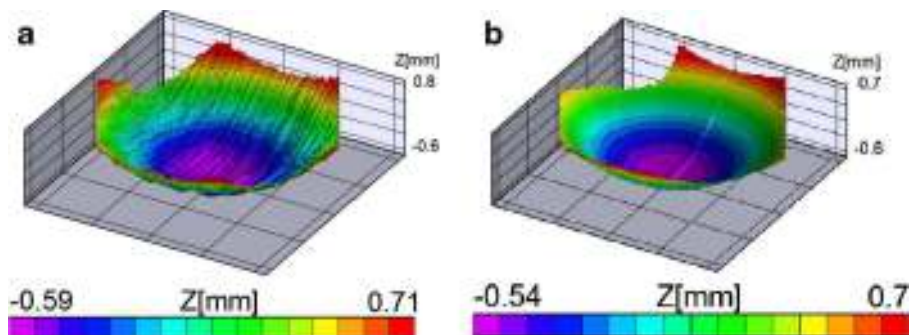

Fig. 3 Point cloud of the measured object acquired with 3D DIC method: (**a**) observation through the window, (**b**) direct observation (*with opened door*)
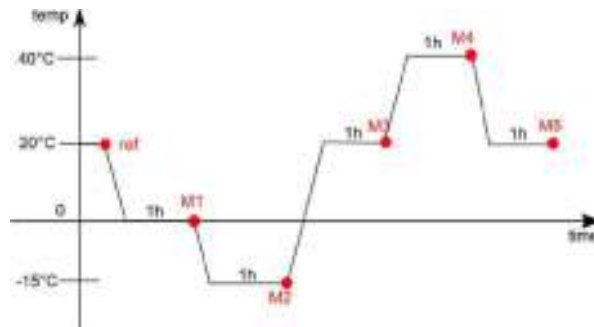
Fig. 4 Cycle of temperature changes implemented during the measurements; steady states are indicated with *red dots*

the intermediate layer on the mirror deformation when the ambient temperature is changed.

Example *U, V* and *W* displacement maps (obtained after rigid body movements have been removed) of the mirror with the intermediate layer are presented in Fig. 6.

As one can observe in Fig. 6, the mirror's radius of curvature decreased with decreasing temperature (negative *W* displacements in the centre of the mirror and positive *W* displacement at the edges) and increased with increasing temperature (positive *W* displacements in the centre of the mirror and negative *W* displacement at the edges). It is also clear that the mirror returns to its original shape once it returns to its initial temperature of 20 °C. However comparing the maps presented in Fig. 6c and e, which theoretically were captured at the same temperature, some differences can be observed. There are a few reasons of these differences. At first it should be noted that at 20 °C the displacement values are smaller by one order of magnitude when compared to other states of load. Actually, due to the systematic error caused by the observation through window of the chamber (see Fig. 3), the values obtained in states M3 and M5 are close to the accuracy limit of the method. The influence of the observation through the window is reflected by the high frequency variations of the presented displacement maps. Secondly, the temperature has been measured with approximately 0.5 °C uncertainty and additionally the temperature could have not been distributed homogeneously over whole surface of the mirror (pointwise sensors measurements differs from each
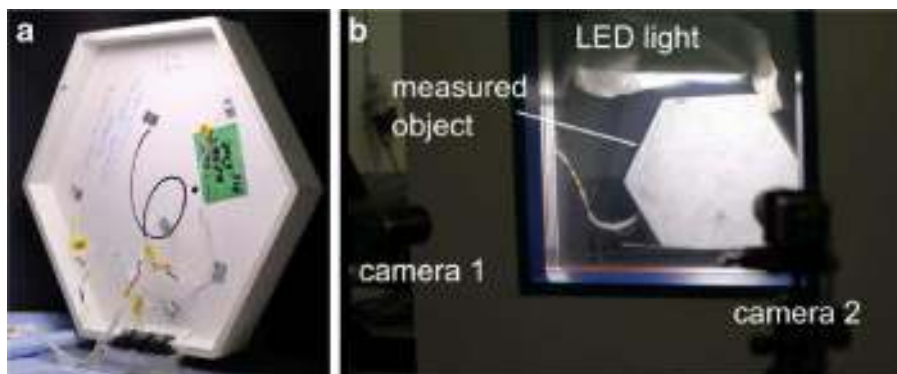

Fig. 5 (**a**) Pointwise temperature sensors glued at the measured mirror, (**b**) 3D DIC measurement setup: cameras of the system and measured mirror enclosed in the climate chamber
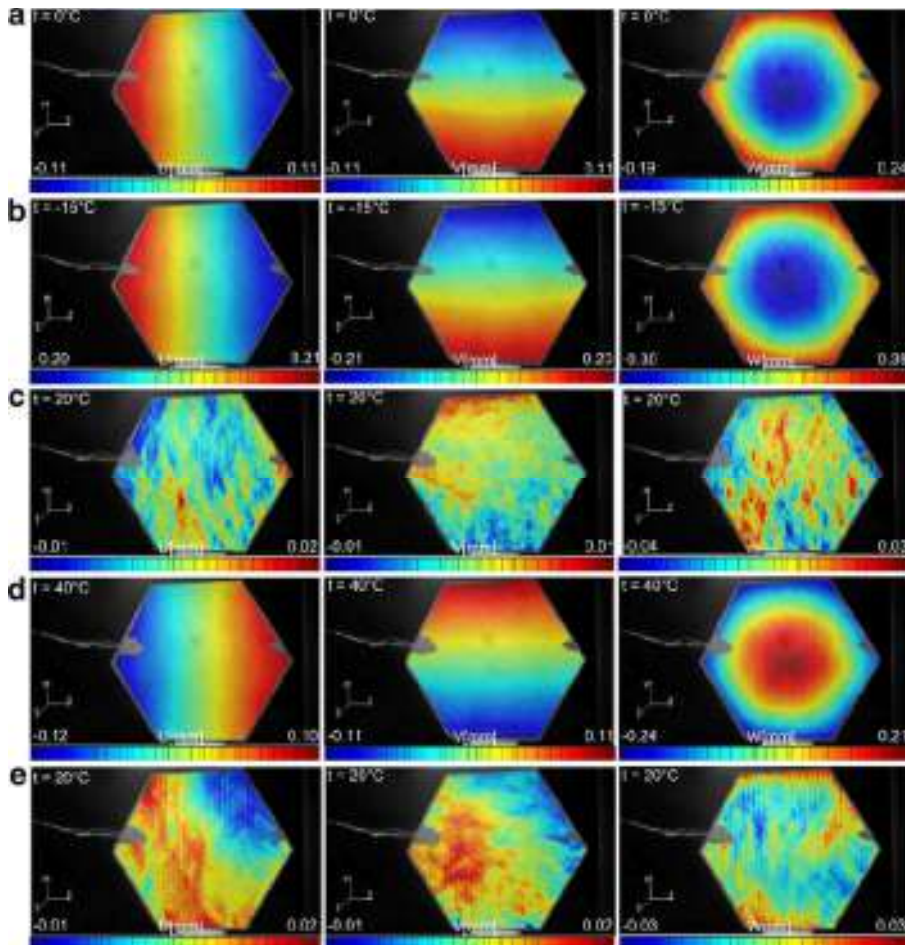
Fig. 6 *U*, *V* and *W* displacement maps in steady states of the mirror: (**a**) M1, 0 °C, (**b**) M2, −20 °C, (**c**) M3, 20 °C, (**d**) M4, 40 °C, (**e**) M5, 20 °C. The maps are at different colour scales, tailored to the minimum and maximum values found in each map

other by a maximum of 0.5 °C). All of these facts influenced the displacement maps acquired in steady states M3 and M5 (even though theoretically temperature was 20 °C in both states). In order to show a more detailed analysis, the displacements extracted from selected points and along selected lines have been plotted as a function of time (actually as a function of file number). The locations of points P1-P7 and line L2 are presented in Fig. 7. The same data processing procedure has been applied to measurements with and without the intermediate layer.

Displacements *U*, *V* and *W* extracted from points P1-P7 are presented in Fig. 8 together with the temperature changes (measured in the centre of the mirror). Plots in Fig. 8 a, c and e represent the first series (for the mirror with the intermediate layer) and plots in Fig. 8 b, d and f represent the results of the second measurement series (the mirror without intermediate layer). In order to minimize the influence of z coordinate modulations (see Fig. 3), the results at each point have been averaged over a small circle (radius of about 10 pixels).
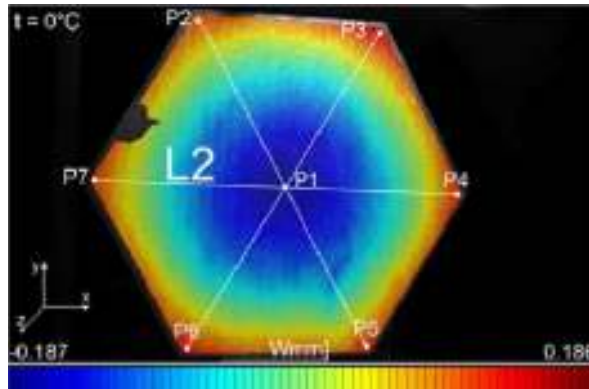
🐾 Springer

Fig. 7 Example *W* displacement map with overlaid points and lines of further analysis

One can observe in Fig. 8 that the temperature of the mirror did not stabilize at negative temperatures. For example, at a steady climate chamber temperature of −15 °C (M2) the temperature measured on the mirror was −18 °C, whereas this was not the case at temperatures above 0 °C. It can also be observed that
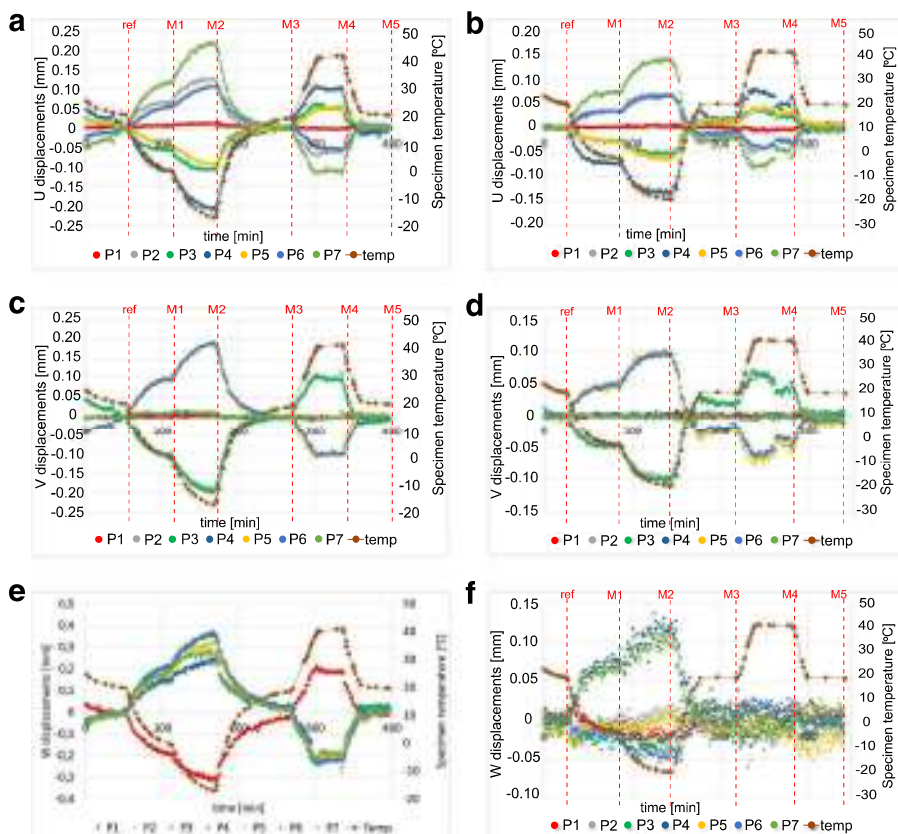

Fig. 8 Displacements extracted from points P1-P7: the first series displacements (**a**) *U*, (**c**) *V*, (**e**) *W* and the second series displacements (**b**) *U*, (**d**) *V*, (**f**) *W*

the specimens shrink as a result of the temperature variations. In-plane displacements U and V at points P2-P7 are distributed symmetrically, while at point P1 their values are negligibly small. All components of displacement vector return to 0 when the temperature returns to the initial value of 20 °C (M3 and M5). This observation is confirmed in the displacement maps (Fig. 6) as well as in the displacements plots (Fig. 8). The very small displacement values that were detected in the steady states M3 and M5 could be an effect of very small temperature differences between the initial and tested states or could be introduced by performing the measurement through the window (vertical displacement gradients are clearly seen on maps with small displacement values). The results of U and V displacement measurements were similar in both series (Fig. 8 a and b). Slightly bigger maximum values were obtained in measurements of the mirror without the intermediate layer, but in both cases displacements are close to zero at the initial temperature of 20 °C. It is different in the case of out-of-plane displacements. The biggest out-of-plane displacements were detected at point P1 (in the centre of the mirror). W displacements at other points had the opposite sign to displacements in P1. The trend in the W displacements indicates the change of the mirror's radius induced by the changing temperature. Much bigger W displacements were obtained in measurements of the complete mirror (Fig. 8e) when compared to the measurements of the mirror without intermediate layer (Fig. 8f). This indicates the considerable influence of the intermediate layer on the overall sensitivity of the mirrors to ambient temperature variations.

In further analysis, trends of the deformations of the mirrors were evaluated. The plots illustrating displacements U, V and W extracted from points along the line L2 as a function of time are presented in Fig. 9, for the mirror with an intermediate layer.

In Fig. 9 one can observe a symmetrical trend of deformations of the measured mirror. Zero displacements did not occur in the centre of the mirror, indicating the deformation of the spherical shape of the mirror which can be a source of additional aberrations. This effect could be caused by the influence of the thickness of the side walls of the mirror.

The changes of U and V displacements in time (Fig. 9a and b) and in space (Fig. 6) caused significant strains in the element. The variations of the strains in time (ε_{xx}, ε_{yy}) calculated along the line L2 are presented in Fig. 10.

The strains ε_{xx} and ε_{yy} at 20 °C (ref, M3, M5) have very small values, while they increase to significant positive values (tensile strains) at 40 °C (M4) and decrease to comparable negative values (compressing strains) at −15 °C (M2). This behavior suggests that significant fatigue stresses will occur in the mirrors at normal operating temperatures. This is an undesirable feature which has to be avoided.

In the last step of the data analysis, the radii of curvature of the mirrors have been calculated. This has been done by fitting a sphere using a least squares method to the point clouds (x, y, z coordinates) of the mirrors acquired in consecutive steady states. The comparison between radii of curvature of mirrors with and without an intermediate layer are presented in Table 1. The values of calculated radii are given together with the uncertainty calculated as a standard deviation of residuals of all points from the fitted point cloud. Differences of
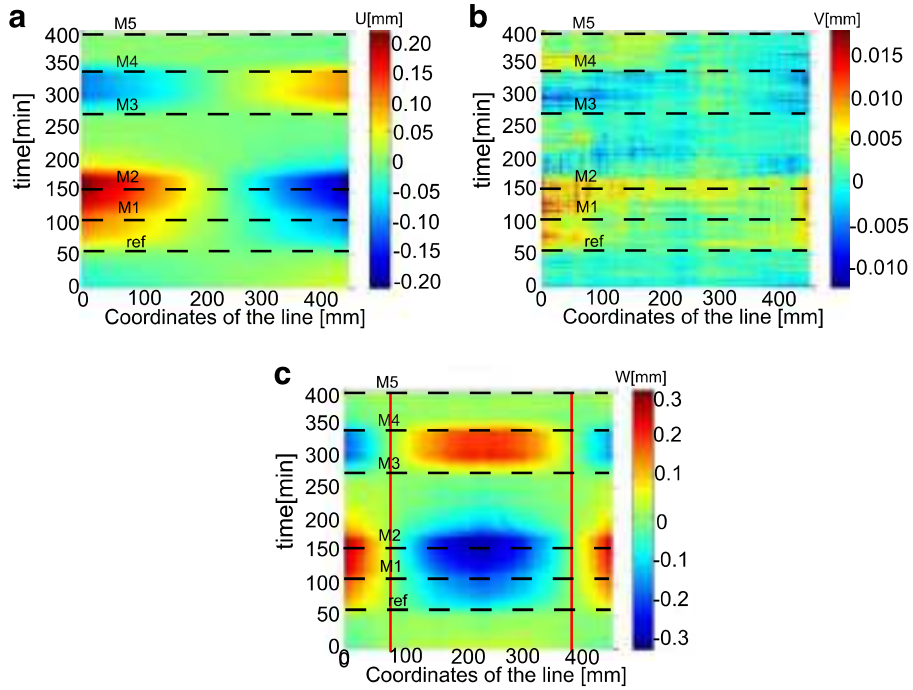
Fig. 9 Displacements extracted from points along line L2 as a function of time: (**a**) U displacements, (**b**) V displacements and (**c**) W displacements. The maps are presented at different colour scales, tailored to the minimum and maximum values found in each map

radii obtained at approximately the same temperature are caused by both uncertainties of temperature measurement and sphere fitting procedure.

At the initial temperature 20 °C (ref), the radii of curvature of both mirrors were approximately 15.5 m. Also in the steady states M3 and M5 (when the temperature was 20 °C again) the radii of curvature returned to their initial values. However, the difference between the radii of the mirrors with and
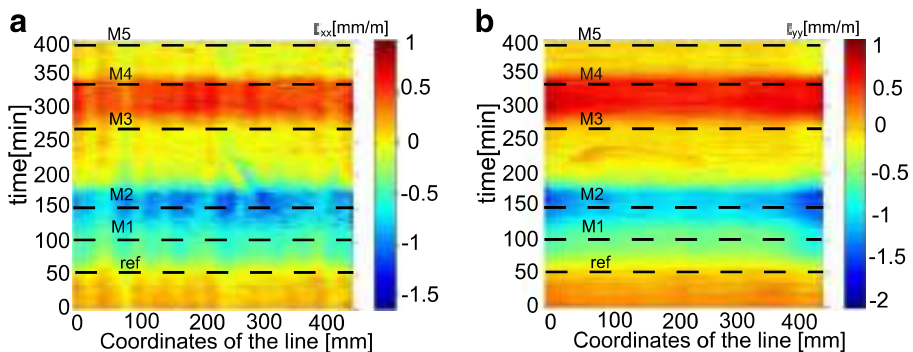

Fig. 10 Strains calculated along line L2 as a function of time: (**a**) strains ε_{xx}, (**b**) strains ε_{yy}. The maps are at different colour scales, tailored to the minimum and maximum values found in each map

🔁 Springer

Table 1 Variation of the radii of curvature of the SMC mirrors with temperature

Steady state	Temperature [°C]	Radius [m]	
		With intermediate layer	Without intermediate layer
ref	20±0.5	15.43±0.09	15.53±0.17
M1	0±0.5	12.40±0.09	15.35±0.17
M2	−15±0.5	11.03±0.09	15.07±0.17
M3	20±0.5	15.59±0.10	15.55±0.17
M4	40±0.5	20.81±0.10	15.59±0.17
M5	20±0.5	15.39±0.09	15.48±0.17

without the intermediate layer can be clearly observed in the steady states M2 and M4. The radius of curvature of the mirror without the intermediate layer remained the same within errors throughout the measurements, while the variations of the radius of curvature of the mirror with intermediate layer changed significantly with temperature. The main cause of this phenomenon is the difference in the coefficient of thermal expansion of the substrate and the intermediate layer. The intermediate layer thickness was initially assumed to be small such that the influence on thermal deformations is negligible. However, in practice, for technical reasons, this layer has a thickness of several mm, which causes significant variation in the radius of curvature of the structure. To minimize this negative impact, it is proposed to make the structure symmetrical by applying an intermediate layer on both sides of the substrate. This technology update is currently under development.

6 Conclusion

The proposed method of measurement of the surface deformation and accompanying strains has proven to be particularly useful for the mirror tests in the operating temperature range. The measurement accuracy obtained, which was better than 10 μm, was sufficient to estimate the deformation of the surface during tests in the thermal chamber. The random texture on the mirrors (a speckle pattern) produced by paint is easy to remove without any damage to the surface. The results obtained helped to identify the main (technological) cause of decreasing optical performance of the element with temperature. These tests resulted in the redesign of the SST-1M composite mirrors. First of all symmetrization of the SMC structure and gel-coat was introduced, together with a reduction in the thickness of the gel-coat layer. Some further changes in the design which improve the technology of the mirror production are being implemented, and the SMC mirror facet technology is close to be finalized within next months. The second batch of SMC mirror prototypes will be tested on the SST-1M telescope structure developed by Institute of Nuclear Physics Polish Academy of Sciences in Krakow [21].

🕿 Springer

128

References

1. Acharya, B.S., Actis, M., Aghajani, T., et al.: For the CTA Consortium, Introducing the CTA concept. Astropart. Phys. **43**, 3–18 (2013)
2. Moderski, R., Aguilar, J.A., Barnacka, A., Płatos, Ł., Seweryn, K., et al.: For the CTA Consortium, 4 m Davies-Cotton telescope for the Cherenkov Telescope Array, arXiv:1307.3137 [astro-ph.IM] (2013)
3. Davies, J.M., Cotton, E.S.: Design of the quartermaster solar furnace. Sol. Energy **1**(2–3), 16–22 (1957)
4. Boccone, V., Aguilar, J. A., Basili, A., Christov, A., della Volpe, M., Montaruli, T., Rameez, M.: For the CTA Consortium, The Photodetector Plane of the 4 m Davies Cotton Small Size Telescope for the Cherenkov Telescope Array, arXiv:1307.2723 [astro-ph.IM] (2013)
5. Pareschi, G., Armstrong, T., Baba, H., Bähr, J., et al.: for the CTA Consortium, Status of the technologies for the production of the Cherenkov Telescope Array mirrors. Proc. SPIE **8861**, 886103 (2013)
6. Orgéas, L., Dumont, P. J. J.: Sheet Molding Compounds. Wiley Encyclopedia of Composites. 1–36 (2012)
7. Sutton, M., Orteu, J. J., Schreier, H.: Image Correlation for shape, motion and deformation measurements. Springer (2009)
8. Pan, B.: Recent progress in digital image correlation. Exp. Mech. **51**(7), 1223–1235 (2011)
9. Hartley, R., Zisserman, A.: Multiple View Geometry in Computer Vision. Cambridge University Press, (2003)
10. Piekarczuk, A., Malesa, M., Kujawińska, M., Malowany, K.: Application of hybrid FEM-DIC method for assessment of low cost building structures. Exp. Mech. **52**(9), 1297–1311 (2012)
11. Malesa, M., Malowany, K., Tomczak, U., Siwek, B., Kujawińska, M., Siemińska-Lewandowska, A.: Application of 3d digital image correlation in 179 maintenance and process control in industry. Comput. Ind. **64**, 1301–1315 (2013)
12. Jin, H., Bruck, H.A.: Pointwise digital image correlation using genetic algorithms. Exp. Tech. **29**(1), 36–39 (2005)
13. Zhang, Z.-F., Kang, Y.-L.: HWang.-W., Qin Q.-H., Qiu Y., Li X.-Q., A novel coarse-fine search scheme for digital image correlation method. Measurement **39**(8), 710–718 (2006)
14. Pan, B.: Reliability-guided digital image correlation for image deformation measurement. Appl. Opt. **48**(8), 1535–1542 (2009)
15. Hu, Z., Xie, H., Lu, J., Hua, T., Zhu, J.: Study of the performance of different subpixel image correlation methods in 3d digital image correlation. Appl. Opt. **49**(21), 4044–4051 (2010)
16. Nguyen, T.N., Huntley, J.M., Burguete, R.L., Coggrave, C.R.: Shape and displacement measurement of discontinuous surfaces by combining fringe projection and digital image correlation. Opt. Eng. **50**(10), 101505 (2011)
17. Pan, B.: Bias error reduction of digital image correlation using gaussian pre-filtering. Opt. Lasers Eng. **51**, 1161–1167 (2013)
18. Pan, B., Li, K., Tong, W.: Fast, robust and accurate digital image correlation calculation without redundant computations. Exp. Mech. (2013). doi:10.1007/s11340-013-9717-6
19. Wang, Y.-Q., Sutton, M.A., Ke, X.-D., Schreier, H.W.: Error Propagation in Stereo Vision: Part I: Theoretical Developments. Exp. Mech. **51**(4), 405–422 (2011)
20. Ke, X.-D., Schreier, H.W., Sutton, M.A., Wang, Y.-Q.: Error Propagation in Stereo Vision: Part II: Experimental Validation. Exp. Mech. **51**(4), 423–441 (2011)
21. Niemiec, J., et al.: For the CTA Consortium, Single-Mirror Small-Size Telescope Structure for the Cherenkov Telescope Array, arXiv:1307.4189 [astro-ph.IM] (2013)
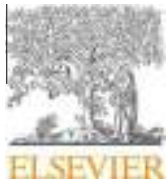
Measurements of geometry of a boiler drum by time-of-flight laser scanning

K. Malowany [a,b], K. Magda [b], J. Rutkiewicz [b], M. Malesa [a,b,*], J. Kantor [c], J. Michoński [a], M. Kujawińska [a]

[a] Warsaw University of Technology, Institute of Micromechanics and Photonics, 8 A. Boboli St., 02-525 Warsaw, Poland
[b] KSM Vision Sp. z o.o., 9/117 Sokołowska St., 01-142 Warsaw, Poland
[c] TAURON Wytwarzanie S.A., Department of Technical Assessment and Diagnosis, 23 Lwowska St., 40-389 Katowice, Poland

ARTICLE INFO

ABSTRACT

In the paper the application of ToF laser scanner in measurements of geometrical parameters of a boiler drum used in a power plant is presented. These parameters are required during renovation works, for verification of correctness of annealing process and optimization of the process of mounting a mechanical steam–water separation. The currently used separations are tightly placed in a boiler drum, so a welding process is not required anymore. This approach saves the time of renovation works, but the geometry of a separation has to be precisely matched against the geometry of the drum to ensure the tightness of connection and, in consequence, to ensure stability of steam parameters (pressure and temperature). Renovation works may include heating processes, after which geometry should also be carefully verified as improperly performed can lead to buckling of a boiler drum. In the presented approach ToF scanner provides cloud of points, which has been subjected to a set of post-processing operations including stitching, cylinder fitting, projection 3D data onto 2D map, 2D data interpolation and filtering. As the result, the required dimensions and tolerances are obtained and are ready for further implementation.

© 2015 Elsevier Ltd. All rights reserved.

1. Introduction

Power generation industry is one of the most vital branches of the economy. In order to ensure safe operation of installations for many years, full-time monitoring and diagnostic tests are carried out, and the resulting data is used while planning overhauls schedule. Lack of adequate maintenance procedures can be a threat to employees as well as to local population and may also cause huge financial losses due to a risk of failures of industrial installations. Currently in most cases monitoring of installations in heat and power generation industry is carried out with utilization of standard pointwise sensors [1,2]. However, due to many unresolved problems, there is still a need to search for alternative techniques for both monitoring and measurement/diagnostic tasks, which could be more accurate, relatively cheaper, and could provide more useful data.

Recently it has been shown that optical measurement techniques may play an important role in maintenance of installations in heat and power generation industry. In [3] the Digital Image Correlation (DIC) method [4] and structured light method [5] have been utilized for displacement and shape measurements of pipelines during start-up. In [6] DIC and thermography have been used for

* Corresponding author at: Warsaw University of Technology, Institute of Micromechanics and Photonics, 8 A. Boboli St., 02-525 Warsaw, Poland. Tel.: +48 608571909; fax: +48 222348601.
E-mail address: m.malesa@mchtr.pw.edu.pl (M. Malesa).

diagnostics of expansion bellows in district heating pipe-lines. In many cases it is also required to monitor displace-ments of pipelines in large volume [7]. Although all mentioned applications proved feasibility of the utilized methods and solved certain engineering problems in heat and power generation industry, for some particular tasks other methods are better suited. This especially includes the tasks in which whole geometry of large objects needs to be determined in a limited time (displacements and strains are not important). An example of such a case is preparation of technical documentation of a boiler drum [8] during repairs.

During renovation works, which include material renewal, holes with material defects are reamed, and removed material is overlaid by welding. After this process whole structure is subjected to the annealing process, in order to ensure material relaxation. Annealing process is performed with the use of eddy-current heating. Due to the length of the structure (16 m without boiler ends), incorrectly performed process of heating will result in buckling. Therefore the geometry should be carefully verified.

During repair process of boiler drums, separations are replaced with new ones, which have to be tightly mounted. The crucial step in mounting new separation is to ensure it fits to the actual geometry of the drum. If this condition is not met, resulting leakages may cause issues with mainte-nance of operational parameters of steam (such as tem-perature and pressure). Precisely described geometry of the boiler drum would significantly facilitate this step, thus saving the time of the process.

Currently technical documentations of boiler drums include the data acquired by surveying. Typically the radius of a boiler drum is measured in 8 points in each seg-ment. The geometry of the boiler drum is described by data merged from all segments. A set of pointwise measure-ments, however, would not be enough to determine geo-metrical parameters such as: cylindricity deviation or segments misalignment. Therefore the full field 3D geome-try measurements have been performed. In power plant the environment is dusty and the accessibility of boiler drum is limited (diameter of input hatch was 0.8 m). Considering this, the three shape scanning methods have been taken into account: measurement arm with triangu-lation based 3D laser scanner (LS) [9,10], structured-light (SL) 3D scanner [5], time-of-flight (ToF) laser scanner [11–15]. First two methods give higher resolution com-pared to ToF method, but the limited size of the measure-ment field would result in a significant increase of the measurement time. Apart from that, large dimensions and limited measurement field imply multiple measure-ments and stitching together resulting point clouds (PCs) that correspond to individual measurements in order to calculate geometrical parameters of the subject being ana-lyzed as a whole. Smaller field of view in the case of LS and SL methods would result in a significant increase in the number of PCs that need to be stitched together when compared to ToF method. This in turn means that longer processing time would be required and lower accuracy could be achieved since every stitching operation introduces some error. Moreover, a ToF scanner is capable

of performing measurements from greater distance, which allows capturing markers and fixed surfaces on opposite ends of the boiler drum during each measurement, and therefore propagation of error connected with PC stitching can be minimalized even further, in contrast to LS and DL methods.

During renovation works the reduction of time is an important issue since installation downtimes cause finan-cial losses, and thus the work described in the paper has been performed with the ToF scanner. Also due to proper selection of ToF parameters and measurement conditions and extensive PC post-processing procedures based on cus-tom-built software we were able to determine geometrical parameters of the drum with sufficient accuracy. In the paper we present at first the measurement methodology and data processing technology chain (Section 2). Then the results of measurement and data processing are reported in Section 3 including: determination of cylindric-ity deviation over the entire length of the drum, Vertical and horizontal deflections along the drum, coaxiality of the drum. Finally, in Section 4, we discuss the practicality of the proposed tools and methodology as well as their acceptance by power generation industry.

2. Methodology

The measurements of geometry of a boiler drum have been carried out in a power plant in Poland. The drum con-sisted of 7 segments and 2 boiler ends (Fig. 1a). The nomi-nal diameter of the measured drum was 1600 mm and its length was 16 m (without boiler ends). The measurement method and the scope of measurements had been carefully planned with power plant technicians.

The goal of the measurements was to determine geo-metrical parameters of the boiler drum. The most impor-tant parameters are:

- cylindricity deviation along the entire length of the drum,
- deflection of individual segments,
- vertical and horizontal deflections along the drum,
- deviation of alignment between sectors of the drum.

All listed parameters have been determined by means of the analysis of the point cloud obtained from the mea-surements. In order to facilitate calculations, the data has been analyzed in cylindrical coordinate system. The obtained point cloud and the orientation of the coordinate system are presented in Fig. 1a.

2.1. Measurements

The measurements have been carried out with Focus 3D S 120 ToF laser scanner manufactured by FARO [16]. ToF is a device that uses laser light to probe the subject. At the heart of the scanner is a time-of-flight laser rangefinder, which only detects the distance of one point in its direction of view. In order to scan the entire field of view, the range finder's direction is changed. The scanner needs to be cali-brated in laboratory in stable conditions before the
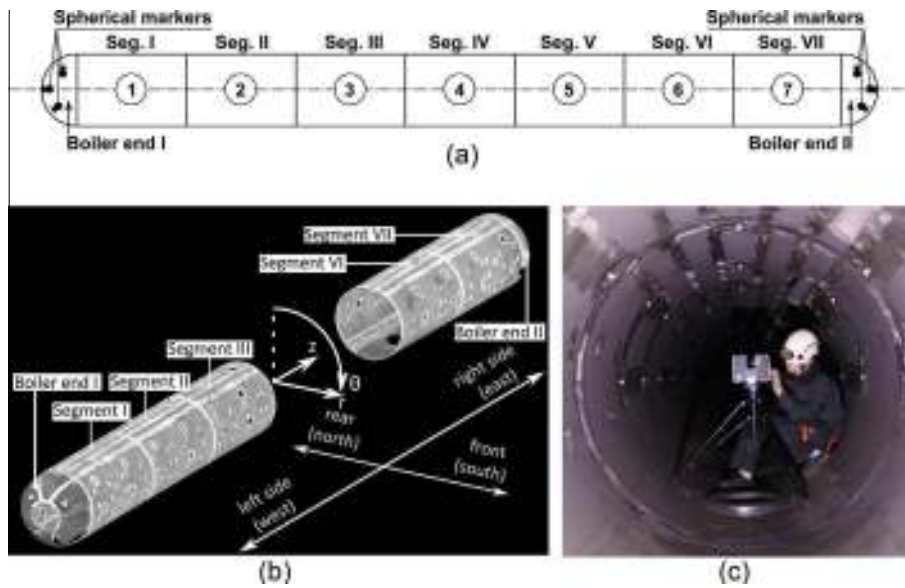
132

Fig. 1. (a) Scheme of the boiler with localization of the spherical markers and successive locations of ToF scanner (numbers inside the circles); (b) point cloud of the measured boiler drum in the cylindrical coordinate system (segments IV and V has not been visualized in order to show the coordinate systems); (c) ToF laser scanner during the measurements inside the boiler drum.

measurements start. Results from ToF scanning are PC representing the geometry of the measured object. The nominal speed of measurements with the particular scanner, that has been used in the measurements, is 976,000 points per second. The nominal range is 0.6–330 m and the accuracy is ±2 mm.

The minimum operating range of the scanner was 0.6 m and the nominal radius of the drum was 0.8 m. In order to ensure good accuracy of measurements, the scanner had to be carefully placed in the center of the boiler drum (see Fig. 1c). Another problem was the length of the drum (approximately 16 m without boiler ends). The best measurement accuracy with ToF scanner can be achieved when the sampling beam is perpendicular to the measured surface. If this condition is not met, the basic accuracy can be decreased. In order to maintain good accuracy along the entire drum, each segment has been scanned separately together with both boiler ends, segments have been scanned one after another starting from one of the boiler ends (Fig. 1a). Light scattering white spheres of app. 15 cm in diameter, delivered with the FARO scanner, have been fixed to the boiler ends in order to facilitate data stitching. Spherical markers have been attached to boiler with the use of magnetic bases. Boiler ends of the drum were visible in each measurement because the drum was empty during the measurements. Each measurement had a "blind spot" beneath the scanner (due to 300° ToF scanner vertical angular range); missing data has been supplemented with data from neighboring measurements.

2.2. Data processing

The input data for the data processing procedure was seven PCs delivered by the measurements with the ToF scanner at the positions shown in Fig. 1a. At the beginning,

each cloud was preprocessed separately. The measurement of each segment was manually edited to cover its area, extended approximately 20 cm along the axis in both directions to ensure overlaps with other segments, and including points representing the boiler ends as well as spherical markers positioned at the ends of the drum in order to facilitate data stitching. The unwanted scanned parts, such as pipes projecting from the boiler drum (see Fig. 2), have also been removed manually. Noise was removed by automatic selection of small groups of points, segmentation was implemented using Hausdorff distance, and by searching for overexposed points. Finally, the PCs of each segment have been stitched together and a cylinder has been fitted to the obtained point cloud. Below the procedures are explained in details.

2.2.1. Point clouds stitching

All operations were performed using custom-built software *Clouds Adjustment* developed by the OGX research group [17–20]. The software is able to perform a number of processing operations on point clouds, such as manual editing, automatic filtering, data segmentation, stitching and color operations. The segments have been stitched starting from the middle segments in the following order: IV, III, V, II, VI, I, VII (see Fig. 1a and b). This sequence allowed to minimize the propagation of error which would occur in the case of sequential stitching of the segments starting from one of the ends. Stitching has been performed in two steps: the first step was coarse semi-manual positioning to ensure a good starting point for fine positioning of segments in the second step; the second step included fine positioning described further in this section.

The coarse positioning was performed with the use of a set of 6 spherical markers placed at the ends of the boiler, 3
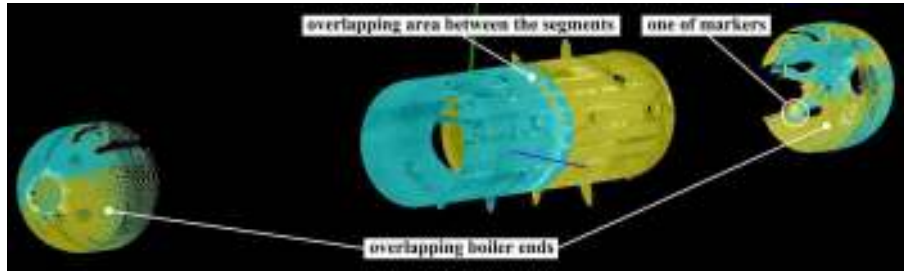
Fig. 2. Two stitched point clouds corresponding to segments IV and V, together with supporting areas corresponding to boiler drum ends with markers. Parts of the scanned pipes projecting from segments IV and V are also visible.

at each end. For each two measurements representing neighboring segments, the markers were identified and labeled manually. Best transformation between the two corresponding sets of markers, consisting of a single rotation and translation, was calculated and applied to one of the segments.

Fine positioning was performed with the use of all available data: spherical markers, overlapping areas between the segments and boiler ends (Figs. 2 and 3). The algorithm used was a modification of the iterative closest point (ICP) point-to-plane algorithm, which iteratively finds the best transformation by minimizing the fitting error [21]. The algorithm consists of four phases. In the first one, the overlapping areas in a stable and fitted PC were found. The areas were identified by searching for points with at least N_O points in their spherical neighborhood of radius equal to d_O (Eq. (1)). This distance is calculated as a multiple of minimum average point-to-point distance d_A in a point cloud.

$$d_O = \sqrt{N_O \cdot d_A/\pi} \qquad (1)$$

The limit N_O was put to ignore areas measured with lower quality (smaller density, which results in less points in neighborhood of defined radius). In this case, N_O equal to

100 was used. Then, from these areas a random sample of points was selected in the stable cloud. In the second phase, each point from the stable subset was paired with its closest point in the fitted cloud. Points in the fitted cloud and their normal vectors were used to calculate plane equations in the third phase. Finally, the optimization algorithm finds the best transformation (translation and rotation) by minimizing the RMS of sum of distances (fitting error σ_{max}) between the current subset of points in the stable cloud and corresponding planes in the fitted cloud. Steps two, three and four were repeated until either the fitting error σ_{max} is below the predefined threshold or maximum number of iterations is reached. The fitting errors σ_{max} obtained during segment stitching were in the range 0.6–0.9 mm.

2.2.2. Cylinder fitting

In order to facilitate calculations all data have been transformed from Cartesian to cylindrical coordinate system (Fig. 4). A cylinder has been fitted to the obtained point cloud with utilization of a least squares algorithm included in the Wild Magic computational library developed by Geometric Tools [22]. The first step of the cylinder fitting algorithm is to find a first approximation of the cylinder axis. This is done by means of fitting a line to a
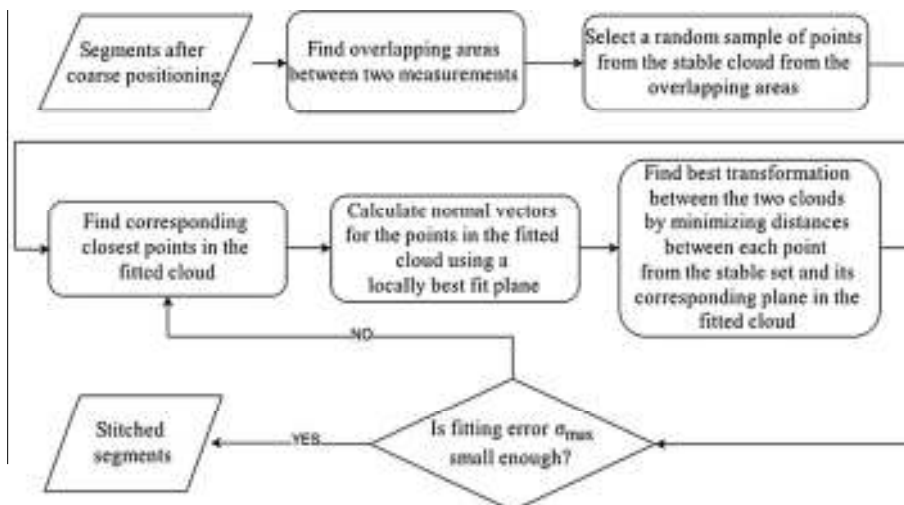

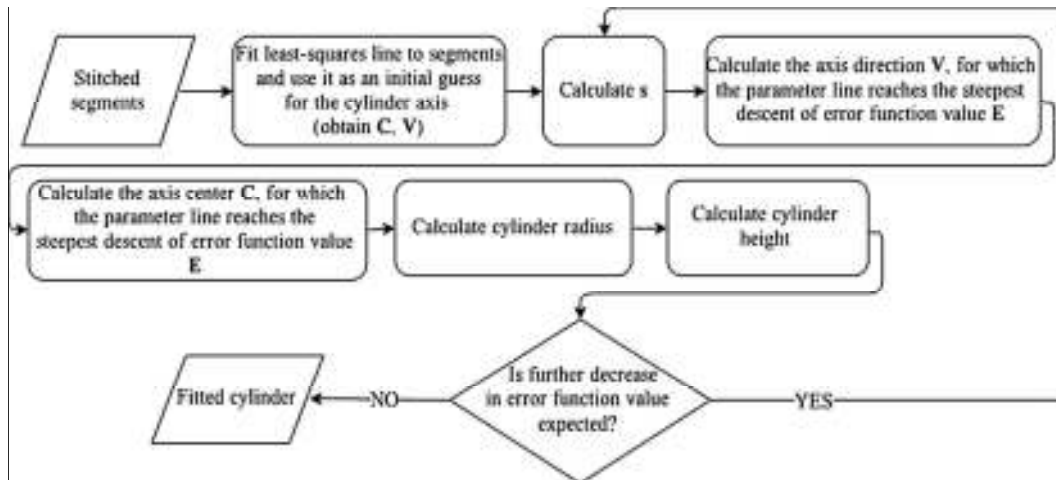**Fig. 3.** The scheme of the fine positioning algorithm.

Fig. 4. Cylinder fitting algorithm.

point cloud data by means of least squares method. The initial guess obtained that way is then used in search for a global minimum of the error function E, which is defined as the sum of squared errors of individual points:

$$E(C,V,s) = \sum_{i=1}^{n}(s(X_i - C)^T(|V|^2 I - VV^T)(X_i - C) - 1)^2 \quad (2)$$

where:

I – identity matrix.
X_i – single measurement point being a part of the point cloud being analyzed, consisting of n points.
$s = 1/(r|V|)^2$.
r – radius of the cylinder being fitted.
V – direction vector of the axis of the cylinder being fitted.
C – point lying on the axis of the cylinder being fitted, also called the axis center point.

As shown in Eq. (2), the error function depends on three key parameters: parameter s, axis direction vector V and axis center point C. During the calculation, first the parameter s is updated, and then vector V and point C are updated in that order with the use of steepest descent method (the search is conducted along the parameter line in the direction of the greatest decrease in error function value). It is possible to use the output of one algorithm iteration as an input for another in order to obtain more accurate results. In case of the boiler drum, 50 iterations have been used as further fitting has not resulted in visible improvements. The algorithm has been described in detail in library documentation [22]. After finding a cylinder that approximates the measurement points in the best way, the axis of the fitted cylinder has been selected as the axis of the new, cylindrical coordinate system.

2.2.3. Noise reduction

For the sake of further analysis, the obtained point cloud representing the cylindrical surface has been projected onto a 2D plane and then interpolated with the use of bilinear interpolation in order to enhance readability of the data. The results contained white noise resulting from the process of measurement with the ToF scanner, and thus the map has been subjected to noise reduction. Since the noise was of high frequency, a low-pass, Gaussian convolution filter has been applied. When the filtration mask reached the bottom edge of the 2D map (Fig. 5), the data for further filtration was taken from the area adjacent to the top edge, due to continuity of map in θ direction which has been preserved after mapping. However, the filtration has been less accurate around the edges of the holes that remained after removal of pipes from the PC (see Fig. 5) since applying Gaussian filter results in edge blurring. Nevertheless, the impact on the results is negligent since the length of the square filtration mask, and thus the affected area, is only 10 pixels, whereas the dimensions of the map being filtrated are approximately 20,000 × 6000 pixels.

3. Measurement results

3.1. Cylindricity deviation over the entire length of the drum

In order to determine the cylindricity deviation over the entire length of the drum, local radius of the drum has been calculated in each point of the cloud. Local radius is a coordinate R in cylindrical coordinate system of point from PC. The results are presented in Fig. 5. In order to facilitate interpretation, the results are visualized as a cylindrical surface mapped onto a plane. To support the assessment of the degree of the cylindrical deviation, the histogram of percentage distribution of dram radius was drawn (Fig. 6).

The range of calculated radiuses of the drum was 794–810 mm. The discrepancy between minimum and maximum radius was 14 mm, which indicates correctness of exploitation and repairs performed previously and we can conclude that the geometry of the drum was not deflected significantly.
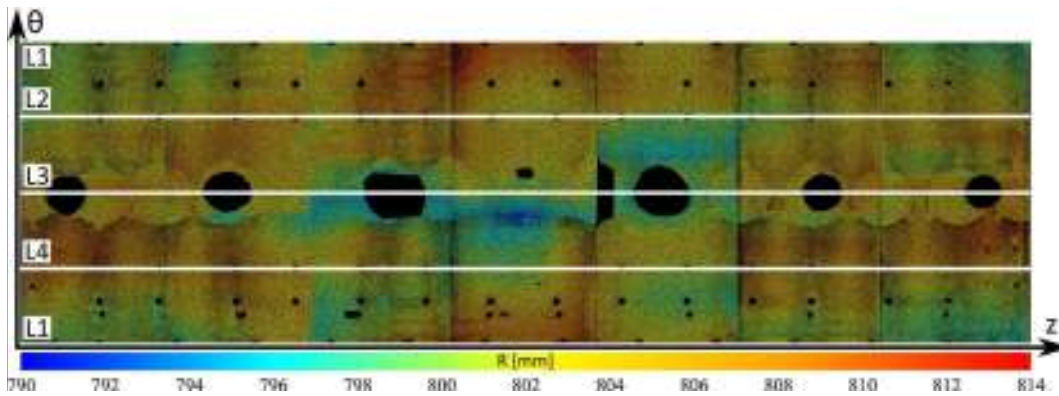
Fig. 5. The radius map of the measured boiler drum after mapping a cylindrical surface onto a plane, with overlaid lines of further analysis; black spots are the result of removing pipes connected to the boiler drum from the PC (large spots on the middle are formed after downcomer inlet [8]).
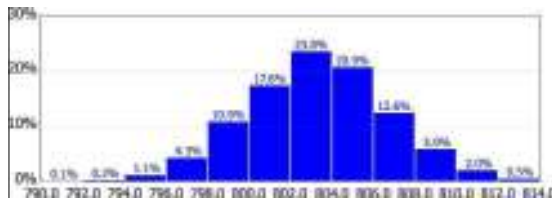

Fig. 6. Histogram of percentage distribution of boiler drum radius.

3.2. Vertical and horizontal deflections along the drum

In order to determine vertical and horizontal deflections along the drum, the obtained point cloud has been cut by two planes (see Fig. 7). Intersections of the planes and the point cloud have been labeled as L1, L2, L3 and L4 lines.

3.2.1. Deflections of radius

Deflections of radius for each segment have been calculated as the maximum deviation of local radius from nominal radius, along lines L1–L4. An exemplary surface profile determined along the line L1 is presented in Fig. 8. Results for all segments and entire drum are presented in Table 1.
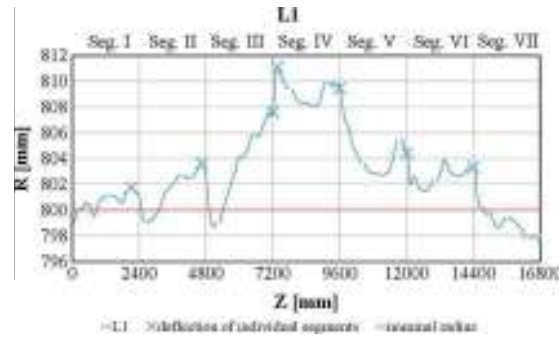

Fig. 8. Radius of the drum distributed along the line L1, with marked maximum deviation from nominal radius (deflections or radius) for individual segments.

Values of deflections of radius did not exceed 11 mm. Taking into account the length of the drum (approximately 16 m), the values of deflections of radius were negligibly small.

3.2.2. Deflections of diameters

In the next step, by adding local radii along lines L1, L3 and L2, L4, vertical and horizontal local diameters have been calculated. Deflections of diameter for each segment
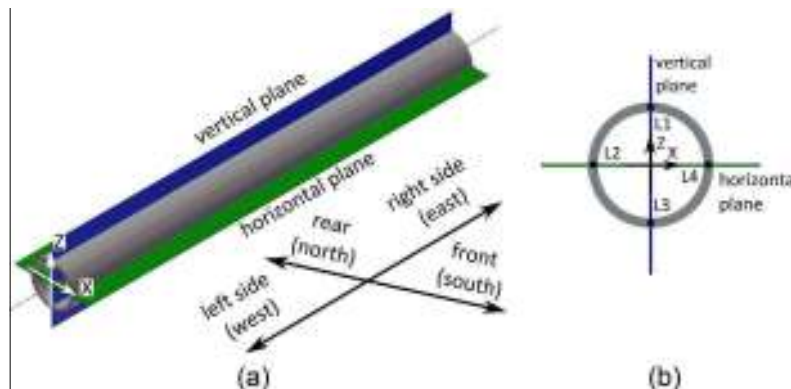

Fig. 7. (a) Visualization of intersection of the drum with the planes (b) view from the front of the drum.

Table 1
Deflections of radius along lines L1, L2 L3 and L4 for each segment and for the entire drum (Max.).

Line	Deflection (mm) in segment							
	I	II	III	IV	V	VI	VII	Max.
L1	2	4	8	11	9	4	3	11
L2	3	6	6	6	3	4	5	6
L3	7	5	−2	2	−2	6	7	7
L4	8	7	3	7	6	6	6	8

Table 2
Deflections of diameters along vertical and horizontal plane for each segment and for the entire drum (Max.).

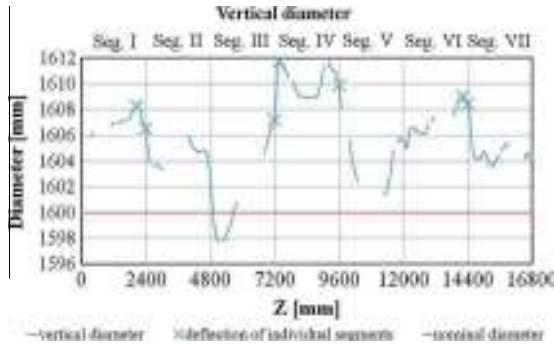| Diameter	Deflection (mm) in segment							
	I	II	III	IV	V	VI	VII	Max.
Horizontal	10	12	9	10	9	8	11	12
Vertical	8	7	7	12	10	9	8	12

Fig. 9. Vertical diameter of the drum, with marked maximum deviation from nominal diameter (deflections of diameter) for individual segments.

have been calculated as the maximum deviation of local diameter from nominal diameter, along the cutting planes showed in Fig. 7. Example diameter distribution along the vertical plane is presented in Fig. 9. Results for all segments and entire drum are presented in Table 2.

Largest deviation from the nominal diameter was 12 mm. Biggest differences of diameter between diameters

of neighboring segments (particularly between sectors 3 and 4) was 14 mm (Fig. 9). Separation between these two segments has been mounted with special care.

3.3. Coaxiality of segments

The calculations were performed in respect to definition of coaxiality tolerance described in the ISO 1101 standard [23]. In order to calculate coaxiality of individual segments relatively to the boiler drum as a whole, the point cloud has been cut by planes perpendicularly to the axis of the drum (Fig. 10a). The location of each plane corresponds to individual segments' ends. As a result, each segment has been limited by two planes. Also, the individual axes of each segment have been determined using algorithm described in Section 2.2.3. For each segment, the intersection between its axis and limiting planes gives two points. The distance between the boiler drum axis and these two points has been calculated and compared, and the greater distance has been chosen as a coaxiality deviation of the considered segment. The procedure is shown in Fig. 10a and b. The results are presented in Fig. 10c.
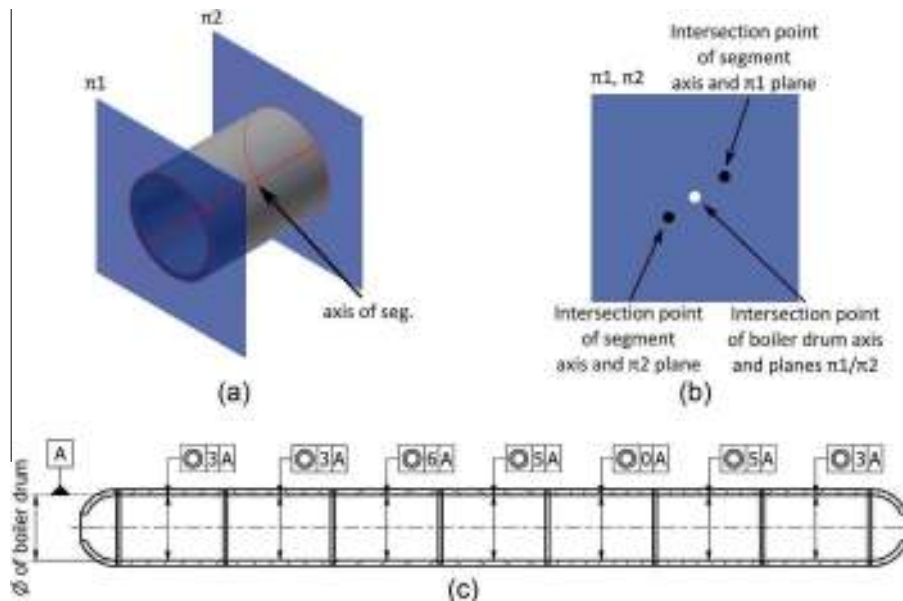

Fig. 10. Visualization of the procedure for calculation of the alignment deviation: (a) cutting planes and the segments (π1 and π2); (b) intersection points of the limiting planes and the segment and boiler drum axes; (c) the result: coaxiality of individual segments relatively to the boiler drum as a whole (A – datum – axis of boiler drum [23]).

Maximum misalignment between sectors of the drum was 6 mm. Taking into account the length of the drum (approximately 16 m) this value is negligibly small.

4. Conclusions

The most important geometrical parameters of the boiler drum have been determined on the basis of the measurement results (in the form of the point cloud) acquired with the ToF scanner. All measurements have been carried out *in-situ* and took less than 2 h. In the presented case the analysis of radii over the entire length of the drum (14 mm discrepancy between minimum and maximum radius) proved the correctness of repairs performed in the past. The results of diameters measurement helped to indicate that separation between sectors no. 3 and 4 had to be mounted with special care (this is because the difference in diameters between these sectors reached as much as 14 mm). Other calculated parameters: deflections of individual sectors and misalignments between the sectors have turned out to be negligibly small.

The amount of the useful data obtained from the measurements can be used to optimize the time of works related to renovation of the boiler drum. This especially applies to the process of mounting mechanical steam–water separation. The obtained geometry of the boiler drum can also be used to control the heating processes connected with renovation works (to verify whether buckling occurred or not). Presented measurement methodology has been accepted by experts from the industry and can be used as a good alternative to the currently used point-wise techniques. In future works we are planning to apply ToF scanning for 3D shape measurements of other crucial parts of a power unit, together with tailored data-processing and analysis. It should be mentioned that the progress in ToF measurement methods, specifically implementation of the phase shifting technology, leads to significant improvement of ToF measurement accuracy. Therefore it is expected that the proposed methodology of a boiler drum (or similar industrial objects) investigation can be in future performed with even better (if needed) accuracy. Another application may include, for example, 3D shape measurement of walls of boiler furnace in order to determine its deformations resulting from inhomogeneous temperature distribution.

Acknowledgments

References

[1] T. Ariman, G. Muleski, A review of the response of buried pipelines under seismic excitations, Earthquake Eng. Struct. Dynam. 9 (1981) 133–152.

[2] J.S. Hyun, G.W. Song, S.Y. Cho, Y.S. Lee, Real-time displacement monitoring system for high temperature steam pipe of fossil power plant, Key Eng. Mater. 297 (2005) 2164–2168.

[3] M. Kujawinska, M. Malesa, K. Malowany, P.M. Błaszczyk, Application of image based methods for monitoring and measurements of structures in power stations, Key Eng. Mater. 518 (2012) 24–36.

[4] M. Sutton, J.J. Orteu, H. Schreier, Image Correlation for Shape, Motion and Deformation Measurements, Springer, New York, 2009.

[5] R. Sitnik, M. Kujawińska, J. Woźnicki, Digital fringe projection system for large-volume 360-deg shape measurement, Opt. Eng. 41 (2002) 443–449.

[6] M. Malesa, M. Kujawińska, K. Malowany, B. Siwek, Diagnostic of structures in heat and power generating industries with utilization of 3d digital image correlation, Proc. SPIE. 8788 (2013) 87881X.

[7] J. Trzeszczyński, System diagnostyczny zapewniający bezpieczną pracę bloków 200 MW eksploatowanych powyżej 300,000 godzin [Diagnostic system for ensuring safe operation of 200 MW power units in electric plants that have been exploited for over 300,000 hours], Dozór Techniczny 2 (2012) 26–30 (in Polish).

[8] <http://www.enggcyclopedia.com/2012/01/drums-mechanical-steam-water-separators/> (19.10.14).

[9] A. McCarthy, R.J. Collins, N.J. Krichel, V. Fernandez, A.M. Wallace, G.S. Buller, Long-range time-of-flight scanning sensor based on high-speed time-correlated single-photon counting, Appl. Opt. 48 (2009) 6241–6251.

[10] S. Pellegrini, G.S. Buller, J.M. Smith, A.M. Wallace, S. Cova, Laser-based distance measurement using picosecond resolution time-correlated single-photon counting, Meas. Sci. Technol. 11 (2000) 712–716.

[11] F. Chen, G.M. Brown, M. Song, Overview of three-dimensional shape measurement using optical methods, Opt. Eng. 39 (2000) 10–22.

[12] D. González-Aguilera, P. Rodríguez-Gonzálvez, J. Armesto, P. Arias, Trimble GX200 and Riegl LMS-Z390i sensor self-calibration, Opt. Express 19 (2011) 2676–2693.

[13] J. Chow, D. Lichti, W. Teskey, Accuracy assessment of the Faro Focus3D and Leica HDS6100 panoramic type terrestrial laser scanner through point-based and plane-based user self-calibration, in: Proc. FIG Working Week, 2012, pp. 1–15.

[14] W. Boehler, M. Bordas Vincent, A. Marbs, Investigating laser scanner accuracy, in: Proc. of XIXth CIPA Symposium, 2003, pp. 696–702.

[15] K. Mechelke, T.P. Kersten, M. Lindstaedt, Comparative investigations into the accuracy behaviour of the new generation of terrestrial laser scanning systems, Optical 3-D Measurement Techniques VIII I (2007) 319–327.

[16] <http://www.faro.com> (19.10.14).

[17] <http://ogx.mchtr.pw.edu.pl> (19.10.14).

[18] R. Sitnik, M. Kujawińska, From cloud-of-point coordinates to three-dimensional virtual environment: the data conversion system, Opt. Eng. 41 (2002) 416–427.

[19] M. Karaszewski, R. Sitnik, E. Bunsch, On-line, collision-free positioning of a scanner during fully automated three-dimensional measurement of cultural heritage objects, Robot. Auton. Syst. 60 (2012) 1205–1219.

[20] R. Sitnik, M. Kujawinska, W. Załuski, 3DMADMAC system: optical 3D shape acquisition and processing path for VR applications, Proc. SPIE. 5857 (2005) 58570E.

[21] K.L. Low, Linear least-squares optimization for point-to-plane ICP surface registration, Technical Report TR04-004, Department of Computer Science, University of North Carolina, 2004, pp. 1–3.

[22] <http://www.geometrictools.com/Documentation/CylinderFitting.pdf> (26.10.13).

[23] ISO 1101:2012, Geometrical Product Specifications (GPS) – Geometrical Tolerancing – Tolerances of Form, Orientation, Location and Run-out, third ed., ISO, 2012.

Original Research Article

Comparative analysis of numerical models of arch-shaped steel sheet sections

Artur Piekarczuk [a,*], Krzysztof Malowany [b]

[a] Building Research Institute, 1 Filtrowa St., 00-611 Warsaw, Poland
[b] Institute of Micromechanics and Photonics, Warsaw University of Technology, 8 Św. A. Boboli St., 02-525 Warsaw, Poland

ABSTRACT

The modern construction industry makes use of innovative production and assembly technologies, whose purpose is to implement reliable and simple structures. One product of such technologies is an arch-shaped steel sheet section that might be used as a self-supporting covering for general construction and industrial building construction. Considering complex geometry and boundary conditions, the FEM model of this structure is sophisticated and may contain errors. This paper presents numerical approaches for the calculation of sheet metal section elements of such coverings, namely two numerical approaches that differ in detailing of the properties of considered physical object. The first approach is based on a model that is characterized by simplified geometry and boundary conditions. The second scenario concerns a detailed FEM model with actual geometry captured by a laser triangulation method, experimentally determined material stress–strain relationship, and load conditions measured on an experimental stand. The results obtained with the use of computer simulations based on both approaches described above and experimental results are compared. The errors caused by simplification of the first numerical model are discussed. Finally, an acceptable reduction of FEM model complexity is proposed for the analyzed structure.

© 2016 Politechnika Wrocławska. Published by Elsevier Sp. z o.o. All rights reserved.

1. Introduction

Self-supporting arch-shaped covering structures originally served as temporary facilities for military and agricultural purposes. This covering type gained popularity mainly due to its simple design, quick installation and relatively low implementation costs compared to traditional types of covering structures (reinforced concrete, wood, and steel elements). Currently, this type of covering (the ABM 240 system) is used more and more often in the construction of public buildings. This technology is used to build coverings with spans ranging from 6 to 30 m with varying rise-to-span ratios [1]. The covering elements referred to as sections are fabricated on-site by the use of mobile rolling mills (Fig. 1), which form individual curved sections by

---

Fig. 1 – Section surfaces.

cold rolling from a single steel sheet (with a thickness of 0.7–1.5 mm).

Once formed, the section features the characteristic corrugated and wavy surfaces (Fig. 1). Individual sections are joined together by rolling down the free edges. The result is a curved surface constituting a self-supporting roof of the structure.

The existing calculation methods are based on the assumptions for steel bar structures analyzed in flat static systems [2–4]. For calculation of the structural components and stability, the following standards have been used: EN 1993-1-1 [5], EN 1993-1-3 [6], EN 1993-1-5 [7] and EN 1993-1-6 [8]. The normative documents present general principles for determining the load bearing capacity and stability, but they are not relevant to arch elements with a corrugated and wavy centre surface. Therefore, it is not possible to estimate the local loss of stability of a shell member with complex geometry. The height of the corrugation and waves of the centre surface of the section can be different depending on the bending radius of the arch and thus have a direct impact on the load bearing capacity and stability of the structure. The first pilot tests of full-sized arch-shaped elements of sheet metal sections were performed in the Building Research Institute [9]. The tests showed a strong impact of the local loss of load capacity on the stability and load capacity of the entire structural system. The mode of local stability loss of corrugated profiles subjected to axial and eccentric compression loads has been investigated in paper [10]. The results of numerical calculations and experimental tests were compared, and they showed a divergence between the results of the tests and those of the calculations due to the local loss of stability; in the presented study, the axial and compression stiffnesses of the tested profiles had not been taken into account. Similar studies were performed in papers [11,12]. These concerned the ABM 120 system. The study used point system measurement and numerical models with geometry created by scanning. The main difference was that the work of Walentynski et al. [11,12] did not take into account local strain measurements. Test results and calculations relate only to critical loads.

The main problem in implementing numerical analysis is the selection of a suitable shell model, which is a representation of the actual real-life working conditions of the system. This article describes the process of searching for the optimal model, taking into account the different levels of modelling precision and the adoption of boundary conditions. As a result of the process, information is obtained about possible errors of the systematic models. This information is useful for further

work on full-sized modelling of covering elements and analysis of structures in real-life load conditions. In paper [13], a comparison between three different FEM models with simple boundary conditions and different levels of geometry simplification were performed, the model that gave results closest to the experimental ones was chosen for further analysis. The article presents the impact of selected modelling parameters on computational results using two numerical model: the first from the previous study [13]; and the second with actual geometry captured by a laser triangulation method, experimentally determined material models assigned to different regions of the structure, and load conditions measured on an experimental stand. The computational results will be compared with the available experimental results.

2. Assumptions

The computations and tests concern a section, which is a fragment of an arch-shaped covering fabricated using the ABM 240 technology. The assessment of simplified numerical models is presented in the article [13]. This article analyses three numerical section models that differed by the accuracy of geometry mapping. The models were assessed by comparing the calculation results with the test results. On the basis of the analysis, a single model that showed good similarity with the test results was selected. It can be assumed that the analysis described in the article [13] is an approximation of the modelling problem for a single reference value, i.e., the breaking force; however, it does not answer the question of how changes of individual parameters affect the computation result of the full range of reference value variation (a force of 0 to a destructive force). To fully compare the results of calculations, the simplified model selected in the article [13] was compared with the results of the model with perfectly mapped geometry, obtained as a result of 3D scanning. The difference between those two FEM models occurs also in boundary conditions, described in detail below.

In the article, two modelling scenarios are considered:

Scenario 1: The bilinear material model (referred to as the plastic web) is assumed on the basis of measuring the yield strength of the steel sheet prior to forming it into a section. After forming a section with the use of a rolling mill, the essential parameters of the geometry are measured (the parameters are marked in Fig. 9, and values are listed in Table 2), allowing for the creation of its own model. On this basis, a numerical model is created in commercial software from ANSYS. The element load method is assumed, i.e., eccentric compression carried out by axial forced displacement as a single-parameter extortion and theoretical support conditions. On the basis of these data, numerical analysis is performed. The result of the computation is the value of the support reaction as a function of forced displacement.

Scenario 2: The numerical model is created by importing a 3D scan of the test item. This model contains all of the geometric details. The conditions for support and load, in the form of displacements and rotation angles of supports, are adopted (multi-parameter geometric extortions) from earlier tests performed and entered as forced in the computational
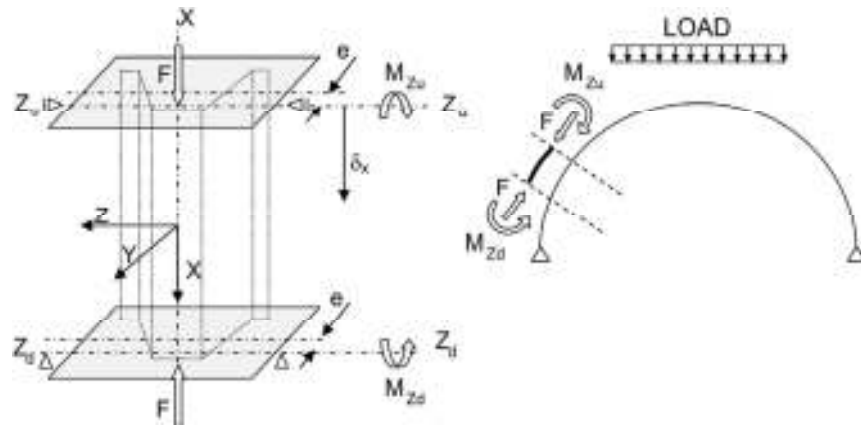
Fig. 2 – Test bench diagram [13].

model. The material model is adopted based on the measured strength properties of samples cut out from the element after the tests. The result of the computation is the value of the support reaction as a function of forced displacement.

It should be emphasized that Scenario 1 contains only vertical displacement as a load condition, in contrast to Scenario 2, which includes displacement and rotation, the same as in the test. Detailed data are summarized in Section 4.4. By comparing results of numerical analysis performed with the use of modelling approaches 1 and 2 against the test results, the model error is determined.

3. Tests

3.1. Tested specimens

The test piece is a section of the arch with a length of 1.0 m and a bending radius of 18 m, made of steel with a nominal thickness of 1.00 mm and the declared class S320GD+Z. The test bench design recreates the interaction of the other parts of the arch-shaped covering so that it maintains the section in a stable position and ensures transmission of internal forces according to the diagram of impacts of the remaining part of the arch. The X-axis is assigned to the specimens in such a way that it passes through the centre of gravity of cross sections, along the longitudinal axis. For test purposes, it was assumed that the load is applied to the

eccentricity (e), which in turn gives rise to the axial force (F), displacement (δ_x), and bending moment (M_{Zu}; M_{Zd}) (Fig. 2). This arrangement of forces corresponds to the actual distribution of forces in the cross-section of internal forces.

The tests of a section length were carried out on a test bench prototype (Fig. 3), which allows for axial and eccentric compression of the test piece. The load was carried out with the use of hydraulic cylinders, and the force was measured with the use of dynamometers coupled with a displacement measuring system. Measurement of displacement as a function of force was carried out continuously until the destruction of the sample.

The test piece (1) is mounted by means of screw connections in the top and bottom stabilization plates (2). The bottom plate is pin-supported. A pressure bar (3) is attached to the top plate, fitted with two dynamometers (4). Force is applied to the dynamometers through the use of a set of tendons and pulleys (5) fixed to hydraulic cylinders (5). The entire weight of the handles and the test piece is compensated by gravity through a set of weights (7) attached to the pressure bar. The measurement system (Fig. 4) consists of 8 inductive sensors, which are marked in the drawing with the symbols A1, A2, B1, B2, B3, B4, C1, and C2.

Sensors are used to measure the displacement X_1 of the upper stabilization plate and the rotation angles of the upper and lower plates: R_{x1}, R_{x2}, R_{y1}, R_{y2}, R_{z1}, R_{z2}. The test results are shown graphically in Fig. 5.
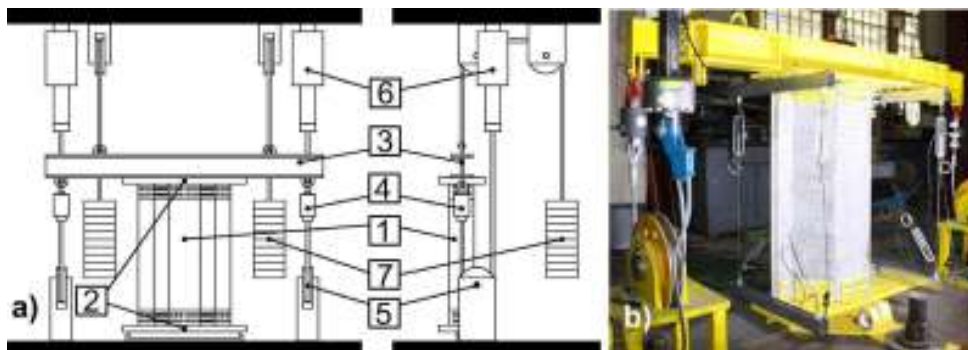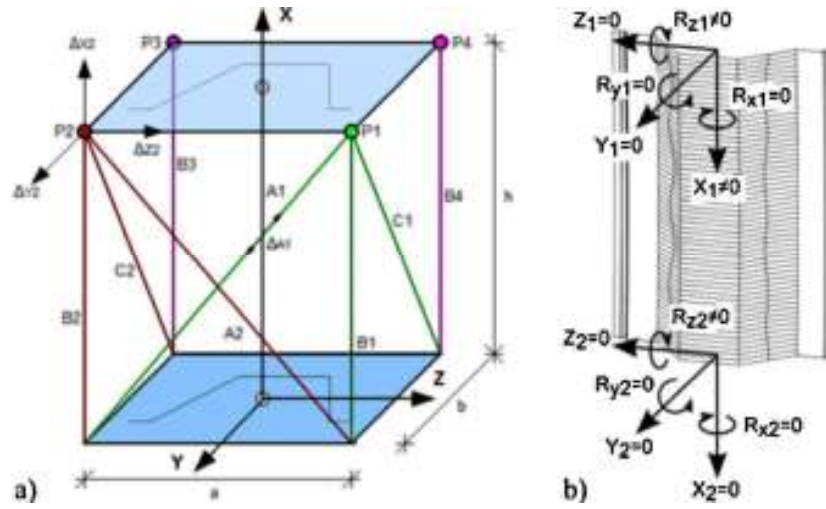

Fig. 3 – Test bench description [13].

Fig. 4 – The measuring system and determination of the measured values, (a) the measuring system, (b) determination of displacements and rotations.
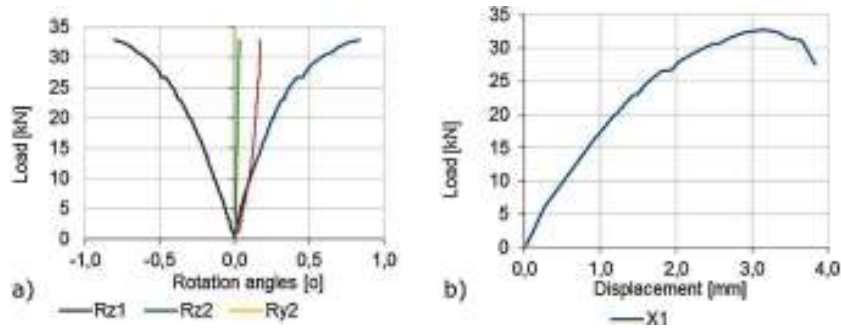

Fig. 5 – Measurement results, (a) the angles of rotation, (b) displacement along X_1 axis.

3.2. Material testing and material stress–strain relationship

The purpose of the test is to determine the actual yield strength and ultimate strength of the test pieces in accordance with EN ISO 6892-1:2009 [14]. Other properties, such as the longitudinal elastic modulus and Poisson's ratio, are adopted in accordance with the standards [5]. On the basis of the test results, a material model will be developed for adoption in the numerical computation. The method for testing the properties of the materials is described in scenarios 1 and 2 (item 2). They include the following:

Scenario 1: Base material tests. Samples were cut out from a flat metal sheet prior to the formation of the section. At this stage, 30 static tensile tests were carried out.
Scenario 2: Testing the material cut out from the test piece. Samples were taken from the three areas marked in Fig. 6.

Samples for the tests were collected from the test piece after tests from areas A, B, and C, outside of the zone of local loss of stability. Area (A) includes the central part of the corrugated surface, area B includes the wavy and corrugated webs, and area (C) refers to the web parts with longitudinal

Fig. 6 – Areas and directions of sampling.

142

Table 1 – The results of the static tensile test.			
Scenario 1	**Scenario 2**		
	Area A (corrugation)	Area B (waves)	Area C (flat)
R_e = 366.3 MPa R_m = 383.6 MPa	R_e = 353.9 MPa R_m = 399.4 MPa	R_e = 374.0 MPa R_m = 391.4 MPa	R_e = 351.8 MPa R_m = 393.5 MPa

ribbing but without corrugation. The direction of sampling in various areas is shown by arrows in Fig. 6. The results of the static tensile tests (average values) in terms of yield strength (R_e) and ultimate strength (R_m) are summarized in Table 1.

The test results were assessed statistically. The purpose of the assessment was to determine whether the test results obtained for sheet samples in areas A, B, and C (scenario 2) did not differ statistically from the results of the flat sheet (scenario 1). To verify the normality of the distribution of the test results, the Shapiro–Wilk test was used for the flat sheet tests (30 trials). The hypothesis of the normal distribution of the results has been confirmed. Further analysis included test results of samples from areas A, B, and C. Test statistics were applied for the average values of Student's t-distribution with and without the assumption that the variances are equal in populations. On the basis of the analyses, it was demonstrated that the test results of samples from areas A, B, and C are significantly different from the results obtained from the flat sheet tests. It was found that, statistically, the results of the samples from areas A, B, and C also differ from each other. This means that the results of the series of 30 flat sheet tests cannot be used as the basis of the development of a material model that will be used in the calculation of geometric models in accordance with scenarios 2. A single model of the material behaviour to be used in the modelling approach 2 also cannot be used. Therefore, different material models were subsequently developed. The results of this work are presented in Section 4.1.

4. Numerical analysis

4.1. Material stress–strain relationship

In scenario 1, a steel stress–strain relationship is assumed to be of elastic–plastic nature with a nominal plateau slope in accordance with [7]. Fig. 7 shows a bilinear model with a solid line and the averaged measurement result of 30 static tensile tests (scenario 1) with a dotted line. The graphical representation of the material model is shown on a scale of strain limited to 0.02%.

Next, the stress–strain relationship has been entered into the Engineering Data Sources module of the ANSYS system [15], into bilinear isotropic hardening.

In scenario 2, the stress–strain relationship adopted for numerical analysis with the use of the ANSYS programme [15] was developed in co-ordinates σ_{true}–ε_{ln}. The steel material properties are adopted as true stress–strain curve modified on the basis of the test results as follows:

$$\epsilon_{ln} = \int_{l_0}^{l} \frac{dl}{l} = \ln\left(\frac{l}{l_0}\right) = \ln\left(\frac{l_0 + \Delta l}{l_0}\right) = \ln\left(1 + \frac{\Delta l}{l_0}\right)$$
$$= \ln(1 + \epsilon_{eng}) \tag{1}$$

$$\sigma_{true} = \sigma_{eng}(1 + \epsilon_{eng}) \tag{2}$$

where ε_{ln} – logarithmic strain, σ_{true} – true stress, σ_{eng} – engineering stress (test result), ε_{eng} – engineering strain (test result), Δl – increase in the sample length [mm], l_0 – initial sample length [mm].

Stress–strain relationship is determined separately for each location on the surface of the section, i.e., areas A (corrugation), B (waves), and C (flat) according to the marks in Fig. 6. A graphical representation of the stress–strain relationship with a scale of strain limited to 0.02% with respect to the test results is shown in Fig. 8. Next, the numerical material stress–strain relationship will be implemented in the module Engineering Data Sources of the ANSYS system, into multilinear isotropic hardening.

The material models were assigned to areas corresponding to the sampling point for strength tests. A graphical representation of the areas with the assigned material model is presented in Fig. 11(b).
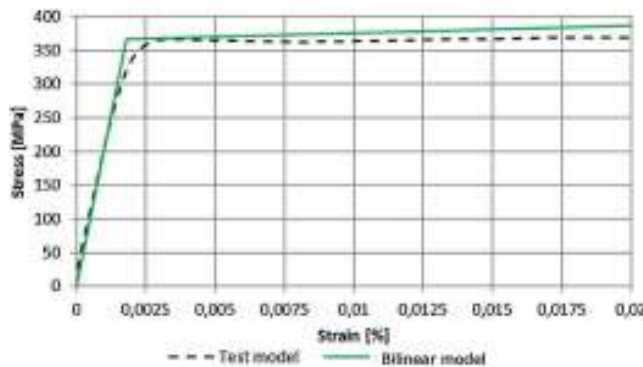

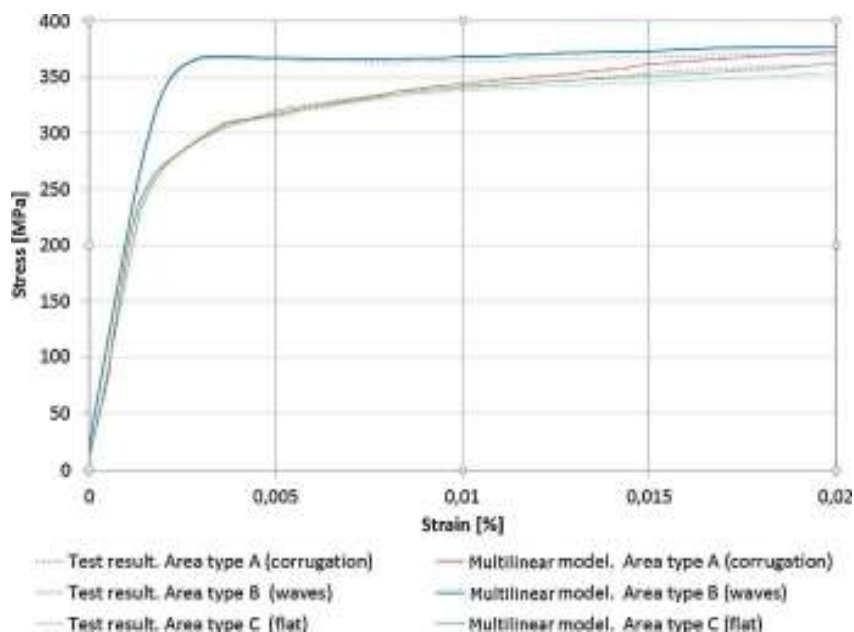Fig. 7 – Material model – Scenario 1.

Fig. 8 – Material model area A (corrugation), B (waves), and C (flat) – Scenario 2.
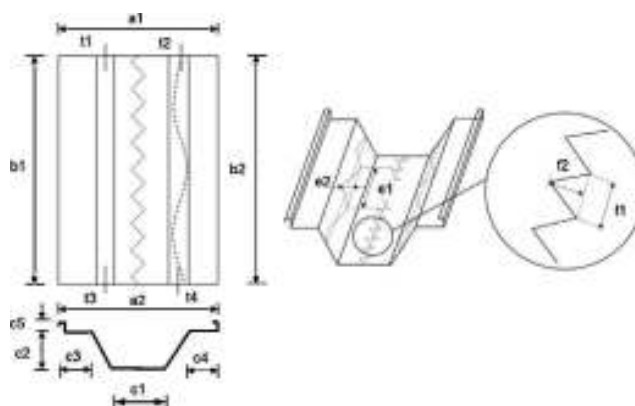

Fig. 9 – Sample view and explanation of symbols used in Table 2 [13].

4.2. Preparation of the geometric data for models

Two models were prepared for computation. The first model (scenario 1) was developed on the basis of the measurement of the test piece and entered into the Workbench module of the ANSYS programme. Geometric data were obtained from the test piece measurements. The identification of dimensions is shown in Fig. 9, and the measurement results are provided in Table 2.

The model includes the corrugation of the central part of the section (sector A), the corrugation and waving of the webs (sector B) and the non-ribbed portions of the webs with the bends (sector C). The longitudinal axis is curved on the arch with a radius of 18 m. The model assumes simplifications, which consist of the omission of bend radii on the border between sectors A, B and C. The longitudinal ribbing on the surface of sector C was also disregarded.

The geometry of the section of profiled steel sheets (second model – scenario 2) was obtained with the use of a handheld scanner, the Nikon ModelMaker MMCx, mounted on 7-axis articulated arm, the Nicon MCAx [16] (Fig. 10). The measurement is based on a laser triangulation method, with the measurement accuracy equal to ±0.1 mm. The obtained geometry is represented as a point cloud, which was loaded into the FEM model.

4.3. Selection of finite elements

In models implemented in scenarios 1 and 2, Shell 281-type elements, shell elements with 8 nodes and six degrees of freedom at each node (three degrees of freedom of displacement and three degrees of freedom of rotation), were used with a quadratic interpolation function [17]. The parameters of the model meshing implemented in scenarios 1 and 2 are summarized in Table 3.

The parameter element quality (EQ) concerns the quality of the finite element mesh. This parameter is in the range

Table 2 – Actual dimensions of the sample (all values are given in mm).																
Width and height of web and flanges									Depth and length of the wave		Depth and length of corrugation		Sheet thickness			
a1	a2	b1	b2	c1	c2	c3	c4	c5	e1	e2	f1	f2	t1	t2	t3	t4
679	659	1018	1015	203.1	169.1	109.9	102.4	26.6	242.1	8.83	34.5	2.73	0.95	0.95	0.95	0.95

Fig. 10 – Geometry measurements of the section of profiled steel sheets.

between 0 and 1, where the value of 0 for the surface area (2D) is defined as an element of poor quality, and the value of 1 denotes a very good mesh. The parameter aspect ratio in the surface arrangement (2D) is defined as the ratio of the longest side to the shortest side of the finite element. The best parameters of the mesh are when the AR coefficient achieves the value of 1.0. Detailed rules for the determination of these

parameters are given in [17]. To evaluate the relationship of qualitative models, a reference level was adopted for the finite element mesh created for Model 2 (the 3D scan). For Model 1, the numbers of elements and nodes were selected in such a way that the discrepancy in relation to the reference model was not greater than 0.5%. EQ and AR parameters are close to 1, which means that the mesh elements are of good quality.

4.4. Conditions for support and load

The upper and lower supports are provided by a type of remote displacement [17] that maintains the Rigid-type relationship. This means that the degrees of freedom of displacement and rotation are associated with the central fulcrum in the local coordinate system. This method of support corresponds to fixing the rigid plate to the upper and lower edges of the section. The values of displacement and the angles of rotation may be released or forced.

Scenario 1 is computed with the assumption that the load is only a kinematic extortion by the displacement, which is applied to the upper support in the X-axis (axial displacement).

Scenario 2 is computed with the assumption that the load is a kinematic extortion by the displacement and the angles of rotation of the upper and bottom support. Extortion values are adopted from the tests. Table 4 presents a detailed description of the support and load conditions.

For the purpose of entering data load as boundary conditions (remote displacements) of the FEM model, the loads have been discretized into 10 intervals. Since scenario 1
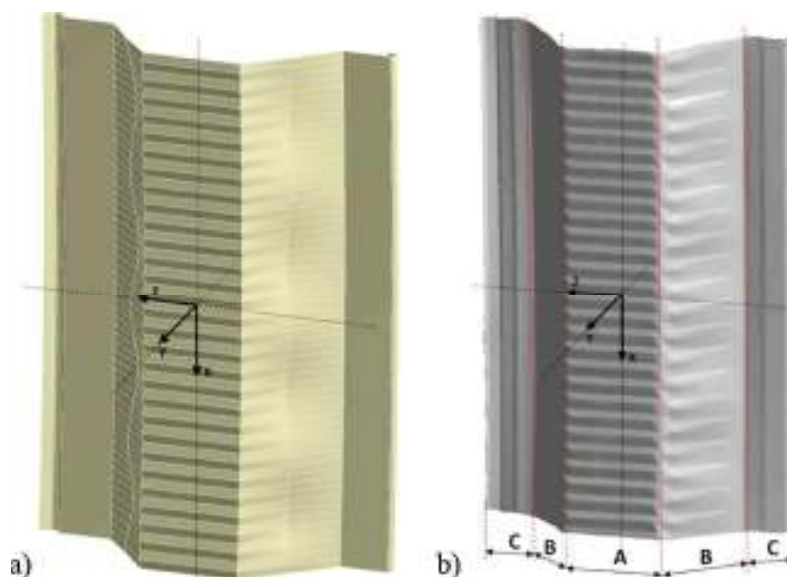

Fig. 11 – Numerical model of the section, (a) model 1 (created in ANSYS workbench), (b) model 2 (3D scan).
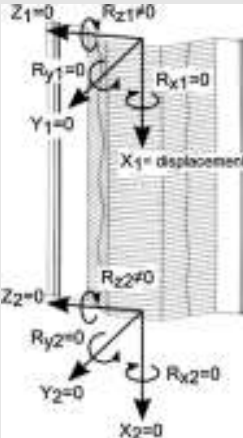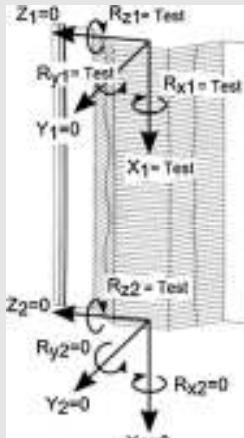
Table 3 – Finite element mesh parameters.

Scenario 1 (model 1)				Scenario 2 (model 2)			
N	E	EQ	AR	N	E	EQ	AR
172.903	57.329	0.988	1.075	172.686	57.567	0.951	1.174

N, number of nodes; E, number of finite elements; EQ, element quality; AR, aspect ratio.

Table 4 – Conditions for support and load.

Scenario 1		Scenario 2	
Top support	Bottom support	Top support	Bottom support
X_1 = displacement	$X_1 = 0$	X_1 = test	$X_1 = 0$
$Z_1 = 0$;	$Z_2 = 0$;	$Z_1 = 0$;	$Z_2 = 0$;
$Y_1 = 0$;	$Y_2 = 0$	$Y_1 = 0$;	$Y_2 = 0$
$R_{x1} = 0$;	$R_{y1} = 0$	R_{x1} = test	$R_{y1} = 0$
$R_{y1} = 0$;	$R_{y2} = 0$	R_{y1} = test	R_{y2} = test
$R_{z1} \neq 0$	$R_{z2} \neq 0$	R_{z1} = test	R_{z2} = test

assumes remote displacements in X_1 direction only, the extortion is composed of 10 equal sequences of displacement, with the value increasing from 0 to 3.0 mm in 0.3-mm intervals. In the scenario 2, the extortions are experimentally measured, therefore displacements and rotations obtained from the tests were discretized into 10 intervals. The discretization of displacements and angles of rotation of supports is presented in Fig. 12. The solid lines show the test results, and the points on the lines are data discretely assigned to 10 sequences.

The computation was performed using the arch-length approach with the full Newton–Raphson method [17].

4.5. Comparison between computational results

The results of the computations for the simplified model (scenario 1) and the scanned 3D model (scenario 2) are summarized in the following configurations:

- a graph showing the displacement–force (reaction) in the full load range with respect to the test and computational results,
- a graph showing the percentage discrepancy of the computational results with respect to the test results and

the mutual evaluation of the divergence of the numerical models,
- maps of reduced stresses, displacements and strains for the reaction peak value caused by the kinematic extortion of appropriate models,
- strain area maps with a size of 200 mm × 200 mm located in the central zone of the computational models.

The results of the analysis of the force as a function of vertical displacement are presented in Fig. 13. The force is obtained as a reaction to the actions of extortion kinematic.

In the graph, the peak forces and the corresponding displacements are identified. The peak force is reached when the strength limit of the element is achieved. When this value is exceeded, the test piece and the computational models lose their stability (falling curve). Table 5 summarizes the tests and computational results, which contain the peak values of forces and their corresponding axial displacements.

Because it is difficult to quantitatively evaluate the deviation of the computational results from the test results for each load level in Fig. 13, the test and computational results are presented in a unified data system for further analysis.
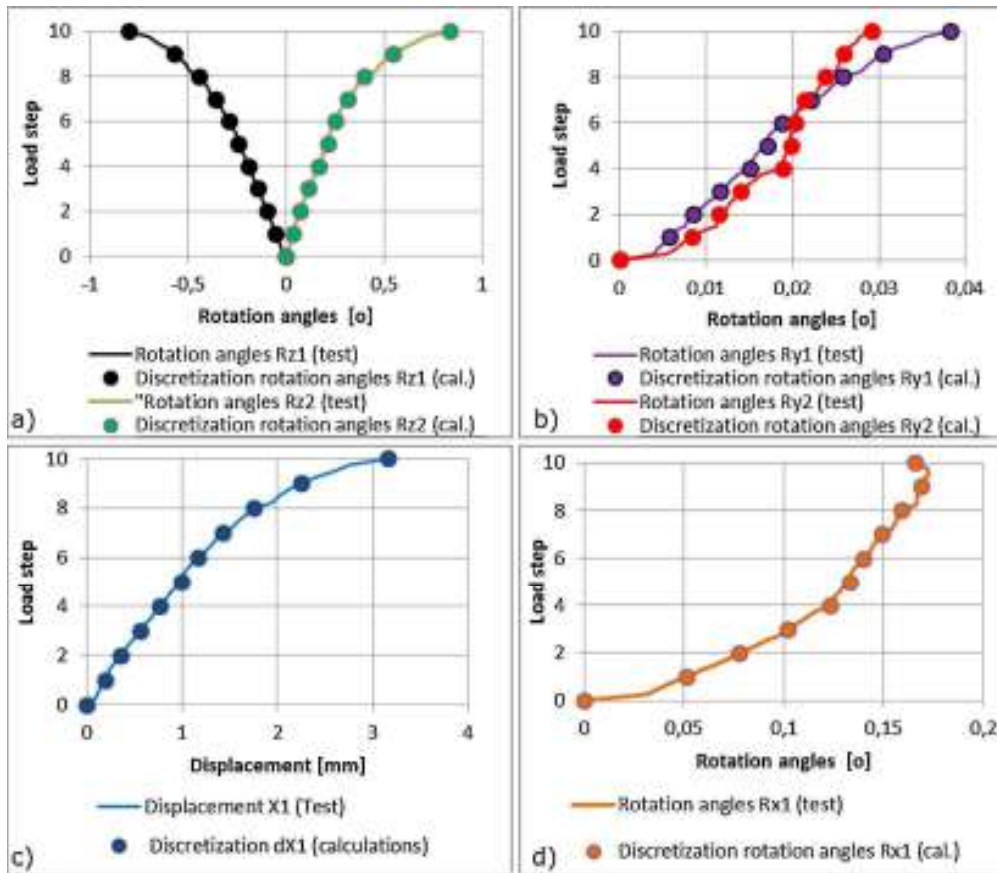
Fig. 12 – Test results and discretization of data in the scale of 10 sequences of extortions (test): (a) rotation angles of the top and bottom support with respect to the z-axis, (b) rotation angles of the top support with respect to the X-axis, (c) displacement of the top support along the X-axis, and (d) rotation of the top support with respect to the X-axis.

Table 6 presents the percentage deviation of the computational models from the test results over the entire range of load, determined with the use of the formula:

$$\Delta_{\%,i} = \frac{F_{\text{test},i} - F_{\text{cal},i}}{F_{\text{test},i}} \cdot 100 \, [\%] \tag{3}$$

where $F_{\text{test},\, i}$ – test result presented as a reaction initiated by kinematic extortion on the ith step (i = 1, 2, …, 10), $F_{\text{cal},\, i}$ – computational result presented as a reaction initiated by kinematic extortion on the ith step (i = 1, 2, …, 10).

A load step shall be understood as a conventional analysis interval used by the ANSYS software, in which a change in the kinematic conditions occurs (see Section 4.4). Table 6 shows the percentage divergences in the entire range of the analysis.

Divergences in computational results with respect to tests in the initial stages of extortion increase, reaching approximately about 13%. In the subsequent steps, as extortion increases, the divergences decrease; in step 5 of the analysis, the computational and test results converge, which corresponds to the force of approximately 22.5 kN. Then, the discrepancy increases and, upon achieving the peak force values, reaches 1.07% for the scenario 2 and 5.52% for the scenario 1.

The computational results are shown as a map of displacements and stresses in Fig. 14. The figure shows the map of reduced stress and the map of axial displacement for reaction peak values caused by kinematic extortion. Additionally, a graph is presented that shows an increase in the reaction and an increase in the stress reduced as a function of the increase (10 steps) of the kinematic extortion. The computational results of the simplified model (scenario 1) indicate the symmetry of the stress and displacement maps. The effect of the simplifications is visible, especially in the transition area between the corrugation web and corrugation flanges (see Fig. 1). The force peak value in Fig. 14(b) is present in the plastic zone. As far as the computations of the 3D model (scenario 2) are concerned, maps at the peak force range of reduced stresses do not show large areas of stress increase as in the simplified model (scenario 1). This is due to the

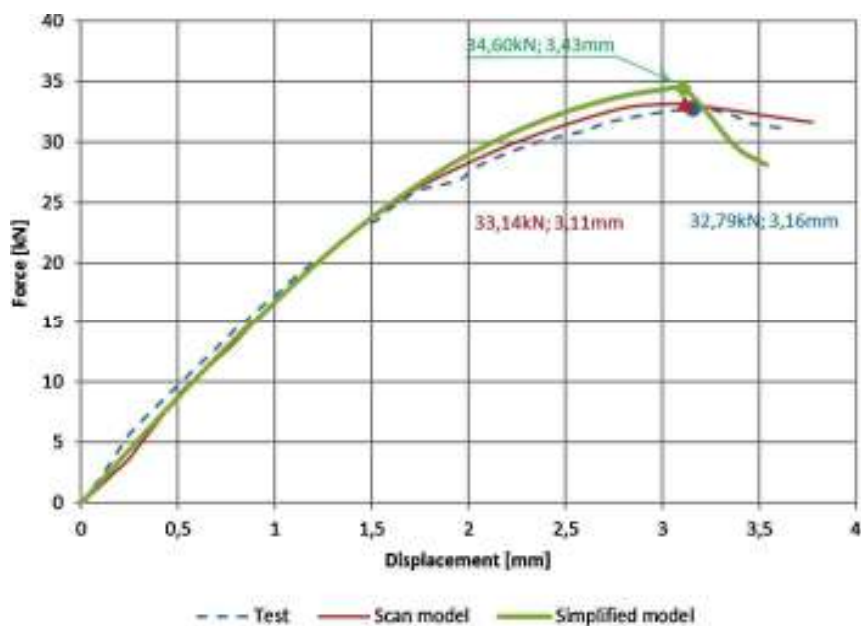| Table 5 – Test and computation results in relation to the force peak value.			
	Test model	Numerical model	
		Scenario 1	Scenario 2
Force [kN]	32.79	34.60	33.14
Displacement [mm]	3.16	3.43	3.11

Fig. 13 – The test and computational results in the coordinate system of force–displacement.

redistribution of stresses in the area of curvature, i.e., the transition of the corrugated and wavy surfaces (areas A and B, Fig. 11b). The map of axial displacement is asymmetric, which means that the computational result is affected by additional kinematic extortion conditions (rotation of the top support; see Table 4). The peak reaction value obtained in the 3D model computation (scenario 2) is in the plastic zone (Fig. 14e), as in the simplified model. In this case, the stress curve as a function of the increase in kinematic extortions has a different nature than in the simplified model. This is due to the use of three material models assigned to the corresponding cross-sectional areas (description item 4.1). In both computational scenarios, the elastic working range of the system is exhausted at a relatively early stage of the load, i.e., at a force of approximately 8 kN, which is approximately 25% of the maximum reaction.

Validation of the numerical models was performed with the utilization of data obtained from the 3D DIC method

[9,13,18]. The DIC 3D method works in full-field and, in experimental data, provides much more information than point-wise techniques. The measurements of displacements are simultaneously performed in all three directions for thousands or millions of points. In-plane strains (ε_{xx}, ε_{zz} – strains along x and z coordinates) are calculated from displacements using the following equations [18]:

$$\epsilon_{xx} = \frac{\partial u}{\partial x} + \frac{1}{2}\left[\left(\frac{\partial u}{\partial x}\right)^2 + \left(\frac{\partial w}{\partial x}\right)^2\right]$$
$$\epsilon_{zz} = \frac{\partial w}{\partial z} + \frac{1}{2}\left[\left(\frac{\partial u}{\partial z}\right)^2 + \left(\frac{\partial w}{\partial z}\right)^2\right] \tag{4}$$

In paper [13] the measurements of section of arch-shaped steel sheets with utilization of 3D DIC method are presented. The resulting displacement maps, obtained over the entire sample surface, have been used for the purpose of qualitative validation of FEM model, estimated accuracy of displacement

Load step	Test	Scenario 2	Scenario 1	Scenario 2	Scenario 1
	F_{test} [kN]	$F_{\text{cal,2}}$ [kN]	$F_{\text{cal,1}}$ [kN]	$\Delta_{\%2}$ [%] formula (3)	$\Delta_{\%1}$ [%] formula (3)
0	0	0	0	0	0
1.0	3.28	2.85	2.86	13.11	12.80
2.0	9.29	8.38	8.43	9.80	9.26
3.0	14.49	13.54	13.64	6.56	5.87
4.0	18.93	18.27	18.43	3.49	2.64
5.0	22.66	22.47	22.73	0.84	−0.31
6.0	25.72	26.08	26.45	−1.40	−2.84
7.0	28.16	29.02	29.54	−3.05	−4.90
8.0	30.03	31.21	31.91	−3.93	−6.26
9.0	31.36	32.58	33.49	−3.89	−6.79
10.0	32.79	33.14	34.60	−1.07	−5.52

Table 6 – Percentage differences between the test and the computational results.
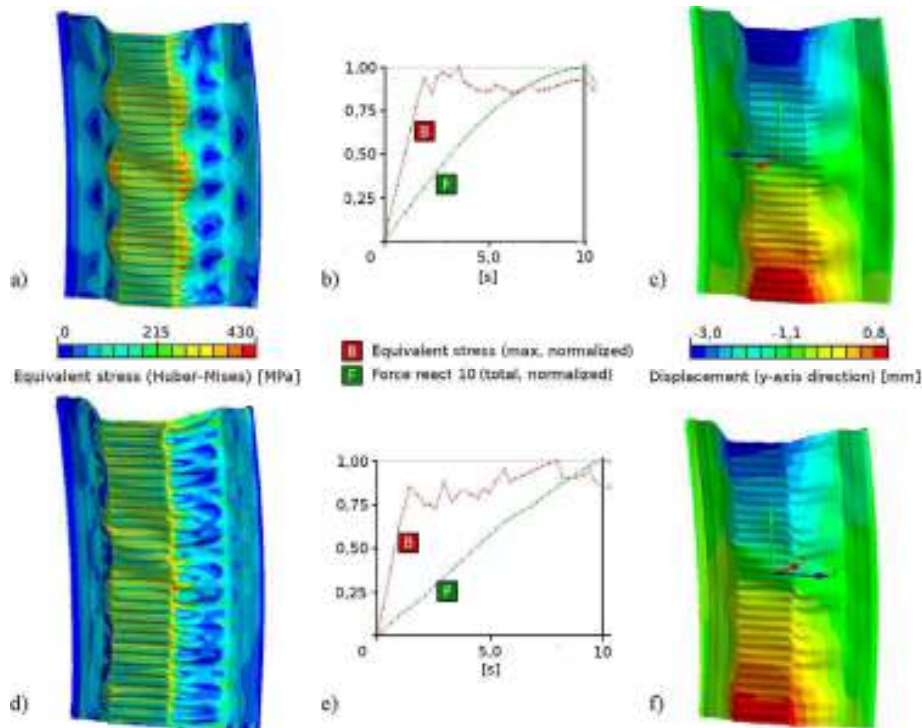
Fig. 14 – Computational results for peak load values, (a) reduced stress map – scenario 1 model, (b) reaction graph, stress as a function of the increase in extortion – scenario 1 model, (c) displacement map – scenario 1 model, (d) reduced stress map – scenario 2 model, (e) reaction graph, stress as a function of the increase in extortion – scenario 2 model, and (f) displacement map – scenario 2 model.

measurements was 20 μm. This accuracy was not suitable for determining accurate strain field distribution that would be used in further analysis. Therefore, in analysis presented in this paper, the area of interest was limited to the centre part of the measured sample. The area of interest (AOI) covers the area of 200 × 200 [mm^2] and is located in relation to the test piece as shown in Fig. 15. The obtained accuracy of displacement

measurements was 5 μm. The measurement set comprises two Point Grey Grasshopper (2448 × 2048 pixels) monochromatic cameras equipped with 70-mm lenses, set at an angle of 30° and pointing to the same AOI of the specimen (Fig. 15). Measured displacements contain two components, the displacement of the sample and the random displacement of the stabilization plates (the bottom stabilization plate was placed on a bearing).
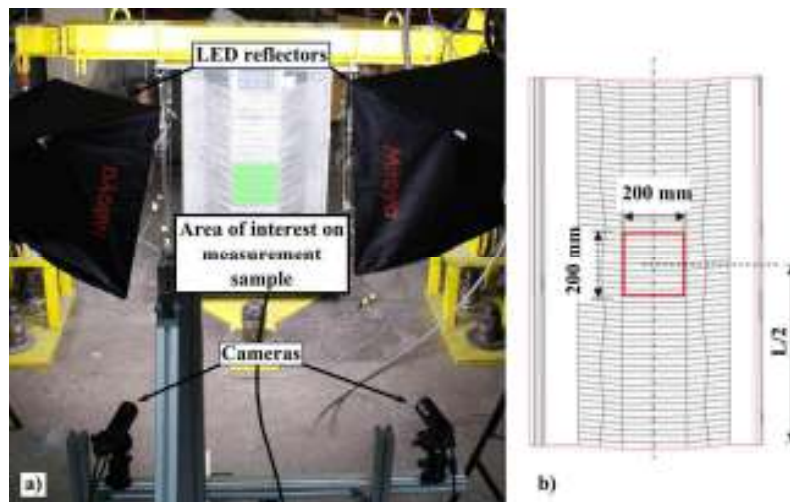

Fig. 15 – (a) Photo of the measurement system based on 3D DIC, (b) technical drawing of the measured sample–front view. Location of the area of interest, is marked on both images, in the picture (a) by green highlight, in the picture (b) by red border.
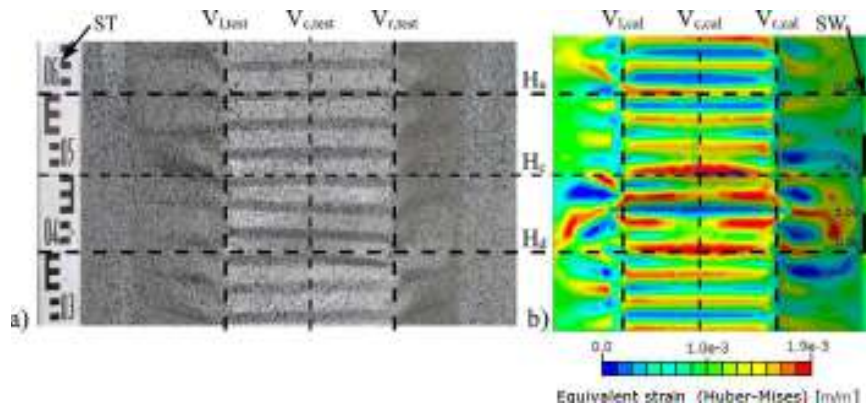
149

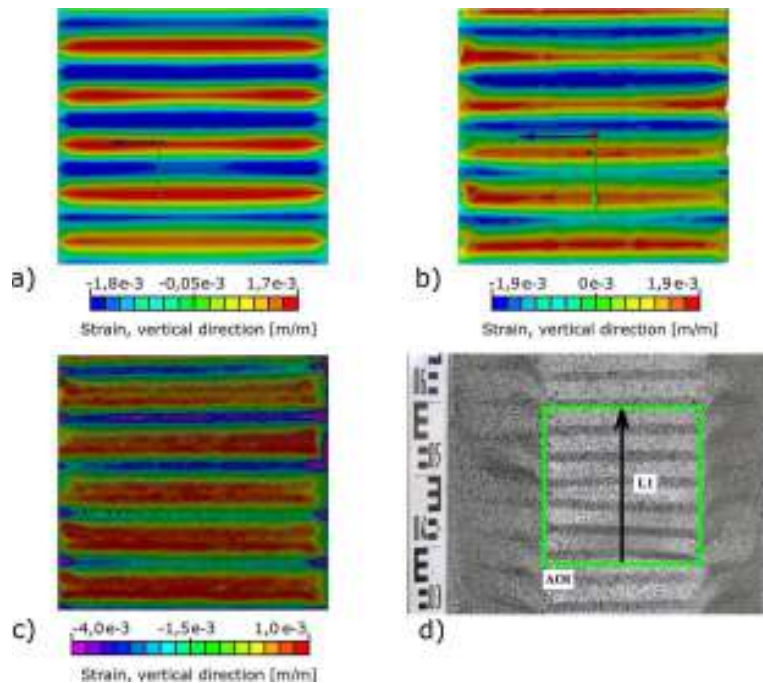**Fig. 16 – Detailed location of the strain observation area, (a) test piece, (b) computational model.**

Fig. 17 – In the pictures areas covering the AOI of 3D DIC analysis are presented: (a) map of elastic strains (X direction) at the peak load value for the scenario 1; (b) map of elastic strains (X direction) at the peak load value for scenario 2; (c) experimental map of the strains (X direction); (d) section of the sample with the black lines marked L1, indicating the position of the cross-section analyzed in Fig. 18.

The displacements of stabilization plates can be treated as rigid body movements, which do not influence the strain calculation of the 3D DIC algorithm. Therefore, for the purposes of validating the numerical models, the obtained strain maps were used.

For the purpose of determining the quantitative and qualitative divergences in the computational results with respect to the strain area, the central area was selected for computational models. The detailed location of the field of observation of Huber–Mises strains is shown in Fig. 16. The horizontal lines indicate the top (H_u), the bottom (H_d) border area and the axial location of the field (H_c) of the area. The vertical lines indicate the left and right vertical boundaries and

the axial location of the field of the observation area for the test piece ($V_{L,test}$, $V_{r,test}$, $V_{c,test}$), and a similar definition is true for the area in the computational model ($V_{l,cal}$, $V_{r,cal}$, $V_{c,cal}$).

The measured sample is corrugated in the X direction, and therefore the strains in the X direction are considered in the following analysis. In Fig. 17a–c, the maps of elastic strains of scenarios 1 and 2 at the peak load value are compared to measure the strain map at maximum load in the AOI. In order to quantitatively compare the results, the profile L (Fig. 17d) of strains ε_{xx} is presented in Fig. 18.

The values of minimum and maximum elastic strains for the 90% of the maximum load ($0.9F_{max}$) fall in the following ranges:
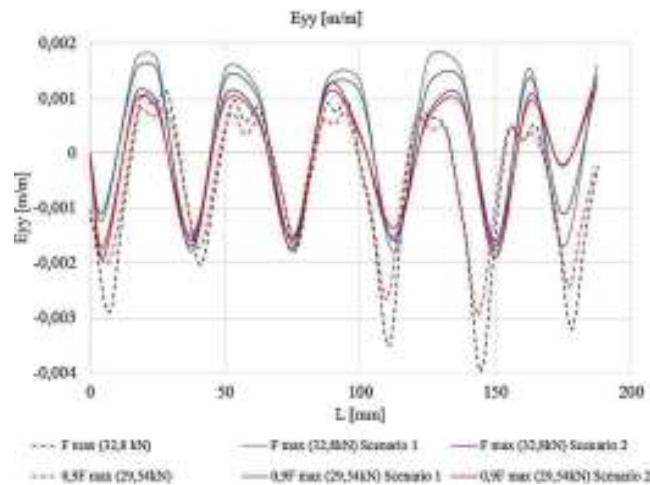
Fig. 18 – Strains in the X direction at points along line L1.

- $\varepsilon_{yy,\ max} = 0.0015$ m/m; $\varepsilon_{yy,\ min} = -0.0016$ m/m; scenario 1
- $\varepsilon_{yy,\ max} = 0.0012$ m/m; $\varepsilon_{yy,\ min} = -0.0017$ m/m; scenario 2
- $\varepsilon_{yy,\ max} = 0.0008$ m/m; $\varepsilon_{yy,\ min} = -0.0029$ m/m; test DIC

The values of maximum and minimum elastic strains for the max load (F_{max}) fall in the following ranges:

- $\varepsilon_{yy,\ max} = 0.0017$ m/m; $\varepsilon_{yy,\ min} = -0.0018$ m/m; scenario 1
- $\varepsilon_{yy,\ max} = 0.0019$ m/m; $\varepsilon_{yy,\ min} = -0.0019$ m/m; scenario 2
- $\varepsilon_{yy,\ max} = 0.0011$ m/m; $\varepsilon_{yy,\ min} = -0.0039$ m/m; test DIC

The maps of elastic strains are of a similar nature and demonstrate the variability of direction in the corrugated area. Divergences of FEM models in strain limits for the two different scenarios are approximately 10%. Strain values along the line L have similar character for both numerical models. Strain values obtained from tests and numerical simulations converge (Fig. 18) for the force of $0.9F_{max}$, along the line L, in its part starting at 25 mm and ending at 100 mm (see Fig. 17). At the same part of line L, strain values convergence of the numerical simulations and experimental results for the peak force (F_{max}) decreases. For the part of line L starting at 100 mm, the strains obtained from the simulation and experiment differ considerably. Difference between the FEM analysis and experimental results increases further with the increase of the applied force, which may be associated with a local loss of stability in this area.

5.   Conclusion and further works

The analysis of arch-shaped covering sections is difficult as both an experimental test and a computational task because of the complex geometry and load conditions. The section geometry results from the conditions of forming by cold rolling, and loads are a representation of the work of a discrete piece of the self-supporting system of a roof covering. The tests concerned the impact of the geometrical parameters of complex numerical models of section and boundary

conditions (the method of the model load on the material) on the searched value, which is the reaction of the kinematic extortion throughout the load range, i.e. from the zero starting point to the destruction of the test piece.

Two scenarios were analyzed. The first concerned a simplified geometry model (our own model), a single parameter extortion (axial displacement) and a bilinear material model. The second model was characterized by precisely mapped geometry obtained by 3D scanning, multi-parameter geometric extortions (axial displacements, angles of rotation of supports), which mapped the test conditions, and different material stress–strain relationship assigned to respective areas on the surface of the model. Computational models were compared with the test results in relation to the same parameter, i.e., the reaction resulting from kinematic extortions.

In the process of the analyses, it was demonstrated that the divergences of the test and computational results of the two models over the entire area of sought values vary within the range of 0.3% to 13%. At the peak load value, the model analyzed in scenario 1 shows a 5.5% divergence of computational results compared to the tests, and 1.1% in scenario 2.

When analyzing the selected displacement field, the computational results of both models are presented only with respect to the elastic strain. Plastic strains diverge considerably.

The strain results in the central 200 mm × 200 mm area being presented in the elastic range. The calculation results most similar to the measurements are those obtained from scenario 2. The results of the calculations in scenario 1 protrude from the others. The reason for this phenomenon may be dependent on the level of detail of material models and section geometries. The ability to assess the deformation in a defined area allows for determining the mechanism and causes of local instability.

In practical applications, the data adopted for the model analysis in accordance with scenario 2 are difficult to implement because some of them (kinematic parameters extortion, material data) are available only after laboratory

tests and after the application of a complex 3D geometry scanning process. The analysis in this case is of a cognitive nature and provides an answer to the question: "how closely can modelling approach the actual test conditions?" Preparing the model implemented in accordance with scenario 1 requires relatively few operations compared to the model of scenario 2. It is sufficient to correctly enter the geometry of the measurable section characteristics (overall dimensions, corrugation, and waves) on the basis of measurements with common instruments and perform verification of the properties of the output material (steel sheet before section mill rolling), adopting a simplified bilinear model of the material on this basis. In this case, some simplifications can be adopted, e.g., certain features of the section geometry can be ignored, and intervals and values of load values (kinematic extortions) can be assumed a priori. Such simplifications do not contribute to substantial errors (only the evaluation of a single parameter, the peak value of reaction and displacement, is affected).

By comparing the computation and test verification results, the ranges for model errors were determined in the full load area. It was demonstrated that some simplifications of the geometry, load conditions and material model implemented in scenario 1 do not significantly affect the result of computations. At the same time, the adopted simplifications significantly reduce the effort necessary to prepare the model.

In future, experimental and numerical studies will be performed on several segments' structure in the laboratory to investigate the global stability of the metal arch. Next, full-scale objects in real-life environments will be investigated and compared to the mathematical model to determine the effects of the actual conditions of the support and full load-bearing capacity and stability of the structure. For numerical studies, an FEM model prepared in accordance to scenario 1 will be used. The experimental studies will be performed with the DIC 3D method, customized for long-term measurements [19,20].

Acknowledgements

R E F E R E N C E S

[1] US Navy Course, Steel Builder, NAVEDTRA 14251, 2 (1996).
[2] Z. Kurzawa, K. Reszut, M. Szumigała, Stalowe konstrukcje prętowe. Część III Konstrukcje z łukami, elementy cienkościenne, przekrycia membranowe, elementy zespolone, belki podsuwnicowe., Wydawnictwo Politechniki Poznańskiej, Poznań, 2015.
[3] A. Biegus, D. Czepiżak, Evaluation of resistance of corrugated sheets under bending by a concentrated loads from the local suspensions, Archives of Civil Engineering (2010) 283–297.
[4] J. Bródka, M. Broniewicz, M. Giżejowski, Kształtowniki gięte: poradnik projektanta, Polskie Wydawnictwo Techniczne 1 (2006) 105–110.
[5] EN 1993-1-1 Eurocode 3: Design of steel structure. General rules and rules for buildings
[6] EN 1993-1-3 Eurocode 3: General rules – Supplementary rules for cold-formed members and sheeting.
[7] EN 1993-1-5: Eurocode 3: General rules – Plated structural elements.
[8] EN 1993-1-6: Eurocode 3: Design of steel structures – Part 1–6: Strength and stability of shell structures.
[9] A. Piekarczuk, M. Malesa, M. Kujawinska, K. Malowany, Application of hybrid FEM-DIC method for assessment of low cost building structures, Experimental Mechanics 52 (2012) 1297–1311. , http://dx.doi.org/10.1007/s11340-012-9616-2.
[10] L.L. Wu, Y.J. Shi, Theoretical and experimental study on interactive local buckling of arch-shaped corrugated steel roof, International Journal of Steel Structures 6 (2006) 45–54.
[11] R. Walentynski, M. Cybulska, R. Cybulski, Influence of geometric imperfections on the local stability of thin-walled elements, Shell Structures: Theory and Applications 3 (2013) 251.
[12] R. Cybulski, R. Walentyński, M. Cybulska, Local buckling of cold-formed elements used in arched building with geometrical imperfections, Journal of Constructional Steel Research 96 (2014) 1–13. , http://dx.doi.org/10.1016/j.jcsr.2014.01.004.
[13] A. Piekarczuk, K. Malowany, P. Więch, M. Kujawińska, P. Sulik, Stability and bearing capacity of arch-shaped corrugated shell elements: experimental and numerical study, Bulletin of the Polish Academy of Sciences Technical Sciences 63 (2015), http://dx.doi.org/10.1515/bpasts-2015-0013.
[14] EN ISO 6892-1:2009: Metallic materials – Tensile testing – Part 1: Method of test at room temperature.
[15] J. Świniarski, M. Królak, K. Kowal-Michalska, Schematyzacja charakterystyki materiału a charakterystyka rzeczywista w analizie porównawczej modelu MES i badań doświadczalnych stateczności dźwigarów cienkościennych, Acta Mechanica et Automatica 2 (1) (2008) 73–76.
[16] http://www.nikonmetrology.com/en_EU/Products/Portable-Measuring (01.10.2015).
[17] P. Kohnke (Ed.), Theory Reference for the Mechanical APDL and Mechanical Applications, Ansys Inc., USA, 2009.
[18] M.A. Sutton, J.-J. Orteu, H. Schreier, Image Correlation for Shape, Motion and Deformation Measurements: Basic Concepts, Theory and Applications, 1st ed., Springer Publishing Company, Incorporated, 2009.
[19] M. Malesa, M. Kujawinska, Modified two-dimensional digital image correlation method with capability of merging of data distributed in time, Applied Optics 51 (2012) 8641, http://dx.doi.org/10.1364/AO.51.008641.
[20] M. Malesa, M. Kujawinska, Deformation measurements by digital image correlation with automatic merging of data distributed in time, Applied Optics 52 (2013) 4681, http://dx.doi.org/10.1364/AO.52.004681.

Contents lists available at ScienceDirect

Engineering Failure Analysis

journal homepage: www.elsevier.com/locate/engfailanal

Non-destructive testing of industrial structures with the use of multi-camera Digital Image Correlation method

Marcin Malesa [a,*], Krzysztof Malowany [a], Jakub Pawlicki [b], Malgorzata Kujawinska [a], Pawel Skrzypczak [a], Artur Piekarczuk [d], Tomasz Lusa [c], Andrzej Zagorski [c]

[a] Institute of Micromechanics and Photonics, Warsaw University of Technology, 8 Sw. A. Boboli St., 02-525 Warsaw, Poland
[b] Institute of Aeronautics and Applied Mechanics, Warsaw University of Technology, 24 Nowowiejska St., 00-665 Warsaw, Poland
[c] Materials Engineers Group Ltd., 141 Woloska St., 02-507 Warsaw, Poland
[d] Building Research Institute, 1 Filtrowa St., 00-611 Warsaw, Poland

ABSTRACT

Although Digital Image Correlation (DIC) provides capabilities of scaling a field-of-view (FOV), dimensions of some industrial installations in many cases are too big to be measured with DIC based on a single camera pair. In this paper we present two strategies of spatial stitching of data obtained with multi-camera DIC systems that can be used for engineering failure analysis, namely strategy for the case when there are overlapping FOVs of 3D DIC setups and strategy for the case when 3D DIC setups are distributed and not necessarily have overlapping FOVs. Data obtained with the presented methodologies can be used to verify or update FEM models of the investigated objects. Two practical applications of the multi-camera DIC system are described in order to show its feasibility in engineering failure analysis.

© 2016 Elsevier Ltd. All rights reserved.

1. Introduction

Analysis of engineering failures are aided with numerical modeling as well as with a wide array of NDT methods. The hybrid numerical–experimental methodology [1] can be used in order to find the cause of failure as well as to prevent future failures. Important group of methods that are extensively used in the field of engineering failure analysis are optical measurement methods (OMM), such as spectroscopy, interferometry, or non-coherent light techniques. One of the most successful OMM is Digital Image Correlation method (DIC) [2]. Recently DIC went through many changes and modifications, what enabled investigation of failed components in laboratory measurements [3–7] as well as to monitor failure process of engineering structures in field conditions [8–10]. In the latter case size of an object is often limited by the field of view of cameras. The problem can be overcome by using multi-camera DIC system. In recent years a few groups of researchers have been working on development of multi-camera DIC systems, in which data obtained with individual systems are stitched together in a common coordinate system. Orteu et al. [11] presented an interesting enhancement of a standard camera calibration procedure, which enabled simultaneous calibration of 4 cameras used in 3D measurements of a sheet metal part during a Single Point Incremental Forming operation. In the calibration procedure a series of $4n$ images of a calibration target is acquired (all cameras are viewing the same target). Than, all unknown calibration parameters (four intrinsic matrices, four distortion vectors and four rigid body transformations) are being solved in the same minimizing procedure (in this case a Sparse Bundle Adjustment). In the presented solution one of the cameras is selected as a master camera and 3D data obtained with any pair of cameras used in the system is automatically referenced to

* Corresponding author.
    E-mail address: m.malesa@mchtr.pw.edu.pl (M. Malesa).

the coordinate system of the master camera. It has to be noticed that calibration procedure is only possible, when all cameras are viewing the same calibration target (so there is a part of field of view which is common for all cameras used in the system). However, when bigger objects need to be measured it is not possible to assure common fields of view of all cameras. In such cases the cameras can be arranged in a wall-of-cameras configuration (for measurements of flat objects), or surrounding cameras (for cylindrical objects). Wang in [12] and Chen in [13] used surrounding cameras configuration for measurements of cylindrical objects. In both papers the authors used each two neighboring cameras as individual 3D DIC system (i.e. in the multi-camera system consisting of 4 cameras there have been three individual 3D DIC pairs: the first pair consisted of camera 1 and camera 2, the second pair consisted of camera 2 and camera 3 and the third pair consisted of camera 3 and camera 4). Each system has been calibrated separately, but with sequential utilization of geometrical transformation between cameras it was possible to reference all data to the common coordinate system. In the presented solution it was required to have some overlaid area in the field of view of neighboring cameras. Similar surrounding DIC system with three cameras has been presented by Hwang in [14]. However in this case, the cameras have been placed on a movable frame, what additionally increased the field of view. Somewhat different approach has been presented in [15] by Leblanc et al. The authors presented displacements and strain measurements of a wind turbine blade with a single, portable 3D DIC system. In this solution, 16 point clouds representing different areas of the object have been stitched together using some markers applied to the structure. The solution with portable 3D DIC system is restricted to static measurements only.

In the paper we present a general approach to stitching of data from a multi-camera DIC system. The presented approach can be applied for measurements in the case, when there are overlaying fields of view of DIC cameras as well as in the case, when fields of view are distributed and there are no overlaying areas. The developed methodology can be used in failure analysis of different types of engineering objects (specifically for industrial objects). In the paper we present also two example applications of the methodology: failure analysis of an installation in a nitrogen plant and development of an accurate numerical model of a graded metal plate hall's arch in order to prevent its future collapses. DIC analysis presented in the paper have been carried out with the use of CCI software, which is being developed at the Institute of Micromechanics and Photonics Warsaw University of Technology.

2. Material and methods

Multi-camera DIC systems can be applied to the wide variety of objects in order to facilitate failure analysis. Thus, spatial data stitching algorithm has to be tailored as to fit different measurement strategies, namely:

• a strategy when there are overlapping areas of fields of view of cameras,
• a strategy when cameras are distant from each other and there are no overlapping areas of fields of view.

General data stitching procedure concerns measurements with multiple 3D DIC setups. The procedure is based on the standard camera calibration and geometrical transformation of the individual point clouds gathered in their own coordinate systems into a common coordinate system. Geometrical transformations between consecutive data sets are estimated using a set of markers whose 3D positions (x_i, y_i, z_i) in an i-th coordinate system are known. At least 4 markers have to be viewed by each 3D DIC setup of the multi-camera DIC system. The positions of markers in a common coordinate system can be obtained throughout different methods, i. e. image processing or geodetic surveying. Determining of the transformation matrix between two coordinate systems (more specifically between two vectors of 3D positions of markers) is based on the Singular Value Decomposition (SVD) method [16]. The general data stitching flowchart is presented in Fig. 1.
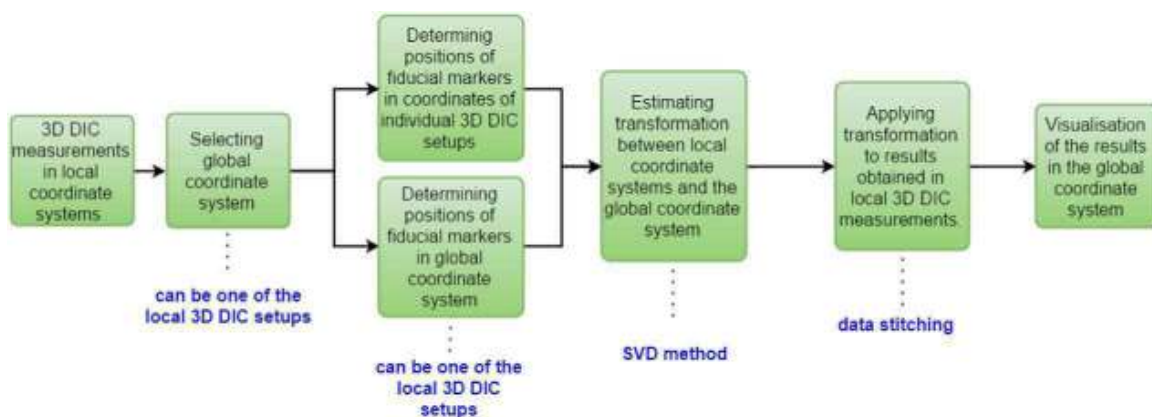

Fig. 1. Flowchart of the general data stitching procedure.

It has to be noted here, that measurement resolution in multi-camera DIC measurements is not constant over fields of view, because distances between individual 3D DIC setups and a measured object can differ. All data processing parameters and thresholds have to be set individually for each 3D DIC setup in order to ensure the best quality of the results.

The difference between the two strategies is the method of indicating the coordinates of markers. More detailed description of both strategies is given below.

2.1. Overlapping fields of view

In this case, additional images of the calibration target viewed by at least two DIC setups have to be acquired to stitch the data sets. For this purpose, for example, a checkerboard can be used. The coordinate system of one of the setups has been selected as the main coordinate system. Knowing the 3D positions of markers in the local coordinate systems of both 3D DIC setups we can determine geometrical transformations between both coordinate systems. This strategy is applied for the first measurement task namely measurements of a 12 m graded metal plate segment. The accuracy of the method has been discussed in [17].

2.2. Distributed fields of view

In industry, the crucial parts of installations can be distanced by tens (or even more) of meters and therefore distributed configuration of multi-camera DIC system (with no overlapping areas of fields of view) has to be used. In order to determine transformations between individual 3D DIC setups, fiducial markers have to be applied to the object. Similarly to the previous strategy, 3D positions of all markers need to be referenced to the common coordinate system. As none of the 3D DIC setups view all markers at the same time, determination of markers' positions has to be aided with another method, such as geodetic surveying. The accuracy of data stitching procedure in this case is dependent on a quality of a standard camera calibration of individual 3D DIC setups and on the accuracy of the aiding method. The second strategy has been applied in the second example described in this paper namely measurements of an installation in a nitrogen plant.

3. Measurements of 12 m graded metal plate segment

The object under investigation was a fragment of 12 m span graded metal plate hall's arch [18–20]. The components of such structures are manufactured directly on building site using a mobile production unit. First, single-wave trapezoidal profile is cold-shaped from thick coiled steel sheet. Next, the curvature of a desired radius is obtained by corrugating the trapezoidal profile. The profiles are subsequently connected to each other by cold pressing of seams situated at the edges of upper flanges. Because of the complex shape of each component, it is difficult to numerically model metal plate hall's arches. Because of the lack of appropriate calculation methods, several collapses of such structures happened in recent years. In order to better understand the cause of collapses of metal plate hall's arches and to prevent future failures it is required to develop an accurate numerical model and validate it with the experimental data.

In the presented experiment the arch constructed from four individual segments has been investigated. The load has been provided by a set of strings and longitudinal and transverse beams. The load has been designed as to simulate the presence of a thick layer of snow on the roof of the arch.

3.1. Calculations

The idea was to develop simplified model of the arch and then update it with the use of experimental data. The simplified model of the hall included only a single segment of the corrugated metal plates. In order to represent true physical conditions (in which halls consist of tens or hundreds of segments), influence of the neighboring segments of the arch has been modeled by boundary conditions. The assumption was that internal segments can move only in force direction (y in global coordinate system) and in z direction (perpendicular to the ground) and cannot move toward the sides (zero displacements in x direction). Support conditions restricted displacements and allow only rotations over x axis. Load has been simulated with four forces (similarly to the experiment). The model has been developed in Ansys software as a Shell 281-type model. The parameters of the model meshing are given in Table 1 (rules for determination of the parameters are given in [21]). The simplified model is presented in Fig. 2a, displacements that occurred at the maximum load (together with the image of buckling that occurred during the experiment) are presented in Fig. 2b.

Displacements extracted from points in which load was applied are presented in Fig. 3 together with the applied load value (note that numerical simulations were performed only in the range of bearing capacity). Data points are labeled similarly to the real experiment (see Fig. 5). One can observe that displacements U and W are distributed symmetrically and displacements

Table 1
Meshing parameters of simplified model of the hall's arch.

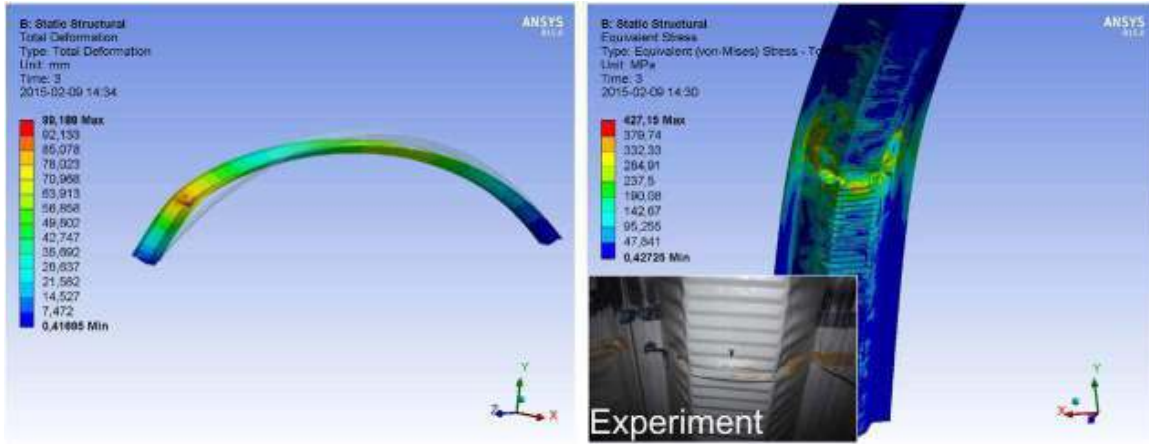| Number of nodes	Number of finite elements	Element quality	Aspect ratio
49291	49,603	0.829	1.261

Fig. 2. a) The simplified model of a single segment of the arch, b) displacements at the maximum load and view of the buckling of real structure that occurred.

V are close to zero. The main task in the analysis was to check if the simulated displacements of the model are in line with the real displacements of the internal segments that occurred during the experiment.

3.2. Measurement procedure and apparatus

The measurements have been carried out with the use of multi-camera DIC system. The system consisted of eight 5MPx (2448×2048) Pointgrey cameras equipped with 8 mm focal length lenses. Appropriate cameras were paired and served as four separate 3D DIC setups. The cameras of all setups were connected to the control computer to synchronize the data acquisition procedure. Distribution of the cameras and locations of the fields of view are presented in Fig. 4a and b. Fields of view were additionally illuminated with LED reflectors.

Each 3D DIC setup has been calibrated with the checkerboard prior the measurements. The quality of calibrations have been expressed as a reprojection error for all systems and a threshold has been set at 0.05*px* (reprojection errors for all 3D DIC setups was smaller that 0.05*px*). Dimensions of the fields of view were approximately 1.8m×1.5m. Taking into account resolution of the cameras, accuracy of displacement measurements of each 3D DIC setup can be estimated at 0.05mm.

The fields of view of neighboring 3D DIC setups overlapped each other (Fig. 4) and therefore it was possible to use additional images of the calibration target (checkerboard in this case) in order to calculate transformations between consecutive 3D DIC setups (see Fig. 4a and b). In each field of view a random speckle pattern has been applied with the use of a spray gun.

As it was mentioned, the main aim of the experiment was to obtain data, which can be used for validation or updating FEM model. For this purpose both types of data full-field and point-wise have been extracted from multi-camera DIC data sets. Distribution of displacements and strain measurement points is presented in Fig. 5. Comparison between numerical and experimental data was possible thanks to carried out transformations that brought the experimental results to the coordinate system of the numerical model.
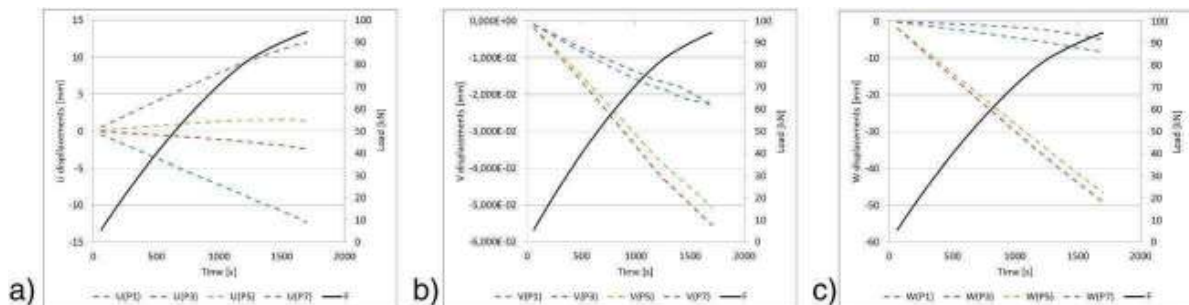

Fig. 3. Simulated displacements *U*, *V* and *W* of selected points (marked in Fig. 5) and applied force plotted against the time. Numerical calculations were performed only to range of bearing capacity. The test results are presented in Fig. 7 applies to the full range of loads, including the results after the loss of stability (see the descending curve of load).
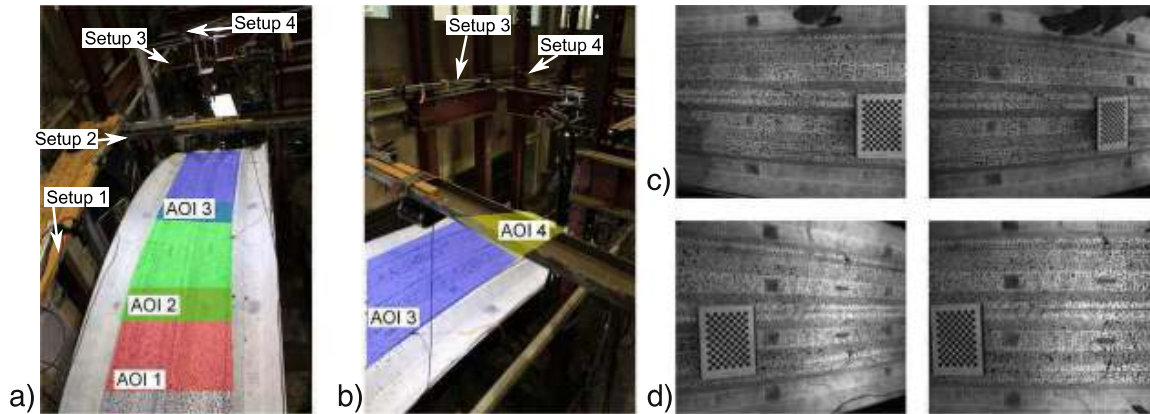
Fig. 4. Distribution of the cameras and field of views during the measurements: a) Setups 1, 2 and 3 b) Setups 3 and 4; images of the calibration artifact used for data stitching, captured by c) 3D DIC Setup 1 and c), d) 3D DIC Setup 2.

Data points labeled in Fig. 5 have been selected purposely in order to answer certain questions, which arose during development of the model. Analysis included in particular:

- Displacements in data points $P1 \div P8$ — which were located on the two internal segments of the arch; locations of these points are also locations of applied load. Data from points $P1 \div P8$ have been used to verify assumptions about symmetry of displacements in x and z directions and zero displacements in y direction in the internal sections of the arch.
- Displacement maps in different load states in order to assess symmetry of the applied forces (asymmetry in load could result in asymmetry in displacement maps).

3.3. Results

3.3.1. Data stitching results

The DIC Setup 2 has been chosen as a master setup and its coordinate system has been selected as the global coordinate system. The fields of view of Setups 1 and 3 overlapped the field of view of Setup 2, thus direct transformation from these setups to Setup 2 could have been determined. The field of view of the Setup 4 overlapped the field of view of Setup 3. Transformation from Setup 4 to Setup 2 could be carried out sequentially: at first transformation from Setup 4 to Setup 3 and after transformation from Setup 3 to Setup 2. Data stitching procedure was in accordance with the flowchart in Fig. 1, however additional step has been made in order to transform the data from the global coordinate system to the coordinate system in which xy plane was parallel to the ground and z axis was perpendicular to the ground. This step was necessary to agree coordinate systems of the measurements and numerical simulations.

The transformations have been determined with the use of simultaneously acquired images of the chessboard calibration artifact. Chessboard corners viewed by each camera have been detected and subsequently used to calculate 3D position of each marker in coordinate systems of the respective DIC setup. The accuracy of determination of 3D positions depends strongly on the quality of the standard camera calibration procedure, which has been carried out before the measurements start.

The obtained results of data stitching (transformation parameters and obtained transformation errors) are presented in Table 2.

One can observe that transformation errors were in the most cases smaller than 0.5mm which is a good result taking into account dimensions of the measured object (please note here that obtained errors are one order of magnitude bigger than
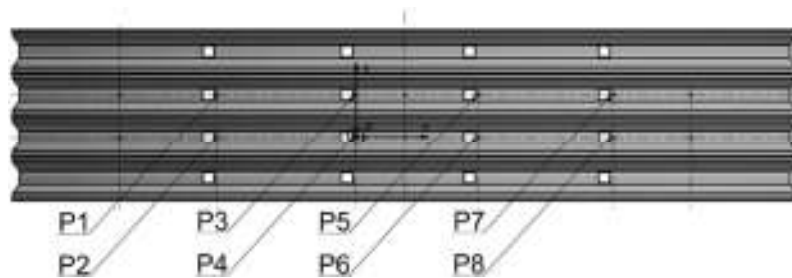

Fig. 5. Distribution of displacements and strain measurement points overlaid on the scheme of the measured object (top view).

Table 2
The results of transformation calculations.

T	Tx[mm]	Ty[mm]	Tz[mm]	Rx[°]	Ry[°]	Rz[°]	T_{error}[mm]
1−2	−536.71	−120.60	−403.82	−0.06	−0.43	−0.03	0.48
3−2	3021.06	−60.17	1577.21	0.012	−0.74	−0.02	0.24
4−3	885.71	−150.78	−322	−0.07	0.39	0.007	0.25

displacement measurement errors obtained in individual 3D DIC setups). Although Setup 4 and Setup 2 did not have an overlaying areas of fields of view, the transformation between these two setups could have been determined sequentially (as a product of 4→3 and 3→2). The final stitching error in this case is a sum of 3→2 and 4→3 errors.

3.3.2. Measurement results

Displacements of two internal segments of the arch calculated for an example load state are presented in Fig. 6. Displacement values have been coded in color and overlaid on the point cloud obtained with the data stitching procedure. Areas between neighboring AOI's (with no data) have been thresholded due to higher correlation error at the edges of the images (because of the depth of focus).

One can observe asymmetry in displacement maps of internal segments of the arch. In *U* displacement map (Fig. 6a) it can be observed that the hall has moved in the direction toward one of the supports, in *V* displacement map (Fig. 6b) it can be seen that internal segments of the hall have drawn aside (by approximately 26mm), in *W* displacement map (Fig. 6c) it can be observed that loading has not been applied symmetrically to the arch. The buckling occurred outside the field of view of the multi-camera DIC system, however, the influence of buckling can be observed in obtained displacement maps (bigger *U displacements* and positive *W* displacements on one of the arch's ends). Mentioned observations are also reflected in displacements versus time plots (presented in Fig. 7).

These observations show imperfection of the real object and are sources of inconsistency between measurement results and FEM simulations of the internal segment (see Fig. 3). Results will be used to update the model and boundary conditions in the next steps.

4. Measurements of installation in a nitrogen plant

The second application of multi-camera DIC system concerns analysis of the ammonia synthesis installation 8. A reactor and synthesis gas pipelines are crucial elements of the installation, which are prone to frequent unsealing, explosions and fires. Operating parameters of the installation are 200bar pressure 300°C÷400°C temperature and highly explosive medium (hydrogen). In the past, explosions and extensive fires of the higher levels of the reactor and pipelines have been occurring frequently. As a result, the pipelines suffered permanent deformations and the properties of a system of suspensions and supports have been changed (actual displacements did not correlate with the design assumptions).

The installation contains three individual pipelines (a supply pipeline and two outlet pipelines), which are connected in a single element (called 'the cube'). There are two locations in which leakages occur: (i) a connection of the valve body with the bell and (ii) a connection of the cube (at the top of the reactor) with the bell. The first of these connections is sealed with the special ring covered with a silver coating, while the second connections is sealed with c-ring or o-ring metal (nickel) gasket.

The main aim of the measurements was to investigate purpose of the frequent malfunctions, develop a new, updated numerical model of the installation and the crucial connectors, simulate actual working conditions, modernize the connections and verify the new types of sealing. The key to determining actual working conditions of the sealed surfaces is to indicate interactions between pipelines and connector pipes in unstable heat states. Due to unstable working conditions of the reactor, the displacements of crucial elements (in the area of connections) had to be measured experimentally.

Kinematic extortion in the form of the measured displacements of the reactor's cube have been used as an input of the new, updated numerical model of the installation. Analysis of the model enabled determination of interactions between pipelines, the cube and the critical connections. Also, the simulations have been used to verify if displacements of suspensions were within the
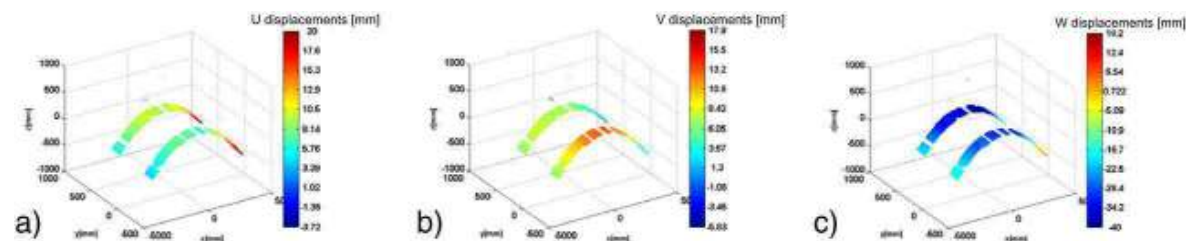

Fig. 6. Example results of displacement measurements obtained with multi-camera DIC data stitching procedure: a) *U* displacements, b) *V* displacements, c) *W* displacements.
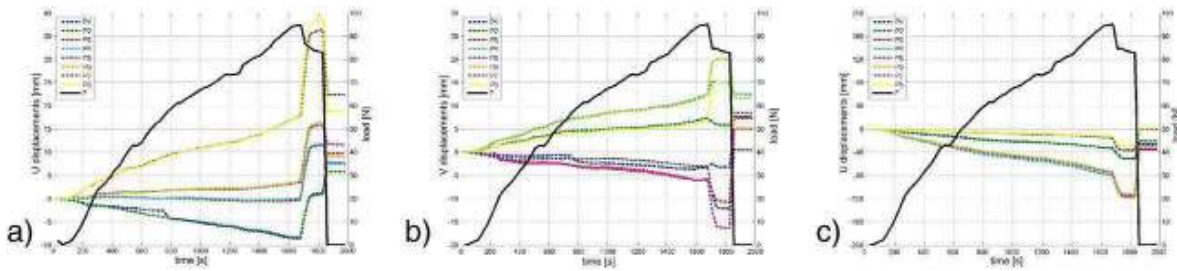
Fig. 7. Displacements *U*, *V* and *W* of selected points and applied force plotted against the time.

designed operating range. Obtained interactions (forces and moments) between pipelines and the cube have been subsequently passed to the detailed model of the sealed connection.

The data about the installations have been gathered over a years of service. Back to 80s or 90s during each overhaul the point displacements have been measured by geodetic surveyings. The modern measurement techniques, such as DIC, enable much more sophisticated analysis but it is important to keep a coherence between results obtained with old and with modern techniques. It can be achieved by referencing the DIC measurements to the global coordinate system (determined by previous measurements). However, because of the dimensions of the installation and its complex shape it was not possible to cover whole installation with the DIC measurements. Instead, a multi-camera DIC system containing three 3D DIC setups has been used to monitor crucial parts of the installation. The multi-camera DIC system provided information about local displacements/strain fields as well as information about total elongation of the pipelines segments. The installation has been monitored during shutdown and during start-up.

4.1. Calculations

Experimental data has been used to identify real structure deflections and validate and update numerical model of the installation. Geometrical dimensions have been adopted from the documentation and geodetic measurements. FE analyses have been done by ANSYS Multiphysics Software. The calculations have been carried out with the use of beam elements, specialized in pipelines analysis. Elements had six degrees of freedom (meshing parameters are given in Table 3). The discretization of the model is presented in Fig. 8b and example displacements (matching measured deflection) in hot state are given in Fig. 9. The computations carried out enabled to determine a force and a force couple reactions of pipelines on the cube in transient load conditions. These loads were then passed to the separate 3D FE model of the crucial flange connection including nonlinear gasket material (Fig. 13). This helped to analyze leakage reasons which were mainly resulting from wrong gasket design. The new gasket system with a protecting ring and adequate bolt prevention solved the outflow problems in the future operation 13. Example displacements in hot state are presented in Fig. 9.

Determined interactions between pipelines and the cube have been passed to the detailed model of the connection.

4.2. Experimental results

Three crucial areas of the installation have been selected to be monitored with 3D DIC setups: (i) the reactor's cube, (ii) vertical fragment of a supply pipeline, (iii) horizontal fragment of one of the outline pipelines. A random speckle pattern has been spray painted on the object in each field of view. Data obtained from the first area have been used as the initial kinematic extortion for the numerical model, while the data obtained from the other two areas have been used to verify correctness of the model.

The locations of 3D DIC setups are shown in Fig. 10a and in Fig. 8b. Areas of interest of DIC setups are marked with green rectangles in Fig. 10a, b and c. Fields of view of were additionally illuminated with LED reflectors. Each 3D DIC setups consisted of a pair of 5Mpx (2448×2048) PointGrey cameras. The cameras were equipped with 8mm or 16mm (the third setup) focal length lenses. All individual 3D DIC setups have been calibrated with a checkerboard prior the measurements. Reprojection error threshold has been set at 0.12*px* in this case (dimensions of fields of view significantly hindered the calibration procedure). Taking into account resolution of the cameras, displacement measurement errors in individual setups can be estimated at 0.15mm, 0.1mm, 0.28mm respectively.

The measurements have been also aided with temperature measurements (IR camera and pyrometer). The IR camera has been installed together with cameras of the DIC system 1 (see Fig. 10a).

Table 3
Meshing parameters of the pipeline model.

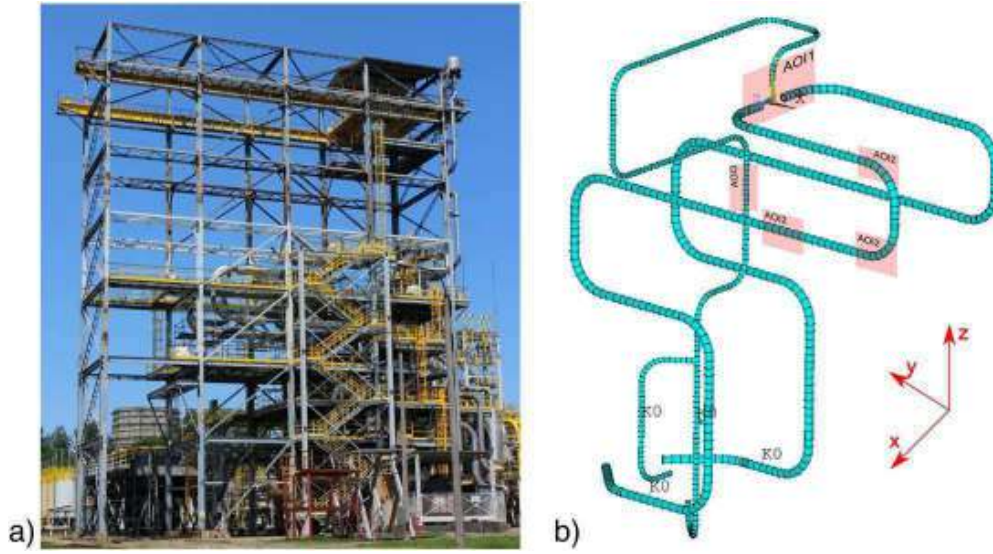| Number of nodes	Number of finite elements	Element quality	Aspect ratio
683	621	NA for 1D model	NA for 1D model

Fig. 8. a) Image of the investigated installation, b) discretization of the model of the pipeline.
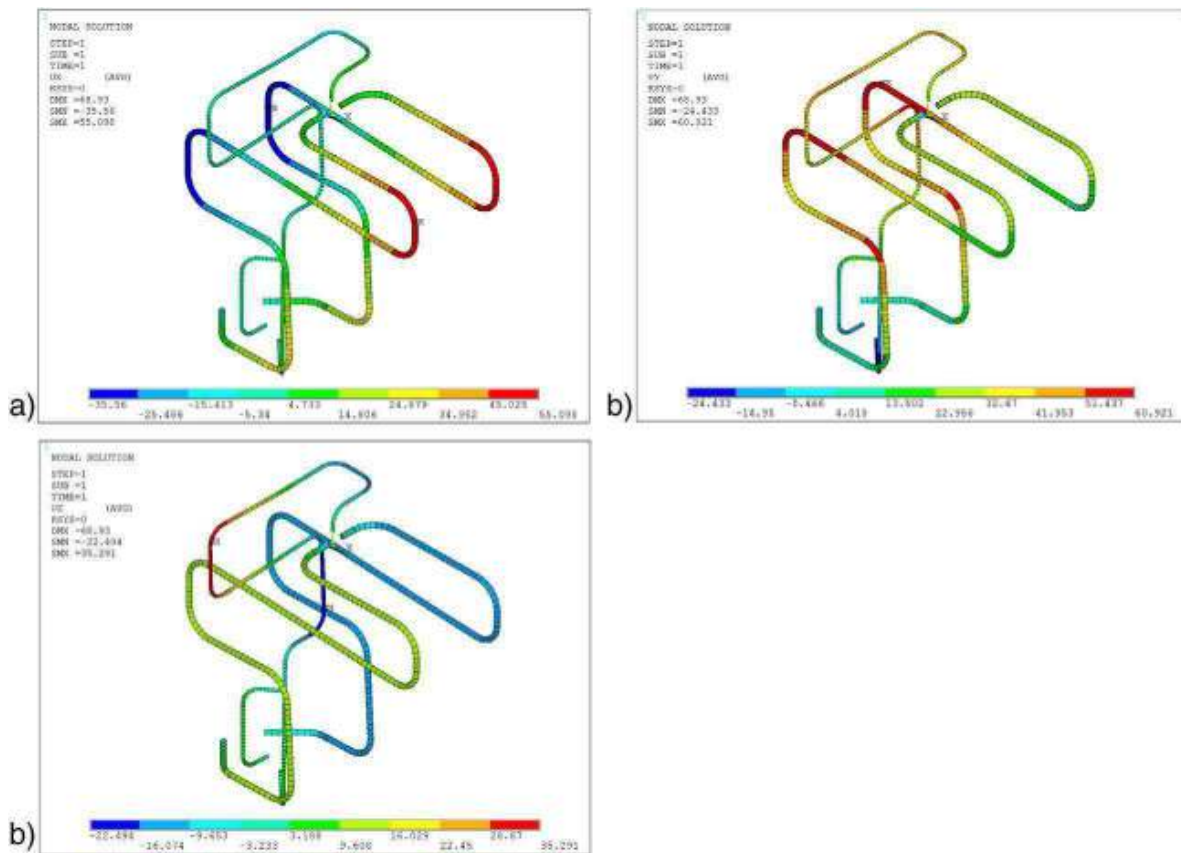

Fig. 9. Displacements calculated with the use of numerical model of the pipeline in the hot state: a) in *x* direction, b) in *y* direction, c) in *z* direction.
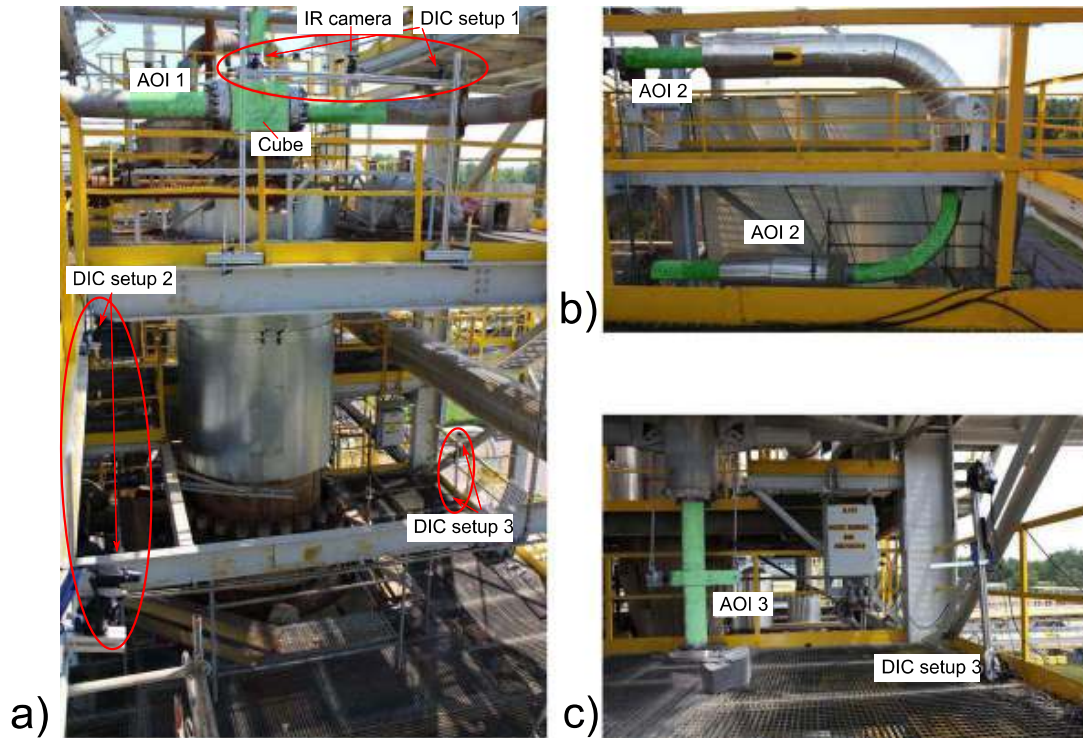
Fig. 10. Monitoring of a nitrogen installation: a) view of the installation with indicated locations of three DIC setups and the location of AOI 1, b) view of the location of AOI2, c) location of the DIC Setup 3 and location of AOI3.

The measurements have been carried out in two series. The first series covered the cooling down of the installation before the repair works and the second series covered the start-up of the installation after finishing the repair works. Both series of measurements lasted for approximately ten hours.

4.2.1. Data stitching results

Because of the dimensions of the installation and distances between selected areas to be monitored, it was necessary to use distributed configuration of the multi-camera DIC system. As one can observe in Fig. 10, it was not possible to determine the transformation between coordinate systems of each setup by using a calibration target viewed by two systems at the same time. Instead, a strategy for distributed fields of view had to be used. For the data stitching procedures a set of fiducial markers had been used. Position of the markers had been determined in a global coordinate system with the use of geodetic surveying. Directions of the global coordinate system are indicated in Fig. 8b.
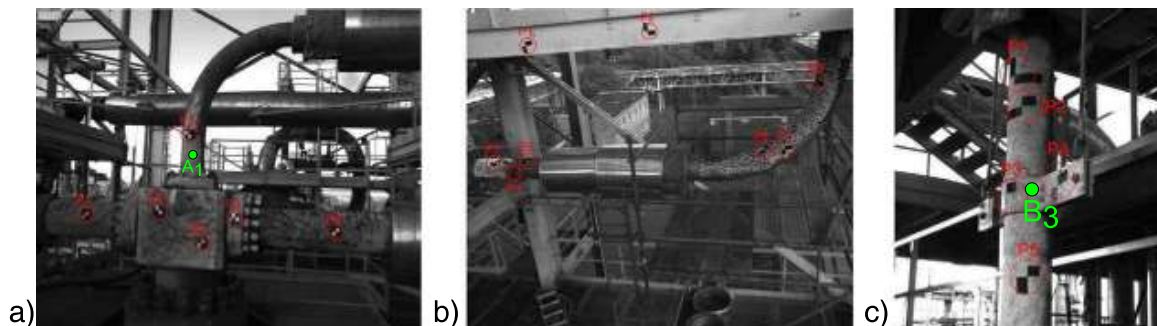

Fig. 11. Field of views with marked positions of fiducial markers used for determination of geometrical transformation between coordinate systems and locations of points of further analysis: a) DIC Setup 1, b) DIC Setup 2, c) DIC Setup 3.

Several checkered markers, which could be easily detected with image based measurement methods, have been placed in the areas of interest. Each DIC setup viewed at least 5 markers. 3D position of each marker in the local coordinate system has been calculated in the coordinate system of appropriate DIC setup. In the next step, 3D position of each marker has been determined by geodetic surveying in the global coordinate system. The global coordinate system was consistent with former surveying and technical drawings of the installation. Example images with fiducial markers acquired by DIC systems are presented in Fig. 11. Markers have been removed before the displacement measurements start as not to obscure the areas of interest.

Similarly to the previous example, 3D positions have been then used to stitch the data obtained with multi-camera DIC system. The difference is that in this case, the aim was to determine transformations between local 3D DIC coordinate systems and the global coordinate system of geodetic surveying. The estimated transformations together with the transformation error are presented in Table 4. The lack of data for DIC Setup 2 in measurement series 2 was due to the fact, that the markers placed in the field of view of the DIC Setup 2 had to be removed before the repair (just after the first measurement series).

As one can observe in Table 4, obtained transformation errors are much bigger that displacement measurement errors obtained in each 3D DIC setup. The biggest T_{error} (more than 50mm) has been obtained for DIC Setup 2 in both measurement series. The DIC Setup 2 covered the biggest area of interest, what made the camera calibration process quite difficult. The obtained calibration error was 0.12px what influenced the accuracy of markers detection and in consequence hindered the estimation of the transformation matrix. Additionally, markers stuck to the structured were close to the edges of the recorded images and out of focus. Using bigger calibration target during calibration process and applying more markers in the area of interest (especially in the central part of the FOV) would significantly increase the quality of transformation estimation process. Transformation errors obtained in other two DIC setups were lower than 10mm what is acceptable in industry. However, it must be pointed out that the accuracy of transformation can be significantly increased in future measurements by:

• utilization of a bigger calibration target,
• application of more markers in the central partof the field of view,
• preparation of markers, which can be more accurately detected by image processing procedures.

4.2.2. Measurement results

Having data from all DIC setups in the common, global coordinate system enabled global analysis of the behavior of the installation and extract the data required as initial parameters for the numerical model. Example W displacement maps for each 3D DIC setup are presented in Fig. 12. The exact locations of the selected data points, that have been used in the model are presented in Fig. 12.

The main advantage of the presented combination of local and global measurements over simple geodetic surveying is that displacements of each point of the installation which is viewed by one of the DIC setups can be individually analyzed after the measurements. This is especially important in the case when behavior of the object is difficult to be predicted (e.g. industrial installations after many years of service). Stitching the data from few DIC setups and transforming obtained data to the global, geodetic coordinate system allows to use more data for modification and validation of a numerical models of pipelines (Fig. 9) as well as to give better estimation of the health of least reliable areas of the installation. The next step was to redesign crucial flange connection applying new gasket set. Detailed FEM analysis showed that both stress level and tightness of new flange connection under common and extreme working conditions are acceptable and safe (Fig. 13). Meshing parameters are given in Table 5.

5. Conclusions

In the paper we presented two different strategies of stitching of data obtained with multi-camera DIC system. Both strategies can be used for proper pre-processing of data used in failure analysis of industrial installations and civil engineering structures. The feasibility of the first strategy has been presented in the example of extending the field of view of the standard 3D DIC system in measurements of a metal plate segment. In this way it was possible to present displacement maps of relatively complex object in a common coordinate system and use the obtained data to update numerical model of the hall's arch. Hybrid experimental–numerical methodology can be used to prevent future failures of similar object. The field of views of individual 3D DIC setups have been purposely set to have overlaying areas of interest. Discrepancies of results obtained in this area after applying the data stitching procedure allowed the assessment of the accuracy of the procedure. It has been shown that errors are related to

Table 4
Parameters of the transformation matrices between local coordinate systems and the global, geodetic coordinate system.

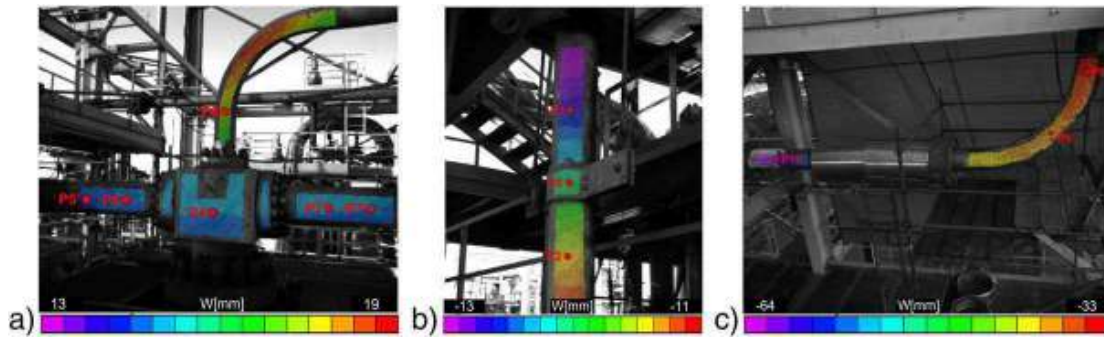| DIC setup	Tx[mm]	Ty[mm]	Tz[mm]	Rx[°]	Ry[°]	Rz[°]	T_{error}[mm]
s1 Setup 1	120,670	−11,685	280,366	−0.02	−3.08	0.05	2.59
s1 Setup 2	279,909	52,561	92,563	0.02	2.93	−1.05	52.08
s1 Setup 3	−3834	198,799	235,607	2.11	0.02	−0.04	5.08
s2 Setup 1	–	–	–	–	–	–	–
s2 Setup 2	289,559	−79,401	17,159	0.03	−2.66	−1.52	58.22
s2 Setup 3	−10,562	197,077	236,683	2.11	0.02	−0.01	9.74

Fig. 12. Example displacement maps referenced to the global coordinate system a) *W* displacement map obtained in AOI1, b) *W* displacement map obtained in AOI2, c) *U* displacement map obtained in AOI3.

the quality of transformation rather than to the load state. Performing more accurate calibration would have reduced the transformation error and would have enabled more precise displacement maps in multi-camera configuration.

The second presented strategy, in which geodetic surveying is used to reference DIC data to the global coordinate system, is well-tailored for measurements of installations in industry. The combination of local and global data can be extremely helpful for calibration of the numerical models of old installations, which after years of service do not operate in accordance to design
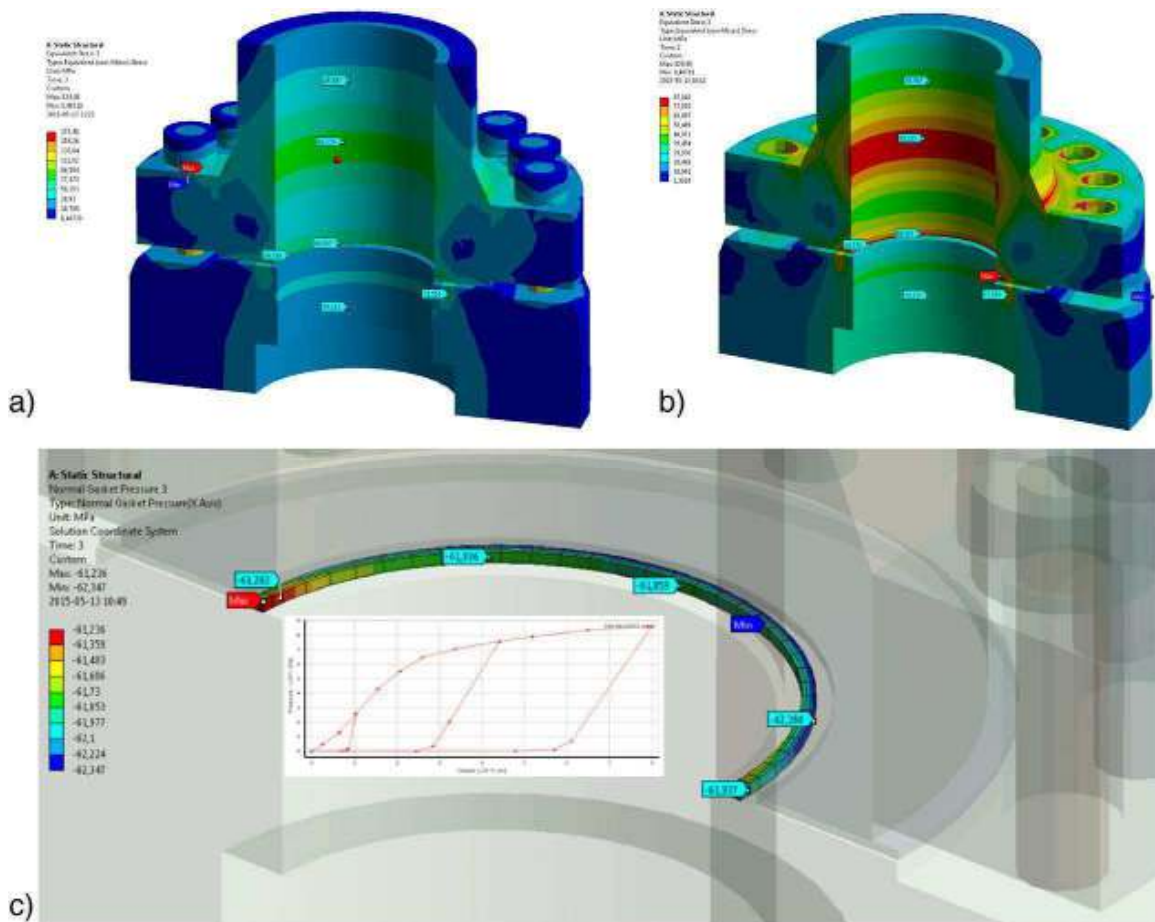

Fig. 13. FEM results for crucial flange connection of pipeline to the reactor's cube (head) at operating conditions (including pipelines deformation and reaction): von Mises equivalent stress distribution [MPa] at connection (a) and flanges (b); gasket pressure distribution [MPa] and gasket pressure-closure properties (c).

Table 5
Meshing parameters of the gasket model.

Number of nodes	Number of finite elements	Element quality	Aspect ratio
	8535	0.756	2.19

assumptions. In the presented case, the methodology has been used to investigate the cause of former failures of the nitrogen installation as well as to prevent its failures in the future. Although accurate displacement measurement results have been obtained in each individual 3D DIC setup, the final results in global coordinate system are error-burdened due to the accuracy of transformation estimation. In two of three field of views an acceptable quality of transformation has been, but there is still some space for the improvement. The quality of estimation of transformation between local (DIC) and global (geodetic) coordinate systems is dependent on the quality of surveyings, quality of calibration of DIC setup and the quality of image processing procedures used for detecting markers. The latter source of possible errors is also connected with the quality of markers itself. Increasing quality of all mentioned components of the data stitching procedure will allow to keep the transformation errors at the level of $2 \div 3$mm.

The results obtained in both examples have been used to validate or calibrate numerical models. This in turn can be used to analyze the cause of failures and to help in indication of locations for further assessment of the structures: i.e. for material analysis, defectoscopy, seal of flange connection. As a final effect, experimentally validated models of the large objects or industrial installations can be used for assessment of structural health of the structures, improvement of their safety and predict the future failures.

The main task in the future works is to decrease transformation error in the case of distributed multi-camera DIC measurements. Some basic steps that can be taken in order to achieve this goal have been indicated in Section 3.3.1 and Section 4.2.1. Another direction of the future works will be to use the method for automatic merging of 3D DIC data distributed in time [22,23] (introduced for a single 3D DIC setup) for temporal stitching of the data obtained with multi-DIC systems. Surveying can be used to calculate transformation between coordinate system of data sets gathered over a long period of time.

Acknowledgments

References

[1] K.-H. Lerman, Hybrid Techniques in Experimental Mechanics, in: Learmann K-H (Ed.), Optical Methods in Experimental Solid Mechanics, Springer, 2000.
[2] M. Sutton, J.J. Orteu, H. Schreier, Image Correlation for Shape, Motion and Deformation Measurements, Springer, 2009.
[3] B. Pan, Bias error reduction of digital image correlation using gaussian pre-filtering, Opt. Lasers Eng. 51 (2013) 1161–1167.
[4] B. Pan, H. Xie, Z. Wang, K. Qian, Z. Wang, Study on subset size selection in digital image correlation for speckle patterns, Opt. Express 16 (10) (2008) 7037–7048.
[5] Y. Zhou, C. Sun, Y. Song, J. Chen, Image Pre-filtering for Measurement Error Reduction in Digital Image Correlation, Optics and Lasers in Engineering (2014), http://dx.doi.org/10.1016/j.optlaseng.2014.04.018i.
[6] B. Pan, K. Li, W. Tong, Fast, robust and accurate digital image correlation calculation without redundant computations, Exp. Mech. (2013), http://dx.doi.org/10.1007/s11340-013-9717-6.
[7] M.A. Sutton, J.H. Yan, V. Tiwari, H.W. Schreier, J.-J. Orteu, The effect of out of plane motion on 2D and 3D digital image correlation measurements, Opt. Lasers Eng. 46 (10) (2006) 746–757.
[8] Z. Tang, J. Liang, Z. Xiao, Large deformation measurement scheme for 3D digital image correlation method, Opt. Laser. Eng. 50 (2) (2012) 122–130.
[9] G. Payen, H. Klocker, A. Lens, D. Wilkinson, J. Embury, Design of an in situ mechanical test for spot-welded joints, Eng. Fract. Mech. 96 (2012) 528–538.
[10] M. Malesa, K. Malowany, U. Tomczak, B. Siwek, M. Kujawinska, A. Sieminska-Lewandowska, Application of 3d digital image correlation in maintenance and process control in industry, Comput. Ind. 64 (9) (2013) 1301–1315.
[11] J.-J. Orteu, F. Bugarin, J. Harvent, L. Robert, V. Velay, Multiple-camera instrumentation of a single point incremental forming process pilot for shape and 3D displacement measurements: methodology and results, Exp. Mech. 51 (2011) 625–639.
[12] Y. Wang, P. Lava, S. Coppieters, P.V. Houtte, D. Debruyne, Application of a multi-camera stereo DIC set-up to assess strain fields in an erichsen test: methodology and validation, Strain 49 (2013) 190–198.
[13] X. Chen, L. Yang, N. Xua, X. Xie, B. Sia, R. Xu, Cluster approach based multi-camera digital image correlation: methodology and its application in large area high temperature measurement, Opt. Lasers Technol. 57 (2014) 318–326.
[14] C.-H. Hwang, W.-C. Wang, Y.-H. Chen, Camera Calibration and 3D Surface Reconstruction for Multi-camera Semi-circular DIC System, Proc. of SPIE, vol. 8769, SPIE, 2014 (876913–1).
[15] B. LeBlanc, C. Niezrecki, P. Avitabile, J. Sherwood, J. Chen, Surface Stitching of a Wind Turbine Blade Using Digital Image Correlation, Conference Proceedings of the Society for Experimental Mechanics, vol. 31, SPIE 2012, pp. 271–284.
[16] P.J. Besl, N.D. McKay, A method for registration of 3-D shapes, IEEE Trans. Pattern Anal. Mach. Intell. 14 (2) (1992) 239–256.
[17] M. Malesa, M. Kujawinska, K. Malowany, Multi-camera DIC system with a spatial data stitching procedure for measurements of engineering objects, Photonics Letters of Poland 6 (4) (2014) 157–159.
[18] A. Piekarczuk, M. Malesa, M. Kujawinska, K. Malowany, Application of hybrid fem-DIC method for assessment of low cost building structures, Exp. Mech. 52 (9) (2012) 1297–1311.
[19] A. Piekarczuk, K. Malowany, P. Wich, M. Kujawinska, P. Sulik, Stability and bearing capacity of arch-shaped corrugated shell elements: experimental and numerical study, Bulletin of the Polish Academy of Sciences 64 (1) (2015).

[20] R. Cybulski, R. Walentyski, M. Cybulska, Local buckling of cold-formed elements used in arched building with geometrical imperfections, J. Constr. Steel Res. 96 (2014) 1–13.
[21] P. Kohnke, Theory Reference for the Mechanical APDL and Mechanical Applications, Ansys Inc., 2009
[22] M. Malesa, M. Kujawinska, Modified two-dimensional digital image correlation method with capability of merging of data distributed in time, Appl. Opt. 51 (36) (2012) 8641–8655.
[23] M. Malesa, M. Kujawinska, Deformation measurements by digital image correlation with automatic merging of data distributed in time, Appl. Opt. 52 (19) (2013) 4681–4692.

Contents lists available at ScienceDirect

Optics and Lasers in Engineering

Multi-camera digital image correlation method with distributed fields of view

Krzysztof Malowany [a,*], Marcin Malesa [a], Tomasz Kowaluk [b], Malgorzata Kujawinska [a]

[a] Institute of Micromechanics and Photonics, Warsaw University of Technology, 8 Sw. A. Boboli St., 02-525 Warsaw, Poland
[b] Institute of Metrology and Biomedical Engineering, Warsaw University of Technology, 8 Sw. A. Boboli St., 02-525 Warsaw, Poland

ARTICLE INFO

ABSTRACT

A multi-camera digital image correlation (DIC) method and system for measurements of large engineering objects with distributed, non-overlapping areas of interest are described. The data obtained with individual 3D DIC systems are stitched by an algorithm which utilizes the positions of fiducial markers determined simultaneously by Stereo-DIC units and laser tracker. The proposed calibration method enables reliable determination of transformations between local (3D DIC) and global coordinate systems. The applicability of the method was proven during *in-situ* measurements of a hall made of arch-shaped (18 m span) self-supporting metal-plates. The proposed method is highly recommended for 3D measurements of shape and displacements of large and complex engineering objects made from multiple directions and it provides the suitable accuracy of data for further advanced structural integrity analysis of such objects.

1. Introduction

The 3D digital image correlation (3D DIC) technique (also known as Stereo-DIC) is the well-established non-coherent light based method which provides full-field, non-contact measurements of shape, displacements and strains of engineering objects [1]. The 3D DIC method is a combination of 2D DIC (which uses a single camera and provides in-plane displacements) and stereo-vision provided by a pair of cameras. The 3D DIC is suitable for shape and deformation measurements of both - planar and curved objects and it can measure all three components of displacements of a test object. The method is characterized by scalable sensitivity and dimensions of a field of view and simple instrumentation. Since its origin in the early eighties [2] it has undergone many changes and modifications, which have improved computation efficiency and accuracy [3–7], adapted to new application fields [8–12], enhanced the hardware [13–15], provided solutions to work in extreme environments [16,17] and enabled new measurement possibilities, such as 3D strain fields determination [18]) or performing measurements distributed in time [19]. Despite all this progress, 3D DIC, similarly to other machine vision based methods, faces the basic problem which is an interdependence of the accuracy and field of view (FoV) of a single 3D DIC system. It means that the accuracy of displacement measurement decreases with the increased FoV. The most frequent solution to this problem is extending a FoV through implementation of multiple cameras and further com-

bining the data by means of a spatial data stitching (SDS) algorithm in which data obtained with individual systems are stitched together into a common coordinate system. A SDS algorithm has to be tailored to fit one of two measurement strategies, namely:

- the strategy with overlapping areas of fields of view of multi-camera DIC,
- the strategy with fields of view of multi-camera DIC distanced from each other and with no overlapping areas.

The first strategy, which is possible only when any two neighboring measurement systems (or all of them) have overlapping area within their fields of view, is described in papers [20–23]. The calibration target in the overlapping area can be viewed by at least two systems at the same time. The knowledge of the 3D position of markers within calibration target in the local coordinate systems of 3D setups enables calculation of the geometrical transformation between coordinate systems of 3D setups. Specifically when big objects need to be measured it is not possible to assure common fields of view of all cameras (in contrast to [20] solution). In such cases, the cameras can be arranged in a wall-of-cameras configuration (for measurements of flat objects), or surrounding cameras (for cylindrical objects). Wang in [21] and Chen in [22] applied surrounding cameras configuration for measurements of cylindrical objects. In both papers the authors used each two neighboring cameras as individual 3D DIC system. Each system has been calibrated separately, but with sequential utilization of geometrical transformation between

* Corresponding author.
  E-mail address: k.malowany@mchtr.pw.edu.pl (K. Malowany).

cameras it was possible to refer all data to the common coordinate system. In the presented solution it was required to have some overlaid area in the field of view of neighboring cameras. Somewhat different approach has been presented in [24] by Leblanc et. al. The Authors realized displacements and strains measurements of a wind turbine blade with a single, portable 3D DIC system. In this solution, 16 point clouds representing different areas of the object have been stitched together using a set of markers applied directly to the structure. The solution with portable 3D DIC system is restricted to an object which is changed in incremental way, while staying static through the entire measurements process.

Although the first measurement strategy extends significantly the ability of 3D DIC method to measure big objects, in many cases it is still insufficient. In industry, the crucial parts of installations can be distanced by tens (or even more) of meters and therefore the second measurement strategy with the distributed configuration of multi-camera DIC system (with no overlapping areas of fields of view) has to be used. When implemented, it is extremely useful for such important tasks as validation of numerical models of complex buildings [24] or civil engineering structures [25], as well as calibration of the numerical models of old installations (e.g. pipeline network in chemical industry), which do not operate in accordance to design assumptions due to many years of service. The first attempt to provide the measurement methodology in this scenario was presented by Malesa et al. in [23]. In this case, the data stitching procedure was performed with the use of external method, namely geodetic surveying. In order to determine transformation between individual 3D DIC setups, fiducial markers were applied to the object. Similarly to the previous strategy, 3D positions of all the markers need to be referenced to the common coordinate system. As none of the 3D DIC setups view all markers at the same time, determination of the markers positions was performed by geodetic surveying. The accuracy of data stitching procedure in this case is dependent on the quality of a standard camera calibration of individual 3D DIC setups and on the accuracy of the aiding method. Unfortunately, the utilization of geodetic surveying technique had not provided the sufficient accuracy of data stitching. In this paper, in order to overcome the limitations of the existing multi-camera 3D-DIC systems employed to displacement measurement for big engineering objects with areas of interests distributed in space, the authors proposed to employ a laser tracker [26] as the aiding method. During the measurements, the laser tracker follows (by means of an angular encoder and interferometry) the position of optical target (marker) with high accuracy. The laser tracker measures the position of markers in a global coordinate system, simultaneously 3D DIC systems measure the position of markers noticeable in their individual fields of view. Information on markers position in global and local coordinate systems, enable transformation of local coordinate systems of each 3D DIC system to common coordinate system. The high accuracy of the transformations has been validated by means of coordinate measuring machine in laboratory conditions. The effectiveness and performance of the proposed method and system are verified performing measurements and monitoring of a hall made of arch-shaped (18 m span) self-supporting metal-plates exposed to weather conditions.

2. General concept of measurements in distributed fields of view

The main challenge during the measurements of an object with distributed (non-overlapping) fields of view is connected with transforming many local coordination systems of a single 3D DIC setups into a single global coordinating system. The procedure is based on a standard geometric transformation between local coordinate systems $(OX_1Y_1Z_1, \ldots, OX_nY_nZ_n$ - related to each individual 3D DIC setup, where n indicates the number of 3D DIC system) and global coordinate system $(OX_0Y_0Z_0$ - related to the laser tracker). The scheme of two 3D DIC setups representing the general approach with multiple 3D DIC setup is shown in Fig. 1. Geometrical transformations are estimated using multiple positions of a fiducial marker $(P_{11}, \ldots, P_{nm}$, where n - index
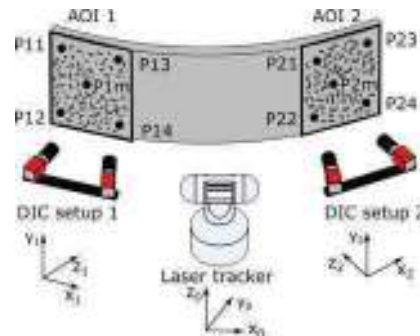

Fig. 1. Schematic drawing of configuration of multiple (here: n=2) 3D DIC setup applied for distributed FOV measurement scenario, with laser tracker.

of 3D DIC measurement setup, m - position of point within n-th AOI), which is sequentially placed in the area of interest (AOI) of local 3D DIC setups. 3D positions of the marker in local coordinate systems are determined with the use of image processing algorithms (to find its 2D pixel coordinates) and triangulation (to calculate real world 3D coordinates). At the same time, positions of the marker in the global coordinate system are determined by a laser tracker. Transformation parameters (rotation: R_x, R_y, R_z and translation: T_x, T_y, T_z) between local and global coordinate systems (more specifically between vectors of 3D positions of markers) are obtained with utilization of Singular Value Decomposition (SVD) method [27]. The general data stitching flowchart is presented in Fig. 2.

2.1. Measurements of positions of a fiducial marker

The main difficulty in simultaneous measurements of 3D positions of markers with 3D DIC setups and laser tracker is that an optical target (which is used for laser tracker) is not suited for image processing algorithms. The optical target is a retro-reflector in a spherical, polished, steel housing. Precise detection of the center of the optical target with the image processing procedures would be difficult if not impossible (Fig. 3a)). In order to overcome this obstacle, the optical target was replaced by ball bearing painted with white matt paint (Fig. 3b)). Repeatability of the positioning of the optical target (for laser tracker) and ball bearing (for 3D DIC setup) has been ensured by using magnetic holder, consisting of large magnet attached to the measured metal sheet and a smaller magnet with cylindrical hole for the optical target and ball bearing (Fig. 3c)). The position of the center of the white ball bearing was determined with utilization of the image processing procedures (chapter 5 [28]). In order to achieve proper contrast at captured images, a black sheet of paper was placed below the magnet with a cylindrical hole (Fig. 3d)). The diameter of the ball bearing was the same as the diameter of the optical target's housing. In order to avoid the measurement error which could be caused by the thickness of paint layer, the area of ball bearing which was attached to the magnetic holder was not painted. This approach assured the repeatability of the position of the center of optical target and ball bearing in a magnetic holder. Each measurement of the position of a fiducial marker was proceeded in three steps, (i) the position of optical target was measured by the laser tracker, (ii) the optical target was replaced by ball bearing and its position was measured by stereoscopic system, (iii) the ball bearing was replaced by optical target in order to verify the position of a magnetic holder by the laser tracker. If the shift of position was larger than 0,1 mm the measurement procedure was repeated. In order to capture multiple positions, the magnetic holder was moved within AOI ($m > 4$, m - the number of fiducial marker position).
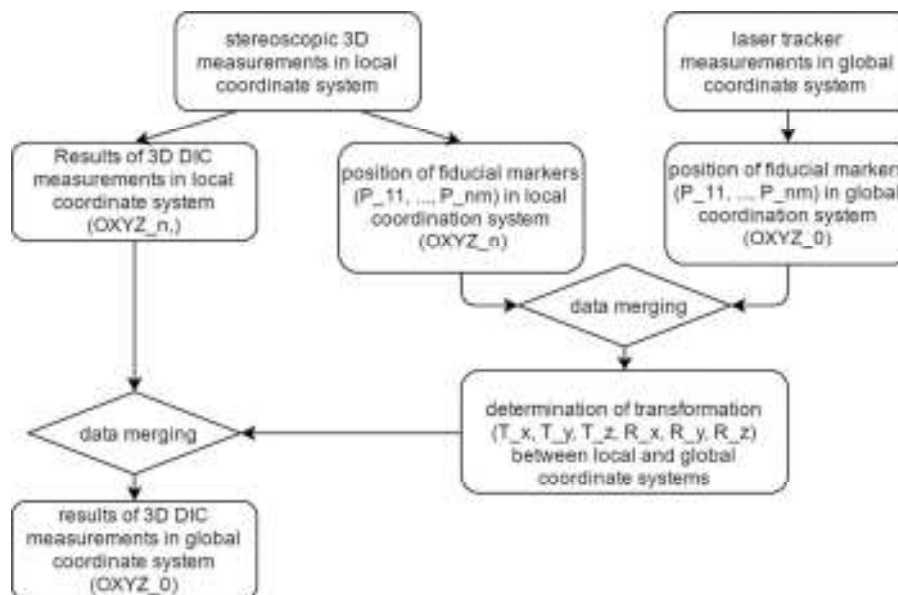
Fig. 2. Flowchart of the data stitching procedure, n - indicates the number of 3D DIC systems.

Fig. 3. Fiducial markers: a) optical target, b) ball bearing painted white matt, c) magnetic holder with a cylindrical hole for fiducial markers, d) a fragment of image with ball bearing captured by one of cameras.

2.2. The accuracy of displacement measurements

The 3D DIC method is mainly used to determine the displacements of the measured object, as in this case. Therefore, during development of new DIC configurations the determination of the accuracy of displacement measurements is very important. In the case of multi-camera DIC method with distributed fields of view the error analysis considers:

- the accuracy of displacement measurement of individual 3D DIC setups,
- an impact of data transformation between local and global coordinate systems.

The accuracy of displacement measurements of multi-camera 3D DIC system will be determined by the lowest accuracy of a component 3D DIC setup.

Good estimation of the accuracy of 3D displacement measurements can be reprojection error, which will be considered in this work as the displacement measurement error. The reprojection error signifies an image distance between a projected point and a measured point. The 3D coordinates of the projected point are determined with triangulation equations after the stereo-calibration procedure.

The accuracy of estimation of a transformation between local and global coordinate systems can be determined by calculating mean square errors of distances between 3D positions of markers in the global coordinate system (obtained by laser tracker) and 3D positions of markers (obtained by stereo vision system) after transformation from local coordinate systems. In the case of displacement measurements, the transformation error obtained in the data stitching procedure cannot be directly taken into account, this error determines the misalignment between the global coordinate system and local coordinate system of individual 3D DIC systems, which cause cosine error in the case of displacement measurements. In order to determine the influence of this error on the accuracy, the angle between the two planes matched to the two groups of points will be calculated. First group includes position of fiducial markers (optical target) determined by laser tracker, second group includes positions of the corresponding fiducial markers (ball bearing) but determined by stereoscopic system transformation to global coordinate systems.

3. Validation of the accuracy of displacements measurements

The performed tests consider the validation of the accuracy of displacements measurements, which in multi-camera 3D DIC system is determined by the lowest accuracy of a component 3D DIC setup. Therefore, the laboratory tests were performed with utilization of a single 3D DIC setup. The obtained displacement measurements results were transformed into global coordination system (according to the proposed methodology) and compared to reference data. In laboratory conditions the field of view (FOV) was significantly smaller than intended in *in-situ* measurements. In consequence, the accuracy of displacement measurements in laboratory conditions increased when compared to *in-situ* measurements. According to metrological practice, a measurement method

Table 1
Estimated transformation parameters and estimation errors.

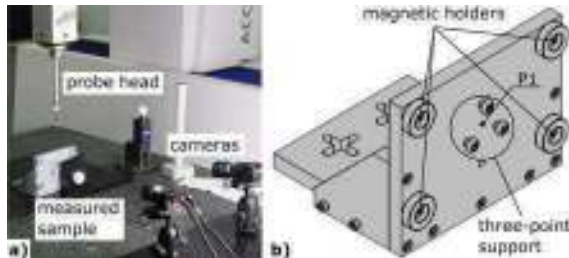| Tx [mm]	Ty [mm]	Tz [mm]	Rx [deg.]	Ry [deg.]	Rz [deg.]	Error [mm]
350.743	−259.542	148.682	−1.756	−0.158	0.183	0.24

Fig. 4. a) measurement setup in a laboratory, b) designed test object.

should be validated by means of a method which accuracy is at least one order of magnitude higher. In the case of laboratory measurements of small objects, the obtained accuracy of 3D DIC system (90 μm) is comparable with the accuracy of a laser tracker system, the maximum accuracy of laser tracker (Leica AT 901 B) would achieve the value of 20 μm. Therefore, the proposed data stitching method has to be validated with utilization of a coordinate measuring machine (CMM), the Carl Zeiss ACCURA 7 with the accuracy of 2 μm.

In order to perform laboratory measurements, a special test object (Fig. 4) had been designed. The test object consists of a flat front plate (size 150 mm × 120 mm) with speckle pattern applied and point P1 marked at the center of the object. Four magnetic holders with cylindrical hole for fiducial marker were fixed to the corners of the front plate. In the middle of the front plate (around point P1), a three-point support was placed, which enables unambiguous positioning of fiducial marker. The bottom plate with mounting holes enabled to fix the test object. Measurements of the sample have been performed with the 3D DIC system, which comprises two 5 MPx (2448 × 2048) Pointgrey cameras equipped with 8 mm focal length lenses, the FOV covered an area of 0.8 m × 1 m. Reprojection error after calibration of 3D DIC system was 0.09 mm.

The validation started with measurements of four positions of the optical target (by CMM) and ball bearing (by 3D DIC) attached to the magnetic holders, which enable calculation of a transformation matrix between local coordination system (related to 3D DIC) and global co-ordination system (related to CMM). Obtained transformation parameters, as well as transformation errors, are given in Table 1. According to Section 2.2, the obtained transformation error is 0.24 mm, the obtained angle was 0.03 degrees, therefore the error caused by this misalignment was 0.08 μm/m. The obtained displacement measurement error equaled 0.09 mm +/− 0.08 μm/m.

Next, the measurements of the position and displacements of point P1 were performed, which have been measured directly by 3D DIC system. CMM measured the position of point P1 indirectly. First, the position of the center of the optical target attached to the three-point support had been measured and then - the position of the front plate Next, the position of the center of the optical target has been projected on the front plate surface. The coordinates of the projected point corresponded to the position of point P1. Reference displacements were calculated as differences in positions of point P1 (referring to the first position) measured by CMM. It is worthwhile to notice that the error of a possible misalignment between the position of point P1 and responding point (obtained as projection of the center of the optical target on the front plate surface) had no effect on displacement measurement error (estimated value below 0.1 μm/m). The measurements of 21 random displacements of point P1 (gauges) were performed. During the mea-
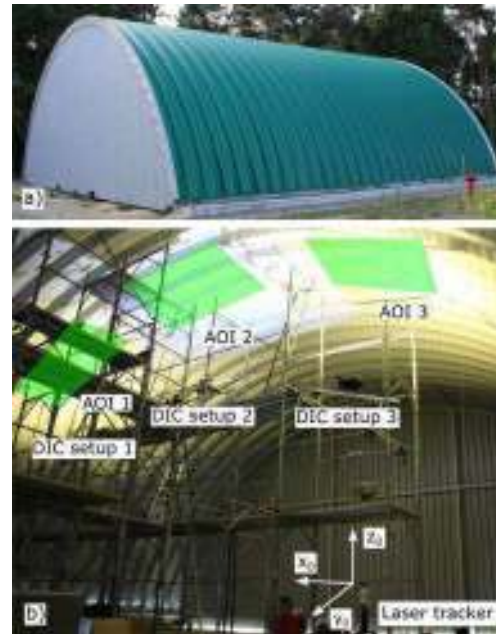

Fig. 5. a) Outside image of the measured hall, b) measurement set-up.

surements, the test object was moved in the range of 27 mm and 15˚. The measurement error was calculated as difference between the CMM reference measurement and the 3D DIC measurements of the displacements of point P1. The maximum error values amounted 0.046 mm, 0.061 mm, 0.025 mm respectively, for X, Y, Z axes of the global coordinate system and 0.084 mm resultant spatial error. Measurement uncertainty at the confidence level of 95% (doubled standard deviation value) amounted 0.047 mm for spatial measurements.

The performed measurements validated the assumed displacement accuracy of multi-camera 3D DIC system which utilizes the proposed procedure of data stitching, the estimated accuracy was 0.09 mm +/- 0.08 μm/m, while the obtained measurement uncertainty was 0.047 mm.

4. Measurement of construction made of self-supporting metal-plate structure

4.1. Measured object

The first implementation of the proposed method was performed during *in-situ* measurements of hall made of arch-shaped self-supporting metal-plates (Fig. 5a)), in cross-section of an arch, 8 m high and 18 m wide. Each arch-shaped metal plate has a cross section of a trough, the arches are jointed by double lock seam. This is a new type of buildings in civil engineering adopted directly from military applications, characterized by low cost and time of production. However, due to complex geometry and boundary condition (due to plastic deformations, cross section of a trough, a goffer pattern), the FEM model of this structure requires updating with utilization of experimental investigation [29–32].

Table 2
Estimated transformation parameters and estimation errors.

Setup	Tx [mm]	Ty [mm]	Tz [mm]	Rx [deg.]	Ry [deg.]	Rz [deg.]	Error [mm]
AOI1	11574.70	−160.80	3940.86	0.7523	−0.0042	3.0481	1.35
AOI2	9316.39	−71.04	4430.90	−0.3642	0.0761	3.0997	1.63
AOI3	4389.34	−149.94	3488.92	0.0461	0.1375	0.0000	3.06

Table 3
Estimation of displacement measurements error for individual AOI.

Setup	Measurement error of each DIC setups [mm]	Angle between planes α [deg]	Cosinuse error (1-cos α) [µm/m]
AOI 1	0.21	0.09	1.27
AOI 2	0.17	0.02	0.05
AOI 3	0.24	0.03	0.16

4.2. Measurement set-up

During the test, multi-camera DIC setup observed three AOI, which covered the localization of points corresponding to the numerically predicted positive and negative maximum displacements (caused by snow and wind). The location of points was calculated with the use of FEM model. Each AOI covers the area of 2.5 m × 1.5 m and distance between neighboring AOIs is approximately 4 m. The speckle pattern was fabricated with the use of white&black paint, the measured AOIs were reachable from the ladder. The measurement setup consisted of six 5 MPx (2448 × 2048) Pointgrey cameras equipped with 8 mm focal lenses. Cameras were connected to one control computer, in order to synchronize the data acquisition procedure. Appropriate cameras were paired and served as three separate 3D DIC setups. Each 3D DIC system was calibrated with utilization of standard chessboard calibration target. In order to ensure appropriate light conditions during the measurements, fields of view were illuminated with LED reflectors. Multi-camera DIC system was placed on the 6 m high and 10 m wide buildings temporary scaffolding (Fig. 5b)). The laser tracker was located 7 m from the scaffolding. In the studies, the Leica AT 901 B laser tracker was used. The accuracy of the system depends on the operating mode. In the interferometer mode the maximum permissible error is 0.004 mm + 0.003 mm/m, whereas in the rangefinder mode it is 0.015 mm + 0.006 mm/m. Due to the conditions during the measurement (interruption of the laser beam during the measurement) the laser tracker was working in the rangefinder mode.

4.3. Transformation between local and global coordinate in in-situ measurements

According to methodology of estimation of the accuracy of transformations between local and global coordinate systems presented in Section 2.2, the transformation parameters and errors had been calculated and presented in Table 2. As one can observe, errors in all setups were kept below 3.1 mm, which is a very good result, taking into account overall dimensions of the measured object.

4.4. The accuracy of displacement measurement in in-situ measurements

According to methodology of estimation of the accuracy of displacement measurement presented in Section 2.2, the errors of displacement measurements for each AOI is summarized in Table 3. The DIC calculations were performed with 45 px subset size and 15 px step size, the affine transform has been used as a shape function. Reprojection errors after calibration of each stereo-vision system were below 0.1 px (below 0.24 mm after scaling to mm), the obtained angle was in the range from 0.02 to 0.09°, therefore the maximum error caused by this misalignment was 1.27 µm/m. As the permissible error of multi-camera

DIC system, the maximum error of individual 3D DIC systems is taken. In this case, the maximum error was obtained in AOI 3, and equaled 0.24 mm +/− 0.16 µm/m. As one can observe, the maximum cosine error caused by transformation occurred in AOI 1, while the maximum displacement measurement error and transformation estimation error have been obtained in AOI 3. This difference shows that the relative position of individual 3D DIC coordinate systems and laser tracker coordinate system influence the final displacement measurement error. This source of error should be evaluated in the future works.

4.5. Measurement results

As a result of the measurements, the displacement maps from three 3D DIC setups in global coordinate system have been obtained. Displacement values have been coded in color and overlaid on the point cloud representing the 3D shape of the measured areas. Fig. 6 presents an exemplary data set, including the displacements in three directions. Each measured metal plate has a cross section of a trough, thus the images in the area of slanted surfaces (in relation to the position of each 3D DIC system) were measured from large angle of observation. Therefore, those areas have been thresholded in DIC analysis due to higher correlation error, as a result, the obtained maps in each AOI are not continuous. On the displacement maps the influence of the 10 °C increase of temperature during 6 h, can be observed. The W displacements are perpendicular to the foundation of the structure. The bottom of the structure is supported by the foundation, thus the biggest displacements are observed at the top of the structure. One can observe asymmetry in displacement maps in U and V directions, this is caused by unevenness of insolation. Results will be used to update the FEM model.

5. Conclusions and future works

This paper presents the procedure that enables reliable determination of transformations between local (3D DIC) and global coordinate systems and therefore allow to perform measurements with a multiple 3D DIC systems with fields of view distributed in space. The proposed methodology was validated in laboratory conditions and implemented in measurements of large scale construction, the obtained data will support the process of updating the FEM model of this construction. The error of transformation between local and global coordinate systems was smaller than 3.1 mm, which is significantly lower than dimensional tolerance of construction. The obtained permissible error of measurements 0.24 mm +/− 0.16 µm/m, enables the comparison of data from the measurements and FEM calculations. Furthermore, from the obtained displacement fields, the strain fields will be calculated.

The method proposed by the authors is specifically valuable when full-field measurements of displacement in 3D and strains in the selected AOIs are required. However, it should be mentioned that in some cases the point wise measurements distributed in space are sufficient. Recently Pan et. al. [12] developed optical based method for real-time, non-contact and targetless measurement of vertical deflection. This method can be easily applied in case of deflections measurements of multiple point on large engineering objects. The method overcomes the disadvantages of 3D DIC method in case of large AOI, including fabrication of speckle pattern and stereo calibration.

As it was mentioned in Section 4.5 the presented measurements included several hours measurement, in this case the temperature influence on the measurement setup was negligible (less than 10 °C). How-
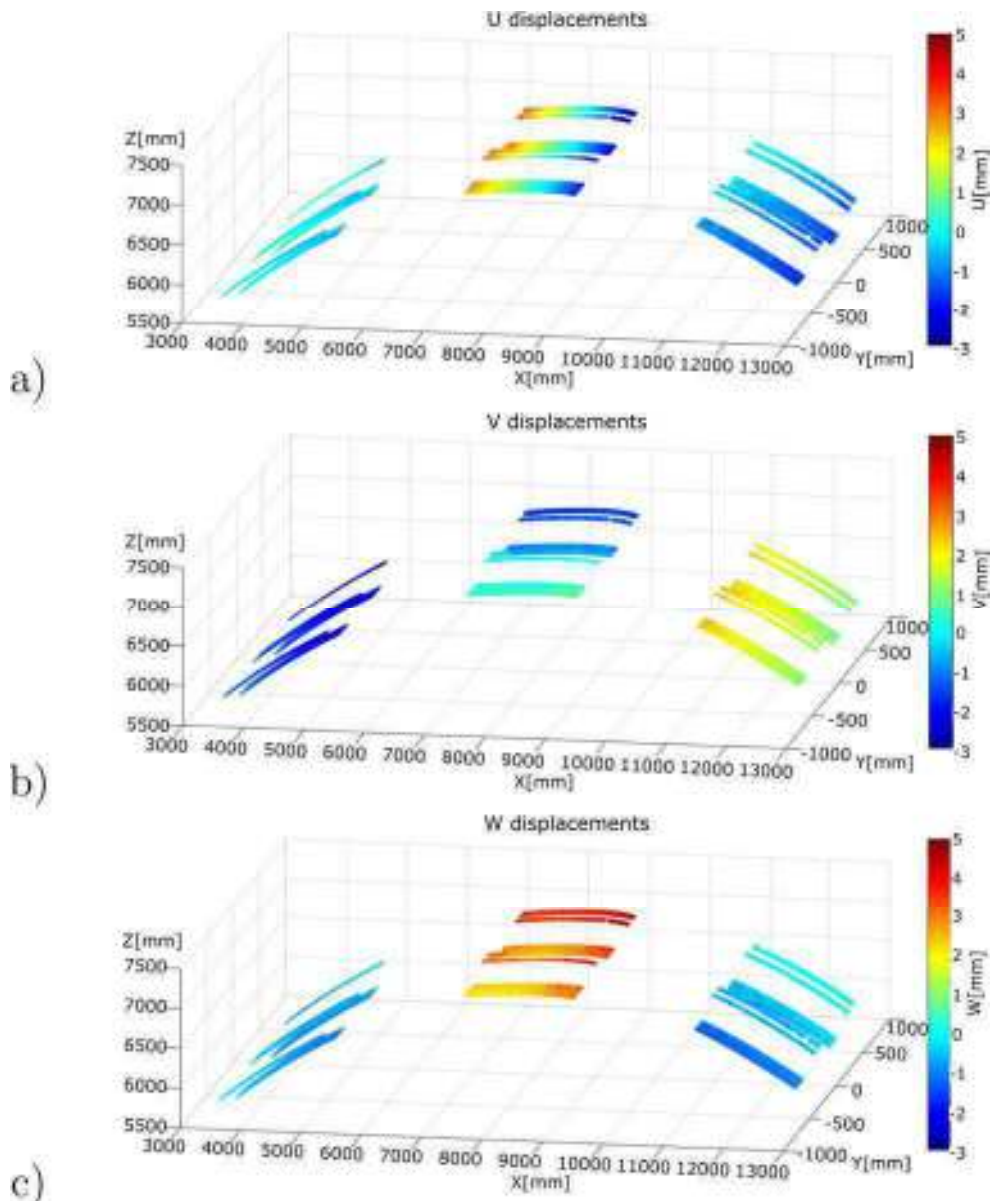
171

Fig. 6. Exemplary results of the measurements stitched in the global coordinate system: a) U displacement map, b) V displacement map, c) W displacement map.

ever, in the case of long term measurements (e.g. during summer and winter seasons) the temperature influence on the measurement setup and development of methodology which enables the neutralization of this influence [16,17] should be considered. These works are crucial in long-term measurements, including summer and winter periods.

Acknowledgments

References

[1] Sutton M, Orteu JJ, Schreier H. Image correlation for shape, motion and deformation measurements. Springer; 2009.
[2] Peters W, Ranson W. Digital imaging techniques in experimental stress analysis. Opt Eng 1982;21(3):427–31.
[3] Pan B. Bias error reduction of digital image correlation using gaussian pre-filtering. Opt Lasers Eng 2013;51:1161–7.
[4] Pan B, Xie H, Wang Z, Qian K, Wang Z. Study on subset size selection in digital image correlation for speckle patterns. Opt Express 2008;16(10):7037–48.
[5] Zhou Y, Sun C, Song Y, Chen J. Image pre-filtering for measurement error reduction in digital image correlation. Opt Lasers Eng 2015;65:46–56. http://dx.doi.org/10.1016/j.optlaseng.2014.04.018i.
[6] Pan B, Li K, Tong W. Fast, robust and accurate digital image correlation calculation without redundant computations. Exp Mech 2013;53:1277–89.

[7] Sutton MA, Yan JH, Tiwari V, Schreier HW, Orteu J-J. The effect of out of plane motion on 2d and 3d digital image correlation measurements. Opt Lasers Eng 2006;46(10):746–57.

[8] Tang Z, Liang J, Xiao Z. Large deformation measurement scheme for 3d digital image correlation method. Opt Lsaers Eng 2012;50(2):122–30.

[9] Payen G, Klocker H, Lens A, Wilkinson D, Embury J. Design of an in situ mechanical test for spot-welded joints. Eng Fract Mech 2012;96:528–38.

[10] Malesa M, Malowany K, Tomczak U, Siwek B, Kujawinska M, Sieminska-Lewandowska A. Application of 3d digital image correlation in maintenance and process control in industry. Comput Ind 2013;64(9):1301–15.

[11] Malowany K, Tyminska-Widmer L, Malesa M, Kujawinska M, Targowski P, Rouba B. The application of 3d digital image correlation to track displacements and strains of canvas paintings exposed to relative humidity changes. Appl Opt 2014;53(9):1739–49.

[12] Pan B, Tian L, Song XL. Real-time, non-contact and targetless measurement of vertical deflection of bridges using off-axis digital image correlation. NDT&E Int 2016;79:73–80.

[13] Pan Z, Xia S, Gdoutou A, Ravichandran G. Diffraction-assisted image correlation for three-dimensional surface profiling. Exp Mech 2015;55(1):155–65.

[14] Wu LF, Zhu JG, Xie HM. Single-lens 3d digital image correlation system based on a bilateral telecentric lens and a bi-prism: validation and application. Appl Opt 2015;54(26):7842–50.

[15] Wu LF, Zhu JG, Xie HM, Zhang Q. An accurate method for shape retrieval and displacement measurement using bi-prism-based single lens 3d digital image correlation. Exp Mech 2016;56(9):1611–24.

[16] Pan B, Wu DF, Yu LP. Optimization of a three-dimensoinal digital image correlation system for deformation measurements in extreme environments. Appl Opt 2012;51(19):4409–19.

[17] Pan B, Shi WT, Lubineau G. Effect of camera temperature variations on stereo-digital image correlation measurements. Appl Opt 2015;54(34):10089–95.

[18] Bay B, Smith T, Fyhrie D, Saad M. Digital volume correlation: three-dimensional strain mapping using x-ray tomography. Exp Mech 1999;39(3):217–26.

[19] Malesa M, Kujawinska M. Deformation measurements by digital image correlation with automatic merging of data distributed in time. Appl Opt 2013;52(19):4681–92.

[20] Orteu J-J, Bugarin F, Harvent J, Robert L, Velay V. Multiple-camera instrumentation of a single point incremental forming process pilot for shape and 3d displacement measurements: methodology and results. Exp Mech 2011;51:625–39.

[21] Wang Y, Lava P, Coppieters S, Houtte PV, Debruyne D. Application of a multi-camera stereo DIC set-up to assess strain fields in an erichsen test: methodology and validation. Strain 2013;49:190–8.

[22] Chen X, Yang L, Xua N, Xie X, Sia B, Xu R. Cluster approach based multi-camera digital image correlation: methodology and its application in large area high temperature measurement. Opt Lasers Technol 2014;57:318–26.

[23] Malesa M, Malowany K, Pawlicki J, Kujawinska M, Skrzypczak P, Piekarczuk A, et al. Non-destructive testing of industrial structures with the use of multi-camera digital image correlation method. Eng Failure Anal 2016;69:122–34.

[24] LeBlanc B, Niezrecki C, Avitabile P, Sherwood J, Chen J. Surface stitching of a wind turbine blade using digital image correlation. In: Conference Proceedings of the Society for Experimental Mechanics, 31. SPIE; 2012. p. 271–84.

[25] Malesa M, Kujawinska M, Malowany K, Siwek B. Diagnostic of structures in heat and power generating industries with utilization of 3d digital image correlation. In: Proc. of SPIE, 8788. SPIE; 2013.

[26] Muralikrishnan B, Phillips S, Sawyer D. Laser trackers for large-scale dimensional metrology: a review. Precis Eng 2016;44:13–28.

[27] Besl PJ, McKay ND. A method for registration of 3-d shapes. IEEE Trans Pattern Anal Mach Intell 1992;14(2):239–56.

[28] Bradski G, Kaehler A. Learning OpenCV: computer vision with the OpenCV library. O'Reilly Media; 2008.

[29] Piekarczuk A, Malesa M, Kujawinska M, Malowany K. Application of hybrid fem-dic method for assessment of low cost building structures. Exp Mech 2012;52(9):1297–311.

[30] Cybulski R, Walentyński R, Cybulska M. Local buckling of cold-formed elements used in arched building with geometrical imperfections. J Construct Steel Res 2014;96:1–13.

[31] Piekarczuk A, Malowany K, Więch P, Kujawinska M, Sulik P. Stability and bearing capacity of arch-shaped corrugated shell elements: experimental and numerical study. Bull Polish Acad Sci 2015;64(1).

[32] Piekarczuk A, Malowany K. Comparative analysis of numerical models of arch-shaped steel sheet sections. Arch Civil Mech Eng 2016;16(4):1–13.

Application of complementary optical methods for strain investigation in composite high pressure vessel

Paweł Gąsior[a,*], Marcin Malesa[b], Jerzy Kaleta[a], Małgorzata Kujawińska[b], Krzysztof Malowany[b], Radosław Rybczyński[a]

[a] Department of Mechanics, Materials Science and Engineering, Wroclaw University of Science and Technology, 25 Smoluchowskiego St, 50-370 Wroclaw, Poland
[b] Institute of Micromechanics and Photonics, Warsaw University of Technology, 8 Sw. A. Boboli St, 02-525 Warsaw, Poland

A B S T R A C T

The work presents the methodology of displacement and strain measurements (in type IV composite high pressure hydrogen and methane storage vessels in areas of the gaseous fuel cell vehicle. The research was conducted in vessels with so called programmed defects in the form of notches and delamination. The complementary optical methods, namely: optical fibre sensing based on Bragg gratings (FBG) and digital image correlation (DIC) method were used for performing local and full-field displacement/strain measurements respectively. It has been shown that DIC can be successfully applied as the method for defect identification in full field of view and that it can support an optimal localization of FBG sensors and their calibration. As FBG sensors are devoted to be integrated with the vessel structure, the proposed methodology constitutes a solution to the difficult problem of building an efficient Structural Health Monitoring (SHM) system for composite high pressure vessels for gaseous fuels. At the same time the measurement data from both systems supports calibration of numerical models of the vessels.

1. Introduction

Composite high pressure vessels are more and more frequently used in automotive industry, aviation, emergency services and power industry. This results from their advantages such as high strength/stiffness-to-weight ratio [1], and excellent resistance to fatigue and corrosion [2,3]. The main area of composite vessels applications is gaseous fuel storage: hydrogen (CH2 vessel), methane (CNG vessel) or their blends. Hydrogen is used mainly in fuel cells (FC). The latest CH2 vessels allow to compress hydrogen at 70 MPa. High pressure enables to provide, despite of low hydrogen density, an appropriate amount of the fuel at reasonable volume, making it possible for a vehicle to cover a range of 600–700 km on one refuelling.

According to the current regulations [4,5], in the case of CH2 vessels, 70 MPa Nominal Working Pressure (NWP), made of the carbon-epoxy composite (CFRC), the Burst Pressure (BP) cannot be lower than 157.5 MPa. In the case of structures reinforced with glass fibre (GFRC) the required BP reaches 255.5 MPa. It means that the material of the vessels with compressed hydrogen or methane works in high-effort conditions which requires monitoring of the health of these structures. Although the binding legal regulations [4,6] require the vessels to undergo periodical checks only, however several currently conducted works [7,8,9,10] aim at applying continuous monitoring. This may allow to decrease high safety coefficients of vessels with a SHM system, including a decrease of their weight and hopefully their costs.

The analysis of recent literature [7,8,11,12,13,14,15,16] and Internet sources [9,10], shows that the best solution is using optical fibre sensors for this purpose. The reason is their resistance to electromagnetic interference, intrinsic safety, easy integration with composite material structure and high sensitivity in a long term measurement. These sensors are permanently fixed on the vessels surface or embedded in the structure of composite material and allow to continuously control technical condition throughout the whole exploitation period. Moreover, apart from embedding in the composite structure, they allow to assess and control the whole manufacturing process (e.g. initial strain, initial fibre tension, hardening temperature, internal pressure) [1,14]. The basic measurement technique used in the analysed works is the fibre-optic technique using sensors with luminous wavelength modulation, the so called Bragg Grating, FBG) [1,8,11,12,13,16,17,18]. Other FO sensors, such as interferometric ones, SOFO®, Fabry-Perot (F-P) type [15,19,20], or distributed sensors [21] are less often applied for this purpose.

The works on applications of optical fibre methods for strain measurements in vessels [8,11,12,13,16] so far have mostly referred to low pressure vessels with thin walls. However, it is of key significance that in the case of CH2 composite vessels with nominal operating pressure 70 MPa, the thickness of the carrying wall of the vessel can be even from 20 up to 50 mm. Hence, in the case of such complex structures the measurement of construction strains in many places, including also on the wall thickness becomes necessary. An introduction of other than optical fibre sensors (with a small cross-section diameter) between the subsequent composite layers results in initial defection of the composite material (a kind of notch). In the case of strain gauge sensors, which are sometimes used, local structure discontinuity occurs (e.g. local delamination) which can be precursors of a fault development during vessel exploitation (cyclical refuelling and using up the fuel in vessels).

On the other hand, there are numerous works in which optical measurement methods are used to analyse strains in composite materials to provide information about a structure behaviour in a full field of view [22]. The most commonly used methods encompass highly-sensitive techniques using coherent light (digital speckle pattern interferometry DSPI and digital speckle pattern shearing interferometry DSPSI [23], grating (moire) interferometry GI [24]) and incoherent light, with lower sensitivity, among which currently the most popular is the digital image correlation method [25]. The major advantage of these techniques is the possibility of simultaneous detecting in full-field of view heterogeneities in a composite material which occur due to different phenomena: defects or cracks within material, mechanical set-ups causing parasitic effects, strain gradients due to distributed mechanical properties. The major disadvantage (due to architecture of interferometric and vision based systems) is connected with difficulties in implementing these techniques for long term monitoring during exploitation of composite structures under investigation.

The above consideration has clearly indicated the necessity to develop a new non-destructive methodology of measurement and monitoring of strain distribution in composite, high-pressure vessels type IV (polymer liner, operating pressure up to 70 MPa) assigned for storage of compressed hydrogen and methane. This methodology should take into account the following requirements:

- ensuring necessary measurement data for the identification of vessel numerical models, additionally these data should "cover" the vessel surface as densely as possible,
- definition of the areas with the biggest effort (critical ones) in the whole vessel and thereby indication of sensor locations,
- continuous diagnostics of a vessel in a vehicle during long lasting exploitation (on-board monitoring system), including refuelling and periodical diagnostics,
- independence of strain measurement of the influence of ambient temperature,
- strain measurement in vessels of various geometry and dimensions (various applications of vessels: automotive, stationary, transportation),
- ensuring measurement of relatively large deformations (in comparison with the ones occurring in metal vessels) and high sensitivity in a wide measurement range,
- guaranteed resistance to electromagnetic interference, spark-proofness and easy integration of sensors with composite material structure,
- defect identification in a vessel resulting from random events and progressing degradation of composite strength parameters due to e.g. fatigue,
- ensured validation of SHM used for a vessel.

Unfortunately, there is no a single measurement method which would satisfy all the above requirements. This is why we have proposed to develop a "hybrid" measurement and data analysis procedure which applies two different optical methods, namely:

- digital image correlation method (DIC) for full-field, global strain determination at the whole surface of a vessel in laboratory conditions;
- optical fibre sensors, FBG type for point-wise, local strain measurement and monitoring during exploitation of a vessel.

The combined use of these methods should allow to benefit from the advantages of each of them, simultaneously discarding their particular limitations.

The application of DIC method, which is mainly a laboratory one, allows to indicate the most critical areas of a vessel, particularly important for its security and exploitation. At these identified locations the FBG sensors, used for "on-board" monitoring of a vessel, will be installed.

The paper is organized as follows: in Section 2 the fundamentals of both methods are described. Next (Section 3) the methodology of investigations performed by the combined methods is described. In Section 4 the results of experimental works together with their discussion are presented. Finally, the conclusions and further works are outlined.

2. Displacement and strain measurement in composite structure investigations

2.1. 3D digital image correlation method

Digital Image Correlation is the well-established method for displacements, strains and shape measurements [25]. 2D DIC (with one digital camera) and 3D DIC (with two digital cameras) variations of the method are widely used and accepted in the field of experimental mechanics [26,27]. The general operation diagram for 2D DIC and 3D DIC methods is shown in Fig. 1

The straightforward measurement procedure requires to acquire a set of images of an object under investigation which is subjected to any kind of load. One of the images is selected as a reference image (in most cases an image acquired before the load is applied) and the remaining images are subjected to the correlation analysis. The reference image is divided into small sub-images or subsets. The subsets are subsequently matched against similar subsets in images acquired in different load states. Repeating the procedure for all subsets from the reference image
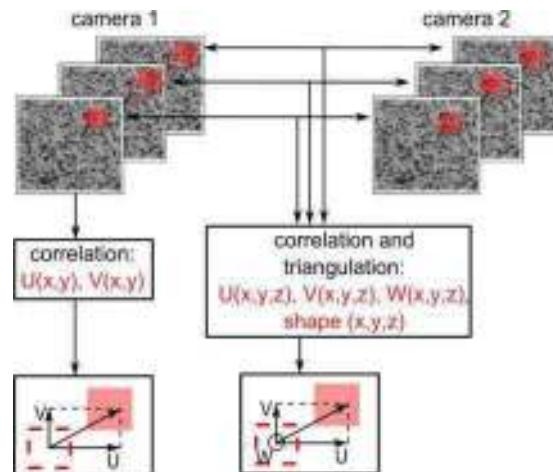

Fig. 1. General DIC method operation diagram: 2D DIC system uses one camera to determine in plane displacements U(x,y) and V(x,y), while 3D DIC system uses two cameras to determine in-plane U(x,y), V(x,y) and out-of-plane displacements W(x,y) and the shape (x,y,z) of a tested object.

yields displacements maps which in the next steps can be used for calculations of strains. In order to allow application of the DIC method, an object under investigation has to exhibit a random texture (speckle pattern) on its surface. The speckle pattern in most cases is introduced to an object surface by spraying paint. The important features of DIC are non-contact, full-field measurements, scalable dimensions of a field of view and accuracy (dependent on cameras resolution) and flexibility in data acquisition frequency (can be used for studies of static as well as dynamic events with the use of fast cameras).

Full-field measurements are especially required in the cases, when failure mechanisms or defects can occur in regions of an investigated objects which are difficult to be predicted before the measurement start. Access to full-field information can significantly increase the value of the data obtained from the measurements when compared to the standard point-wise techniques. Because of this, the DIC method is also often used in the experimental tests of composite structures [28,29,30] as well as in inspection of structures in industry [31].

2D DIC and 3D DIC are limited to measurements of displacements and strains that occur on a surface of objects under investigation. Digital Volume Correlation [32] is a rapidly growing modification of 2D DIC method which enables volumetric measurements of strains distributions by combination of the DIC and volumetric imaging methods such as X-Ray or tomography. DVC is also frequently used in measurements of composites [33], however, current applications are limited to small volumes and static loads.

2.2. FBG optical fibre sensors

The most common optical fibre sensor used to measure strains and temperature changes of construction and composite elements is the sensor based on Fibre Bragg Grating (FBG). Thanks to its small size, it is a typical point-wise transducer which can also be easily integrated with composite material (without any negative influence on a structure). The length of a single grating is in the range of 5–10 mm, and the external diameter is about 200–250 μm. Because of its perfect multiplexing capabilities, it is possible to combine many FBGs to form a network of sensors, the so called quasi-distributed systems, which is especially important in the case of complex SHM-type systems.

The Fibre Bragg Grating is a structure formed in the core of an optical fibre (Fig. 2), characterised by periodical changes of the refractive index value [34]. The measured value (deformation, temperature) is directly proportional to the displacement of the so called Bragg wave (λ_B) which depends on the change of the grating period (Λ), resulting from the changes in fibre size (compressing, stretching) and thermal effects (thermal expansion of the material and the thermo-optic effect for the refractive index) [35]. The principle of operation of FGB sensor is shown in Fig. 2.

Fibre Bragg Gratings can be used as equivalents of standard electrical strain gauges and temperature sensors (resistance tensometers, thermoelements). Apart from the advantages which are closely related to the general properties of optical fibre, it is important that the change
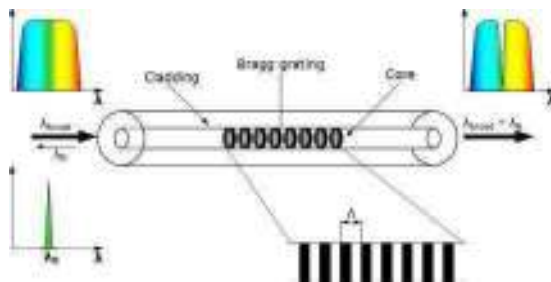

Fig. 3. The tested vessel CNG-4 type with marks indicating the localization of a flaw and the installed FBG sensor.

of the Bragg wavelength is a linear function of the measured value in a wide range.

3. Methodology of investigations

3.1. Composite vessels and pressure tests procedures

The objects of the research were commercial, composite, high-pressure vessels, type IV (polymer liner) used to store compressed hydrogen (CH2) and methane (CNG). Some of the vessels had programmed defects. For the purpose of DIC measurements, their surface was covered with a thin layer of primer and a reference layer in order to create a random texture. Next FBG deformation sensors were attached. During the tests the vessels were filled with water and quasi-statically loaded in the range of their Nominal Working Pressure (NWP).

The first series of tests was conducted on the CNG type IV vessel with programmed defects, NWP = 200 bar (Fig. 3). Two different composite structures were used in the vessel carrier layer: coal tar epoxy coating (CFRC) and glass epoxy resin coating (GFRC). This solution allowed to optimise the costs of vessel manufacturing and simultaneously maintain high security level during exploitation. The programmed defects in the form of notches and delamination were to simulate external flaws which could occur during vessel exploitation. These defects, often quite small, frequently make their detection impossible during the periodical, visual inspection of a vessel (it is also due to the location of the vessel in a vehicle, e.g. under a thermal casing). This is why it is essential to develop a measurement method/system which would allow to detect and localise them. A notch was made in the composite carrier layer of the vessel, it was parallel to the vessel main axis, notch dimensions: 200 mm long × 0.75 mm deep. It is standardising defect defined in the vessel specification for the "Composite flaw tolerance test" [4–6].

At the next stage of the research the tested vessel was a new, commercial type IV vessel designed to store hydrogen at 700 bar (Fig. 4). The carrier layer (strengthening) was made of coal tar epoxy coating composite (CFRC).

The vessels were loaded with internal pressure by an external hydraulic system. The quasi-static pressure test and step-by-step loading were conducted. The CNG vessel was loaded in the range of 0–100 bar, while CH2 – 0–600 bar. In both cases, for safety reasons (the tests were

Fig. 2. The principle of operation of the Fibre Bragg Grating [34].

Fig. 4. Type IV vessel for hydrogen storage with marked localization of the installed FBG sensors.

conducted outside a special chamber) a decision was made not to exceed the allowable working pressures. The change of deformation field (3D DIC method) and local deformation values (FBG) were simultaneously recorded during the tests.

3.2. Fiber Bragg grating based measurement system

FBG sensors, "bare fibre" type with Ormocer® coating were used in the research. They are characterised by a lack of an additional buffer coating, which improves the transfer of loadings between a monitored object and a transducer. The optical fibre sensors were integrated with the object using X60 glue which is a two component adhesive for strain gages. Before attaching the sensors, the surface was degreased and locally the paint coating enabling DIC measurements had been also removed. The sensors were attached pointwise at two ends of the Bragg grating. Thanks to this potential, local inhomogeneity of deformations along the sensor axis were isolated and the measured value of deformations is averaged in the segment between attachment points. The interrogator SI401, HBM, was used to record signals. It allows to take measurements at 1 Hz frequency and 1 pm accuracy (corresponding to $2\,\mu\varepsilon$ accuracy).

Four FBG sensors were used to assess the state of local deformations in the CNG vessel, they were installed in the circumferential direction near the programmed defect. Their distribution is presented in Fig. 3.

In the case of the hydrogen vessel, three FBG transducers were used: two in the circumferential direction (FBG1 and FBG2) and one in the longitudinal direction (FBG3), there were also additional temperature sensors. Their distribution is shown in Fig. 4.

3.3. 3D DIC measurement system

The cameras of the DIC measurement system were mounted on a tripod approximately 80 cm away from the vessel. The 3D CKO system was composed of two AVT Stingray 16Mpx cameras, equipped with a lens with a focal length of 50 mm. A typically obtained set of results from a single 3D DIC measurement is referenced to the Cartesian coordinate system and includes the shape in the form of a cloud of points (x,y,z), two components of in-plane displacements: U(x,y), V(x,y) and out-of-plane displacement map W(x,y). Strains can be calculated from displacement maps, as described in the following equations [25]:

$$\varepsilon_{xx} = \frac{\partial u}{\partial x} + \frac{1}{2}\left[\left(\frac{\partial u}{\partial x}\right)^2 + \left(\frac{\partial v}{\partial x}\right)^2\right]$$
$$\varepsilon_{yy} = \frac{\partial v}{\partial y} + \frac{1}{2}\left[\left(\frac{\partial u}{\partial y}\right)^2 + \left(\frac{\partial v}{\partial y}\right)^2\right]$$
$$\varepsilon_{xy} = \frac{1}{2}\left(\frac{\partial u}{\partial y} + \frac{\partial v}{\partial x}\right) + \frac{1}{2}\left(\frac{\partial u}{\partial x}\frac{\partial u}{\partial y} + \frac{\partial v}{\partial x}\frac{\partial v}{\partial y}\right) \quad (1)$$

The strain maps are calculated by differentiation of the displacement maps obtained in 'xy' plane. The cylindrical shape of the vessel surface in this case is not taken into account according to Eq. (1), what may be a source of a small measurement error. This error is neglected in further analysis as obtained maps represent well the behaviour of the vessel under pressure load and can be used for initial identification of highly stressed regions.

To facilitate interpretation of the results, the displacements were transformed into a cylindrical coordinate system connected with the axis of each of the tested vessels [36]. In the new coordinate system the dR (radial displacement), dZ (displacement along Z axis) and dq (angular displacement) displacements were defined. The photo of test stand and the orientation of the cylindrical coordinate system are presented in Fig. 5a and b respectively.

For the purpose of comparing the results of 3D DIC measurements and the FBG measurements, the virtual extensometers were used. The virtual extensometers are used to calculate strains between two points defined on the obtained data (e.g. one of the displacements maps). The field nature of the results obtained with the DIC method allows any

localization of the so called virtual extensometers on the recorded displacement maps. 3D positions (x, y, z) of selected points are known from DIC analysis. The virtual extensometer tool calculates the reference distance L between points in reference data set (calculated from first pair of images) and change of this distance ΔL in remaining data sets. The engineering strains are obtained as ΔL divided by the reference distance L. The virtual extensometers are placed as close to the FBG sensors as possible, so that the results of both measurements should be comparable. However, the strain measurements with the virtual extensometers is encumbered with a systematic error related to the local shape of the tested object. The source of this error is indicated in Fig. 5b, where measurements points P1 and P2 are marked. According to the used calculation procedure, the basis of the virtual extensometer is a straight section between points P1 and P2 (dP1P2 interval), while the basis for the corresponding FBG sensor is an arc section (LP1P2 interval). It was assumed that differences in the length of virtual extensometers and FBG transducers are so small that the error can be disregarded.

Summarizing, the data obtained in Cartesian coordinate system can be used for qualitative analysis of the vessel's behaviour (e.g. localization of stress concentration), while data transformed to the cylindrical coordinate system and data from the virtual extensometers can be used for quantitative analysis.

4. Experimental results of pressure tests

4.1. CNG vessel with programmed defects

The CNG vessel was loaded by increasing the pressure in the range from 0 to 100 bar. The example set of the measured displacements U, V, W and strain maps ε_{xx}, ε_{yy}, ε_{xy} are shown in Fig. 6 and Fig. 7. Example displacement maps 'dz', 'dq' and 'dR' (in the cylindrical system) recorded for the maximum pressure (100 bar) during the quasi-static test, are shown in Fig. 8.

However in order to perform quantitative comparison of strain values provided by DIC and FBG sensors the analysis had been conducted on the basis of virtual extensometers (DIC E1 and DIC E2) located as close as possible to physical optical fibre sensors (Fig. 9). The results of the strain measurements performed by the virtual extensometers E1 and E2 and the direct measurements of circumferential deformations with optical fibre sensors (FBG1-FBG4) are presented in Fig. 9a. Good compatibility of the results obtained by both methods had been obtained.

The differences between the strain measured with FBG3 and E2 (approx. 750 µε), located closest to the defect, and the results of the other sensors (FBG2 and E1), whose results are in the range of 3100–3250 µε, are clearly visible. This results from the direction of the strengthening fibre in the last (notched) layer of the tested vessel on which the measurements were made. The fibres are nearly at an angle of 90° angle to the main axis (circumferential direction). As a consequence, when it is cut off, the ovalization of the vessel takes place and, as a result, the coefficient of straight line inclination ε = f(P) is changed for each sensor, i.e. the "susceptibility' of the vessel to strain under the influence of internal pressure changes [37].

4.2. Hydrogen vessel (CH2)

The hydrogen vessel was loaded by "step-by-step" loading in the range from 0 to 600 bar. Again the analysis of 3D DIC encompassed the determination of strains at the same areas and on the same basis as the optical fibre sensors. The optical fibre sensors and their locations (transducer end points) were visible in the recorded images. The distribution of virtual extensometers applied for 3D DIC data is presented in Fig. 10 against the background of the map of coordinate R (i.e. vessel radius after transformation to the cylindrical coordinate system). For the purpose of comparing the results obtained with both methods, the
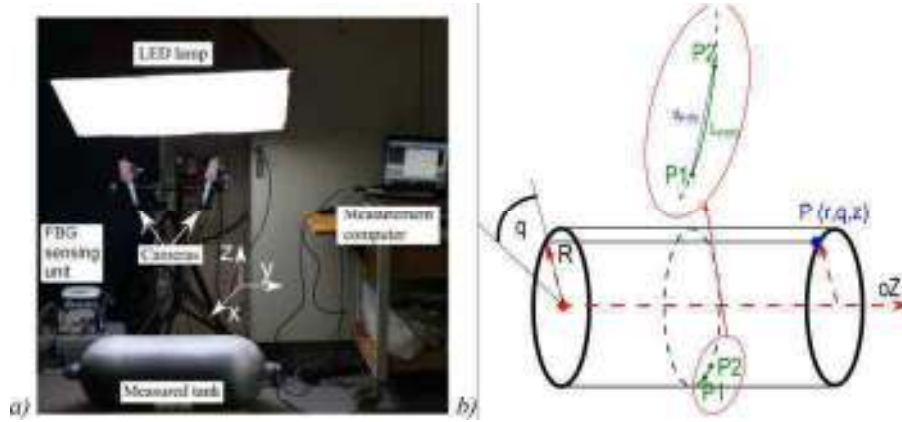
Fig. 5. The photo of test stand for composite vessels (a) and the orientation of the cylindrical coordinate system (b).
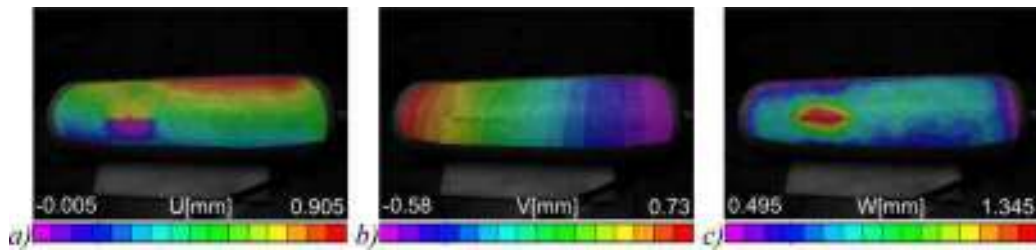

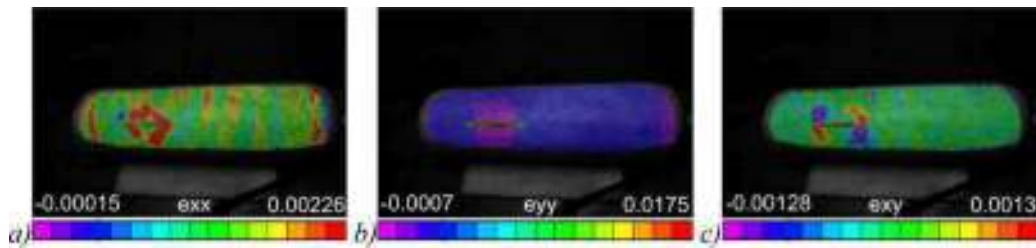**Fig. 6.** The example displacement a) u, b) v, c) w maps obtained for the CNG vessel at 100 bars.

Fig. 7. The example calculated strain maps a) ε_{xx}, b) ε_{yy} and c) ε_{xy} obtained for the CNG vessel at 100 bars.
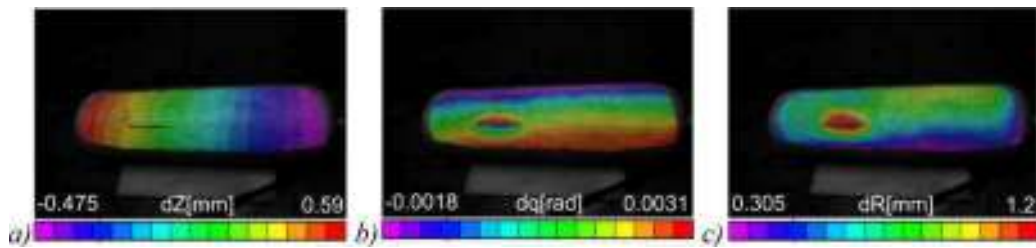
Fig. 8. The example displacement maps a) dz, b) dq and c) dR obtained for the CNG vessel at 100 bars.

following notation for virtual extensometers was taken: DIC E1, DIC E2 and DIC E3. Their location corresponds with the physical location of optical fibre sensors on the vessel (FBG1, FBG2 and FBG3 respectively).

The shape of the vessel reported as the map of the coordinate R of the vessel (Fig. 10) allows to analyse the real shape of the object after the manufacturing process. This makes it possible to conduct a preliminary quality assessment on the basis of a comparison between the model and the real object. Due to the specificity of the manufacturing process of composite vessels (wrapping carbon fibre on a polymer liner at various angles as well as gelation and resin hardening), the final shape can slightly deviate from the intended one, which can be seen in Fig. 10.
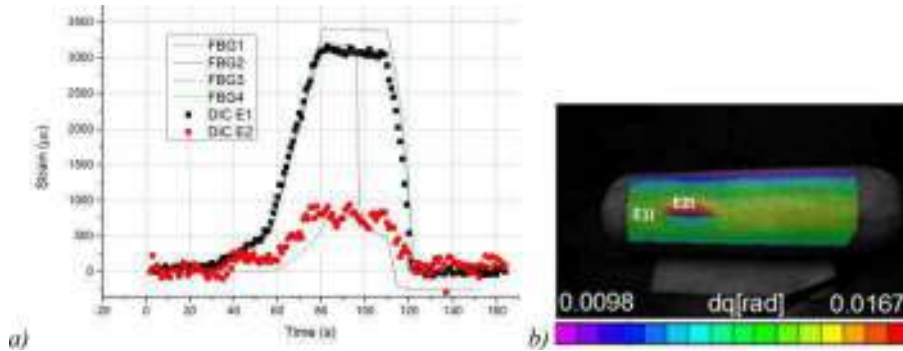
Fig. 9. CNG vessel investigations: a) the strain changes in the function of time (load) measurement for the vessel with virtual extensometers E1 and E2 and optical fibre sensors (FBG) in the pressure range of 0–100 bar and localization of E1 and E2 virtual extensometers.
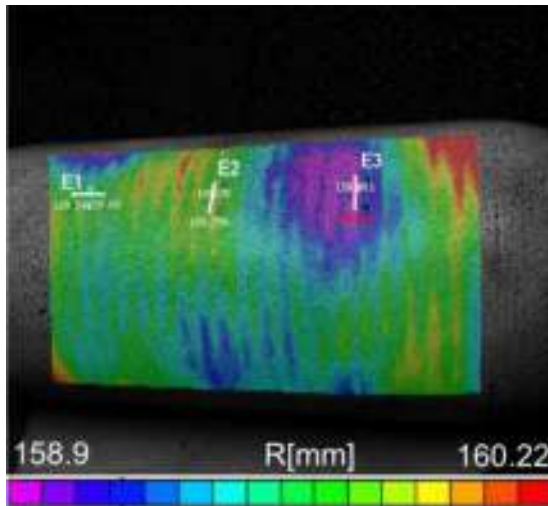

Fig. 10. The shape of the hydrogen vessel given as the map of its radius R (after transformation to the shape in Cartesian coordinates into cylindrical coordinate system) and the location of virtual extensometers.

During the "step-by-step" test the vessel was loaded every 50 bars, until the pressure of 350 bar was obtained (Fig. 11). Maximum values of circumferential strains were 2303 µε (FBG2) and 2174 µε (FBG3) and in the longitudinal direction 1495 µε (FBG4). The corresponding deformation values, estimated on the basis of DIC (virtual extensometers), were: 2041–2310 µε (DIC E3), 2234–2031 µε (DIC E2) and
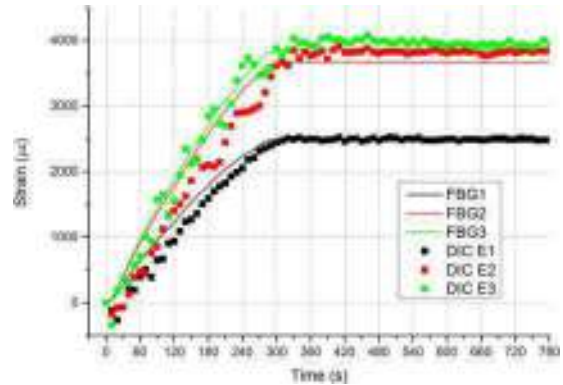

Fig. 12. Quasi-static tests of the hydrogen vessel in the pressure range from 0 to 600 bars: changes of local deformations recorded by FBG sensors and determined with the DIC method by means of virtual extensometers located as shown in Fig. 10.

1551–1668 µε (DIC E1), respectively. The results of DIC follow well the FBG results. The dispersion of results occurring in the DIC measurements result from noise in the measurement images of the speckle nature, the size of the subsets and the interpolation procedures.

During the subsequent test, a quasi-static test for the pressure range from 0 to 600 bars was performed on the same vessel. The maximum pressure was maintained for ~10 min. During this time, similarly to the earlier research, local strains were registered using FBG sensors (Fig. 12) and the measurements of strain maps were performed using virtual extensometers tool. The values of local strains at the points
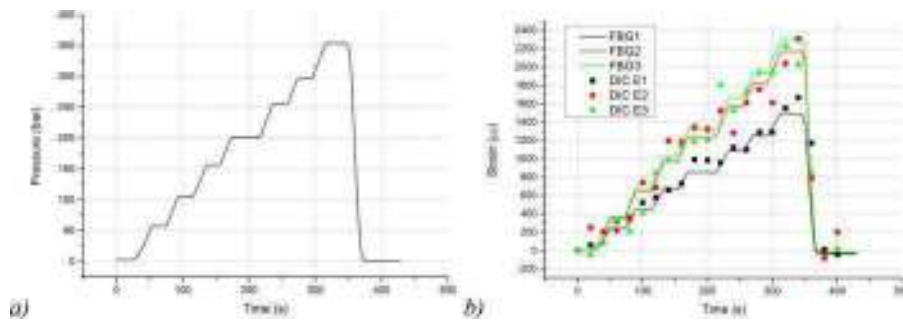

Fig. 11. "Step-by-step" type test: change of internal pressure (a) and strains (b).

180

where the FBG transducers were installed were established on this basis.

It is worth mentioning that the indications of both measurement methods are correlated with each other and differences occurring during the increase of pressure are not big (Fig. 12). The values of circumferential deformations recorded at various points are similar.

5. Conclusions and future works

The subject of this work was the analysis of strain distribution in composite high-pressure vessels designed for gas fuel storage in automotive applications for the purpose of assessment of their exploitation safety. The pressure tests were conducted on commercial objects (composite pressure vessels, COPV) used to store hydrogen (700 bar) and methane (200 bar) in cars. Two complementary NDE methods were used to assess strain fields in laboratory conditions: optical fibre (FBG) based sensors and 3D digital image correlation method. The combined application of both methods allowed to benefit from the advantages of each of them and simultaneously eradicate limitations/flaws particular to each of them.

The DIC method allowed to perform full-field measurements and quantitative monitoring of displacements and strains, hence offering a possibility to assess the operation of the whole vessel under the influence of internal pressure. Thanks to this it was possible to register defects, which could develop during vessel exploitation, at an early stage and it was also possible to validate the numerical models for this kind of objects. The use of the DIC field method allowed also the experimental location of critical areas of the vessel, thus it was possible to optimise the localization of FBG sensors on the vessel. However, this method cannot be used in continuous monitoring of vessels installed in a car.

Pointwise optical fibre sensors of FBG type allowed to develop a multi-point measurement system which can continuously monitor the technical condition of a vessel during normal exploitation (refuelling, using up the fuel, checks) and even during manufacturing. First of all, thanks to this it is possible to assess the degradation of composite material making the so called carrier layer of a vessel. A comparative analysis of measurement signals registered at may points of the vessel allows to detect and localise defects on a macro scale (e.g. programmed defects). On the other hand the use of FBG sensors for measurements during the manufacturing process allows to control this process (e.g. through preliminary pull-out of the fibre, internal pressure regulation, resin hardening temperature) and also to assess the "quality" of the end product (registration of residual strain).

It was shown that the proposed measurement methods can be complementarily used to assess the technical condition of high-stressed composite structures, including localisation of defects at the design and use stage of high-pressure vessels. Ultimately it is possible to use them as the basis to develop a dedicated, integrated SHM system for continuous safety assessment of composite high-pressure vessels exploitation based on FBG sensors.

Acknowledgments

References

[1] Błażejewski W, Gąsior P, Kaleta J. Application of optical fibre sensors to measuring the mechanical properties of composite materials and structures. In: Attaf B, editor. Advances in Composite Materials – Ecodesign and Analysis. InTech; 2011.

[2] Züttel A. Materials for hydrogen storage. Mater. Today 2008;6(9):24–33.

[3] Takeichi N, et al. Hybrid hydrogen storage vessel", a novel high-pressure hydrogen storage vessel combined with hydrogen storage material. Int J Hydrogen Energy 2003;28(10):1121–9.

[4] Commision Regulation (EU) No 406/2010; April 2010.

[5] ISO/DIS15869.3. Gaseous hydrogen and hydrogen blends — Land vehicle fuel tanks; 2008.

[6] Regulation No. 110, Rev.2/Add.109/Rev.1.

[7] Sulatisky M, Hay B, Mourre D. Damage detection in high-pressure cylinders. In: 18th World Hydrogen Energy Conference (WHEC 2010), Essen; 2010.

[8] Foedinger RC, et al. Embedded fiber optic sensor arrays for structural health monitoring of filament wound composite pressure vessels. In: Smart Structures and Materials 1999: Sensory Phenomena and Measurement Instrumentation for Smart Structures and Materials, Proc.of SPIE, vol. 3670, Newport Beach; 1999. p. 289–301.

[9] http://www.hycomp.eu/.

[10] http://www.project-copernic.com/.

[11] Degrieck J, De Waele W, Verleysen P. Monitoring of fibre reinforced composites with embedded optical fibre Bragg sensors, with application to filament wound pressure vessels. NDT&E Int 2001;34:289–96.

[12] Kang DH, Kim CU, Kim CG. The embedment of fiber Bragg grating sensors into filament wound pressure tanks considering multiplexing. NDT&E Int 2006;39:109–16.

[13] Hernández-Moreno H, Collombet F, Douchin B, Choqueuse D, Davies P. Entire life time monitoring of filament wound composite cylinders using Bragg grating sensors III in-service external pressure loading. Appl Compos Mater 2009;16:135–47.

[14] Błażejewski W, Czulak A, Gasior P, Kaleta J, Mech R. SMART composite high pressure vessels with integrated optical fiber sensors. In: Sensors and Smart Structures Technologies for Civil, Mechanical, and Aerospace Systems 2010, Proc. of SPIE Vol. 7647 764712-1, San Diego; 2010.

[15] Glisic B, Inaudi D. Health monitoring of a full composite CNG tanks using long-gage fiber optic sensors. In: 11th SPIE's Annual International Symposium on Smart Structures and Materials, Proc. of SPIE, vol. 5384-7, San Diego; 2004.

[16] Frias C, Faria H, Frazão O, Vieira P, Marques AT. Manufacturing and testing composite overwrapped pressure vessels with embedded sensors. Mater Des 2010;31:4016–22.

[17] Hao JC, Leng JS, Wei Z. Non-destructive evaluation of composite pressure vessel by using FBG sensors. Chin J Aeronaut 2007;20(2):120–3.

[18] Kinet D, et al. Fiber Bragg grating sensors toward structural health monitoring in composite materials: challenges and solutions. Sensors 2014;14:7394–419.

[19] Starbuck JM, Beshears DL. Smart onboard inspection of high pressure gas fuel cylinders. [Online]. http://web.ornl.gov/~webworks/cpr/pres/104041.pdf.

[20] Leng J, Asundi A. Structural health monitoring of smart composite materials by using EFPI and FBG sensors. Sens Actuat 2003;A(103):330–40.

[21] Gifford DK, Metry DR, Froggatt ME, Rogers ME, Sang AK. Monitoring strain during composite manufacturing using embedded distributed optical fiber sensing. In: SAMPE Technical Conference Proceedings, Long Beach, CA; 2011.

[22] Grediac M. The use of full-field measurement methods in composite material characterization: interest and limitations. Compos Part A: Appl Sci Manuf 2004;35:751–61.

[23] Kobayashi A. Handbook on experimental mechanics. Weinheim: Society for Experimental Mechanics, VCH publishers Inc; 1999.

[24] Post D. High sensitivity moiré: experimental analysis for mechanics and materials. Berlin: Springer; 1994.

[25] Sutton M, Orteu JJ, Schreier H. Image Correlation for shape, motion and deformation measurements. Springer; 2009.

[26] Pan B. Recent progress in digital image correlation. Exp Mech 2011;51(7):1223–35.

[27] Orteu JJ. 3-D computer vision in experimental mechanics. Opt Lasers Eng 2009;47:282–91.

[28] Brynk T, Molak RM, Janiszewska M, Pakiela Z. Digital image correlation measurements as a tool of composites deformation description. Comput Mater Sci 2012;64:157–61.

[29] Koohbor B, Mallon S, Kidane A, Sutton MA. A dic-based study of in-plane mechanical response and fracture of orthotropic carbon fiber reinforced composite. Compos B Eng 2014;66:388–99.

[30] Pollock P, et al. Full-field measurements for determining orthotropic elastic parameters of woven glass-epoxy composites using off-axis tensile specimens. Exp Tech 2012;38:61–71.

[31] Malesa M, et al. Application of 3d digital image correlation in maintenance and process control in industry. Comput Ind 2013;64(9):1301–15.

[32] Bay B, Smith T, Fyhrie D, Saad M. Digital volume correlation: three-dimensional strain mapping using X-ray tomography. Exp Mech 1999;39(3):217–26.

[33] Brault R, et al. In-situ analysis of laminated composite materials by X-ray microcomputed tomography and digital volume correlation. Exp Mech 2013;53(7):1143–51.

[34] Yu F, Yin S. Fiber optic sensors. New York: Marcel Dekker Inc.; 2002.

[35] Xu MG, Archambault JL, Reekie L, Dakin P. Discrimination between strain and temperature effects using dual-wavelength fibre grating sensor. Electron Lett 1994;30(13):1085–7.

[36] Malowany K, et al. Measurements of geometry of a boiler drum by Time-of-Flight laser scanning. Measurements 2015;72(1):88–95.

[37] Gąsior P, Kaleta J, Sankowska A. Optical fiber sensors in health monitoring of composite high pressure vessels for hydrogen. In: Optical Measurement Systems for Industrial Inspection V, Proc. of SPIE 66163G-1-66163G-10, vol. 6616, Munich; 2007.

Article

Application of 3D Digital Image Correlation for Development and Validation of FEM Model of Self-Supporting Arch Structures

Krzysztof Malowany [1],*, Artur Piekarczuk [2], Marcin Malesa [1], Małgorzata Kujawińska [1] and Przemysław Więch [2]

[1] Warsaw University of Technology, Institute of Micromechanics and Photonics, 8 Św. A. Boboli St., 02-525 Warsaw, Poland; m.malesa@mchtr.pw.edu.pl (M.M.); m.kujawinska@mchtr.pw.edu.pl (M.K.)
[2] Instytut Techniki Budowlanej, 1 Filtrowa St., 00-611 Warsaw, Poland; a.piekarczuk@itb.pl (A.P.); p.wiech@itb.pl (P.W.)
* Correspondence: k.malowany@mchtr.pw.edu.pl

Abstract: Many building structures, due to a complex geometry and non-linear material properties, are cumbersome to analyze with finite element method (FEM). A good example is a self-supporting arch-shaped steel sheets. Considering the uncommon geometry and material profile of an arch (due to plastic deformations, cross section of a trough, a goffer pattern), the local loss of stability can occur in unexpected regions. Therefore, the hybrid experimental-numerical methodology of analysis and optimization of arch structures have been proposed. The methodology is based on three steps of development and validation of a FEM with utilization of a digital image correlation (DIC) method. The experiments are performed by means of 3D DIC systems adopted sequentially for each measurement step conditions from small size sections, through few segment constructions up to full scale in situ objects.

1. Introduction

The development of large-scale and complex engineering structures creates new challenges for designers and constructors, who need to meet the demands of increasing safety, extended component lifetime and simultaneously reduced investment and operation costs. To fulfill these requirements new materials (e.g., composites) and assembly technologies are being developed. An example of this type of construction is a self-supporting arch structure. Such structures had been initially built as temporary buildings used for military purposes. Adaptations of this technology for civil purposes, required extension of the designed lifetime and consideration of different environmental conditions, and therefore design problems, especially in terms of stability and load transfers occurred [1–5]. In order to ensure safety and proper operational parameters during their lifetime, hybrid experimental-numerical methods are being used during design and exploitation stages [6]. The common practice in experimental mechanics is to validate the numerical model using point wise sensors (e.g., strain gauges). They are attached to a tested structure in places in which the highest stress concentrations are expected (based on the analysis of a numerical model). This is a simple and low-cost approach, but a problem can occur if an inaccurate numerical model does not indicate all the places in which stress concentrations occur. This, in turn, may cause errors in the process of validation of the numerical model. Therefore, an advanced evaluation of numerical model is more often supported with the data obtained by means of full-field optical measurement methods, which determine

displacements and deformations in critical areas of the objects [7,8]. In the case of investigations of large engineering structures, the most commonly used techniques are terrestrial laser scanning [9–11] and the 3D digital image correlation (3D DIC) method [1,12–17]. Terrestrial laser scanning systems enable 3D measurements of shape of object. By comparison of the acquired shapes in different load conditions, deformation of an object under the load can be calculated [10,11]. The method is simple to use, however, due to time required for measurement (from few second up to few minutes), its utilization is limited to static measurements. 3D DIC measurement systems combine digital image correlation and triangulation methods. 3D DIC provides directly 3D displacement vector **d** distribution (displacement maps (u,v,w) in x, y and z directions respectively) in a measured field of view [18]. Utilization of the 3D DIC method requires modification of a measured surface (applying a paint coat that provides a random texture) therefore it is more difficult to use compared to terrestrial laser scanning systems. Nonetheless the 3D DIC system enables measurements of an investigated object under varying in time conditions, and therefore this method have been used in the presented application. Numerical modeling of a self-supporting arch structure is cumbersome, considering the uncommon geometry and material characteristics (due to plastic deformations, the cross section of a trough, goffer pattern). Thus, the development and validation of a FEM model of a full-sized construction made of self-supporting arch sheets described in Section 2, was divided into three steps starting from small sized sections (Section 4), through few segment constructions (Section 5), to full scale in situ objects (Section 6). Each step required a tailored approach to the measurements with 3D DIC due to different: accuracies, sizes of fields of view, forms of outcome data, environmental conditions. Some aspects of this work had been presented in our previous papers. In papers [2,3] the investigation of 1 m long section of arch-shaped steel sheets was presented, the goals of this work was to simulate local loss of stability and to determine a geometric model of the surface shape for FEM analysis. In papers [1,13] the investigation of segments of arch-shaped steel sheets in laboratory conditions were presented; the goals of this work were to investigate the global stability and to determine the mechanical behavior of supports. The measurements presented in paper [13] were performed with utilization of multi-camera DIC system with overlapping areas of fields of view of cameras. In paper [16] the performed measurements of the full-scale construction made of arch-shaped self-supporting metal plates was presented, and in order to enable these measurements the multi-camera DIC system with distributed field of view (FOV) was developed. In this paper we summarize the development of 3D DIC systems and present the combined three-steps hybrid experimental-numerical methodology of analysis and optimization of arch structures.

2. Characteristic of the Investigated Object and General Procedure Supporting Development and Validation of a Finite Element Model

2.1. Specification of Arch-Shaped Steel Sheets Used as a Self-Supporting Arch Structures

A self-supporting arch-shaped covering of steel sheet sections is used in civil engineering [19]. Typical radii of the assembled arch coverings varies in the range of 6 m to 30 m (Figure 1a). Due to the simple design, quick installation and relatively low implementation costs, this type of covering gained significant popularity. Arch-shaped steel sheets are cold formed in two stages. At first, the flat metal plates (stored in a roller) are bended in order to receive plates with trapezoidal cross section, then the plates are goffered (local plastic deformation) in order to receive arches (Figure 1b). A full scale object is obtained from a number of single arches connected to each other with double lock standing seams. Considering the trapezoidal cross section, the differences in radius of the arch cause waiving in the surface between shelves.

Figure 1. (**a**) Outside image of the measured hall as an example of typical self-supporting arch-shaped covering, (**b**) section surfaces.

2.2. Three-Step Development and Validation of a Numerical Model

Considering the uncommon geometry and material characteristic of an arch, development of a FEM model of such a structure required a specific approach and its validation at different stages of advancement. The development of a FEM model of the full-sized construction made of the self-supporting arch has been heavily supported by the experiments performed by means of 3D DIC within three steps. At first, the tests have been carried out on single sections of the arch in order to determine which geometric model of the surface shape (planar, corrugation or corrugation and wavy model) should be applied in the further steps for FEM analysis. The considered sections were 1 m long and 0.7 m wide. In the next step, a structure composed of four individual segments with the geometry selected at step 1 has been used in laboratory tests with controlled loading conditions in order to investigate the global stability and to determine the mechanical behavior of supports, in particular to define the rotational stiffness of supports used in a FEM model of arches. The measured object was of 12 m span and 2.8 m wide. The final step was based on the tests of a full-scale object: 8 m high covering the area of 18 × 18 m. The outcomes of this test is the validation of a complete FEM model in which the knowledge gained in steps 1 and 2 had been implemented. It has been proven that the model accurately simulates construction deformations under the environmental loads. The model can be scaled to larger constructions. The general procedure supporting the development and validation of a FEM model has been summarized and presented in Figure 2. This procedure is described in detail in Sections 5 and 6.
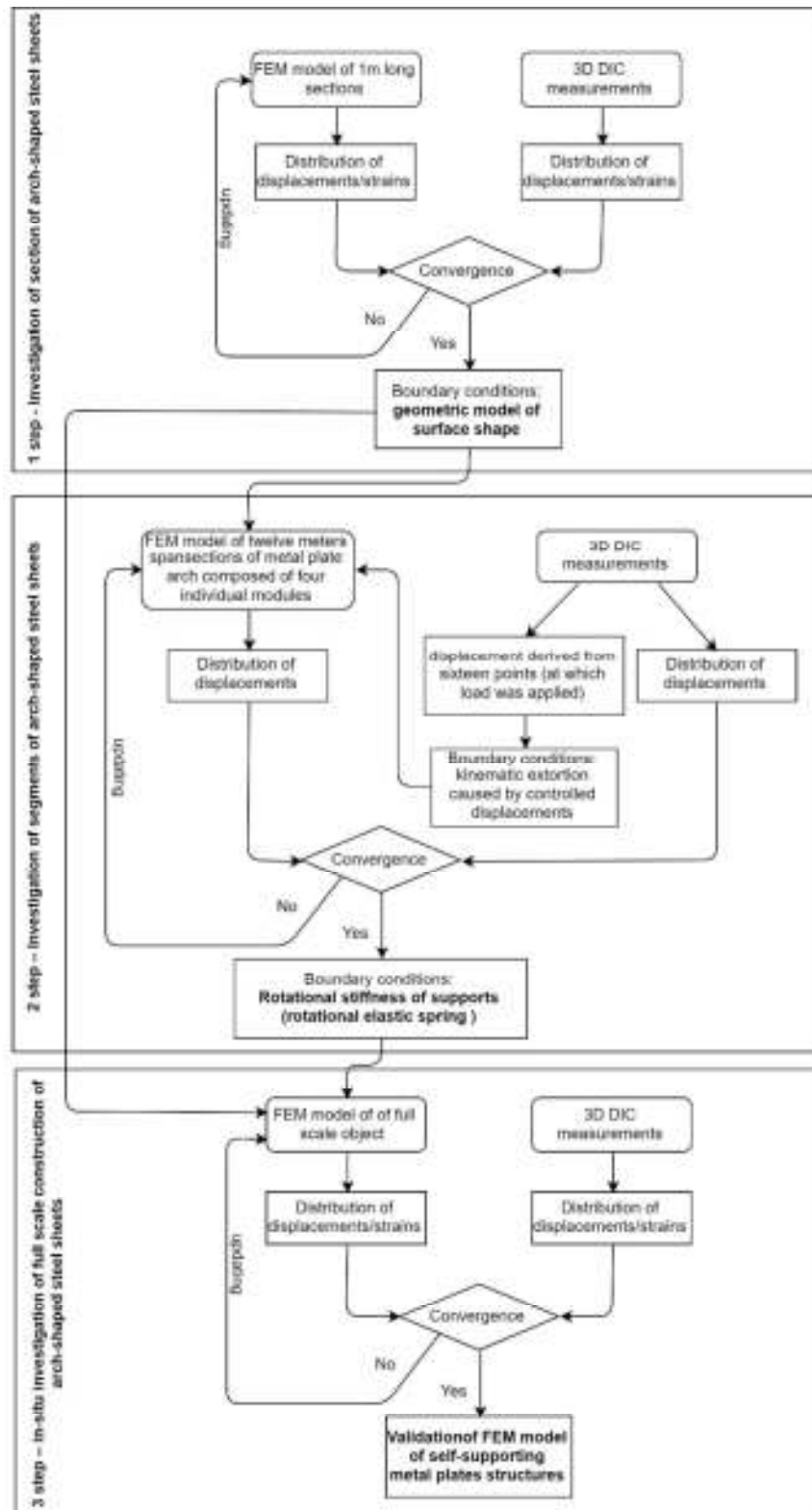
Figure 2. Flowchart of the 3-steps updating and validation of numerical model of self-supporting arch structures with utilization of 3D digital image correlation method.

3. Digital Image Correlation Method

At each stage of the procedure described in Section 2 full-field measurements of displacement vector **d** (u,v,w) of the investigated structures are required. The method which is best fitted to the measurement requirements is digital image correlation [18]. DIC is based on acquisition of a set of images of a tested object which is subjected to load. The surface of an object under investigation has to be covered with a random texture. The 2D DIC version uses a single camera. One of the acquired images is selected as a reference for the others. The reference image is divided into small regions (or subsets), a position of each subset is tracked in the remaining images, using the maximum zero-mean normalized sum of squared difference function as the criterion (or any other correlation metric). The image can be divided into hundreds or thousands of subsets, thus 2D DIC provides in-plane displacement maps over the selected area of interest (AOI). The 3D DIC is a technique that combines the 2D DIC with stereovision by using two cameras for observation of the same AOI. 3D DIC provides: the 3D shape of a surface, in-plane and out-of-plane displacement maps. The in-plane strain maps are calculated by differentiation of the in-plane displacement maps. According to [20], the minimum displacement measurement error can be less than 0.001 pixels, however, it must be noted that in real applications the accuracy of measurements strongly depends on factors such as image noise and stability of experimental conditions. Moreover, the out-of-plane measurement error is larger than the in-plane one, and strongly depends on a stereo angle between the cameras as set [20,21]. The accuracy of displacement measurements is scalable with the resolution of the cameras (larger camera's resolution and smaller FOV indicate higher displacement measurement accuracy). The displacements in the "x" direction are given as "u" in [pixels] and after scaling are expressed as "U" in [mm]; similarly, displacements in the "y" and "z" direction are given as "v [pixels] ", "V[mm] ", and "w[pixels] ", "W[mm] ", respectively.

4. Investigation of Section of Arch-Shaped Steel Sheets

At this stage, the test bench was designed in order to simulate local loss of stability in 1 m long sections [2,3]. The examined sample was fastened between two horizontal rigid plates, with defined degrees of freedom. The force was eccentrically applied in the direction of the axis that passes through the center of gravity of the cross sections. With this arrangement, the compression force on 1 m long interval of the arch (having a radius of 18 m) was mapped.

4.1. 3D Digital Image Correlation Setup

The 3D DIC system used in this measurements comprises two AVT Pike F-1600 (4872 × 3248 pixels) monochromatic cameras equipped with 28 mm lenses, set on an angle of 30°. The setup was mounted on an aluminum frame to enable easy geometric modifications. The surface of the examined specimen was illuminated with two 200 W light-emitting diode (LED) lamps (13,000 lumen) equipped with a light diffuser ("soft box"), in order to eliminate shadows on the surface. The FOV of the system was 1.5 m × 1 m, covering the entire area of the sample (Figure 3).
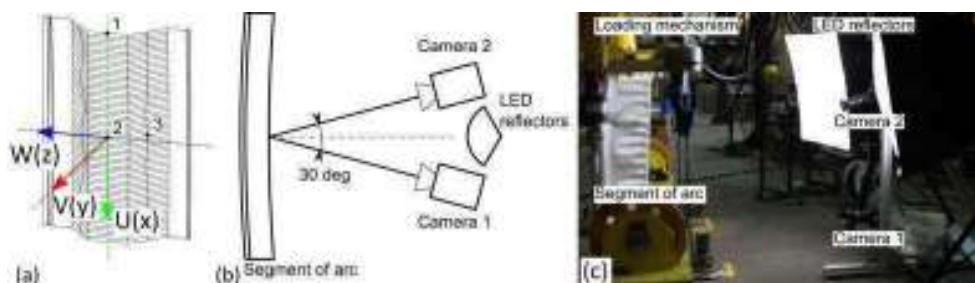

Figure 3. The experimental setup: (**a**) orientation of coordinate system and location of three points adopted for further analysis; (**b**) scheme and (**c**) photo of the measurement system based on 3D DIC [2].

4.2. FEM Model of the Section of Arch-Shaped Steel Sheets

Calculations covered 3 numerical models with different specificity of geometry mapping. The first model (A) (Figure 4a) was devoid of characteristic web corrugations and waviness, the second model (B) (Figure 4b) had corrugated surfaces mapped but with no waves, and the third one (C) (Figure 4c) had all the web corrugations and waves characteristic of such a profile. The models (Figure 4a–c) were developed in the ANSYS graphic module making use of the data from real element measurements. Furthermore, when describing the behaviour of the particular models, the aforementioned A, B and C signs will be used. The elastic-plastic steel model was used for the calculations, developed on the basis of the tests of steel samples [3]. The support and load conditions were accepted according to the assumptions included in the article [3]. Calculations and tests were performed in the form of axial compression of the sample.
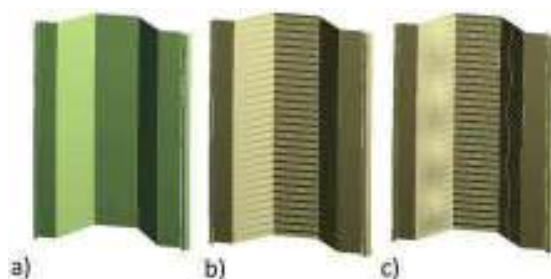

Figure 4. The geometry of numerical models: (**a**) planar model (A), (**b**) corrugation model (B) and (**c**) corrugation and wavy model (C).

4.3. Utilization of 3D DIC Measurements in the Process of Validation of FEM Model of the Section

The results of 3D DIC measurement were utilized in order to determine whether the simplification of the geometry of the model is allowed. At first, in order to perform quantitative analysis, the comparison between the displacements extracted from selected points of the structure from three models and experimental data has been performed. Points are distributed over the entire surface of the sample, in places corresponding to maximum displacements, according to FEM models. Locations of the points allowed for the assessment of representative movements for the entire sample. Exemplary data are presented in Figure 5, point 2 concerns the maximum V displacements of the sample. The best correlation between experimental and numerical results have been obtained with the FEM model comprising the most detailed geometry (C model). The results obtained from the two remaining models (of simplified geometry) differ significantly from the experimental results. Therefore, the simplifications of a FEM model have not been allowed in further analysis. Subsequently, the full-field qualitative comparison of the failure mode maps between DIC and numerical (C model) displacement maps has been carried out. Exemplary maps are presented in Figure 6. The displacement maps obtained with the numerical analysis show good agreement with the experimental data, considering its character and values. Some discrepancies that can be observed could be caused by unavoidable deviation of geometry of the sample and support conditions (e.g., inaccuracy in direction of applied force). The presented analysis validated the assumptions made in the C model, and has proven them to be useful in the analysis below.
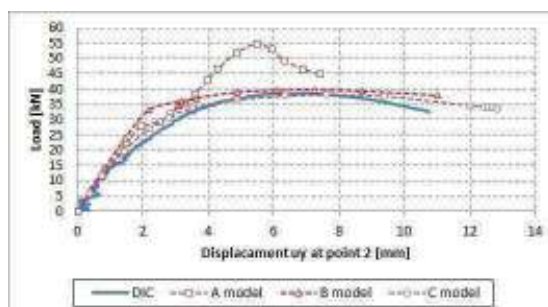
Figure 5. The comparison of V displacement functions obtained for three numerical models and experimental data (results for point 2) [2].
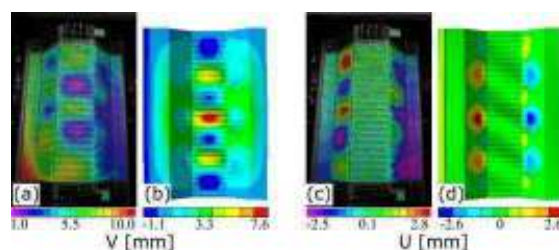

Figure 6. V displacement maps derived from (**a**) experiment and (**b**) the C model, and U displacement maps derived from (**c**) experiment and (**d**) the C model [2].

5. Investigation of Segments of Arch-Shaped Steel Sheets

The 12 m span sections of metal plate arch composed of four individual modules have been examined with the use of custom-made laboratory stands, which made it possible to apply force equivalent to a natural load caused by snow and wind [22,23]. The loading mechanism consisted of pulleys and beams which transferred point load (applied with hydraulic actuator) into 16 points (4 points for each module). The load was recorded by the actuator mounted onto the main beam, which reduced the force loss of the pulleys.

5.1. Multi-Camera DIC System with Overlapping Field of View

Considering the length of 12 m of arch segments, the measurements have been carried out with the use of multi-camera DIC system in which the field of view of neighboring 3D setups overlapped each other. As a result, the obtained, stitched FOV was 7 × 4 m (Figure 7a). For stitching we used the method described in the papers [13,24,25], while the general measurement procedure of the segments of arch-shaped steel sheets are presented in [13]. The multi-camera DIC system used in this measurements comprised eight 5 MPx (2448 × 2048) Pointgrey cameras equipped with 8mm focal length lenses. The cameras were connected to the control computer in order to synchronize the data acquisition procedure. The calibration procedure comprised two steps. In the first stage, 3D DIC setups have been calibrated separately with the checkerboard before the measurements. The quality of calibrations has been expressed as a reprojection error, which was smaller than 0.05 px for all 3D DIC setups. After the scaling (from pixels to mm), the accuracy of displacement measurements of each 3D DIC setup can be estimated at 0.05 mm. In the second stage, the transformation of individual coordinate systems of separate 3D DIC systems into a common coordinate system has been determined. The fields of view of neighboring 3D DIC setups overlapped each other (Figure 7) in order to make it possible to capture the images of the same calibration target (checkerboard in this case) with two systems simultaneously. Checkerboard corners (markers) viewed by each camera have been detected and their positions in two 3D DIC coordination systems were obtained. The knowledge of position of markers in two separate coordination systems was used to obtain geometrical transformation between these two systems. The common coordination system (CS) is associated with one of the two systems. Here the coordination system of DIC setup 2 has been selected as the global CS. The transformation between CSs of setup no. 1 and 3 into CS of setup no. 2 has been determined directly. The transformation of CS of setup no. 4 was obtained indirectly—at the beginning, the transformation into CS of setup no. 3 was obtained, and then transformation from CS of setup no. 3 into CS of setup no. 2 was performed. The transformation errors obtained were below 0.5 mm. In order to correlate CSs of the measurements with numerical simulations, the data from the global coordination system (associated with setup no. 2) was transferred to the coordinate system, in which the xy plane was parallel to the ground and z axis was perpendicular to the ground (Figure 7b). AOI covers the area of corrugated web surface of two middle arches and additionally eight points

on two external arches, corresponding to the locations of force extortion. Data obtained from upper (flat lip according to Figure 1) and middle (corrugated flange according to Figure 1) surfaces of the middle arches have been thresholded due to a higher correlation error (because of the loss of depth of focus).
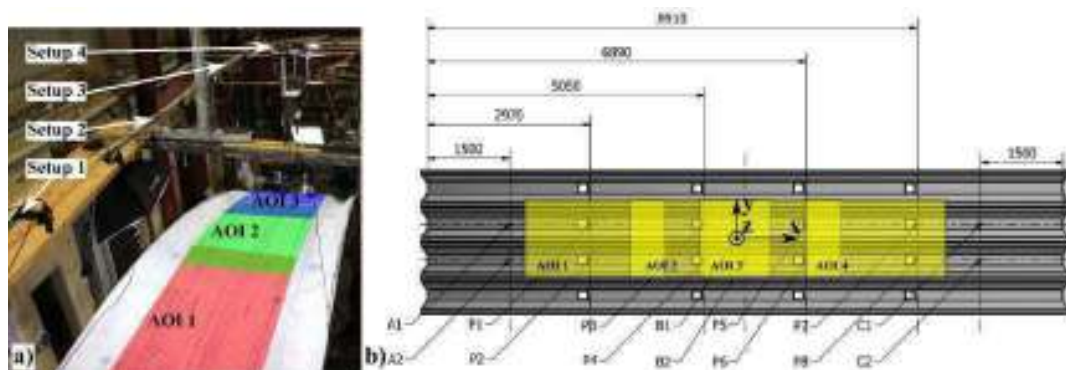

Figure 7. (**a**) Location of the cameras and field of views during the measurements; (**b**) scheme of the investigated segments of arch-shaped steel sheets with marked areas of interest (AOIs), characteristic points (for analysis) and orientation of coordinate system (top view) [4].

5.2. FEM Model of Segments of Arch-Shaped Steel Sheets

The geometry of the full-sized model has been adopted on the basis of the analysis performed in Subsection 4.2. The model with corrugation and waviness of the middle surfaces (model C according to the description from Section 4.2) was used for calculations. The full-sized numerical model is an image of the examined element in terms of dimensions and load mode.

In order to accurately simulate the load caused by snow cover, the kinematic extortion forced by controlled displacements of 16 points (at which load was applied) was used (Figure 7b, points A1, A2, B1, B2, C1, C2). Constraints utilized in FEM model (in particular rotational stiffness of supports) were updated through comparison with experimental data, and this process is described below.

5.3. Utilization of 3D DIC Measurements in Process of Validation of FEM Model of Segments of Section of Arch-Shaped Steel Sheets

Displacements of the chosen points (Figure 7b, points A1, A2, B1, B2, C1, C2) were derived on the basis of the multi-camera DIC analysis. In order to update the support conditions of the FEM model, a comparison between displacements' distribution obtained from the FEM model and multi-camera DIC system was made. In Figure 8, an exemplary comparison has been presented that shows half of maximum load. The FEM simulation comprises two supports on both ends of the arch. Both supports are modelled by a rotational elastic spring that allows the structural member to rotate (limited by rotational stiffness), but not to translate in any direction. As the first approximation, the rotational stiffness of supports is based on the simplified theoretical calculations. Subsequently, through comparison of experimental results and theoretical calculation, the value of rotational stiffness of elastic support was determined. The results of the comparison of experimental and numerical displacements after updating the numerical one at selected points is presented on a diagram of displacements towards 3 directions (U, V, W) in the function of force increment (Figure 9). The results of the comparison of DIC tests and FEM numerical analyses are presented as balance paths with reference to proper reference points. The directions of the displacements are referred to the coordinate system as in Figure 7b. The displacements are marked as follows: U(X), V(Y) and W(Z). The horizontal displacements U (X) — Figure 9a, i.e., in the arch plane are compatible in the reference points U (3, 4), U (5, 6) and U (7, 8), whereas balance path of the reference points U (1, 2) obtained in the tests diverge from those determined in calculations. The situation is similar in vertical

displacements W (Z)—Figure 9c. This means that the test element was deformed asymmetrically. The diagram comparing horizontal displacements of the reference points in the arch plane of V(Y)—Figure 9b proves that. The test model tilts erratically in the range up to 3 mm whereas the calculations show slight deviation of the reference points within 0.5 mm. The asymmetrical deformation of the test element is probably caused by imprecise assembly and slight deviations in the load symmetry. The computational model does not include random events related to the assembly or load mode. The only disorders of the geometry of the computational model are related to the introduction of geometrical imperfections, which only slightly change the symmetry of the displacements of the reference points.
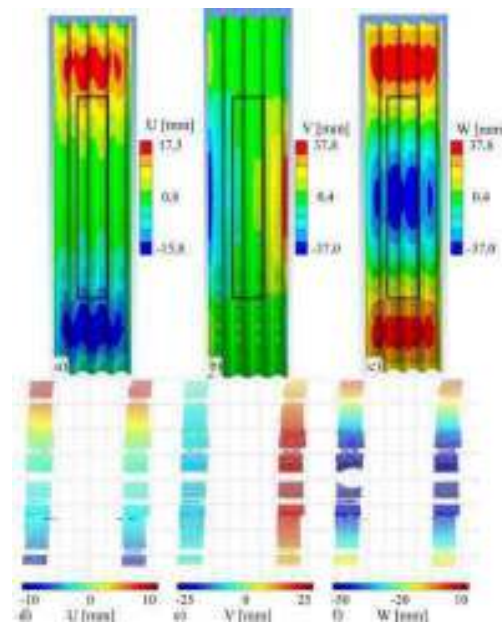

Figure 8. The comparison of displacements distribution: top view of displacements obtained from the finite element model (**a–c**), of the entire specimen, and experimental results (**d–f**) for the AOI covering the 7 m long area of lower surface (corrugated web according to Figure 1) of two middle arches. Rectangular areas marked with lines correspond to the areas on the experimental specimen that has the two middle arches that are being measured [4].
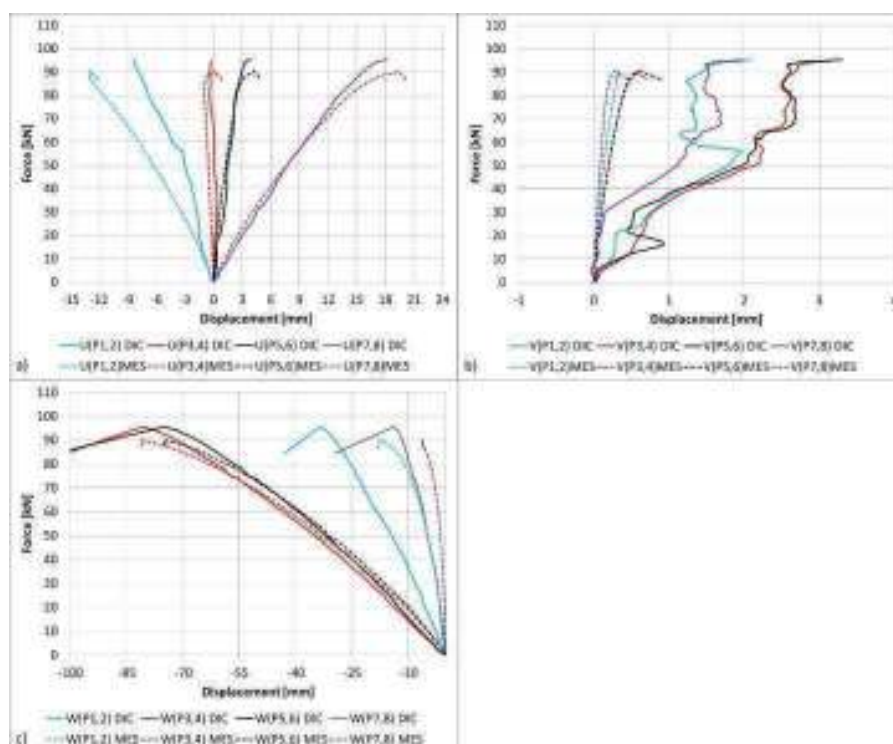
191

Figure 9. The comparison of load (**a**) U, (**b**) V, (**c**) W displacement functions obtained for numerical models and experimental data (results for referential points).

6. In Situ Investigation of Full-Scale Construction of Arch-Shaped Steel Sheets

Finally the full-scale construction made of arch-shaped self-supporting metal plates (Figure 1a) has been examined. The dimensions of the hall were ([span × length]/[height]) 18 × 18 m/7 m. Such a construction can be exposed to environmental loads caused by the presence of snow or wind [22,23] and changes of temperature.

6.1. Multi-Camera DIC System with Distributed Field of View

In order to cover the localization of points corresponding to the numerically predicted maximum displacements (caused by environmental loads), the measurements system consisted of three 3D DIC setups (six cameras in total). Each FOV of 3D DIC setup covered the area of 2.5 × 1.5 m and distance between neighboring AOIs was approximately 4 m. In order to perform the measurements in distributed FOV, the dedicated multi-camera DIC system was developed. This system and is described in detail in [16]. The multi-camera DIC system used in these measurements comprised six 5 MPx (2448 × 2048) Pointgrey cameras equipped with 8 mm focal length lenses. The cameras were connected to the control computer in order to synchronize the data acquisition procedure. The calibration procedure comprised two steps. In the first step, each 3D DIC system was calibrated with utilization of a standard chessboard calibration target. In the second calibration step, the transformation of individual coordinate systems of separate 3D DIC systems into a common coordinate system has been determined, with the additional support of a laser tracker [26]. Geometrical transformations were determined by using multiple positions of a fiducial marker, which was sequentially placed in the FOV of each 3D DIC setups. The 3D positions of the marker in local coordinate systems were determined with the use of three-dimensional computer vision algorithms [18]. Simultaneously, the positions of the marker in the global coordinate system were determined by a laser tracker. A global coordination system was related to the foundations of the building. Transformation parameters (rotation: Rx; Ry; Rz and translation: Tx; Ty; Tz) between local

and global coordinate systems were obtained by using the singular value decomposition (SVD) method [27]. The obtained accuracy of displacement measurements in each 3D DIC setup was below 0.3 mm (detailed description of calculation of displacement error is presented in [16]).

A multi-camera DIC system was placed on the 6 m high and 10 m wide buildings' temporary scaffolding (Figure 10), and the measurements were carried out for a few months (from March to October 2016). Therefore, the temperature influence on displacements of measurement setup was noticeable. In order to neutralize this influence, the displacements of the 3D DIC systems as a function of temperature, caused by the thermal expansions of aluminum scaffolding were measured by means of a laser tracker. The correction obtained was included in the results of displacement measurements. The temperature inside the hall was measured using a weather station.
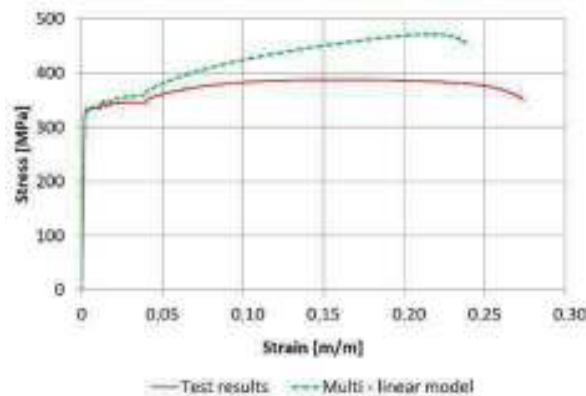

Figure 10. Stress–strain curves.

6.2. FEM Model of Full-Scale Construction

A model being the representation of the arch in the central part of the hall was used for calculations. The model consists of a single ABM 240 profile with the geometry adopted on the basis of the previous analyses. Material constants (modulus of elasticity, Poisson's modulus, shear modulus and coefficient of linear thermal expansion) have been adopted for structural analysis in accordance with EN 1993-1-1 standard [28].

The computation adopted an elastic-plastic multi-linear material model, determined according to the tests. The strength characteristics of steel were identified through a series of laboratory tests on 10 samples of steel sheet with a nominal thickness of 1.40 mm. The obtained mean yield strength amounted to f_y = 340 MPa, and ultimate strength was f_u = 390 MPa. A typical course of the stress–strain relationship in a single test, and elastic-plastic multi–linear material model is presented in Figure 10.

The test data were implemented via transformation functions in the σ_{true}–ε_{ln} system (elastic-plastic multi-linear material model) [3] according to the Equations (1), (2) presented below:

$$\varepsilon_{ln} = ln\big(1 + \varepsilon_{eng}\big) \qquad (1)$$

$$\sigma_{true} = \sigma_{eng}\big(1 + \varepsilon_{eng}\big) \qquad (2)$$

where:

ε_{ln}—relative logarithmic strain,

σ_{true}—true stress,

σ_{eng}—engineering stress (test result),

ε_{eng}—engineering strain (test result).

The free ends of the model are propped up in joints (a possibility to rotate towards X axis). The remaining degrees of freedom are blocked. On the side edges, boundary conditions are assumed that

map the cooperation of the adjacent profiles (remote point). In the remote point system, displacement towards Z and Y are released, the remaining degrees of freedom are blocked. Due to lack of snow during the measurement period in winter, and the negligible influence of the pressure of wind on construction, only the thermal load was considered.

The purpose of the test was to determine the displacements and stress of the characteristic points located on the surface of the test object exposed to the action of thermal loads. For numerical calculations, the external and internal temperature of arch structure from three areas (corresponding to measured AOIs) was adopted. The temperature was measured precisely with the utilization of thermoelements.

6.3. Utilization of 3D DIC Measurements for Validation of FEM Model of Full-Scale Construction of Arch-Shaped Steel Sheets

Displacement measurements were taken in AOI1, AOI2 and AOI3 areas and 3 reference points were selected for each area (Figure 11) to validate the numerical model, 9 points in total. The tests lasted for several months, however validation of the numerical model was limited to a much shorter period. Below (Figures 12 and 13) we present exemplary results of measurements, which were performed in 12 h and 25 min. during a cold night and sunny day in April (largest external as well as internal temperature gradient occurred). The obtained results allowed to validate the numerical model, that can be used to calculate load capacity and stability of the coverings of the thin-walled arch-shaped sheet metals.
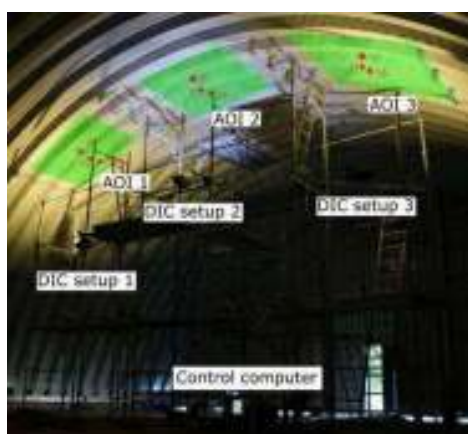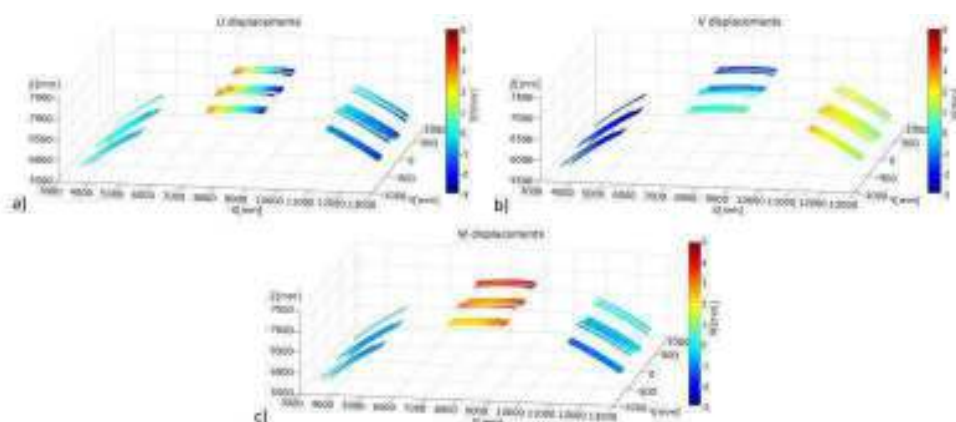

Figure 11. Measurement set-up.

Figure 12. Exemplary results of the measurements stitched in the global coordinate system: (**a**) U displacement map, (**b**) V displacement map, (**c**) W displacement map [16].
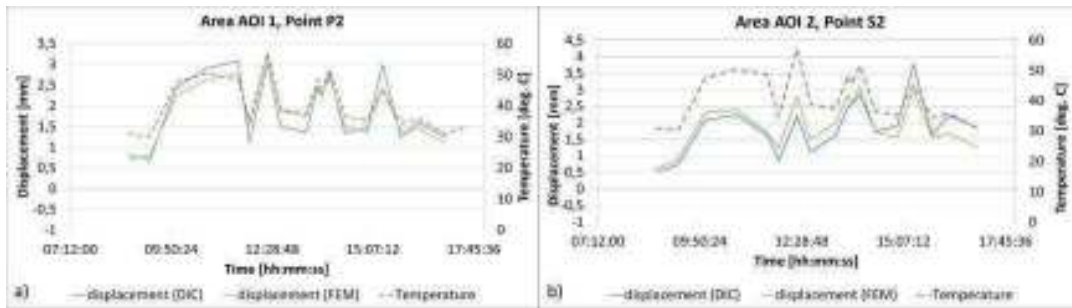
194

Figure 13. The comparison of displacement functions obtained for numerical models and experimental data, (**a**) point P2 (AOI 1), (**b**) point P2 (AOI 2).

Figure 13 presents the results of the displacements measurement and those of numerical calculations for the chosen reference points from the analysed measurement areas. The results were juxtaposed in relation to the change of temperature depending on the time of measurement. Displacements measured and determined on the basis of calculations are compatible in terms of increment directions and have similar values. Additionally, Figure 14 shows the analysis of the discrepancies of the calculation results and the test results depending on the value of temperature gradient. A certain regularity may be noticed in the distribution of discrepancies of the results. At high temperature gradients (over 18 °C), the discrepancies of neither test nor calculations results exceed 10%, at lower temperature gradients—the discrepancies of the tests results are much higher. This is probably due to the fact that numerical model did not take into account the boundary conditions related to the cooperation of the adjacent profiles, i.e., the friction between the cooperating profiles was not included in the calculations. Assuming that the friction at the jointing of the adjacent profiles has a constant value, its influence is much more visible at small displacements than at large displacements related to the effect of the higher temperature gradient.
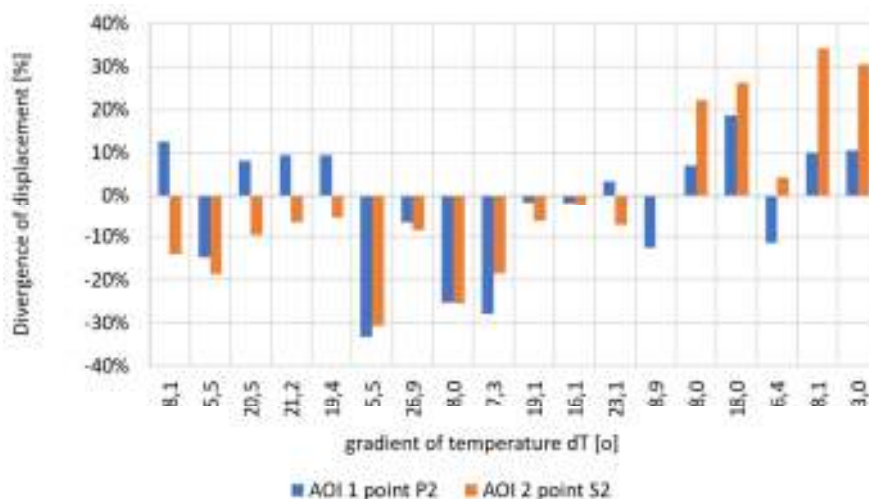

Figure 14. The analysis of the divergence of the measurement and calculations results.

7. Conclusions

So far, the DIC method applied in the construction industry has been considered a prototypical solution, more likely intended for testing/monitoring the elements of buildings, not for proper measurements used in a certification process in accordance with accepted standards. The methodology presented in this paper has shown the possibility and advantages of replacing conventional measuring methods based at point extensometers and applied at different stages of the

analysis and testing of complicated building structures by applying the 3D DIC method. Its potential lies not only in the capability to measure in full field of view, but mostly in the possibility to digitally link the measurement with the numerical calculations, thus creating efficient hybrid experimental-numerical system with huge information resources useful, for instance, in the process of design optimization, FEM validation or diagnostics of complicated building structures. It should be pointed out that the presented methodology requires a complex measurement setup and is labor-intensive, therefore it should be utilized in the case of investigation of truly complex structures, in which stress concentrations can occurr in unexpected locations.

The procedure presented in Figure 2 and explained in detail in Sections 4–6 concerns the way to implement the particular stages when analysing self-supporting arch-shaped structures from profiled steel sheets with the use of numerical calculation methods supported by physical experiments. Each stage is used to determine and validate the optimal procedure to be applied in a FEM which, in the opinion of the authors, adequately indicates the solution to the most important problems related to the design of arch-shaped structures. The multistage research verification process enables the development of a reliable numerical model that is very useful and allows for the analysis of arch-shaped profiled steel sheets at diversified geometry and any load conditions.

The methodology presented in the paper may be used to determine the strength and functional properties of various varieties of the K-span system, which are required during the process of implementing the product for use in the construction industry (Polish and European technical assessments). The material presented in the paper may also be used in the future to develop an annex to the national standards in question regarding the design of thin-walled elements.

Author Contributions: Conceptualization, M.K.; methodology, K.M., A.P. and M.M.; investigation K.M., M.M. and P.W.; formal analysis, K.M., M.M. and A.P., validation, K.M. and A.P.; supervision, M.K.; funding acquisition, M.K. and A.P.; visualization, K.M. and A.P.; writing—original draft, K.M. and A.P.; writing—review and editing K.M., M.K. and A.P.
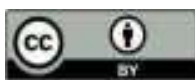
Conflicts of Interest: The authors declare no conflict of interest.

References

1. Piekarczuk, A.; Malesa, M.; Kujawinska, M.; Malowany, K. Application of hybrid FEM-DIC method for assessment of low cost building structures. *Exp. Mech.* **2012**, *52*, 1297–1311.
2. Piekarczuk, A.; Malowany, K.; Więch, P.; Kujawińska, M.; Sulik, P. Stability and bearing capacity of arch-shaped corrugated shell elements: Experimental and numerical study. *Bull. Pol. Acad. Sci.* **2015**, *64*, 113–123.
3. Piekarczuk, A.; Więch, P.; Malowany, K. Numerical investigation into plastic hinge formation in arched corrugated thin-walled profiles. *Thin Walled Struct.* **2017**, *119*, 13–21.
4. Malowany, K.; Malesa, M.; Piekarczuk, A.; Kujawińska, M.; Skrzypczak, P.; Więch, P. Application of 3D digital image correlation for development and validation of FEM model of self-supporting metal plates structures. *Proc. Spie Int. Soc. Opt. Eng.* **2016**, *9803*, 98033W.
5. Cybulski, R.; Walentyński, R.; Cybulska, M. Local buckling of cold-formed elements used in arched building with geometrical imperfections. *J. Constr. Steel Res.* **2014**, *96*, 1–13.
6. Laermann, K.H. Hybrid techniques in experimental solid mechanics. In *Optical Methods in Experimental Solid Mechanics*; Springer: Vienna, , 2000; pp. 1–72.
7. Sebastian, C.; Patterson, E.; Ostberg, D. Comparison of numerical and experimental strain measurements of a composite panel using image decomposition *Appl. Mech. Mater.* **2011**, *70*, 63–68.
8. Lampeas, G.N.; Pasialis, V.P. A hybrid framework for nonlinear dynamic simulations including full- ield optical measurements and image decomposition algorithms. *J. Strain Anal. Eng. Des.* **2013**, *48*, 5–15.
9. Malesa, M.; Malowany, K.; Tomczak, U.; Siwek, B.; Kujawińska, M.; Siemińska-Lewandowska, A. Application of 3D digital image correlation in maintenance and process control in industry. *Comput. Ind.* **2013**, *64*, 1301–1315.

10. Mechelke, K.; Kersten, T.P.; Lindstaedt, M. Comparative investigations into the accuracy behaviour of the new generation of terrestrial laser scanning systems. *Opt. 3D Meas. Tech. VIII* **2007**, *1*, 319–327.

11. Yang, H.; Xu, X.; Neumann, I. The benefit of 3D laser scanning technology in the generation and calibration of FEM models for health assessment of concrete structures *Sensors* **2014**, *14*, 21889–21904.

12. Xu, X.; Bureick, J.; Yang. H.; Neumann, I. TLS-based composite structure deformation analysis validated with laser tracker. *Compos. Struct.* **2018**, *202*, 60–65.

13. Malesa, M.; Malowany, K.; Pawlicki, J.; Kujawinska, M.; Skrzypczak, P.; Piekarczuk, A.; Lusa, T.; Zagorski, A. Non-destructive testing of industrial structures with the use of multi-camera digital image correlation method. *Eng. Fail. Anal.* **2016**, *69*, 122–134.

14. Shao, X.; Dai, X.; Chen, Z.; Dai, Y.; Dong, S.; He, X. Calibration of stereo-digital image correlation for deformation measurement of large engineering components *Meas. Sci. Technol.* **2016**, *27*, 125010.

15. Dong, S.; Yu, S.; Huang, Z.; Song, S.; Shao, X.; Kang, X.; He, X. Target-based calibration method for multifields of view measurement using multiple stereo digital image correlation systems *Opt. Eng.* **2017**, *56*, 124102.

16. Malowany, K.; Malesa, M.; Kowaluk, T.; Kujawinska, M. Multi-camera digital image correlation method with distributed fields of view. *Opt. Lasers Eng.* **2017**, *98*, 198–204.

17. Pan, B. Digital image correlation for surface deformation measurement: Historical developments, recent advances and future goals. *Meas. Sci. Technol.* **2018**, *29*, 082001.

18. Sutton, M.; Orteu, J.-J.; Schreier, H. *Image Correlation for Shape, Motion and Deformation Measurements: Basic Concepts, Theory and Applications*; Springer: New York, NY, USA, 2009.

19. Roye, K.L. *Metal Building Construction Using the MIC-240 ABM K-Span Machine*; Naval Postgraduate School: Monterey, CA, USA, 1996.

20. Wang, Y.-Q.; Sutton, M.A.; Ke, X.-D.; Schreier, H.W. Error Propagation in Stereo Vision: Part I: Theoretical Developments *Exp. Mech.* **2011**, *51*, 405–422.

21. Ke, X.-D.; Schreier, H.W.; Sutton, M.A.; Wang, Y.-Q. Error propagation in stereo vision: Part II: Experimental validation *Exp. Mech.* **2011**, *51*, 423–441.

22. EN 1991-1-3 Eurocode 1: Actions on Structures—Part 1-3: General Actions—Snow Loads; European Committee for Standardization, The European Union: Brussels, Belgium, 2003.

23. EN 1991-1-4 Eurocode 1: Actions on Structures—Part 1-4: General Actions—Wind Action; European Committee for Standardization, The European Union: Brussels, Belgium, 2005.

24. Orteu, J.-J.; Bugarin, F.; Harvent, J.; Robert, L.; Velay, V. Multiple camera instrumentation of a single point incremental forming process pilot for shape and 3D displacement measurements: Methodology and results. *Exp. Mech.* **2011**, *51*, 625–639.

25. Chen, X.; Yang, L.; Xua, N.; Xie, X.; Sia, B.; Xu, R. Cluster approach based multi-camera digital image correlation: Methodology and its application in large area high temperature measurement. *Opt. Lasers Technol.* **2014**, *57*, 318–326.

26. Muralikrishnan, B.; Phillips, S.; Sawyer, D. Laser trackers for large-scale dimensional metrology: A review, *Precis. Eng.* **2016**, *44*, 13–28.

27. Besl, P.J.; McKay, N.D. A method for registration of 3-d shapes *IEEE Trans. Pattern Anal. Mach. Intell.* **1992**, *14*, 239–256.

28. EN 1993-1-1: Eurocode 3: Design of Steel Structures—Part 1-1: General Rules and Rules for Buildings; European Committee for Standardization, The European Union: Brussels, Belgium, 2005.